TEMPORAL FEATURES IN RESTING STATE FMRI DATA

EDITED BY: Xiaoping Philip Hu and Nanyin Zhang
PUBLISHED IN: Frontiers in Neuroscience

frontiers Research Topics

frontiers

ISSN 1664-8714
ISBN 978-2-88966-408-5
DOI 10.3389/978-2-88966-408-5

About Frontiers

Frontiers is more than just an open-access publisher of scholarly articles: it is a pioneering approach to the world of academia, radically improving the way scholarly research is managed. The grand vision of Frontiers is a world where all people have an equal opportunity to seek, share and generate knowledge. Frontiers provides immediate and permanent online open access to all its publications, but this alone is not enough to realize our grand goals.

Frontiers Journal Series

The Frontiers Journal Series is a multi-tier and interdisciplinary set of open-access, online journals, promising a paradigm shift from the current review, selection and dissemination processes in academic publishing. All Frontiers journals are driven by researchers for researchers; therefore, they constitute a service to the scholarly community. At the same time, the Frontiers Journal Series operates on a revolutionary invention, the tiered publishing system, initially addressing specific communities of scholars, and gradually climbing up to broader public understanding, thus serving the interests of the lay society, too.

Dedication to Quality

Each Frontiers article is a landmark of the highest quality, thanks to genuinely collaborative interactions between authors and review editors, who include some of the world's best academicians. Research must be certified by peers before entering a stream of knowledge that may eventually reach the public - and shape society; therefore, Frontiers only applies the most rigorous and unbiased reviews.
Frontiers revolutionizes research publishing by freely delivering the most outstanding research, evaluated with no bias from both the academic and social point of view. By applying the most advanced information technologies, Frontiers is catapulting scholarly publishing into a new generation.

What are Frontiers Research Topics?

Frontiers Research Topics are very popular trademarks of the Frontiers Journals Series: they are collections of at least ten articles, all centered on a particular subject. With their unique mix of varied contributions from Original Research to Review Articles, Frontiers Research Topics unify the most influential researchers, the latest key findings and historical advances in a hot research area! Find out more on how to host your own Frontiers Research Topic or contribute to one as an author by contacting the Frontiers Editorial Office: researchtopics@frontiersin.org

TEMPORAL FEATURES IN RESTING STATE FMRI DATA

Topic Editors:
Xiaoping Philip Hu, University of California, Riverside, United States
Nanyin Zhang, Pennsylvania State University (PSU), United States

Citation: Hu, X. P., Zhang, N., eds. (2021). Temporal Features in Resting State fMRI Data. Lausanne: Frontiers Media SA. doi: 10.3389/978-2-88966-408-5

Table of Contents

frontiers in Neuroscience

EDITORIAL
published: 08 December 2020
doi: 10.3389/fnins.2020.616513

Editorial: Temporal Features in Resting State fMRI Data

Nanyin Zhang[1]* *and Xiaoping Hu*[2]*

[1] Pennsylvania State University, University Park, PA, United States, [2] University of California, Riverside, Riverside, CA, United States

Keywords: resting-state fMRI, temporal features, functional connectivity (FC), brain network, neural circuit

Editorial on the Research Topic

Temporal Features in Resting State fMRI Data

It has become increasingly clear that functional connectivity derived from resting-state functional magnetic resonance imaging (rsfMRI) data is not stationary, but contains ample dynamic information (Hutchison et al., 2013). However, how to extract and quantify the temporal features in rsfMRI data, and how these features help us better understand the function of neural circuitries and networks in health and disease remain active Research Topics. This special issue includes a group of papers specifically investigating temporal features in rsfMRI data.

The utilization of temporal features in rsfMRI data has considerably enhanced our understanding of the neuropathophysiology and improved the diagnosis of brain disorders. Zhu et al. investigated the temporal variability on the connectivity profiles in Parkinson's disease (PD) using a sliding-window method. They found that PD patients exhibited greater temporal variability in both cortical and subcortical networks. Importantly, this dynamic connectivity measure was associated with the severity of clinical symptoms in patients (Zhu et al.). In another study, by integrating the strength and temporal variability of complex-network properties derived from effective connectivity networks in patients with post-traumatic stress disorder (PTSD), patients with PTSD with comorbid mild-traumatic brain injury (mTBI) and healthy controls, Rangaprakash et al. identified dysregulation of prefrontal regions over subcortical and visual regions in PTSD/mTBI. These patients displayed lower variability over time in all network properties, which can be an indicator of poorer flexibility. Importantly, authors show that network properties, including dynamic ones, of the prefrontal-subcortical pathway are not only significantly correlated to symptom severity and neurocognitive performance, but also provide predicative value in classifying these disorders (Rangaprakash et al.). Furthermore, using a novel high-order dynamic functional connectivity networks (D-FCNs), Zhao et al. achieved a classification accuracy of 83% for autism spectrum disorder (ASD). This method can overcome the problems of conventional sliding-window-based D-FCNs, such as lack of high-level interactions across regions and the temporal mismatching issue (Zhao et al.).

Temporal features in rsfMRI data are also tightly linked to physiology. For instance, converging evidence suggests that arousal may have profound effects on rsfMRI signals and connectivity dynamics. Gu et al. reviewed the relationship between rsfMRI and brain arousal. Authors also discussed the potential impact of arousal on spurious relationship between functional connectivity measures and physiology/behavior (Gu et al.). In addition, Wang et al. advanced the capacity of individual identification based on rsfMRI data by including temporal features in convolutional recurrent neural networks (ConvRNN). They demonstrate that ConvRNN can achieve a higher identification accuracy than conventional RNN (Wang et al.).

OPEN ACCESS

Edited and reviewed by:
Nathalie Just,
INRA Centre Val de Loire, France

***Correspondence:**
Nanyin Zhang
nuz2@psu.edu
Xiaoping Hu
xhu@engr.ucr.edu

Specialty section:
This article was submitted to Brain Imaging Methods, a section of the journal Frontiers in Neuroscience

Received: *12 October 2020*
Accepted: *19 November 2020*
Published: *08 December 2020*

Citation:
Zhang N and Hu X (2020) Editorial: Temporal Features in Resting State fMRI Data. Front. Neurosci. 14:616513. doi: 10.3389/fnins.2020.616513

Methodology development continues to improve our capacity to extract temporal features of rsfMRI. Zhou et al. proposed a protocol designed to track dynamical whole-brain functional connectivity states, using signed community clustering with the optimized modularity by two-step procedures. This method makes it possible to track rapid dynamical change in functional connectivity (Zhou et al.). Chen et al. constructed brain networks using unwrapped fMRI phase image, instead of the magnitude of fMRI data conventionally used. The functional network connectivity matrix obtained based on phase fMRI was more sparsely distributed across the brain, with connections having more balanced positive/negative correlations. Their findings open a new avenue to understanding brain function connectivity (Chen et al.). Yang et al. went beyond the conventional method of regressing out motion parameters, and developed an automated convolutional neural network (CNN) model to obtain optimal motion regressors, which can better reduce motion-related artifacts.

Finally, we have a better understanding of temporal features in rsfMRI data. Guan et al. studied the linearity and stationarity of fMRI time series in individual resting-state brain networks, and found that different networks had distinct properties of non-stationarity and non-linearity. Nezafati et al. examined the complexity of regional brain activity measured by rsfMRI data using sample entropy. They found that the brain exhibited significant spatial heterogeneity in levels of entropy/complexity. In addition, the entropy of brain activity was also modulated by task performance (Nezafati et al.).

Taken together, the studies in this special issue demonstrate the importance of investigating temporal features in rsfMRI data, and exemplify the potential impact of applying these features to better understand brain function in health and disease.

AUTHOR CONTRIBUTIONS

NZ and XH wrote the editorial. Both authors contributed to the article and approved the submitted version.

REFERENCES

Hutchison, R. M., Womelsdorf, T., Allen, E. A., Bandettini, P. A., Calhoun, V. D., Corbetta, M., et al. (2013). Dynamic functional connectivity: promise, issues, and interpretations. *Neuroimage* 80, 360–378. doi: 10.1016/j.neuroimage.2013.05.079

Conflict of Interest: The authors declare that the research was conducted in the absence of any commercial or financial relationships that could be construed as a potential conflict of interest.

frontiers in Neuroscience

ORIGINAL RESEARCH
published: 19 February 2019
doi: 10.3389/fnins.2019.00080

Abnormal Dynamic Functional Connectivity Associated With Subcortical Networks in Parkinson's Disease: A Temporal Variability Perspective

Hong Zhu[1†], Juan Huang[2†], Lifu Deng[3], Naying He[2], Lin Cheng[3], Pin Shu[1], Fuhua Yan[2], Shanbao Tong[3], Junfeng Sun[1] and Huawei Ling[2*]*

[1] Shanghai Med-X Engineering Research Center, School of Biomedical Engineering, Shanghai Jiao Tong University, Shanghai, China, [2] Department of Radiology, Ruijin Hospital, Shanghai Jiao Tong University School of Medicine, Shanghai, China, [3] School of Biomedical Engineering, Shanghai Jiao Tong University, Shanghai, China

Parkinson's disease (PD) is a neurodegenerative disease characterized by dysfunction in distributed functional brain networks. Previous studies have reported abnormal changes in static functional connectivity using resting-state functional magnetic resonance imaging (fMRI). However, the dynamic characteristics of brain networks in PD is still poorly understood. This study aimed to quantify the characteristics of dynamic functional connectivity in PD patients at nodal, intra- and inter-subnetwork levels. Resting-state fMRI data of a total of 42 PD patients and 40 normal controls (NCs) were investigated from the perspective of the temporal variability on the connectivity profiles across sliding windows. The results revealed that PD patients had greater nodal variability in precentral and postcentral area (in sensorimotor network, SMN), middle occipital gyrus (in visual network), putamen (in subcortical network) and cerebellum, compared with NCs. Furthermore, at the subnetwork level, PD patients had greater intra-network variability for the subcortical network, salience network and visual network, and distributed changes of inter-network variability across several subnetwork pairs. Specifically, the temporal variability within and between subcortical network and other cortical subnetworks involving SMN, visual, ventral and dorsal attention networks as well as cerebellum was positively associated with the severity of clinical symptoms in PD patients. Additionally, the increased inter-network variability of cerebellum-auditory pair was also correlated with clinical severity of symptoms in PD patients. These observations indicate that temporal variability can detect the distributed abnormalities of dynamic functional network of PD patients at nodal, intra- and inter-subnetwork scales, and may provide new insights into understanding PD.

Keywords: Parkinson's disease, dynamic functional connectivity, resting-state fMRI, subcortical networks, temporal variability

OPEN ACCESS

Edited by:
Nanyin Zhang,
The Pennsylvania State University, United States

Reviewed by:
Rui Li,
Institute of Psychology (CAS), China
Changwei Wesley Wu,
Taipei Medical University, Taiwan

***Correspondence:**
Junfeng Sun
jfsun@sjtu.edu.cn
Huawei Ling
lhw10427@rjh.com.cn

† These authors have contributed equally to this work

Specialty section:
This article was submitted to Brain Imaging Methods, a section of the journal Frontiers in Neuroscience

Received: *02 August 2018*
Accepted: *25 January 2019*
Published: *19 February 2019*

Citation:
Zhu H, Huang J, Deng L, He N, Cheng L, Shu P, Yan F, Tong S, Sun J and Ling H (2019) Abnormal Dynamic Functional Connectivity Associated With Subcortical Networks in Parkinson's Disease: A Temporal Variability Perspective. Front. Neurosci. 13:80. doi: 10.3389/fnins.2019.00080

INTRODUCTION

Parkinson's disease (PD) is a progressive neurodegenerative disease that affects millions of people around the world. The prominent symptoms in PD are the motor deficits including tremor, rigidity, and bradykinesia, which are mainly due to the loss of dopaminergic neurons in the substantia nigra (Kalia and Lang, 2015; Ma et al., 2016). Previous studies had proposed that the dysfunction of corticostriatal network pathways and neural circuits is related to the impairments in PD (Hacker et al., 2012; Agosta et al., 2013; Luo et al., 2014; Amboni et al., 2015; Alia et al., 2016). Despite being extensively investigated, mechanisms underlying disturbances in PD are still poorly understood.

The past decade has seen remarkable growth of network neuroscience and neuroimaging techniques and their applications to abnormal brain connectivity in psychiatric and neurological disorders. Several previous studies highlighted that PD could be considered as a disease related to the disruptions in several networks using diffusion tensor imaging (DTI) (Melzer et al., 2013; Lopes et al., 2017), resting-state functional magnetic resonance imaging (fMRI) (Luo et al., 2014), task fMRI (Shine et al., 2013b) and other imaging techniques (Brooks and Pavese, 2011). Functional network analysis based on resting-state fMRI data, accounting for the intrinsic blood oxygen level-dependent (BOLD) fluctuations, offers an effective tool for characterizing interactions between brain regions and quantifying abnormal organization of brain network in disorders (Bullmore and Sporns, 2009; Smith et al., 2009, 2011). Previous studies on large-scale network of PD patients by graph theoretic analysis revealed disruptions in the topological properties of brain networks and these network measures have been demonstrated to serve as potential biomarkers of PD for clinical diagnosis (Amboni et al., 2015). Furthermore, altered modular organization of functional brain networks in PD patients has also been reported (Ma et al., 2016; Peraza et al., 2017), implying an abnormal functional integration of PD.

However, the majority of earlier studies have adopted a "static" point of view, whereas functional connectivity (FC) between regions are actually associated with dynamic brain activity over time (Hutchison et al., 2013; An et al., 2017). Dynamic functional connectivity (dFC) analysis has been directed to assess relevant FC fluctuations and examine how functional organization evolves over time. It sheds new insights on the dynamic spatiotemporal organization of resting brain activity and captures FC alterations induced by disease pathologies (Preti et al., 2016; Khambhati et al., 2017). For example, previous studies have found that Schizophrenia (SZ) patients displayed within-network disruptions of the DMN (Du et al., 2016) as well as weaker across-network connectivity between DMN and other resting-state networks (RSNs) (Rashid et al., 2014; Su et al., 2016). In addition, the dynamic connectivity patterns have served as features to gain better identification output in the classification of MCI subjects (Wee et al., 2016) and of autism patients (Price et al., 2014) than the standard static approaches. These results suggest that the abnormal network characteristics of PD may emerge from dynamic functional connections that cannot be completely captured by static approaches and may help deepen our understanding of this disease.

Despite these applications, alterations in the dynamic properties of PD individuals still remain largely unknown. Kim et al. (2017) first investigated the temporal states of dFC and variability of network topology in PD patients using k-means clustering, and found that PD patients showed a decrease in the sparsely connected State I, paralleled by an increase in the stronger interconnected State II, suggesting the altered functional segregation and abnormal global integration in brain networks. Sourty et al. (2016) employed Product Hidden Markov Models (PHMM) to assess the connectivity state changes between a set of RSNs in dementia with Lewy bodies, a disease sharing similar features to PD, and figured out networks (i.e., occipito-parieto-frontal network, the medial occipital network and the right fronto-parietal network) related to impairment of cognitive function in patients. However, these studies mainly focused on the connectivity state changes of the whole brain, ignoring the dynamic connectivity profile of particular brain regions. A recent work (Zhang et al., 2016) investigated the temporal properties of dFC by defining the temporal variability of FCs associated with a specific brain region, and the temporal variability reveled a strong correlation with BOLD/EEG activity. This approach allows localization of regions showing significant variability between groups, thus helping to reveal the abnormality of regional dynamics of functional brain networks in various brain diseases. Another work (Jie et al., 2018) integrated both temporal and spatial variabilities of dynamic functional networks for automatic diagnosis of Alzheimer's Disease and boosted the diagnosis performance, demonstrating that the spatio-temporal interaction patterns can provide important information on the underlying nature of neurodegenerative disease. Actually, PD is a disease associated with a disruption across diffuse areas of brain and interactions of multiscale organization. However, the temporal properties of subnetworks (e.g., the intra- and inter-network variability) have not been investigated yet. Temporal variability may help elucidate the aberrant changes underlying PD patients from the perspective of regional dynamics of functional brain networks. A systematic examination of dFC patterns and temporal variability in aspects of nodal, intra- and inter- subnetworks may further deepen our understanding of PD.

In this study, we performed dFC analysis built on non-overlapping networks to investigate the aberrant dFC patterns in PD patients. With a focus on temporal variability of FC profiles, we systematically examined the dFC changes at nodal, intra- and inter- subnetwork levels. Our major goal was to demonstrate whether: (1) the temporal variability could characterize the underlying alterations in the PD cohort and/or (2) the changes in temporal variability could account for some clinical symptoms of PD.

MATERIALS AND METHODS

Participants and Assessment

Forty-four PD subjects were recruited from Ruijin Hospital affiliated to Shanghai Jiao Tong University. The inclusion criteria

included: (i) a diagnosis of PD without any record of other neurological or psychiatric disorders; (ii) age ≥ 45 years; (iii) Mini Mental State Examination [MMSE (Folstein et al., 1975)] ≥ 24; (iii) no depressive symptoms [evaluated by Beck Depression Inventory (BDI) (Beck et al., 1961)]. Clinical evaluation was assessed with Hoehn and Yahr (H-Y) score (Hoehn and Yahr, 1998) for the disease stage and the Unified Parkinson's Disease Rating Scale-Part III (UPDRS-III) (Chai et al., 2017) for severity of motor symptoms. Forty-three normal controls (NCs) were also included for the study. Three normal participants with head motion >2 mm of translation or >2 degree of rotation and two PD patients with poor co-registration in cerebellum were excluded in the following analysis (see section "Data Preprocessing" for details), leaving 42 patients and 40 normal controls for analysis. The relevant demographic and clinical information are summarized in **Table 1**. This study was carried out in accordance with the recommendations of the "ethics committee of Ruijin Hospital, Shanghai Jiao Tong University School of Medicine, Shanghai, China" with written informed consent from all subjects.

MRI Acquisition

Data acquisition was carried out on a GE 3.0 T HDxt MRI scanner with an 8-channel phased-array head coil. High-resolution T1-weighted MRI scans were acquired using a fast, spoiled gradient echo sequence (FSPGR) with the following parameters: repetition time (TR) = 5.528 ms, echo time (TE) = 1.74 ms, matrix size = 256 × 256, flip angle = 12°, slice thickness = 1 mm, 196 sagittal slices. A total of 210 volumes of resting-state fMRI data were acquired using an EPI sequence with the following parameters: TR = 2000 ms, TE = 30 ms, matrix size = 64 × 64, flip angle = 90°, voxel size = 3.75 × 3.75 × 4 mm^3. Subjects were required to remain still and awake with eyes closed during the scan.

Data Preprocessing

Preprocessing of fMRI data was performed using the DPARSF toolbox (Yan and Zang, 2010). The first 10 volumes of each functional time series were discarded considering instability of the initial MRI signal and adaptation of participants to the circumstance, leaving 200 volumes in total for processing as follows: slice-timing, realignment to the mean image, co-registration to the T1 image, motion correction, normalized to a standard template (Montreal Neurological Institute), reslicing to 3 × 3 × 3 mm^3, spatial smoothing (FWMH = 6 mm) and band pass filtered (0.01–0.1 Hz). Finally, the nuisance covariates, including 24 head motion parameters, white matter signal, and CSF signal were regressed out. The resulting time courses were used for the following brain network construction and analysis. In order to limit the impact of head motion, we excluded the subjects with head motion greater than 2 mm of translation motion or more than 2 degrees of rotation.

TABLE 1 | Demographic data on patients and normal controls.

	PD (n = 42)	NC (n = 40)	p value
Gender men/women	23M, 19F	21M, 19F	0.837
Age (years)	61.14(7.13)	62.68 (5.73)	0.288
UPDRS-III (motor)	15.50(6.36)	–	–
Disease duration (years)	2.96(1.80)	–	–
Hoehn and Yahr (H-Y) score	1.33(0.45)	–	–

All data are given as mean (standard deviation). Chi-square test was used to test differences in gender distribution; two sample t-tests were used for other variables. PD = Parkinson's disease; NC = Normal controls; UPDRS-III = Unified Parkinson's Disease Rating Scale-Part III.

Definition of Functional Brain Networks

We adopted the spherical 264 functional Region of Interests (ROIs) defined by Power et al. (2011) across cortical, subcortical, and cerebellar structures, and extracted a representative BOLD time series by averaging signal in all voxels within each ROI. These brain regions were defined by resting-state FC mapping and multiple task fMRI meta-analysis, ensuring the functional significance of network nodes. In brain network analysis, each ROI was defined as a node, and the functional connectivity between ROIs was estimated from the corresponding representative BOLD time series. Consistent with previous study (Cole et al., 2013), the whole brain were mapped into 13 putative functional modules, including sensorimotor (SMN), default mode (DMN), cingulo-opercular (CON), fronto-parietal (FPN), subcortical, salience (SAN), auditory, visual, ventral attention (VAN), dorsal attention (DAN), memory retrieval, cerebellum, and uncertain networks (**Figure 1A**). This parcellation offers a comprehensive view for the study of functional brain modules, allowing to identify connectivity patterns and interactions between different modules. In this study, we would mainly report and discuss the results related to the 12 main networks but paying no attention to the "Uncertain" network, as it does not constitute specific cortical networks with explicable function.

For better interpretation for the anatomical location of specific regions, the Automated Anatomical Labeling (AAL) atlas (Tzouriomazoyer et al., 2002) was also used in this study.

Temporal Variability

For each participant, dFC were computed based on sliding temporal window approach. Following the strategy in Zhang's work (Zhang et al., 2016), we used segments of BOLD time series without overlapping to calculate temporal variability (nodal, intra- and inter-network variability). Briefly, the entire BOLD time series for each subject was divided into non-overlapping windows. Then within each window, connectivity between each pair of nodes was estimated by the Pearson's correlation coefficients of the BOLD time series (**Figure 1B**).

Nodal Variability

To characterize the dynamic configuration of a specific region across all time windows, we calculated the temporal variability of each node (Mueller et al., 2013; Zhang et al., 2016). For a given region k, the connectivity profile at time window i can be denoted as $F_{i,k}$, which is a vector with M values that describes the connection map based on the connectivity between region k with all other regions. Then the connectivity vectors in different

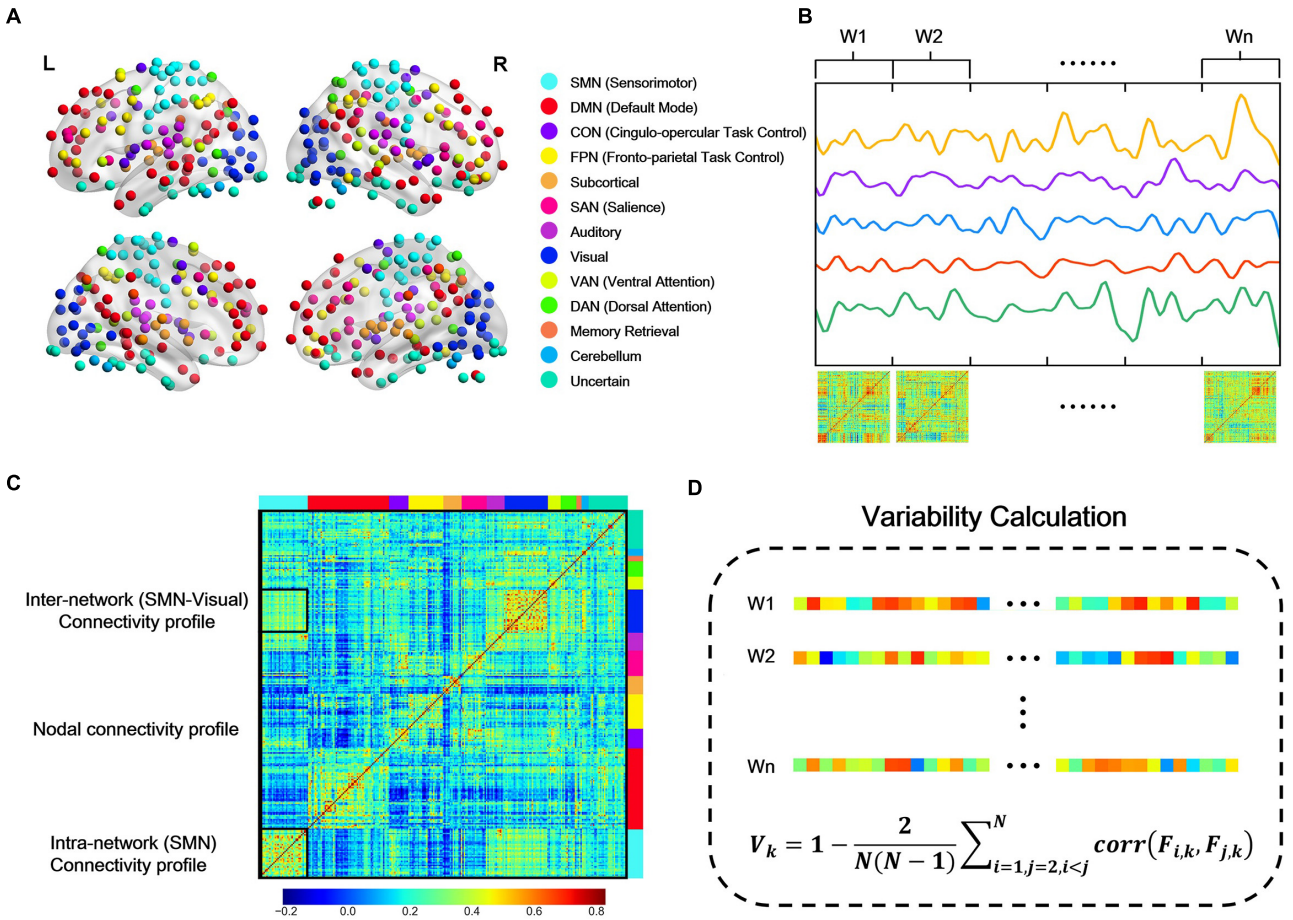

FIGURE 1 | Schematic overview of the temporal variability calculation. **(A)** Network partition of 264 putative functional regions defined by Power et al. (2011) L, Left; R, right. **(B)** Each regional BOLD signal was segmented into non-overlapping windows, and the whole brain functional connectivity network was constructed using Pearson correlation of the representation BOLD time series in each window. **(C)** From the raw functional connectivity matrix in one time window, nodal connectivity profile is the vector that describes its connectivity with all the other nodes (e.g., the column marked by black line); intra-subnetwork connectivity profile is the upper triangle (due to symmetry) of the connectivity matrix within one subnetwork (e.g., SMN); inter-network connectivity profile is the connectivity matrix between two subnetworks (e.g., SMN-visual, as the block marked by a small black rectangular window). **(D)** Calculation of temporal variability. The nodal, intra- and inter-network connectivity profile in each window was unfolded into connectivity vectors, respectively, and the temporal variability was calculated as the average correlation coefficients of the connectivity vectors across different windows with a deduction from 1.

windows were subsequently used to estimate the variability V_k of brain region k, which is defined as one minus the average correlation of that region's connectivity profile across all time windows (Mueller et al., 2013; Zhang et al., 2016), that is,

$$V_k = 1 - \frac{2}{N(N-1)} \sum_{i=1,j=2,i<j}^{N} corr\left(F_{i,k}, F_{j,k}\right),$$

where N denotes the number of windows (**Figures 1C,D**). The second part of V_k is the averaged correlation values between any two connectivity profiles derived from different time windows, indicating the similarity between connectivity profiles. A small value of variability V_k indicates a high correlation of a node's functional architecture across different time windows.

As for the parameters selection, previous studies suggested that window size around 30–60 s should be suitable to capture the resting-state dFC fluctuations and produce robust results (Keilholz et al., 2012; Li et al., 2014; Deng et al., 2016). And another study (Li et al., 2014) showed that changes of brain connectivity are not sensitive to the specific time-window length (in the range of 10–20 TRs, 20–40 s). We performed the variability analysis at different window length (l = 10, 11, 12, …, 20 volumes, corresponding to 20, 22, 24, …, 40 s, respectively), and found that variability obtained from different window lengths produced highly correlated results ($r > 0.98$, **Supplementary Figure S1**), indicating that this metric is not sensitive to the choice of window length. Therefore, in the following sections, we reported the results obtained with the window size of 20TRs (40 s).

Intra- and Inter-Network Variability

The connectivity patterns within and between subnetworks also fluctuate dynamically over a short period of time (Kiviniemi

et al., 2011; Takamitsu et al., 2013; Ma et al., 2014). In order to assess the dynamic interactions within and between subnetworks and identify the system-level dynamic brain organization, we defined the intra- and inter- network variability in a way similar to the definition of nodal variability. For a subnetwork, all the intra-network connectivity in each window were unfolded into a long connectivity vector, and then the intra-network variability was estimated as the average correlation coefficients of the connectivity vectors across different windows with a deduction from 1 (**Figures 1C,D**). Intra-network variability characterizes the changes of connectivity within subnetwork over time. High value of intra-network variability means the functional architecture within the network is poorly correlated across different time windows, implying an unstable state. Similarly, for two subnetworks, all the connectivity between the two subnetworks were unfolded into a long connectivity vector, and then the inter-network variability was estimated as the average correlation coefficients of the connectivity vectors across windows with a deduction from 1 (**Figures 1C,D**). High value of inter-network variability means that the interactions between the two networks reconfigure frequently but not maintain a stable pattern.

Statistical Analysis

Non-parametric permutation tests (Nichols and Holmes, 2002; Bassett et al., 2011) were applied to test the between-group differences in nodal, intra- and inter-network variability. In each permutation, each subject was randomly reassigned to one of a pair of groups with the same number of subjects as in the original patient and control groups. Then the nodal, intra- and inter-network variability were computed for each randomized group and the between-group difference for all the metrics was calculated, respectively. This randomization procedure was repeated 10000 times, resulting in a sampled null between-group difference permutation distributions for each metric. Finally, the p-value was then calculated as the proportion of total entries resulting from the permutation distribution that were greater than (or smaller than) the observed group effect.

Statistical analysis for head motion parameters and demographic measures were performed using two sample t-test. Spearman correlation analysis was performed between altered temporal variability and clinical variables of disease severity (UPDRS-III score and Hoehn and Yahr staging) at a threshold for statistical significance of $p < 0.05$. Statistical analysis of all the metrics were implemented using Matlab (version 2014a; MathWorks). Visualization of results were performed using Python.

Validation Analysis

To evaluate the robustness of our main results, we conducted some validation analysis. (i) Parcellation scheme: given that the variability may be affected by the topological spatial constraints and definition of ROIs, we also constructed functional brain networks using an additional functional whole-brain parcellation scheme consisting of 268 ROIs (Shen et al., 2013) (referred to as Shen268 atlas), in which all the ROIs are assigned to eight different functional networks. (ii) Window length: to investigate the potential effects of window length, we performed the correlation analysis of temporal variability obtained at different window lengths, and also repeated the analysis with the average value of variability across different window lengths, following the strategy used in Zhang et al. (2016).

RESULTS

Nodal Variability

We found significant nodal variability changes in PD patients across several regions. The nodal variability of precentral and postcentral gyrus (in SMN), middle occipital gyrus (in visual network), putamen (in subcortical network) and cerebellum in patients showed significantly increased variability ($p < 0.005$, 10000 permutations, uncorrected) compared to NCs (**Table 2**). While in this PD cohort, no nodes showed significantly decreased variability.

Intra-Network Variability

Among the 13 subnetworks, we found that subnetworks including subcortical network, SAN and visual network tended to display greater intra-network variability in PD than NCs ($p < 0.05$, 10000 permutations, **Figure 2A**). Only the variability of intra-subcortical network showed a positive correlation with UPDRS-III by spearman correlation analysis (**Figures 2B,C**).

Inter-Network Variability

Distributed Difference of Inter-Network Variability

We explored inter-network variability among all subnetwork pairs. **Figures 3A,B** show the mean intra- and inter- network variability matrices in NCs and PD patients, respectively. Generally, the intra-network variability of a particular subnetwork demonstrated a relatively lower value than the inter-network variability of that subnetwork with other subnetworks, respectively in both PD and NC groups (**Figure 3**, NC group: all p-values no larger than 0.0181, 10000 permutations; PD group: all p-values no larger than 0.0001, 10000 permutations). Between group comparisons for the variability matrices revealed significantly greater inter-network variability in PD patients compared with NCs in several subnetwork pairs associated with SMN, visual, subcortical networks and cerebellum.

Correlation Between Inter-Network Variability and UPDRS-III

We further identified the subnetwork pairs which showed significant correlation ($p < 0.05$, Spearman correlation) to the clinical status. To ensure correlations are not driven by a few extreme values, we removed outliers in the data prior to performing linear regression. We defined an outlier as a value outside of 3 standard deviation from the group mean. Performing regression with and without outliers actually did not qualitatively change the results.

Significant correlation between inter-network variability and UPDRS-III mainly appeared in subnetwork pairs associated with

TABLE 2 | Regions showing significant higher nodal variability in PD patients than normal controls.

ROI Index	MNI coordinate	Nodal Variability		*p*-value (uncorrected)	Subnetwork	Brain region (AAL atlas)
		NC	PD			
8	–37, –29, –26	0.8033	0.8508	0.0033	Uncertain	Fusiform_L
28	20, –29, 60	0.7350	0.8013	0.0005	SMN	NA
34	–21, –31, 61	0.7486	0.8042	0.0035	SMN	Postcentral_L
41	38, –17, 45	0.7229	0.7980	0.0008	SMN	Precentral_R
147	–28, –79, 19	0.7360	0.7817	0.0044	Visual	Occipital_Mid_L
227	–22, 7, –5	0.8031	0.8474	0.0026	Subcortical	Putamen_L
232	–31, –11, 0	0.8072	0.8565	0.0029	Subcortical	Putamen_L
245	22, –58, –23	0.7492	0.8034	0.0046	Cerebellum	Cerebellum

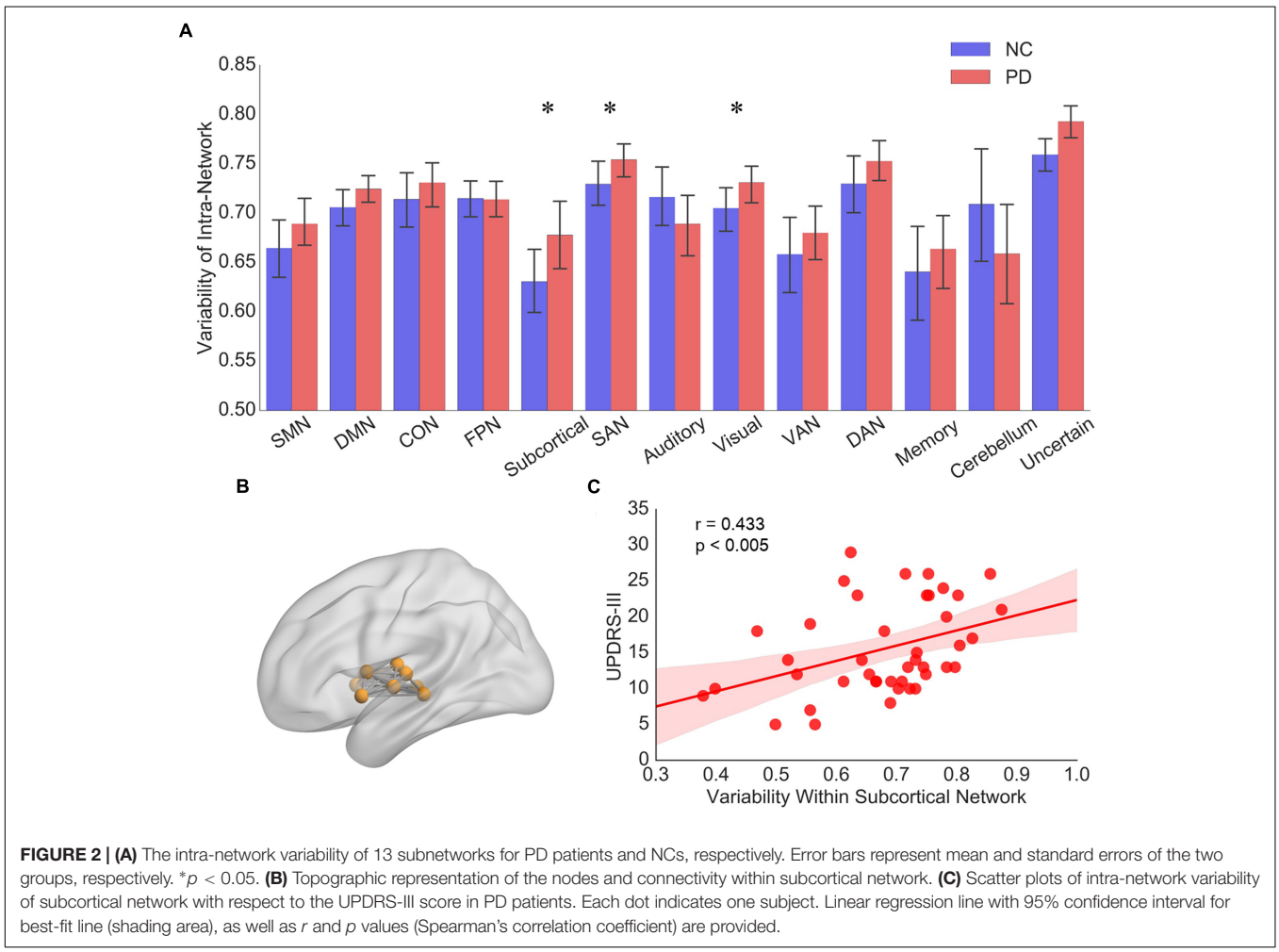

FIGURE 2 | (A) The intra-network variability of 13 subnetworks for PD patients and NCs, respectively. Error bars represent mean and standard errors of the two groups, respectively. $^*p < 0.05$. **(B)** Topographic representation of the nodes and connectivity within subcortical network. **(C)** Scatter plots of intra-network variability of subcortical network with respect to the UPDRS-III score in PD patients. Each dot indicates one subject. Linear regression line with 95% confidence interval for best-fit line (shading area), as well as *r* and *p* values (Spearman's correlation coefficient) are provided.

subcortical network and cerebellum (**Supplementary Figure S5**). Compared with NCs, PD group had greater inter-network variabilities for the subnetwork pairs of subcortical network with respect to sensorimotor, visual, ventral attention, dorsal attention, and cerebellum networks, and their variability also had significant positive correlation with UPDRS-III in PD patients (**Figures 4A–E**). In addition, the inter-network variability for subnetwork pairs of cerebellum and auditory network also showed group difference as well as significant positive correlation with UPDRS-III (**Figure 4F**). We have also evaluated the correlation between temporal variability and H-Y scores, while the results showed that the nodal/intra- and inter-network variability had a weak correlation (all $r < 0.23$, all $p > 0.14$) with H-Y scores.

Validation Results

We validated our main findings using different analysis strategies, involving sliding window lengths (**Supplementary Table S1**

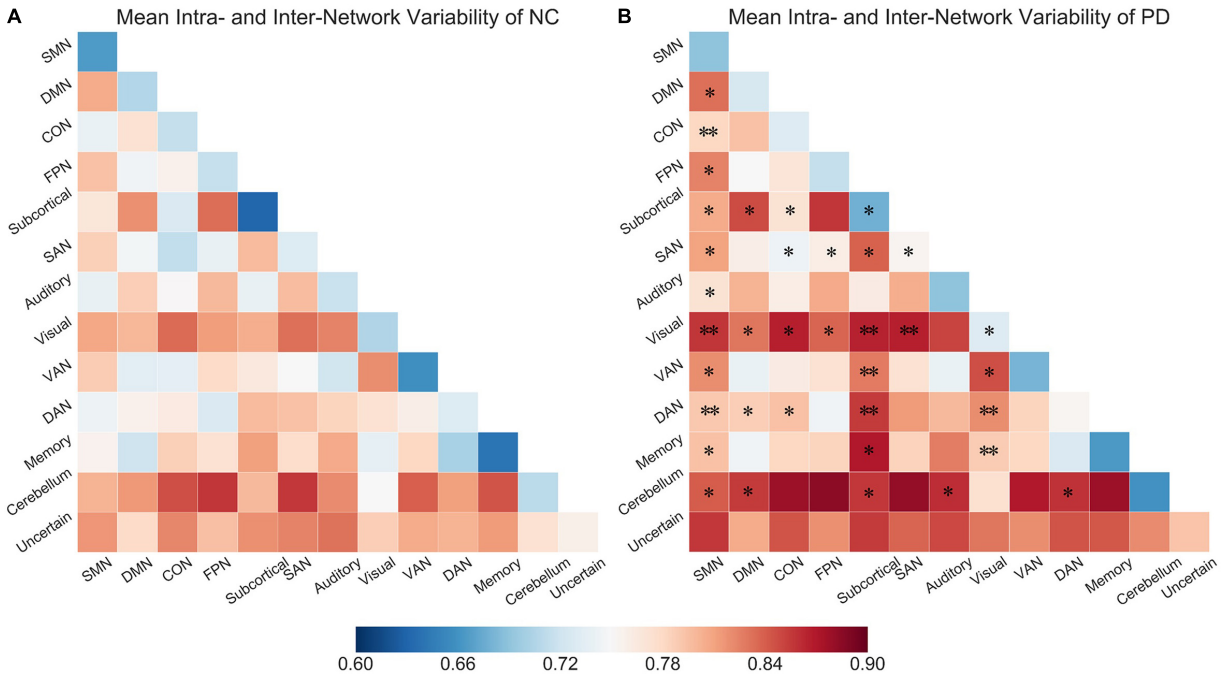

FIGURE 3 | (A) Mean intra- and inter-network variability matrix of NCs. **(B)** Mean intra- and inter- network variability matrix of PD patients. Asterisks (*) labeled on the PD matrix indicate the subnetwork pairs showing significantly increased intra- or inter-network variability in PD patients compared than control subjects. *$p < 0.05$, **$p < 0.005$.

and **Supplementary Figures S1–S4**), parcellation schemes (**Supplementary Table S2** and **Supplementary Figures S6–S8**). We found that the temporal variability including nodal, intra- and inter- network variability estimated from windows of different lengths were highly correlated, indicating that these metrics is not sensitive to the choice of window length. For further validation of the results, we also used the average variability across different window lengths for the same analysis procedures, the main results are highly similar with those at window length of 20TRs. For the results obtained at Shen268 atlas, we observed similar pattern of variability difference of two groups, which were mainly located at Subcortical-cerebellum, Motor, and Visual (Visual I, Visual II, Visual association) networks. Besides, the significant correlation between temporal variability and UPDRS-III also mainly appeared in subnetwork pairs associated with Subcortical-cerebellum network. These results replicated the main findings obtained with Power-264 atlas.

DISCUSSION

In the present study, we investigated the variability of the dynamic functional brain network of PD patients at nodal, intra- and inter-network levels. Our results demonstrated that PD patients exhibited increased nodal variability involving precentral and postcentral areas, occipital area, putamen, and cerebellum. Moreover, PD patients demonstrated significantly increased intra-network variability within subcortical, salience and visual networks, as well as distributed increase in inter-network variability of several subnetwork pairs. Furthermore, the intra-network variability of subcortical network and the inter-network variability of subcortical network with respect to SMN, visual network, VAN, DAN and cerebellum showed significant correlation with the clinical score UPDRS-III, suggesting the special role of subcortical network in functional abnormality of PD. Besides, the inter-network variability of the cerebellum-auditory pair also had significant correlation with the clinical score UPDRS-III. These results suggest that PD patients showed widespread functional network abnormalities in term of temporal variability, and the abnormal temporal variability also correlated with clinical manifestations and thus offering new insights in understanding PD.

Distributed Variability Changes in PD Patients

At the nodal and intra-network level, we found a widespread pattern of increased variability in PD patients, encompassing sensorimotor (SMN), visual, subcortical networks and cerebellum. A similar pattern was also observed in ROIs defined by the Shen268 atlas, that is, the variability difference was mainly located in Subcortical-cerebellum, Motor, and Visual (Visual I, Visual II, Visual association) subnetworks (**Supplementary Table S2** and **Supplementary Figures S6,S7**). Previous study has reported that the primary sensorimotor area in normal subjects changed little over time (Power et al., 2011; Bassett et al., 2013). Conversely, in this study, the precentral and postcentral areas (in sensorimotor network) revealed higher

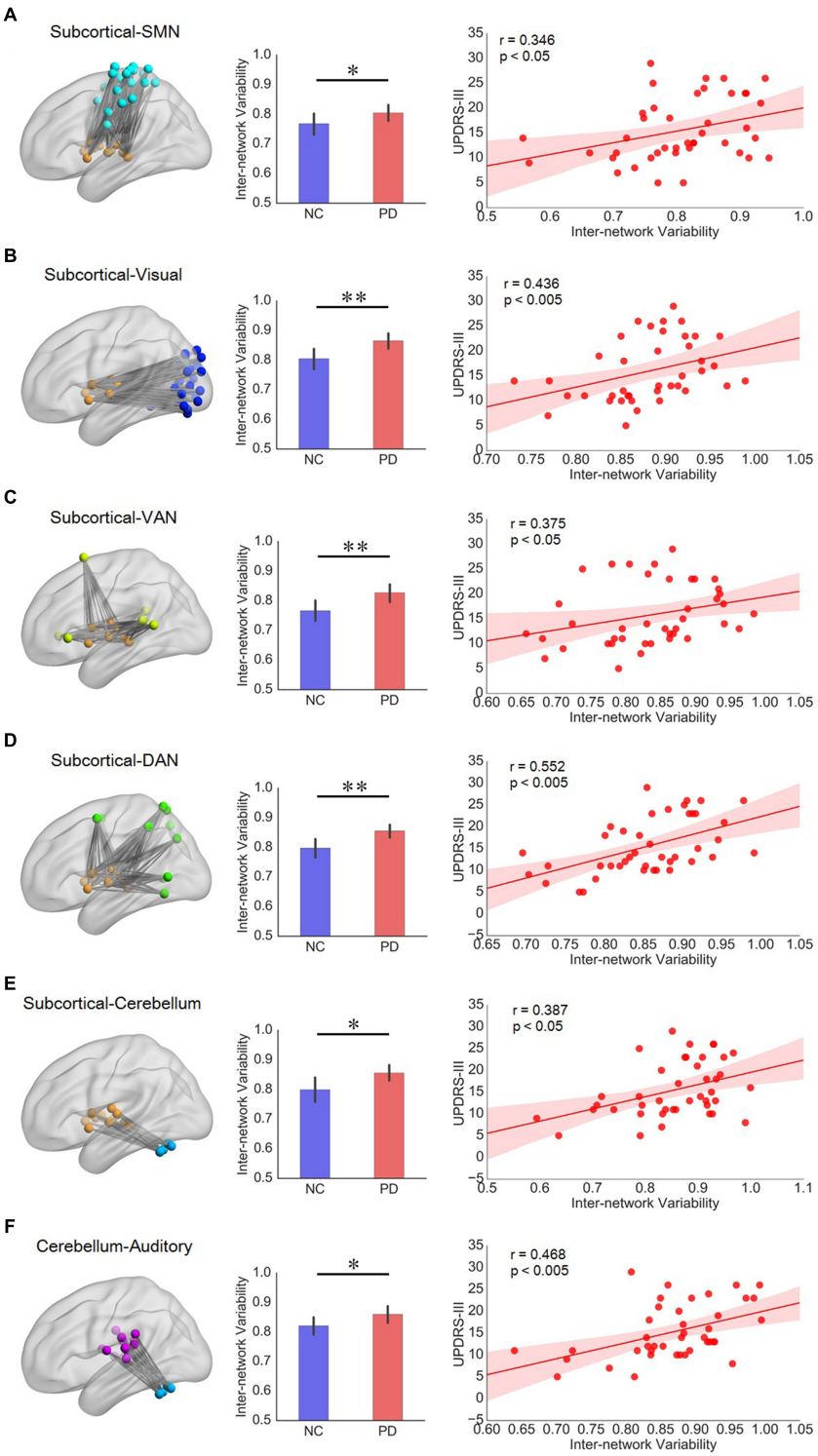

FIGURE 4 | (A–E) Subnetwork pairs associated with subcortical network had increased inter-network variability as well as significant correlation with UPDRS-III. **(F)** The cerebellum-auditory subnetwork pair which had increased inter-network variability as well as significant correlation with UPDRS-III in PD patients. For each row from A to F, the left panel is the topographic representation of the nodes and the inter-network connectivity within the corresponding subnetwork pairs, respectively; the middle panel is the boxplot of inter-network variability for NC and PD groups, respectively; and the right panel is the scatterplot of the inter-network variability with respect to the UPDRS-III score for PD patients, with each dot indicating one subject, excluding outliers (outside of 3 standard deviation from the group mean). Error bars represent mean and standard errors of the two groups, respectively. Linear regression line with 95% confidence interval for best-fit line (shading area), as well as r and p values (Spearman's correlation coefficient) are provided. *$p < 0.05$, **$p < 0.005$.

variability in patients, unveiling that nodes in SMN of PD patients demonstrated a non-stationary functional configuration with other regions. In fact, several studies have identified abnormal functional connectivity in SMN which is indicative of impaired sensorimotor integration occurred in PD (Lewis and Byblow, 2002; Tessitore et al., 2014). Besides, the increased variability has also been observed in visual network both at nodal and intra-network levels. Indeed, visual network is another major complex sensory domain affected by PD, and PD may lead to visual hallucinations, perceptual, executive and sleep dysfunction (Archibald et al., 2011; Wu et al., 2011; Weil et al., 2016). These results together suggest that the altered dFC patterns observed in our study may be related to the deficits in these sensory regions. Moreover, the salience network, mainly comprised of the anterior insula, is a central hub involved in integrating the somatosensory and cognitive-affective information to guide behavior (Kurth et al., 2010). The increased intra-salience network variability found in our data corroborated previous findings of reduced hub role (Tinaz et al., 2016) and abnormal activation patterns in insula in PD patients (Christopher et al., 2014, 2015). In addition, there were other between-group differences in regional or inter-subnetwork variability associated with subcortical network and cerebellum, many of which have been suggested to be related to structural or functional impairment in PD patients (Brooks et al., 2010). Taken together, the abnormality of regional variability identified in our study indicates altered dFC across distributed nodes and subnetworks, reflecting those regions are at an unstable state.

For the inter-network variability, we found that the inter-motor variability was higher than intra-motor variability, which is consistent with previous studies (Elton and Gao, 2015) that lower variability within subnetwork may maintain a more stable configuration. In addition, significant higher inter-network variability was found across distributed subsystem pairs. The varying interactions between subsystems may be tied to functional coordination between subnetworks (Zalesky et al., 2014), the increased inter-network variability in PD patients implies an unstable state and more dynamic interactions. Our observations was consistent with Kim et al. (2017), which reported an increase in the number of transitions between states and higher variability in global efficiency of brain network of PD patients, implying a less efficient and more unstable information transfer within/between functional subnetworks. Furthermore, substantial efforts have been made in previous studies to elucidate the neural basis of PD, with mounting evidence indicating deficits of distributed brain networks and wide-spread white matter damage in PD (Brooks and Pavese, 2011; Canu et al., 2016; Koshimori et al., 2016). Our results putatively reflect the abnormal global integration of the brain networks in PD from the dynamic perspective.

Variability Associated With Subcortical Network

Despite the distributed alteration of temporal variability in PD patients, the variability showing significant correlation with clinical score was particularly associated subcortical network (**Supplementary Figure S5**), suggesting its clinical significance in PD. Results obtained with the Shen268 atlas showed a similar trend, which were mainly associated with the Subcortical-cerebellum subnetwork (**Supplementary Figure S8**). At nodal and intra-network levels, a higher nodal variability in putamen and intra-network variability within subcortical network was observed, which is compatible with previous study highlighting the severely affected striatal dopamine depletion in putamen and reduced connectivity between striatal and thalamus within subcortical network (Hacker et al., 2012). At the inter-network level, the increased inter-network variability between subcortical network and cortical networks (sensorimotor, visual, and attention network) in PD patients also correlated with worsening motor symptoms in PD. All these cortical networks are known to play a critical role in the pathogenesis of PD (Kim et al., 2017), and the dysfunction of cortico-BG-thalamo-cortical circuit associated with motor deficits is well documented in PD patients (Alexander et al., 1986). More specifically, altered functional connection and integration of subcortical to sensorimotor and visual networks have been reported in PD (Tremblay et al., 2010; Hacker et al., 2012; Wymbs et al., 2012). Connectivity changes and dysfunctional integration in attention work (including dorsal attention network (DAN) and ventral attention network (VAN)) have also been reported in PD patients with mild cognitive impairment and visual hallucinations, respectively (Shine et al., 2013a; Baggio et al., 2015). Here the higher level variability of FC profile in subcortical-cortical coupling may therefore provide further information for the prediction of disease severity. Furthermore, a significantly increased variability of cerebellum-subcortical coupling in PD patients was positive associated with UPDRS-III in our study. According to Bostan et al. (2013), the reciprocal connections between basal ganglia and the cerebellum provide the anatomical substrate for the cerebellar contributions to a wide range of behaviors. The increased variability pattern between cerebellum and subcortical network, could also support the markedly lower striatal connectivity with cerebellum in PD group reported in Hacker et al. (2012), thus reinforcing the relevance to parkinsonism of the described circuits connecting the cerebellum to the basal ganglia (Hoshi et al., 2005; Bostan et al., 2010).

Variability Associated With Cerebellum

Interestingly, in the present study, the node in the cerebellum showed significantly increased nodal variability in PD patients. Studies have shown that the cerebellum is involved in motor coordination (Thach, 1998) as well as integration of motor and cognitive networks. Pathological changes in the cerebellum have been reported in a previous study (Wu and Hallett, 2013). Considering this, our results revealed an abnormal dynamic connectivity profile between nodes in the cerebellum with other regions, which may be related to the dysfunction of cerebellum in PD patients.

We also found that a significantly increased inter-network variability between cerebellum and cortical network (auditory

network) showed positive correlation with UPDRS-III. This emphasizes that the unstable dynamic interaction between the cerebellum and auditory network may also relate to the motor symptom of PD. Similar to basal ganglia in subcortical network, cerebellum has also shown anatomical loops between cerebellum and nearly all cortical subnetworks, suggesting its high global brain connectivity (Middleton and Strick, 1994; Kelly and Strick, 2003; Cole et al., 2010). Combined with the observations that the inter-network variability between subcortical network and other cortical subnetworks as well as cerebellum were also correlated with clinical score (UPDRS-III) noted above, our results uncover the fact that cerebellum also serve as an important role in PD pathology.

In fact, the subcortical network in this study (mainly comprised of basal ganglia and thalamus) and the cerebellum are densely interconnected at the subcortical level and formed an integrated network (Bostan and Strick, 2018). These subcortical systems support the convergence of diverse cortical and subcortical afferents, as well as neuromodulatory signals from the brainstem, thus serving as a hub for large-scale network integration in the human brain (Bell and Shine, 2016). Previous studies revealed that pathological lesions of most disorders were concentrated in hub regions, especially in the striatum and thalamus, implying that subcortical hubs represent key pathological foci across multiple brain disorders (Crossley et al., 2014). Evidence from previous studies has shown that cortico-subcortical circuits are linked to a diverse range of limbic, cognitive and motor control functions (Chudasama and Robbins, 2006; Pennartz et al., 2009). PD is a neurodegenerative disorder characterized by severe and early subcortical pathology as well as clinical impairments extend across cognitive and motor domains. Our results provide further evidence of a subcortical hub by capturing the dynamic variability changes in the subcortical network of PD, suggesting that the subcortical dysfunction may contribute to pathological changes in PD.

Limitations

Several limitations of this study should be recognized. First, motor manifestations of PD subjects are evaluated only using the motor portion of UPDRS without other neuropsychological tests for the diagnosis of PD. There are other substantial non-motor symptoms such as cognitive impairment, autonomic dysfunction and sleep disorders experienced by PD patients (Wu et al., 2011). Future work could investigate variability metrics and their association with other neuropsychological scores and cognitive performance to establish the relationship between dynamic analysis and clinical diagnosis. Second, PD is a heterogeneous disorder with different symptoms and functional connectivity patterns (Zhang et al., 2015). Due to the diversity of possible status of drug use, personality, or genetic factors in our data and a large number of comparisons, some results didn't pass a false discovery rate (FDR) for multiple comparisons correction. Accordingly, we reported the results by setting a relative low significance level ($p < 0.005$) in nodal variability and different statistic levels ($p < 0.05$ and $p < 0.005$) in intra- and inter-network variability. Actually, a more heterogeneous status in the patients' group will most likely lead to higher statistical variance, rendering it more difficult to detect significant functional connectivity differences between patients and controls. Therefore, a larger sample size and more strict inclusion criteria will be needed in further study to reveal temporal variability differences.

CONCLUSION

This study reported alterations of temporal variability in PD patients at nodal, intra- and inter-network levels. Our analysis showed that PD patients have higher nodal variability in precentral and postcentral area, middle occipital gyrus, putamen, cerebellum as well as the increased intra- and inter-motor variability across several distributed subnetworks compared with normal controls. Moreover, the higher intra- and inter-network variability associated with the subcortical network and cerebellum showed significant correlation with UPDRS-III motor score, suggesting its clinical significance. Our results suggest that temporal variability of functional connectivity profile can detect the aberrant dynamic connectivity patterns, which were associated with the clinical deficits in PD and thus may deepen our understanding of the disease.

DATA AVAILABILITY STATEMENT

The dynamic functional connectivity matrix used in our analysis are available from the authors upon reasonable request.

AUTHOR CONTRIBUTIONS

HZ, JH, JS, and HL conceived and designed the study. HZ, LD, LC, and PS analyzed the data. JH, FY, NH, and HL performed the data acquisition. JS and HL supervised the study. HZ drafted the manuscript. JS, ST, and NH involved manuscript review and critique. All authors approved the final manuscript.

FUNDING

This work was supported by grants from National Natural Science Foundation of China (No. 61673267 and 61571295), National Key R&D Program of China (No. 2017YFC0909200), Natural Science Foundation of Shanghai (No. 16ZR1446600) and the Fundamental Research Funds for the Central Universities (No. 16JXRZ05).

SUPPLEMENTARY MATERIAL

The Supplementary Material for this article can be found online at: https://www.frontiersin.org/articles/10.3389/fnins.2019.00080/full#supplementary-material

REFERENCES

Agosta, F., Canu, E., Stefanova, E., Sarro, L., Tomiæ, A., Špica, V., et al. (2013). Mild cognitive impairment in parkinson's disease is associated with a distributed pattern of brain white matter damage. *Hum. Brain Mapp.* 35, 1921–1929. doi: 10.1002/hbm.22302

Alexander, G. E., Delong, M. R., and Strick, P. L. (1986). Parallel organization of functionally segregated circuits linking basal ganglia and cortex. *Annu. Rev. Neurosci.* 9, 357–381. doi: 10.1146/annurev.ne.09.030186.002041

Alia, T., Rachna, J., and Jog, M. S. (2016). The striatum and subthalamic nucleus as independent and collaborative structures in motor control. *Front. Syst. Neurosci.* 10:17. doi: 10.3389/fnsys.2016.00017

Amboni, M., Tessitore, A., Esposito, F., Santangelo, G., Picillo, M., Vitale, C., et al. (2015). Resting-state functional connectivity associated with mild cognitive impairment in parkinson's disease. *J. Neurol.* 262, 425–434. doi: 10.1007/s00415-014-7591-5

An, V., Sako, W., Fujita, K., Peng, S., Mattis, P. J., Skidmore, F. M., et al. (2017). Parkinson's disease-related network topographies characterized with resting state functional MRI. *Hum. Brain Mapp.* 38, 617–630. doi: 10.1002/hbm.23260

Archibald, N. K., Clarke, M. P., Mosimann, U. P., and Burn, D. J. (2011). Visual symptoms in parkinson's disease and parkinson's disease dementia. *Mov. Disord.* 26, 2387–2395. doi: 10.1002/mds.23891

Baggio, H. C., Segura, B., Sala-Llonch, R., Marti, M. J., Valldeoriola, F., Compta, Y., et al. (2015). Cognitive impairment and resting-state network connectivity in Parkinson's disease. *Hum. Brain Mapp.* 36, 199–212. doi: 10.1002/hbm.22622

Bassett, D. S., Bullmore, E., Verchinski, B. A., Mattay, V. S., Weinberger, D. R., and Meyerlindenberg, A. (2011). Hierarchical organization of human cortical networks in health and schizophrenia. *J. Neurosci.* 28, 9239–9248. doi: 10.1523/JNEUROSCI.1929-08.2008

Bassett, D. S., Wymbs, N. F., Rombach, M. P., Porter, M. A., Mucha, P. J., and Grafton, S. T. (2013). Task-based core-periphery organization of human brain dynamics. *PLoS Comput. Biol.* 9:e1003171. doi: 10.1371/journal.pcbi.1003171

Beck, A. T., Ward, C. H., Mendelson, M., Mock, J., and Erbaugh, J. (1961). An inventory for measuring depression. *Arch. General Psychiatr.* 4, 561–571. doi: 10.1001/archpsyc.1961.01710120031004

Bell, P. T., and Shine, J. M. (2016). Subcortical Contributions to Large-Scale Network Communication. *Neurosci. Biobehav. Rev.* 71, 313–322. doi: 10.1016/j.neubiorev.2016.08.036

Bostan, A. C., Dum, R. P., and Strick, P. L. (2010). The basal ganglia communicate with the cerebellum. *Proc. Natl. Acad. Sci. U.S.A.* 107, 8452–8456. doi: 10.1073/pnas.1000496107

Bostan, A. C., Dum, R. P., and Strick, P. L. (2013). Cerebellar networks with the cerebral cortex and basal ganglia. *Trends Cogn. Sci.* 17, 241–254. doi: 10.1016/j.tics.2013.03.003

Bostan, A. C., and Strick, P. L. (2018). The basal ganglia and the cerebellum: nodes in an integrated network. *Nat. Rev. Neurosci.* 19, 338–350. doi: 10.1038/s41583-018-0002-7

Brooks, D. J., Ibanez, V., Sawle, G. V., Quinn, N., Lees, A. J., Mathias, C. J., et al. (2010). Differing patterns of striatal 18F-dopa uptake in parkinson's disease, multiple system atrophy, and progressive supranuclear palsy. *Ann. Neurol.* 28, 547–555. doi: 10.1002/ana.410280412

Brooks, D. J., and Pavese, N. (2011). Imaging biomarkers in parkinson's disease. *Prog. Neurobiol.* 95, 614–628. doi: 10.1016/j.pneurobio.2011.08.009

Bullmore, E., and Sporns, O. (2009). Complex brain networks: graph theoretical analysis of structural and functional systems. *Nat. Rev. Neurosci.* 10, 186–198. doi: 10.1038/nrn2575

Canu, E., Agosta, F., Sarasso, E., Volontè, M. A., Basaia, S., Stojkovic, T., et al. (2016). Brain structural and functional connectivity in parkinson's disease with freezing of gait. *Hum. Brain Mapp.* 36, 5064–5078. doi: 10.1002/hbm.22994

Chai, L. R., Khambhati, A. N., Ciric, R., Moore, T., Gur, R. C., Gur, R. E., et al. (2017). Evolution of brain network dynamics in neurodevelopment. *Netw. Neurosci.* 1, 14–30. doi: 10.1162/NETN_a_00001

Christopher, L., Duffcanning, S., Koshimori, Y., Segura, B., Boileau, I., Chen, R., et al. (2015). Salience network and parahippocampal dopamine dysfunction in memory-impaired parkinson disease. *Ann. Neurol.* 77, 269–280. doi: 10.1002/ana.24323

Christopher, L., Koshimori, Y., Lang, A. E., Criaud, M., and Strafella, A. P. (2014). Uncovering the role of the insula in non-motor symptoms of parkinson's disease. *Brain* 137(Pt 8), 2143–2154. doi: 10.1093/brain/awu084

Chudasama, Y., and Robbins, T. W. (2006). Functions of frontostriatal systems in cognition: comparative neuropsychopharmacological studies in rats, monkeys and humans. *Biol. Psychol.* 73, 19–38. doi: 10.1016/j.biopsycho.2006.01.005

Cole, M. W., Pathak, S., and Schneider, W. (2010). Identifying the brain's most globally connected regions. *Neuroimage* 49, 3132–3148. doi: 10.1016/j.neuroimage.2009.11.001

Cole, M. W., Reynolds, J. R., Power, J. D., Repovs, G., Anticevic, A., and Braver, T. S. (2013). Multi-task connectivity reveals flexible hubs for adaptive task control. *Nat. Neurosci.* 16, 1348–1355. doi: 10.1038/nn.3470

Crossley, N. A., Mechelli, A., Scott, J., Carletti, F., Fox, P. T., Mcguire, P., et al. (2014). The hubs of the human connectome are generally implicated in the anatomy of brain disorders. *Brain* 137(Pt 8), 2382–2395. doi: 10.1093/brain/awu132

Deng, L., Sun, J., Cheng, L., and Tong, S. (2016). Characterizing dynamic local functional connectivity in the human brain. *Sci. Rep.* 6:26976. doi: 10.1038/srep26976

Du, Y., Pearlson, G. D., Yu, Q., He, H., Lin, D., Sui, J., et al. (2016). Interaction among subsystems within default mode network diminished in schizophrenia patients: a dynamic connectivity approach. *Schizophr. Res.* 170, 55–65. doi: 10.1016/j.schres.2015.11.021

Elton, A., and Gao, W. (2015). Task-related modulation of functional connectivity variability and its behavioral correlations. *Hum. Brain Mapp.* 36, 3260–3272. doi: 10.1002/hbm.22847

Folstein, M. F., Folstein, S. E., and Mchugh, P. R. (1975). Mini-mental state. A practical method for grading the cognitive state of patients for the clinician. *J. Psychiatr. Res.* 12, 189–198. doi: 10.1016/0022-3956(75)90026-6

Hacker, C. D., Perlmutter, J. S., Criswell, S. R., Ances, B. M., and Snyder, A. Z. (2012). Resting state functional connectivity of the striatum in parkinson's disease. *Brain* 135(Pt 12), 3699–3711. doi: 10.1093/brain/aws281

Hoehn, M. M., and Yahr, M. D. (1998). Parkinsonism: onset, progression and mortality. *Neurology* 50, 427–442. doi: 10.1212/WNL.50.2.318

Hoshi, E., Tremblay, L., Féger, J., Carras, P. L., and Strick, P. L. (2005). The cerebellum communicates with the basal ganglia. *Nat. Neurosci.* 8, 1491–1493. doi: 10.1038/nn1544

Hutchison, R. M., Womelsdorf, T., Allen, E. A., Bandettini, P. A., Calhoun, V. D., Corbetta, M., et al. (2013). Dynamic functional connectivity: promise, issues, and interpretations. *Neuroimage* 80, 360–378. doi: 10.1016/j.neuroimage.2013.05.079

Jie, B., Liu, M., and Shen, D. (2018). Integration of temporal and spatial properties of dynamic connectivity networks for automatic diagnosis of brain disease. *Med. Image Anal.* 47, 81–94. doi: 10.1016/j.media.2018.03.013

Kalia, L. V., and Lang, A. E. (2015). Parkinson's disease. *Lancet* 386, 896–912. doi: 10.1016/S0140-6736(14)61393-3

Keilholz, S. D., Magnuson, M. E., Pan, W. J., Willis, M., and Thompson, G. J. (2012). Dynamic Properties of Functional Connectivity in the Rodent. *Brain Connect.* 3, 31–40. doi: 10.1089/brain.2012.0115

Kelly, R. M., and Strick, P. L. (2003). Cerebellar loops with motor cortex and prefrontal cortex of a nonhuman primate. *J. Neurosci.* 23, 8432–8444. doi: 10.1523/jneurosci.23-23-08432.2003

Khambhati, A. N., Sizemore, A. E., Betzel, R. F., and Bassett, D. S. (2017). Modelling and interpreting mesoscale network dynamics. *Neuroimage* 180, 337–349. doi: 10.1016/j.neuroimage.2017.06.029

Kim, J., Criaud, M., Cho, S. S., Díez-Cirarda, M., Mihaescu, A., Coakeley, S., et al. (2017). Abnormal intrinsic brain functional network dynamics in parkinson's disease. *Brain* 140, 2955–2967. doi: 10.1093/brain/awx233

Kiviniemi, V., Vire, T., Remes, J., Elseoud, A. A., Starck, T., Tervonen, O., et al. (2011). A sliding time-window ICA reveals spatial variability of the default mode network in time. *Brain Connect.* 1, 339–347. doi: 10.1089/brain.2011.0036

Koshimori, Y., Cho, S. S., Criaud, M., Christopher, L., Jacobs, M., Ghadery, C., et al. (2016). Disrupted nodal and hub organization account for brain network abnormalities in parkinson's disease. *Front. Neurosci.* 8:259. doi: 10.3389/fnagi.2016.00259

Kurth, F., Zilles, K., Fox, P. T., Laird, A. R., and Eickhoff, S. B. (2010). A link between the systems: functional differentiation and integration within the human insula revealed by meta-analysis. *Brain Struct. Funct.* 214, 519–534. doi: 10.1007/s00429-010-0255-z

Lewis, G. N., and Byblow, W. D. (2002). Altered sensorimotor integration in parkinson's disease. *Brain* 125(Pt 9), 2089–2099. doi: 10.1093/brain/awf200

Li, X., Zhu, D., Jiang, X., Jin, C., Zhang, X., Guo, L., et al. (2014). Dynamic functional connectomics signatures for characterization and differentiation of PTSD patients. *Hum. Brain Mapp.* 35, 1761–1778. doi: 10.1002/hbm.22290

Lopes, R., Delmaire, C., Defebvre, L., Moonen, A. J., Duits, A. A., Hofman, P., et al. (2017). Cognitive phenotypes in parkinson's disease differ in terms of brain-network organization and connectivity. *Hum. Brain Mapp.* 38, 1604–1621. doi: 10.1002/hbm.23474

Luo, C. Y., Song, W., Chen, Q., Zheng, Z. Z., Chen, K., Cao, B., et al. (2014). Reduced functional connectivity in early-stage drug-naive parkinson's disease: a resting-state fMRI study. *Neurobiol. Aging* 35, 431–441. doi: 10.1016/j.neurobiolaging.2013.08.018

Ma, Q., Huang, B., Wang, J., Seger, C., Yang, W., Li, C., et al. (2016). Altered modular organization of intrinsic brain functional networks in patients with Parkinson's disease. *Brain Imaging Behav.* 11, 1–14. doi: 10.1007/s11682-016-9524-7

Ma, S., Calhoun, V. D., Phlypo, R., and Adalı, T. (2014). Dynamic changes of spatial functional network connectivity in healthy individuals and schizophrenia patients using independent vector analysis. *Neuroimage* 90, 196–206. doi: 10.1016/j.neuroimage.2013.12.063

Melzer, T. R., Watts, R., Macaskill, M. R., Pitcher, T. L., Livingston, L., Keenan, R. J., et al. (2013). White matter microstructure deteriorates across cognitive stages in Parkinson disease. *Neurology* 80, 1841–1849. doi: 10.1212/WNL.0b013e3182929f62

Middleton, F. A., and Strick, P. L. (1994). Anatomical evidence for cerebellar and basal ganglia involvement in higher cognitive function. *Science* 266, 458–461. doi: 10.1126/science.7939688

Mueller, S., Wang, D., Fox, M., Yeo, B. T. T., Sepulcre, J., Sabuncu, M., et al. (2013). Individual variability in functional connectivity architecture of the human brain. *Neuron* 77, 586–595. doi: 10.1016/j.neuron.2012.12.028

Nichols, T. E., and Holmes, A. P. (2002). Nonparametric permutation tests for functional neuroimaging: a primer with examples. *Hum. Brain Mapp.* 15, 1–25. doi: 10.1002/hbm.1058

Pennartz, C. M., Berke, J. D., Graybiel, A. M., Ito, R., Lansink, C. S., Van, D. M. M., et al. (2009). Corticostriatal interactions during learning, memory processing, and decision making. *J. Neurosci.* 29, 12831–12838. doi: 10.1523/JNEUROSCI.3177-09.2009

Peraza, L. R., Nesbitt, D., Lawson, R. A., Duncan, G. W., Yarnall, A. J., Khoo, T. K., et al. (2017). Intra- and inter-network functional alterations in parkinson's disease with mild cognitive impairment. *Hum. Brain Mapp.* 38, 1702–1715. doi: 10.1002/hbm.23499

Power, J. D., Cohen, A. L., Nelson, S. M., Wig, G. S., Barnes, K. A., Church, J. A., et al. (2011). Functional network organization of the human brain. *Neuron* 72, 665–678. doi: 10.1016/j.neuron.2011.09.006

Preti, M. G., Bolton, T. A., and Ville, D. V. D. (2016). The dynamic functional connectome: state-of-the-art and perspectives. *Neuroimage* 160, 41–54. doi: 10.1016/j.neuroimage.2016.12.061

Price, T., Wee, C. Y., Gao, W., and Shen, D. (2014). "Multiple-network classification of childhood autism using functional connectivity dynamics," in *International Conference on Medical Image Computing and Computer-Assisted Intervention*, (Spain), 177–184. doi: 10.1007/978-3-319-10443-0_23

Rashid, B., Damaraju, E., Pearlson, G. D., and Calhoun, V. D. (2014). Dynamic connectivity states estimated from resting fMRI Identify differences among schizophrenia, bipolar disorder, and healthy control subjects. *Front. Hum. Neurosci.* 8:897. doi: 10.3389/fnhum.2014.00897

Shen, X., Tokoglu, F., Papademetris, X., and Constable, R. T. (2013). Groupwise whole-brain parcellation from resting-state fMRI data for network node identification. *Neuroimage* 82, 403–415. doi: 10.1016/j.neuroimage.2013.05.081

Shine, J. M., Halliday, G. M., Gilat, M., Matar, E., Bolitho, S. J., Carlos, M., et al. (2013a). The role of dysfunctional attentional control networks in visual misperceptions in Parkinson's disease. *Hum. Brain Mapp.* 35, 2206–2219. doi: 10.1002/hbm.22321

Shine, J. M., Matar, E., Ward, P. B., Frank, M. J., Moustafa, A. A., Pearson, M., et al. (2013b). Freezing of gait in Parkinson's disease is associated with functional decoupling between the cognitive control network and the basal ganglia. *Brain* 136(Pt 12), 3671–3681. doi: 10.1093/brain/awt272

Smith, S. M., Fox, P. T., Miller, K. L., Glahn, D. C., Fox, P. M., Mackay, C. E., et al. (2009). Correspondence of the brain's functional architecture during activation and rest. *Proc. Natl. Acad. Sci. U.S.A.* 106, 13040–13045. doi: 10.1073/pnas.0905267106

Smith, S. M., Miller, K. L., Salimi-Khorshidi, G., Webster, M., Beckmann, C. F., Nichols, T. E., et al. (2011). Network modelling methods for FMRI. *Neuroimage* 54, 875–891. doi: 10.1016/j.neuroimage.2010.08.063

Sourty, M., Thoraval, L., Roquet, D., Armspach, J. P., Foucher, J., and Blanc, F. (2016). Identifying dynamic functional connectivity changes in dementia with lewy bodies based on product hidden markov models. *Front. Comput. Neurosci.* 10:60. doi: 10.3389/fncom.2016.00060

Su, J., Shen, H., Zeng, L. L., Qin, J., Liu, Z., and Hu, D. (2016). Heredity characteristics of schizophrenia shown by dynamic functional connectivity analysis of resting-state functional MRI scans of unaffected siblings. *Neuroreport* 27, 843–848. doi: 10.1097/WNR.0000000000000622

Takamitsu, W., Satoshi, H., Hiroyuki, W., Yoshio, I., Toru, M., Ichiro, S., et al. (2013). A pairwise maximum entropy model accurately describes resting-state human brain networks. *Nat. Commun.* 4:1370. doi: 10.1038/ncomms2388

Tessitore, A., Giordano, A., De, R. M., Russo, A., and Tedeschi, G. (2014). Sensorimotor connectivity in parkinson's disease: the role of functional neuroimaging. *Front. Neurol.* 5:180. doi: 10.3389/fneur.2014.00180

Thach, W. T. (1998). A role for the cerebellum in learning movement coordination. *Neurobiol. Learn. Mem.* 70, 177–188. doi: 10.1006/nlme.1998.3846

Tinaz, S., Lauro, P., Hallett, M., and Horovitz, S. G. (2016). Deficits in task-set maintenance and execution networks in parkinson's disease. *Brain Struct. Funct.* 221, 1413–1425. doi: 10.1007/s00429-014-0981-8

Tremblay, P. L., Bedard, M. A., Langlois, D., Blanchet, P. J., Lemay, M., and Parent, M. (2010). Movement chunking during sequence learning is a dopamine-dependant process: a study conducted in parkinson's disease. *Exp. Brain Res.* 205, 375–385. doi: 10.1007/s00221-010-2372-6

Tzouriomazoyer, N., Landeau, B., Papathanassiou, D., Crivello, F., Etard, O., Delcroix, N., et al. (2002). Automated anatomical labeling of activations in SPM using a macroscopic anatomical parcellation of the MNI MRI single-subject brain. *Neuroimage* 15, 273–289. doi: 10.1006/nimg.2001.0978

Wee, C. Y., Yang, S., Yap, P. T., and Shen, D. (2016). Sparse temporally dynamic resting-state functional connectivity networks for early MCI identification. *Brain Imaging Behav.* 10, 342–356. doi: 10.1007/s11682-015-9408-2

Weil, R. S., Schrag, A. E., Warren, J. D., Crutch, S. J., Lees, A. J., and Morris, H. R. (2016). Visual dysfunction in parkinson's disease. *Brain* 139, 2827–2843. doi: 10.1093/brain/aww175

Wu, T., and Hallett, M. (2013). The cerebellum in parkinson's disease. *Brain* 136, 696–709. doi: 10.1093/brain/aws360

Wu, T., Long, X., Wang, L., Hallett, M., Zang, Y., Li, K., et al. (2011). Functional connectivity of cortical motor areas in the resting state in parkinson's disease. *Hum. Brain Mapp.* 32, 1443–1457. doi: 10.1002/hbm.21118

Wymbs, N. F., Bassett, D. S., Mucha, P. J., Porter, M. A., and Grafton, S. T. (2012). Differential recruitment of the sensorimotor putamen and frontoparietal cortex during motor chunking in humans. *Neuron* 74, 936–946. doi: 10.1016/j.neuron.2012.03.038

Yan, C., and Zang, Y. (2010). DPARSF: a matlab toolbox for "pipeline" data analysis of resting-state fMRI. *Front. Syst. Neurosci.* 4:13. doi: 10.3389/fnsys.2010.00013

Zalesky, A., Fornito, A., Cocchi, L., Gollo, L. L., and Breakspear, M. (2014). Time-resolved resting-state brain networks. *Proc. Natl. Acad. Sci. U.S.A.* 111, 10341–10346. doi: 10.1073/pnas.1400181111

Zhang, J., Cheng, W., Liu, Z., Zhang, K., Xu, L., Ye, Y., et al. (2016). Neural, electrophysiological and anatomical basis of brain-network variability and its characteristic changes in mental disorders. *Brain* 139, 2307–2321. doi: 10.1093/brain/aww143

Zhang, J., Wei, L., Hu, X., Xie, B., Zhang, Y., Wu, G. R., et al. (2015). Akinetic-rigid and tremor-dominant Parkinson's disease patients show different patterns of intrinsic brain activity. *Parkinsonism Relat. Disord.* 21, 23–30. doi: 10.1016/j.parkreldis.2014.10.017

Conflict of Interest Statement: The authors declare that the research was conducted in the absence of any commercial or financial relationships that could be construed as a potential conflict of interest.

frontiers in Neuroscience

ORIGINAL RESEARCH
published: 28 February 2019
doi: 10.3389/fnins.2019.00169

Robust Motion Regression of Resting-State Data Using a Convolutional Neural Network Model

Zhengshi Yang[1], Xiaowei Zhuang[1], Karthik Sreenivasan[1], Virendra Mishra[1], Dietmar Cordes[1,2] and the Alzheimer's Disease Neuroimaging Initiative[†]*

[1] Cleveland Clinic Lou Ruvo Center for Brain Health, Las Vegas, NV, United States, [2] Department of Psychology and Neuroscience, University of Colorado, Boulder, Boulder, CO, United States

OPEN ACCESS

Edited by:
Xiaoping Philip Hu, University of California, Riverside, United States

Reviewed by:
Aiguo Song, Southeast University, China
Xiang-Zhen Kong, Max Planck Institute for Psycholinguistics, Netherlands

***Correspondence:**
Dietmar Cordes
cordesd@ccf.org

[†]Data used in preparation of this article were obtained from the Alzheimer's Disease Neuroimaging Initiative (ADNI) database (http://adni.loni.usc.edu/). As such, the investigators within the ADNI contributed to the design and implementation of ADNI and/or provided data but did not participate in analysis or writing of this report. A complete listing of ADNI investigators can be found at http://adni.loni.usc.edu/wp-content/uploads/how_to_apply/ADNI_Acknowledgement_List.pdf

Specialty section:
This article was submitted to Brain Imaging Methods, a section of the journal Frontiers in Neuroscience

Received: *01 December 2018*
Accepted: *13 February 2019*
Published: *28 February 2019*

Citation:
Yang Z, Zhuang X, Sreenivasan K, Mishra V, Cordes D and the Alzheimer's Disease Neuroimaging Initiative (2019) Robust Motion Regression of Resting-State Data Using a Convolutional Neural Network Model. Front. Neurosci. 13:169. doi: 10.3389/fnins.2019.00169

Resting-state functional magnetic resonance imaging (rs-fMRI) based on the blood-oxygen-level-dependent (BOLD) signal has been widely used in healthy individuals and patients to investigate brain functions when the subjects are in a resting or task-negative state. Head motion considerably confounds the interpretation of rs-fMRI data. Nuisance regression is commonly used to reduce motion-related artifacts with six motion parameters estimated from rigid-body realignment as regressors. To further compensate for the effect of head movement, the first-order temporal derivatives of motion parameters and squared motion parameters were proposed previously as possible motion regressors. However, these additional regressors may not be sufficient to model the impact of head motion because of the complexity of motion artifacts. In addition, while using more motion-related regressors could explain more variance in the data, the neural signal may also be removed with increasing number of motion regressors. To better model how in-scanner motion affects rs-fMRI data, a robust and automated convolutional neural network (CNN) model is developed in this study to obtain optimal motion regressors. The CNN network consists of two temporal convolutional layers and the output from the network are the derived motion regressors used in the following nuisance regression. The temporal convolutional layer in the network can non-parametrically model the prolonged effect of head motion. The set of regressors derived from the neural network is compared with the same number of regressors used in a traditional nuisance regression approach. It is demonstrated that the CNN-derived regressors can more effectively reduce motion-related artifacts.

Keywords: fMRI, denoising, convolutional neural network, motion artifact, nuisance regression

INTRODUCTION

Resting-state functional magnetic resonance imaging (rs-fMRI) based on the blood-oxygen-level-dependent (BOLD) signal has been widely used to investigate brain functions when the subject is in a resting or task-negative state. The BOLD signal, however, is contaminated by multiple noise sources, including head motion, cardiac and respiratory motion, thermal motion inherent to electrical circuits, instrumental drift, and changes in blood pressure and cerebral autoregulation mechanisms, which may severely corrupt BOLD fMRI time series (Murphy et al., 2013). A few recent studies have demonstrated that head motion can significantly confound the analysis of rs-fMRI data (Power et al., 2012; Satterthwaite et al., 2012; Van Dijk et al., 2012). These studies came to a consensus that motion overall tends to increase short-range correlations to nearby voxels, causing

functional connectivity (FC) to vary with distance between regions. Even small amounts of motion can have considerable influence on connectivity measurement (Yan et al., 2013).

The origin of motion-related signal changes can be explained in terms of three interrelated aspects (Caballero-Gaudes and Reynolds, 2017). First, any alteration in tissue composition due to head motion can cause a change in net magnetization and thus proportionally change the amplitude of the signal in a voxel. Second, the number of excited spins depends on the position of a voxel at the current time point and previous time points. Head movement alters the timing between successive spin excitations in the voxel, potentially generating spin history artifacts and thus impacting the signal even beyond the instantaneous time points. Third, the inhomogeneous magnetic field induced by head movement changes the spatial distribution of the local magnetic susceptibility gradients and exacerbates distortions and signal dropouts in regions sensitive to these effects (Jiang et al., 1995).

In the last decade, nuisance regression has been a popular preprocessing strategy to remove motion artifact in rs-fMRI data. A set of motion regressors, referred as nuisance regressors, is first specified to characterize motion-related fluctuations in the data. The denoised data is then obtained by regressing out the contributions from the motion regressors from the original data.

The selection of nuisance regressors is a critical factor influencing the performance of nuisance regression. Inappropriate regressors may have negligible effect or even be detrimental to the analysis. For example, inclusion of the global signal (i.e., the average fMRI signal across the whole brain) as a nuisance regressor has been heavily debated in the past. Multiple studies have shown that global signal regression (GSR) may introduce a negative bias in the estimated BOLD response (Macey et al., 2004; Saad et al., 2012), artificially generate anti-correlation between brain regions (Murphy et al., 2009), and strengthen the relationship between motion-connectivity correlation and regional Euclidian distance (Satterthwaite et al., 2013). The most common motion regressors are simply the six head motion parameters (R = [X Y Z pitch yaw roll]) estimated from the fMRI rigid-body realignment pre-processing step. To further reduce motion-induced spin history artifacts, 12, 24, or even 36 motion-related regressors are used in recent studies, which incorporate original motion parameters, their first-order derivatives, their squared functions, motion parameters with one or two temporal shifts or average tissue-based [gray matter (GM), white matter (WM), cerebrospinal fluid (CSF)] regressors (Friston et al., 1996; Power et al., 2012; Van Dijk et al., 2012; Satterthwaite et al., 2013; Yan et al., 2013). An alternative strategy for carrying out motion correction is to scrub contaminated volumes from fMRI data prior to data analysis (Lemieux et al., 2007; Power et al., 2011, 2012). Typically, time points are first identified as motion-induced artifacts by thresholding certain motion measurements, e.g., framewise displacement, then spike regressors are created with a single non-zero value at each identified time point as well as its neighboring time points, and finally these spikes are regressed out to generate spike-free data. This scrubbing strategy can be treated as excluding contaminated time points from subsequent analysis. The combination of scrubbing and motion regression was shown to have the greatest reduction in motion-related artifacts (Satterthwaite et al., 2013). However, there is a tradeoff between the data quality and remaining time points. Similar to general nuisance regression, including more motion regressors can be detrimental to the following analysis since it is unclear whether significant amount of the neuronal-related BOLD signal is also removed. In addition, scrubbing has the potential limitation of removing a large proportion of time series from a single subject, leading to significant variation in the number of remaining time points from one subject to another (Yan et al., 2013).

While there are other approaches to reduce motion-related artifacts such as slice-wise motion correction (Beall and Lowe, 2014), acquiring data with multi-echo EPI sequences (Kundu et al., 2012) and ICA-based motion correction approaches (Griffanti et al., 2014; Pruim et al., 2015), this study focuses on using the head motion parameters estimated from rigid-body realignment to derive optimal motion-related fluctuations in rs-fMRI data. The relationship between head motion and the resulting change in the MR signal remains unclear, the realignment parameters and their temporal derivatives or squared functions may not be sufficient to model the non-linear MR signal change in the data. We have developed a robust and automated convolutional neural network (CNN) model to derive improved motion regressors. In the recent past, CNN networks achieved classification accuracy record with ImageNet data (Krizhevsky et al., 2012) and have been successfully applied in different fields such as object recognition and sentence classification (Kim, 2014; Liang and Hu, 2015). In our proposed CNN model, the motion parameters estimated from rigid-body realignment are the input to the network. Considering that voxels within white matter and CSF share similar motion-related artifacts as the voxels within GM but do not have neural contributions, time series from WM and CSF but not GM are used for optimizing model parameters to avoid reducing neural activations.

The CNN network consists of two temporal convolutional layers and the output data from the network are the optimized motion regressors used in a subsequent motion regression. The temporal convolutional layer in the network is particularly useful for non-parametrically modeling the prolonged effect of head motion (Power et al., 2014). The regressors derived from the neural network are compared with the same number of regressors used in a traditional motion regression approach. A comprehensive comparison of these two methods of motion regression is presented using fMRI data from a publicly available database.

MATERIALS AND METHODS

Subjects

The structural MRI and rs-fMRI data used in this study were downloaded from the publicly available ADNI database[1]. The ADNI was launched in 2003 as a public-private partnership,

[1] http://adni.loni.usc.edu/

led by Principal Investigator Michael W. Weiner, MD. The primary goal of ADNI has been to test whether serial MRI, positron emission tomography, other biological markers, and clinical and neuropsychological assessment can be combined to measure the progression of mild cognitive impairment and early Alzheimer's disease.

Only the subjects identified as normal controls by site investigators were used in this study. All subjects were scanned on a 3.0-Tesla Philips MRI scanner. All data were downloaded from the ADNI database before September 2016, and 76 subjects (age 74.1 ± 6.6 years, MMSE 28.9 ± 1.3, handedness 67 right/9 left, gender 33 male/43 female) were found satisfying the conditions described above. The subject ID, scanning parameters and demographical information can be found in **Supplementary Table S1**. The magnetization prepared rapid acquisition gradient echo (MP-RAGE) sequence was used to acquire T1-weighted structural images by the investigators of the ADNI consortium. The structural MRI scans were collected with a 24 cm field of view and a resolution of 256 × 256 × 170 to yield a voxel size of 1 mm × 1 mm × 1.2 mm. The rs-fMRI data were acquired using an echo-planar imaging sequence with parameters: 140 time points; TR/TE = 3000/30 ms; flip angle = 80 degrees; 48 slices; spatial resolution = 3.3 mm × 3.3 mm × 3.3 mm and imaging matrix = 64 × 64. Details of the ADNI MRI protocol can be found on the ADNI website[2]. If a subject had multiple MRI/fMRI scans satisfying the requirements specified above, the first available MRI/fMRI data set was used for analysis.

General fMRI Preprocessing

Functional and structural MRI imaging data are processed using the SPM[3] and ANTs[4] toolbox. The first five volumes of rs-fMRI data are discarded to avoid data with unsaturated T1 signal. Before motion regression, the following fMRI preprocessing steps are applied: (i) slice timing correction; (ii) rigid-body head motion correction to the mean EPI image using 7th order B-Spline interpolation to estimate realignment parameters; (iii) co-registration to the skull-stripped structural image; (iv) standard space normalization to the MNI152 2 mm template; (v) spatial smoothing with 6 mm full width at half maximum; (vi) linear detrending. Motion regression is applied after these general fMRI preprocessing steps are completed. Temporal filtering is a preprocessing step commonly used after motion regression (Satterthwaite et al., 2013; Power et al., 2014). Since we aimed to develop an automated method modeling motion fluctuation and compare it with traditional motion regressors, temporal filtering is not used to give a direct comparison of motion-corrected fMRI data.

Deep Neural Network for Denoising

The CNN denoising network is implemented using Keras[5] with Theano[6] as backend. The schematic diagram of the CNN network is shown in **Figure 1A**. The two sequential layers used in the CNN network are a 1-dimensional convolutional layer along the temporal direction. Previous studies showed that motion can have a prolonged and varying effect in the data (Patel et al., 2014; Power et al., 2014) and small amounts of movement could have substantial impact on the BOLD signal in fMRI data (Yan et al., 2013). The CNN network is proposed to learn the influence from the data without manual interference. Both layers have filter size $f = 5$, stride length $s = 1$ and *same* padding so that the output has the same length as the original input. The filter size is defined as the number of neighboring time points included when performing the convolution, and the stride length $s = 1$ means that the filter convolves the input volume by shifting one unit at a time. **Figure 1B** shows how the filters in the first convolutional layer are applied on the input with filter size and stride length defined and more detailed explanation about these hyperparameters (i.e., filter size, stride, and *same* padding) can be found on the Keras website. In these two convolutional layers, 32 temporal filters (filter dimension 5 × 6 × 32 as shown in **Figure 1C** with bias vector 32 × 1) are specified for the first one, and 12 temporal filters (filter dimension 5 × 32 × 12 with bias vector 12 × 1) are specified for the second one to match the number of traditional motion regressors used in this study, leading to 2,924 parameters in total in the neural network. We have also applied the network with different hyperparameters, including filter size and the number of temporal filters for the first layer. The setting described above achieved the least validation error and is selected in this study.

The realignment parameters $\boldsymbol{R} \in \mathcal{R}^{T\times 6}$ are the only input data to our constructed CNN network, where T is the number of time points. The realignment parameters $\boldsymbol{R}$ are replicated to match the number of voxels within WM and CSF masks. Each replicate is linked with different time series within WM and CSF masks to make each pair unique. Naturally, thousands of WM and CSF time series paired with the duplicates of realignment parameters are the large number of samples required to optimize designed network, and each pair can be treated as a sample. With the assumption that WM and CSF voxels share similar motion-related artifacts as GM voxels but are not likely to have neural signals, voxels limited to non-GM (i.e., WM and CSF) are used to derive optimal motion regressors without erroneously modeling neural signals. Many (if not all) standard denoising techniques (Behzadi et al., 2007; Griffanti et al., 2014; Pruim et al., 2015) have used this assumption to reduce motion artifacts or physiological noise. While a few studies showed activation also in white matter (Gawryluk et al., 2014; Courtemanche et al., 2018), the question whether there is BOLD signal in white matter is debatable because of the lack of neurons in white matter.

These non-GM voxels are randomly assigned to a set of batches with batch size $n = 500$. In each batch, the input motion parameters $\boldsymbol{R}$ are replicated n times to match the number of voxels in the batch. These duplicate samples become unique and meaningful when they are linked to different voxel time series. In detail, the replicated motion parameters are forward-propagated through the convolutional layers and the output with dimension $n \times T \times 12$ is obtained for this batch. Naturally, each "sample" has the same output regressor with dimension

[2]http://adni.loni.usc.edu/

[3]https://www.fil.ion.ucl.ac.uk/spm/

[4]http://stnava.github.io/ANTs/

[5]https://keras.io/

[6]http://deeplearning.net/software/theano/

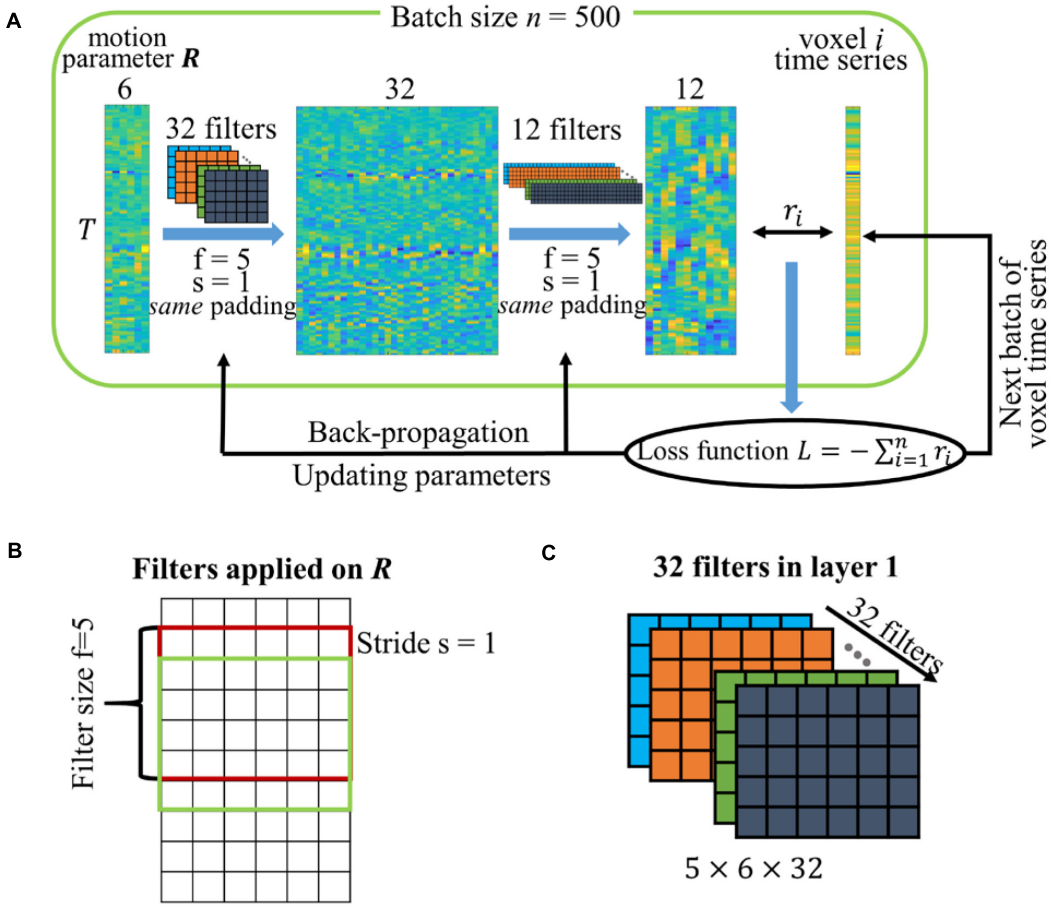

FIGURE 1 | (A) Schematic diagram of the CNN network. The network has two temporal convolutional layers with 32 and 12 filters. The filters are specified with filter size *f* = 5, stride length *s* = 1 and the *same padding* so that the output length is the same as the original input. The motion parameters are replicated n times to match the number of voxels in the batch. The correlations between voxel time series and output regressors are used to calculate the loss function for model optimization. **(B)** Graphical explanation of filter size and stride. **(C)** Dimension of the 32 filters in the first convolutional layer.

$\tilde{\boldsymbol{R}} \in \mathcal{R}^{\mathrm{T}\times 12}$. The correlation r_i between voxel time series and the 12 output regressors is calculated and the sum of correlation across all voxels in the batch with a minus sign is defined as the loss function to be minimized, namely $L = -\sum_{\mathrm{i}=1}^{\mathrm{n}} r_\mathrm{i}$.

There are two choices to calculate the correlation between time series and the regressors $\tilde{\boldsymbol{R}}$. The first one is by applying the general linear model (GLM) to fit the time series $\boldsymbol{y}_\mathrm{i}$ from voxel i to the regressors $\tilde{\boldsymbol{R}}$ and then calculating the correlation between $\boldsymbol{y}_\mathrm{i}$ with the estimated time series $\hat{\boldsymbol{y}}_\mathrm{i} = \mathrm{GLM}(\tilde{\boldsymbol{R}}, \boldsymbol{y}_\mathrm{i})$, namely,

$$\text{choice 1}: r_\mathrm{i} = \mathrm{corr}(\boldsymbol{y}_\mathrm{i}, \hat{\boldsymbol{y}}_\mathrm{i}) \text{ and } \hat{\boldsymbol{y}}_\mathrm{i} = \mathrm{GLM}(\tilde{\boldsymbol{R}}, \boldsymbol{y}_\mathrm{i}) = \tilde{\boldsymbol{R}}\,\tilde{\boldsymbol{R}}^{+}\boldsymbol{y}_\mathrm{i}. \quad (1)$$

The second choice is by calculating the maximal correlation between $\boldsymbol{y}_\mathrm{i}$ and each single regressor in $\tilde{\boldsymbol{R}}$ with sign ignored, namely,

$$\text{choice 2}: r_\mathrm{i} = \max_\mathrm{j}|\mathrm{corr}(\boldsymbol{y}_\mathrm{i}, \tilde{\boldsymbol{R}}_\mathrm{j})|, \quad \mathrm{j} = 1, \ldots, 12. \quad (2)$$

Considering that the pseudoinverse of output regressor matrix $\tilde{\boldsymbol{R}}$, namely $\tilde{\boldsymbol{R}}^{+}$, is required for choice 1 and needs to be updated for each batch, choice 2 is more computational efficient and is used to compute the loss function in this study. Once the loss function is obtained, its gradients are computed for updating the model parameters by back-propagation and the current batch of time series is replaced with another batch for the next iteration. Running through all batches once is called one epoch. The CNN network converges in less than 40 epochs for the fMRI data with 135 time points. The computational time for each subject is less than 2 min on a Tesla K40c GPU with 2,880 cores and approximately 10 min per subject with GPU disabled.

While all subjects share the same network architecture, the CNN network is optimized for each subject separately to achieve subject-specific model (the same architecture but different parameters). During the optimization, 90% of voxels are assigned to update model parameters and the remaining 10% of voxels are assigned to monitor whether the network suffers from over-fitting or under-fitting leading to high bias or variance, respectively. The initial parameters are randomly sampled from the *Xavier uniform initializer* (Glorot and Bengio, 2010). The parameters are updated with the *Adam* stochastic gradient-based optimization algorithm (Kingma and Ba, 2015),

which adapts the parameter learning rates by taking advantage of both the average first moment (mean) and the average of the second moments of the gradients (uncentered variance). The *Adam* optimizer is parameterized with learning rate $\eta = 0.01$, learning rate decay $\gamma = 0.05$, exponential decay rate for the first moment estimates $\beta_1 = 0.9$ and exponential decay rate for the second moments estimates $\beta_2 = 0.999$. The neural network is tested with different activation functions including linear, sigmoid and rectified linear units (ReLU) (Nair and Hinton, 2010) to derive motion regressors. Linear and sigmoid activation functions have comparable performance, but ReLU sometimes leads to invalid loss function due to numerical instabilities. The result obtained with linear activation function is shown in the current study. The subject-specific optimal output regressors are applied on the same subject for reducing motion-related fluctuation.

White Matter and Cerebrospinal Fluid Mask

The segmentation of the T1 image is carried out in the native space of each individual subject and the resultant tissue masks are normalized to the standard MNI152 space. The WM and CSF masks are eroded to reduce partial volume effects from neighboring GM voxels. Eroding the masks is crucial in our study because of the following two aspects. First, because non-GM time series are used in the CNN network to train the parameters in the model, the output regressors can account for some of the variance of BOLD signal if masks are not eroded. Second, the average time series of WM and CSF are used as nuisance regressors in our analysis and these two tissue-based regressors within un-eroded masks can also contain some BOLD signal. Inclusion of BOLD signal in nuisance regression has the potential of reduce the statistical power of fMRI data in the subsequent analysis. WM and CSF masks are eroded by the SPM *spm_erode.m* function. The CSF mask is eroded once as suggested in Power et al. (2014). To have enough WM voxels to train the CNN network and also minimize partial volume effects, the WM mask is eroded multiple times but contains at least 10,000 voxels. Both the non-GM time series used in the neural network and the average tissue-based regressors are extracted based on eroded masks.

Motion Regressors

The CNN network designed above has 12 output regressors, referred as *cnn12* in the following. Unless explicitly specified, the input data to *cnn12* are the motion parameters $\boldsymbol{R}$. The *cnn12* regressors for all subjects can be found in the **Supplementary Material**. The motion parameters $\boldsymbol{R}$ and their temporal backward derivative $\boldsymbol{R'}$, referred to as *mot12*, are used in traditional motion modeling. The [$\boldsymbol{R}$ $\boldsymbol{R'}$] motion regressors in *mot12* are equivalent to another set of 12 motion regressors [$\boldsymbol{R}$ $\boldsymbol{R}_{t-1}$] used in other studies (Friston et al., 1996; Yan et al., 2013), where t-1 refers to the immediately preceding time point and the first row for regressors $\boldsymbol{R}_{t-1}$ for $t = 1$ is traditionally filled with zeros. While previous studies employed varying number of regressors, including 6 regressors ($\boldsymbol{R}$), 12 regressors ([$\boldsymbol{R}$, $\boldsymbol{R'}$]), 24 regressors ([$\boldsymbol{R}$ $\boldsymbol{R}^2$ $\boldsymbol{R}_{t-1}$ $\boldsymbol{R}_{t-1}{}^2$]) and 36 regressors ([$\boldsymbol{R}$ $\boldsymbol{R}^2$ $\boldsymbol{R}_{t-1}$ $\boldsymbol{R}_{t-1}{}^2$ $\boldsymbol{R}_{t-2}$ $\boldsymbol{R}_{t-2}{}^2$]) (Friston et al., 1996; Power et al., 2012, 2014; Satterthwaite et al., 2013; Wilke, 2012; Yan et al., 2013), only *mot12* is compared in detail with *cnn12* in this study. Tissue-based signals are also used as nuisance regressors in part of our analysis and computed as the average signal across the voxels within either eroded WM or eroded CSF masks as described in the previous section. The inclusion of GSR has been heavily debated in the recent past (Murphy et al., 2009; Weissenbacher et al., 2009; Satterthwaite et al., 2013; Power et al., 2014, 2018), hence GSR is not used in this study. Unless explicitly specified, the functional atlas with 264 regions of interest (ROIs) (Power et al., 2011) is used to compute FC.

Motion Measurements

Framewise displacement (FD) (Power et al., 2012), root-mean-square framewise displacement (rmsFD) (Satterthwaite et al., 2013), and DVARS, where D is referring to temporal derivative of time courses and VARS referring to root-mean-square of the variance over voxels (Smyser et al., 2010), are the measurements defined to provide a single estimated head motion parameter for each time point. We also use mean whole-brain standard deviation and modularity quality (Q) to provide a single measurement for each subject.

The motion measurements FD and rmsFD are derived from rigid-body realignment parameters, including three translational and 3 rotational parameters specified by $\boldsymbol{R}$ = [X Y Z yaw pitch roll]. The value of FD is defined as the sum of absolute derivatives of these six parameters with the three rotational parameters converted to distance by multiplying with a radius of 50 mm. The value of rmsFD is defined as the root mean square of relative displacement of two neighboring volumes. The subjects having mean FD $\geq$ 0.25 mm are assigned to the high-motion group (41 subjects, age 74.9 $\pm$ 7.2 years, MMSE 28.7 $\pm$ 1.6, handedness 36 right/5 left, gender 20 male/19 female) and the subjects having mean FD $<$ 0.25 mm are assigned to the low-motion group (35 subjects, age 73.2 $\pm$ 5.8 years, MMSE 29.1 $\pm$ 0.9, handedness 31 right/4 left, gender 13 male/22 female). Unlike FD and rmsFD that are derived from estimated motion parameters, DVARS (Smyser et al., 2010) and mean whole-brain variance are computed based on fMRI data itself. DVARS is defined as the root mean square of the temporal change of the fMRI voxel-wise signal at each time point. Mean whole-brain variance for one subject is computed by first converting fMRI time series to percent signal change and then calculating the mean of the variance of all voxels across the entire brain. In this study we used modularity quality Q to evaluate whether BOLD signal is removed in addition to motion-related fluctuation. The Q-value is determined by applying community detection on each subject's functional network using the Louvain heuristic (Blondel et al., 2008), which maximizes the Q-value as the criterion to partition the functional connectome into sub-networks. Subject motion has been shown to be negatively correlated to the Q-value in Satterthwaite et al. (2012), and the Q-value is expected to decline if the signal is removed (Ciric et al., 2017). An increased Q-value would indicate that the denoising method effectively reduces noise in the data without changing the signal.

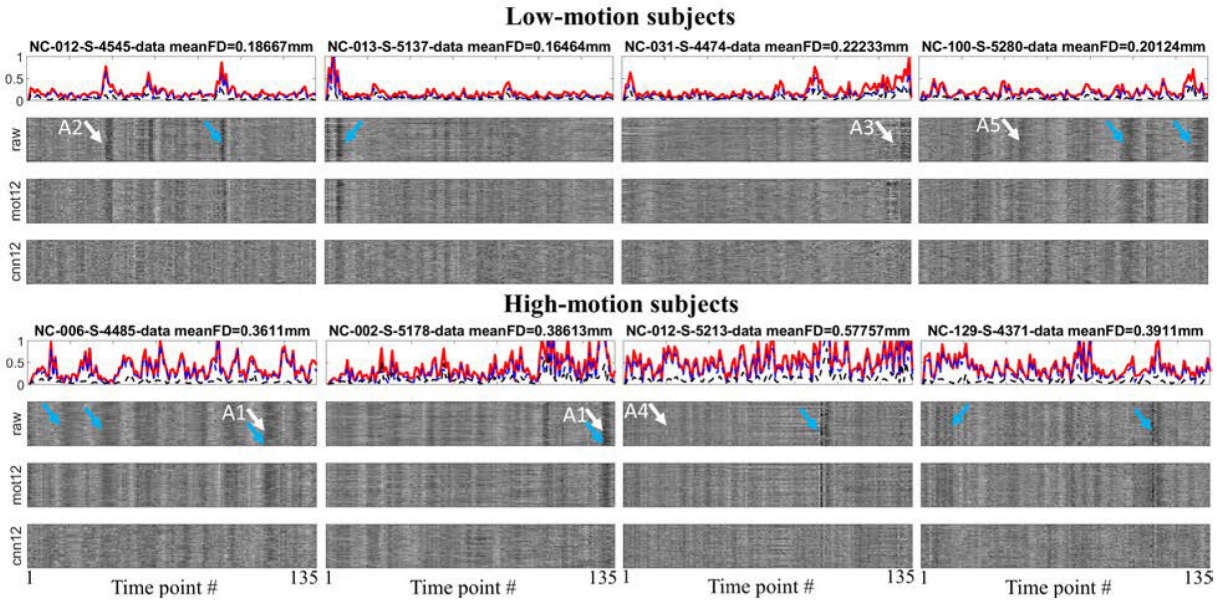

FIGURE 2 | Time-dependent whole brain motion measurements and different preprocessed time series within the GM mask for 4 low-motion and 4 high-motion subjects. White arrows are used to point effects of motion on fMRI signal. Blue arrows are used to point out the performance difference between *cnn12* and *mot12*. The motion measurements include FD (red), sum of absolute translational parameters (blue) and sum of absolute rotational parameters (black).

RESULTS

To visualize the influence of motion regression, motion measurements and fMRI time series for 8 subjects are shown in **Figure 2**. The figures for all subjects can be found in the **Supplementary Material**. The FD (red), sum of absolute translational parameters (blue) and sum of absolute rotational parameters (black) are presented in the top panel for each subject. The normalized time series within GM mask processed with only general preprocessing steps (raw), traditional motion regression *mot12* and CNN-derived motion regression *cnn12* are plotted on the second, third, and fourth panel, respectively. Head movements are observed to have highly variable influences on fMRI signal in terms of three aspects: (1) motion can corrupt fMRI signal with varying duration (the width of dark band in the plot, e.g., arrows A1), (2) the direction of signal change could be mostly in the same direction (e.g., arrow A2) or be opposite at different voxels (e.g., arrow A3), (3) a large head movement may not have visually obvious effect (e.g., arrow A4) but a small head movement can produce marked effect (e.g., arrow A5). By visually inspecting these time series, *cnn12* has a better performance than *mot12* in reducing marked effects, particularly at the time points marked by blue arrows. A quantitative comparison is presented in the following.

Similar to Power et al. (2012) we have calculated FC difference before and after motion correction to evaluate the performance. Functional connectivity is computed as Pearson correlation between regional time series. For both high-motion and low-motion subjects, the scatter plot of between-region connectivity using raw fMRI data versus inter-node distance is shown in **Figure 3A**. The high-motion (black) and low-motion (red) group have shown negative linear relationship with Euclidean distance between ROIs with slope of -3.4 $\times$ 10^{-3} and -2.2 $\times$ 10^{-3}, respectively. The dependency for the high-motion group is significantly stronger than the dependency for the low-motion group ($p < 10^{-4}$). The plots of correlation difference Δr versus Euclidean distance between ROIs are shown in **Figure 3B**, where $\Delta r < 0$ indicates reduced correlation and $\Delta r > 0$ indicates increased correlation after motion regression. The *cnn12*-processed data (blue) shows significantly ($p < 10^{-3}$) stronger trend and lower intercept (larger magnitude) than *mot12*-processed data (black) for both high- and low-motion groups. Furthermore, the trend between Δr and distance is significantly ($p < 10^{-4}$) stronger and the intercept is also significantly ($p < 10^{-4}$) lower in the high-motion group for both *cnn12* and *mot12* processed data.

With the 264-ROI FC matrices, the modularity quality Q was computed for each subject. **Figure 4** shows the scatter plot of *Q*-values for denoised data versus the *Q*-values for raw data. The proposed *cnn12* method (blue dots in **Figure 4**) significantly (paired *t*-test, $p < 0.01$) improves the *Q*-value compared to raw fMRI data. In contrast, the *Q*-value for *mot12*-processed data (gray dots in **Figure 4**) is not significantly (paired *t*-test, $p > 0.05$) different from the value for raw data.

Figure 5A shows the remaining variance (in %) of regional time series after motion regressing using *cnn12* or *mot12*. This plot is generated with all data from 76 subjects. The histograms for *cnn12* and *mot12* are shown in blue and gray color, respectively. The remaining variance of *cnn12*-processed time series is significantly lower than the remaining variance of *mot12*-processed time series with $p < 10^{-4}$. 98.5% of *cnn12*-processed time series have remaining variance lower

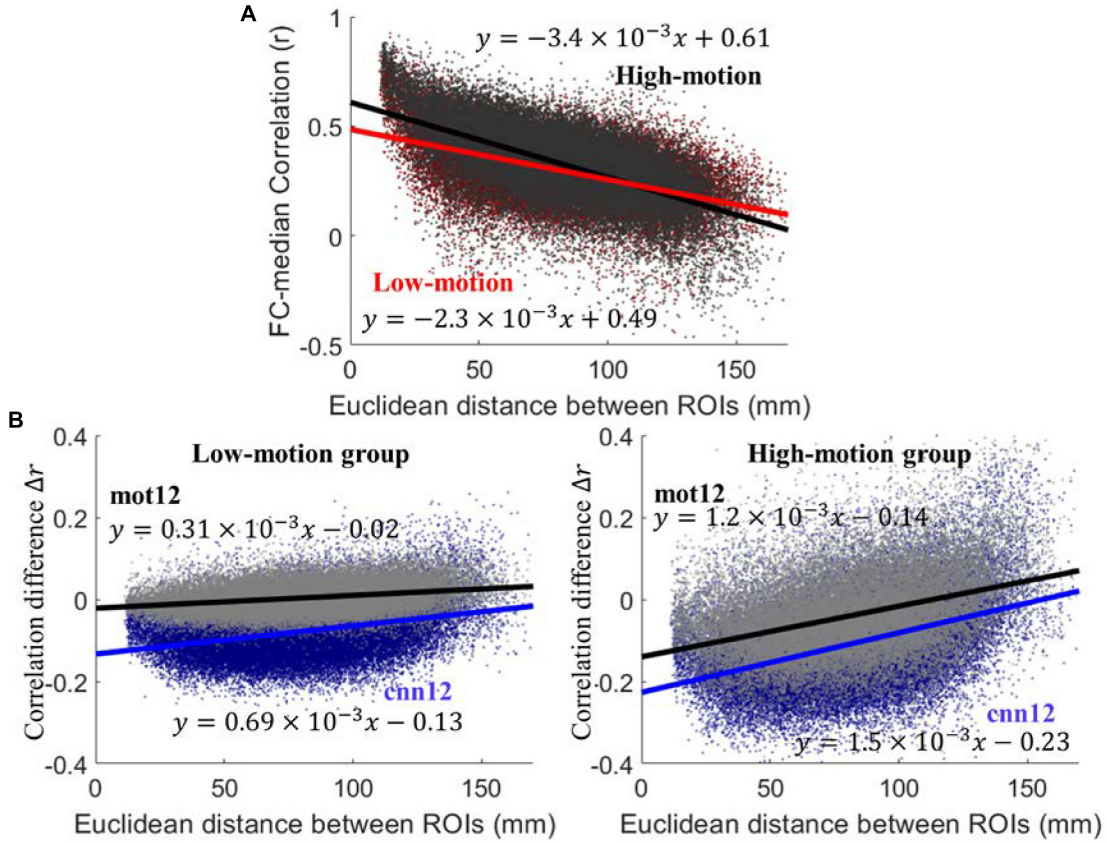

FIGURE 3 | (A) Plots of functional connectivity versus Euclidean distance between ROIs using raw data. **(B)** Plots of functional connectivity versus Euclidean distance for low- and high-motion groups. Pearson correlation coefficient *r* is used to calculate functional connectivity and Δr is defined as $\Delta r = r$(after motion regression) - r(before motion regression).

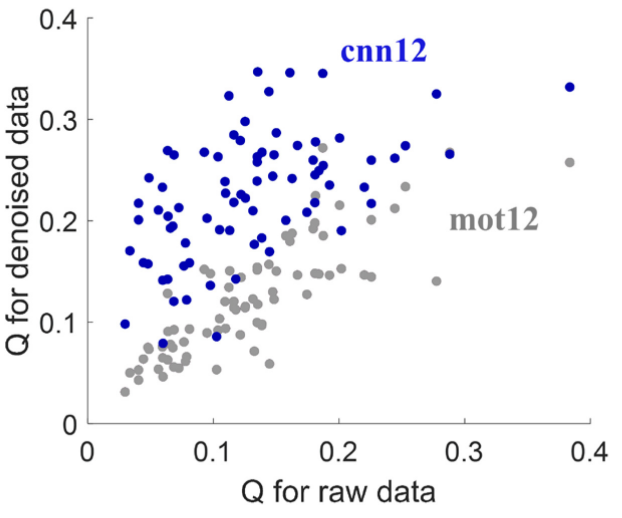

FIGURE 4 | Modularity quantity Q measurement for different processed data. The *Q*-value is computed by applying community detection on each subject's functional network using the Louvain heuristic, which maximizes the *Q*-value as the criterion to partition the network into sub-networks.

than the corresponding time series regressed by *mot12*. The median percentages of variance retained for *cnn12* and *mot12* were 52.7 and 76.0%, respectively. In addition, we have also computed the remaining variance by including average time series within WM or CSF masks as additional regressors (**Figure 5B**). Consistent with the finding described above, the time series regressed with [*cnn12* WM CSF] have remaining variance significantly ($p < 10^{-4}$) less than the corresponding time series regressed with [*mot12* WM CSF]. The median percentage of remaining variance for *cnn12* and *mot12* with average WM and CSF time series as regressors are 43.7 and 58.4%, respectively.

As shown in **Figures 6A,B**, the mean whole-brain variance for raw fMRI data is observed to have a significant ($p < 0.05$) positive linear relationship with FD (see **Figure 6A** blue dots, slope ± 95% confidence interval (CI): 4.3 ± 2.4) and rmsFD (see **Figure 6B** blue dots, slope ± CI: 16.4 ± 10.4). Thus, a reduction of the mean whole-brain variance after motion regression can be treated as a measurement derived from fMRI data itself to evaluate the improvement of applying different motion regressors. The linear relationship between mean whole-brain variance and quality control measurements including FD

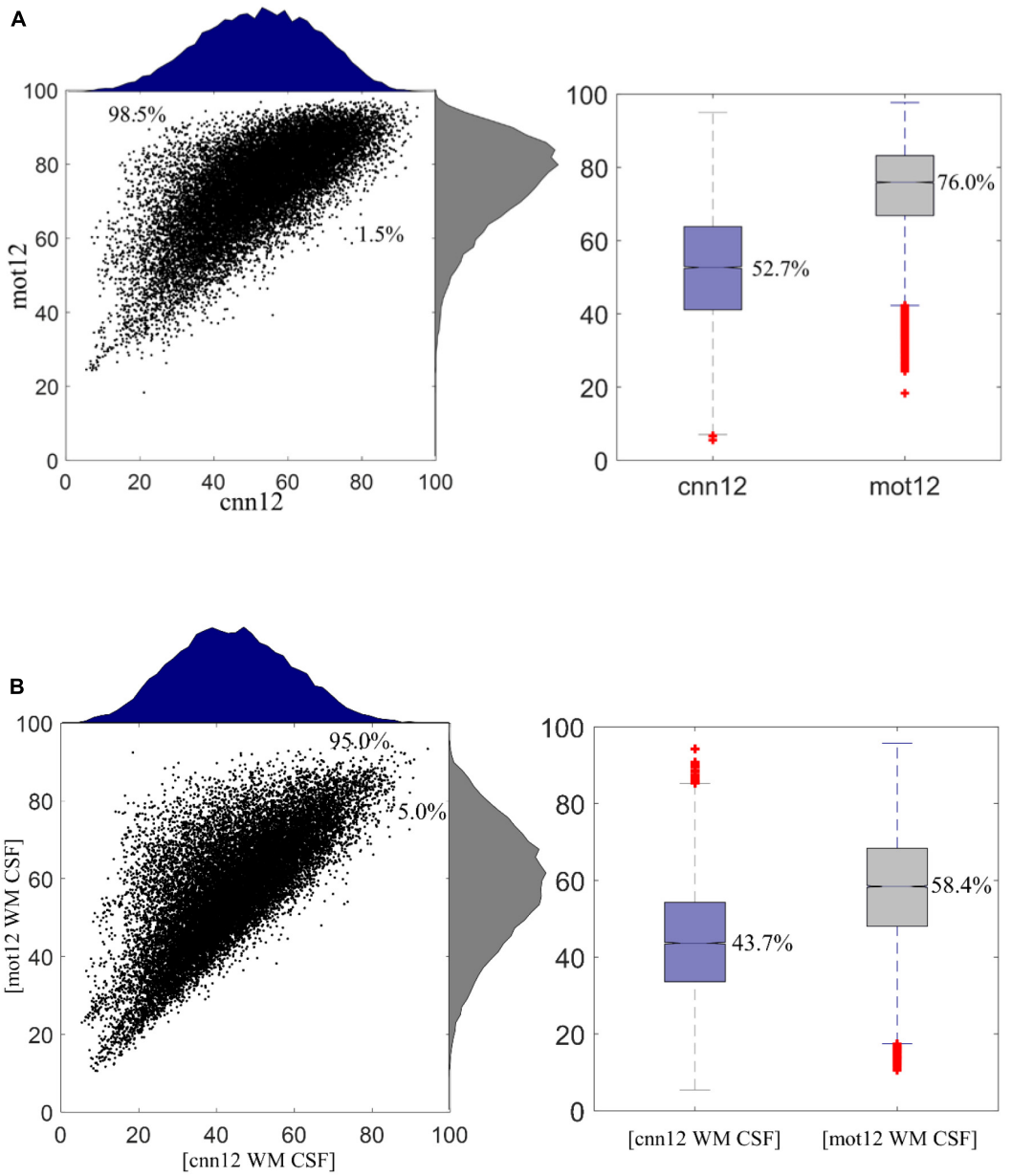

FIGURE 5 | (A) Remaining variance of regional time series after motion regression. 98.5% ROI time series after *mot12* motion regression have a larger variance than using *cnn12* motion regression. The median percentage of remaining variance for *cnn12* and *mot12* regression are 52.7 and 76.0%, respectively. **(B)** Remaining variance of regional time series after nuisance regression with average WM and CSF time series as additional regressors. 95.0% ROI time series using [*mot12* WM CSF] regression have a larger variance than using [*cnn12* WM CSF] regression. The median percentage of remaining variance for *cnn12* and *mot12* regression are 43.7 and 58.4%, respectively.

and rmsFD suggests that greater reduction of motion artifacts is expected to have weaker linear dependency between the variance and motion measurements, and lower mean whole-brain variance value. Using *mot12* regressors, the trend of mean whole-brain variance with mean FD and rmsFD is reduced to 2.8 ± 1.6 and 10.8 ± 6.7, respectively. Using *cnn12* regressors, the trend of mean whole-brain variance with mean FD and rmsFD is reduced to 1.9 ± 1.0 and 7.2 ± 4.4, respectively. The slope of *cnn12* is significantly ($p < 0.01$) flatter than the slope of *mot12* in the linear relationship between mean whole-brain variance and FD or rmsFD. Boxplot of mean whole-brain variance ratio for different motion regressors are shown in **Figure 6C**. Mean whole-brain variance ratio for a single subject is defined as the ratio of the variance after motion regression over the variance before motion regression. Naturally, the ratio of raw fMRI data (only processed with general preprocessing steps) is equal to

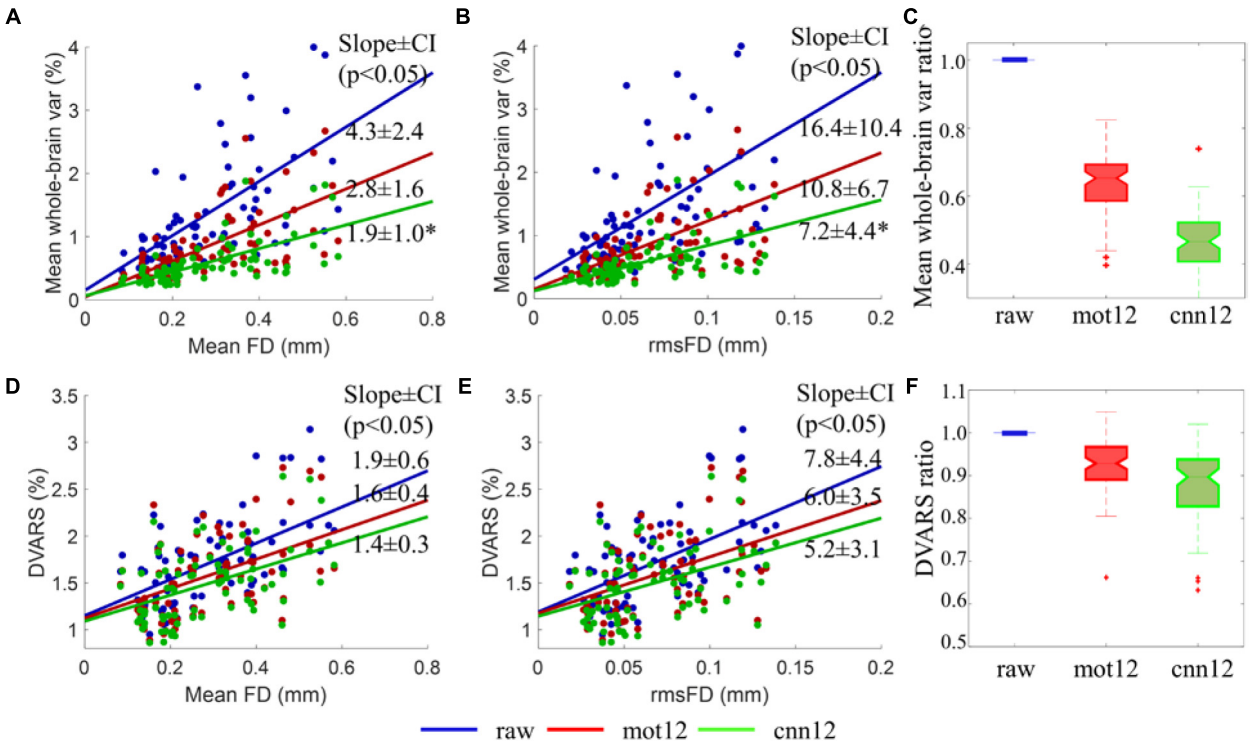

FIGURE 6 | Comparison of different motion regressors using *mean whole-brain variance* and DVARS of intensity-normalized BOLD signal. **(A,B,D,E)** Scatter plots of fMRI data derived measurements (mean whole-brain variance and DVARS) versus quality control measurements (mean FD and rmsFD). The mean whole-brain variance is computed by first converting fMRI time series to percent signal change and then calculating the mean of the variance of all voxels time series across the entire brain. **(C,F)** Boxplots of the ratio of mean whole-brain variance and DVARS. The ratios of mean whole-brain variance and DVARS are defined as the ratio of the measurements after motion regression over the value before motion regression. Data from all 76 subjects are used for the analysis. The slopes of the trend with 95% confidence interval between mean whole-brain standard deviation and mean FD or rmsFD are listed in the figure.

one for all subjects. A ratio less than one indicates that the mean whole-brain variance is reduced in comparison to raw fMRI data. Both *mot12* (median ratio 0.65) and *cnn12* (median ratio 0.47) have a ratio lower than the value for raw data, and the ratio for *cnn12* is significantly ($p < 10^{-4}$) lower than the ratio for *mot12*.

Similar to the mean whole-brain variance, the DVARS for fMRI data without any additional preprocessing steps also has a significant ($p < 0.01$) positive linear relation with motion measurements including FD (see **Figure 6D** blue dots, slope ± CI: 1.9 ± 0.6) and rmsFD (see **Figure 6E** blue dots, slope ± CI: 7.8 ± 4.4). Both *mot12* (slope ± CI with FD: 1.6 ± 0.4; slope ± CI with rmsFD: 6.0 ± 3.5) and *cnn12* (slope ± CI with FD: 1.4 ± 0.3; slope ± CI with rmsFD: 5.2 ± 3.1) decrease the dependency on quality control measurements. The *cnn12* method achieves the weakest linear relationship but the change of slope does not pass a significance level of $p < 0.05$. Boxplots of DVARS ratio for different motion regressors are shown in **Figure 6F**. DVARS ratio for a single subject is defined as the ratio of the mean DVARS across time points after motion regression over the mean value before motion regression. Both *mot12* (median ratio 0.93) and *cnn12* (median ratio 0.89) overall have reduced DVARS values. Furthermore, *cnn12* has a DVARS ratio significantly ($p < 10^{-4}$) less than *mot12*.

We have also applied the CNN network with $\boldsymbol{R}$ as input but determined 6, 12, 24, and 36 output regressors. The remaining variance after motion regression is compared with corresponding traditional motion regressors. The detail of these traditional regressors can be seen in section *Motion regressors*. **Figure 7** shows the median percentage of remaining variance after regression. Using more regressors naturally explains additional variance and thus leads to less variance remaining. The CNN-derived regressors have a relatively flatter curve and less variance than traditional regressors. Traditional method requires more regressors than the neural network to achieve comparable variance reduction. The traditional method requires 36 regressors (51.1% remaining variance) to have comparable remaining variance with the network with 12 output regressors, namely *cnn12* (52.7% remaining variance). Adding average WM and CSF time series as additional regressors further lowers the remaining variance for both methods, but consistently shows similar difference between CNN-derived and traditional regressors.

One interesting question for *cnn12* is whether more *input* motion regressors are beneficial for the output regressors. We have computed the percentage of variance in regressor set 2 explained by regressor set 1 using the notation {regressor set 1, regressor set 2}. For the pair {regressor set 1, regressor set 2},

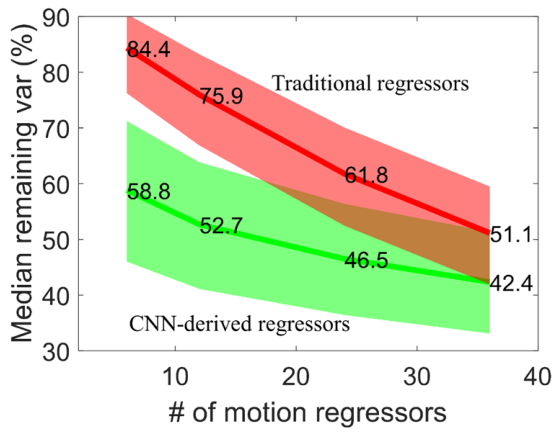

FIGURE 7 | Median percentage of remaining variance with 6, 12, 24, and 36 motion regressors. The 25th and 75th percentiles are used to generate the shaded area for both CNN-derived regressors (green) and traditional regressors (red).

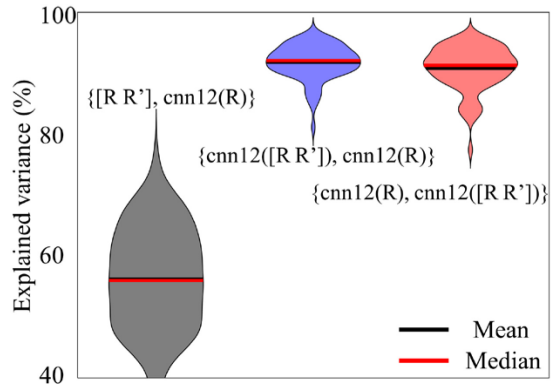

FIGURE 8 | Violin plots of the variance explained (in %) between different sets of regressors. The notation {regressor set 1, regressor set 2} denotes the variance explained for each of the regressors in set 2 by the matrix of regressors in set 1 by linear regression and averaged for all regressors in set 2.

the variance explained for each of the regressors in set 2 by the matrix of regressors in set 1 is computed by linear regression and averaged for all regressors in set 2. The explained variance (in %) is used for the violin plot in **Figure 8**. In all analyses above, the input data to the neural network are the 6 motion parameters $\boldsymbol{R}$, namely *cnn12*($\boldsymbol{R}$), and the input is omitted for simplicity. In this part, we have also applied the neural network with the derivative of motion parameters $\boldsymbol{R}$ as additional input, namely *cnn12*([$\boldsymbol{R}$ $\boldsymbol{R}$']), and all the other settings are exactly the same as in *cnn12*($\boldsymbol{R}$). As shown in **Figure 8**, *cnn12*([$\boldsymbol{R}$ $\boldsymbol{R}$']) explained the variance of *cnn12*($\boldsymbol{R}$) (blue) with a median and mean percentage more than 90%, and vice versa (red). In contrast, [$\boldsymbol{R}$ $\boldsymbol{R}$'] could only explain about 56% of variance in *cnn12*($\boldsymbol{R}$). Furthermore, *cnn12*-derived regressors have a mean correlation of 0.65 with raw motion time series across all subjects and a mean correlation of 0.47 with mask-averaged WM and CSF time series.

DISCUSSION

Motion-related artifacts are a major problem in the analysis of rs-fMRI data. Modeling and reducing these artifacts are critical for improving fMRI analysis. In this study, we have designed a CNN framework for modeling rigid-body motion artifacts in rs-fMRI data. To the best of our knowledge, this is the first study where a deep neural network is designed for denoising resting-state functional MRI data. The proposed subject-level CNN model is constructed with two sequential 1-dim temporal convolutional layers. With the assumption that the voxels within WM or CSF masks share similar motion-related fluctuation as the voxels in GM mask but do not contain any BOLD signal of neural origin, the time series used in the CNN network are limited to voxel locations within the non-GM mask to avoid BOLD signal modeled erroneously in the output regressors. The estimated motion parameters during rigid-body realignment are replicated to match the number of non-GM voxels and then each repetition is treated as a sample to optimize the CNN model. The correlation between non-GM time series and output regressors is used to compute the loss function for optimizing the parameters in the model. The 12-regressor CNN network, *cnn12*, is compared with traditional motion regression, namely *mot12*, for data from 76 subjects downloaded from the ADNI database. While *cnn12* and *mot12* have the same number of regressors, *cnn12* takes advantage of the flexibility in the network to model signal disruption of rigid-body head movements without prior assumptions. The proposed *cnn12* was shown to be superior to *mot12* in terms of multiple quantitative measurements.

High-Motion and Low-Motion Groups

Two prominent effects of motion are the increase of pairwise correlations for nearby voxels and the increase of whole-brain correlations if the signal disruption is widespread and similar over the entire brain (Power et al., 2015). Consistent with these two effects, the high-motion group has more significant linear relationship with Euclidean distance between ROIs, and higher FC than the low-motion group (see **Figure 3A**). With the assumption that signal disruption is more severe in the high-motion group, the difference between the high-motion and the low-motion groups can be explained by these two effects. These findings suggest that motion artifacts considerably influence the analysis and interpretation of fMRI data. Considering the distance dependent FC, a larger slope of Δr as a function of the inter-ROI distance indicates that motion regression is more effective in reducing motion-related fluctuations. The negative intercept is a sign of decreased correlations. Since the high-motion group is more severely affected by motion-related artifacts, the two techniques including *mot12* and *cnn12*, as expected, have a steeper slope and smaller intercept (in magnitude) for the plot of Δr versus distance. However, *cnn12* has significantly reduced motion-related artifacts compared to *mot12*, in terms of slope and intercept, for both high- and low-motion groups.

We would like to point out that both *cnn12* and *mot12* can only reduce but not completely remove motion-related artifacts. After motion regression, the FC in denoised data is

still strongly associated with Euclidean distance between ROIs. A fixed set of motion regressors for the entire brain can only partially explain motion artifacts because of the potential variability of motion artifacts across voxels. Multiple studies have demonstrated that motion regression should be applied together with other processing steps to further reduce signal contamination. For example, Patel et al. (2014) applied wavelet- or time-domain de-spiking before nuisance regression and Power et al. (2012) proposed a "scrubbing" technique to remove motion-related spikes as a complementary strategy to motion regression. The CNN-derived regressors can also be combined with these denoising strategies by simply replacing traditional motion regressors with the derived regressors to further reduce the influence of head motion. Voxel-specific motion parameters (Wilke, 2012; Yan et al., 2013) potentially can also be combined with *cnn12* regressors to further reduce artifacts.

Further Comparison of *mot12* and *cnn12*

Multiple studies indicate that neurobiological signals in human fMRI data only occupy 5–20% of signal variance (Bianciardi et al., 2009; Marcus et al., 2013). We observe that the remaining variance by *mot12* is significantly higher than *cnn12*. More than 90% of *mot12*-regressed time series have variance higher than *cnn12*-regressed time series regardless whether additional tissue-based regressors are used. The median percentage of remaining variance for *cnn12* is 23.3% less than *mot12*, and the variance difference is reduced to 14.7% less than *mot12* if average WM and CSF time series are also included for regression. The decreased variance difference may be because tissue-based regressors share more common information with *cnn12* but less with *mot12* regressors. We have applied motion regression with 6, 12, 24, and 36 regressors. The CNN-derived regressors always explain more variance than traditional regressors, leading to less remaining variance. Even though *cnn12* removes more variance than *mot12*, *cnn12* remains a higher network modularity. Considering that the modularity quality is expected to decline if BOLD signal is removed along with noise in motion regression, this finding suggests that the extra variance removed by *cnn12* is more likely to be motion-related noise instead of the BOLD signal.

Both mean whole-brain variance and DVARS are measurements computed from fMRI data itself to evaluate the influence of motion regression. The positive linear relationship in **Figure 6** shows that the magnitude of these two measurements are heavily driven by head movement. The weaker linear relationship with FD or rmsFD, and smaller value of these two measurements indicate improved data quality. Compared to *mot12*, *cnn12* had significantly flatter slope between mean whole-brain variance and FD or rmsFD. While the slope difference between *cnn12* and *mot12* is not significant, *cnn12* still achieved the flattest slope between DVARS and FD or rmsFD. For both mean whole-brain variance and DVARS, *cnn12* achieves a ratio value less than *mot12*. The weaker linear relationship and smaller ratio value consistently suggest that *cnn12* outperforms *mot12*.

Potential Modification of the Network

As mentioned in section *Architecture of CNN network*, the realignment parameters are replicated and paired with different time series within non-GM mask to form a large number of samples for optimizing the designed CNN network, as demonstrated in **Figure 1**. One potential way to modify the network is to switch the time series and parameters $\boldsymbol{R}$ in the CNN network and thus output voxel-wise motion regressors instead of volume-wise motion regressors. In other words, non-GM time series are used as input data and along with $\boldsymbol{R}$ to compute the loss function and thus voxel-specific motion regressors could be obtained with such a revised network. The CNN network is highly flexible because of the large amount of model parameters in the network, however, the flexibility can be beneficial or detrimental to the following analysis depending on the input. The flexibility in the alternative neural network can easily make the output of arbitrary input time series highly correlated with parameters $\boldsymbol{R}$ to achieve optimal loss function but does not extract any useful information. In contrast, the current framework requires the output regressors to optimize the summation of correlations over all non-GM voxels. Output regressors that are highly correlated with a single time series are not optimal because they have a minor effect in the loss function due to the summation over all voxels. While voxel-specific regressors may be more useful than a fixed set of regressors for the entire brain, the current framework with switched time series and realignment parameters has difficulty to extract voxel-specific regressors properly.

The *cnn12* network can also be applied with more motion parameters as input. We have compared the *cnn12* with only $\boldsymbol{R}$ and with [$\boldsymbol{R}$ $\boldsymbol{R}$'] as input. Interestingly, the space spanned by the *cnn12*($\boldsymbol{R}$) regressors is similar to the space spanned by the *cnn12*([$\boldsymbol{R}$ $\boldsymbol{R}$']) since the variance explained of *cnn12*($\boldsymbol{R}$) by *cnn12*([$\boldsymbol{R}$ $\boldsymbol{R}$']) is larger than 90% for all subjects (see **Figure 8**). This finding suggests that adding the derivative as input does not have noticeable impact to the output regressors. The unexplained variance maybe due to the intrinsic randomness in the network. However, the *cnn12*(R) regressors can explain a large proportion of variance that cannot be explained by traditional motion regressors [$\boldsymbol{R}$ $\boldsymbol{R}$'], which may be because motion-related artifacts in fMRI data cannot be sufficiently described by only adding the preceding time point into consideration (Power et al., 2014).

Novelties of the *cnn12* Network

Compared to standard CNN algorithms, the input and loss function in *cnn12* are specified in a novel way. A standard CNN algorithm requires thousands of samples to train the neural network. Though the *cnn12* network seems to have only the six motion parameters as input samples (which is not the case), we associate each set of motion parameters with different voxel time series in the *cnn12* network. Thus, each motion parameter *paired* with voxel time series is treated as a different sample and, consequently, a sufficient number of samples can be generated to train the neural network.

Many cost functions have been developed for the purpose of classification or regression in machine learning or deep learning applications, such as the mean squared error, mean absolute percentage error, cross entropy, Poisson, and cosine proximity cost functions. These cost functions are calculated with the known true values or classes. However, because the ground truth

is unknown, constructing a cost function for *cnn12* denoising faces a significant challenge. To overcome this challenge, we have proposed a customized cost function which does not require knowledge of the true BOLD signal.

Limitations and Future Study

There are a few limitations in this study. First, similar to most motion regression studies, the same regressors are used for all voxels in the brain. While the revised neural network mentioned in the section above potentially can achieve voxel-specific regressors, unfortunately such a network cannot extract useful information. We would like to explore other neural network architectures for modeling voxel-specific motion in a future study. Second, while this study is only focused on modeling the influence of head motion, other artifact sources such as cardiac and respiratory noise also considerably confound fMRI data analysis. Multiple methods (Glover et al., 2000; Beall, 2010) have been proposed to model cardiac and respiratory fluctuation of fMRI data with the assistance of external recordings, which is not available in the ADNI data. It would be interesting to model these physiologic noise sources by using our neural network with input from external recordings. Third, the hyper-parameters, e.g., filter size, number of nodes, and learning rate, in a network are impacted by the data. The hyper-parameters used in this study are tuned for a single standard EPI sequence. Following studies with a large sample size are required to gain more knowledge about the influence of TR, the number of volumes and EPI sequences, such as multi-echo EPI (Kundu et al., 2012) and multi-band EPI sequences (Moeller et al., 2010). In addition to the motion-related artifacts induced in fMRI data, motion may have a neurobiological basis (Zeng et al., 2014) and could reflect individual differences. Genetic differences and impulsivity were found to be factors related to head motion (Kong et al., 2014; Hodgson et al., 2016). The *positive* motion-BOLD relationship (Yan et al., 2013) may reflect neural origins of motion. Therefore, any approaches for removing motion-related artifacts, including *cnn12*, may remove some useful subject-related information.

While the CNN network is developed based on resting-state data, this technique potentially can also be useful for reducing motion-related artifacts in task-based fMRI data, whereas an additional study with large number of subjects is required for further validation.

CONCLUSION

We have proposed a CNN network modeling motion-related signal disruption in rs-fMRI data using estimated realignment parameters and compared the CNN-derived regressors with traditional motion regressors using publicly available data. Visually, *cnn12* is more effective in reducing head-motion effects. Quantitatively, *cnn12* reduces more variance in regional time series, reduces more the trend between motion parameters and other measurements derived from fMRI data itself, makes the data more homogeneous based on between-subject similarity of brain connectivity and leads to a larger modularity Q, when compared to *mot12*.

DATA AVAILABILITY

Publicly available datasets were analyzed in this study. This data can be found here: http://adni.loni.usc.edu/.

AUTHOR CONTRIBUTIONS

ZY and DC conceived and designed the study and acquired, analyzed, and interpreted the data. ZY, XZ, KS, VM, and DC drafted the manuscript, revised the manuscript critically for important intellectual content, and approved the final version of the manuscript to be submitted.

FUNDING

This research project was supported by the NIH (Grant No. 1R01EB014284 and COBRE; 5P20GM109025) and a private grant from Peter and Angela Dal Pezzo. Data collection and sharing for this project was funded by the Alzheimer's Disease Neuroimaging Initiative (ADNI) (National Institutes of Health Grant U01 AG024904) and DOD ADNI (Department of Defense Award No. W81XWH-12-2-0012). ADNI was funded by the National Institute on Aging, the National Institute of Biomedical Imaging and Bioengineering, and through generous contributions from the following: AbbVie, Alzheimer's Association; Alzheimer's Drug Discovery Foundation; Araclon Biotech; BioClinica, Inc.; Biogen; Bristol-Myers Squibb Company; CereSpir, Inc.; Cogstate; Eisai Inc.; Elan Pharmaceuticals, Inc.; Eli Lilly and Company; EuroImmun; F. Hoffmann-La Roche Ltd and its affiliated company Genentech, Inc.; Fujirebio; GE Healthcare; IXICO Ltd.; Janssen Alzheimer Immunotherapy Research & Development, LLC.; Johnson & Johnson Pharmaceutical Research & Development LLC.; Lumosity; Lundbeck; Merck & Co., Inc.; Meso Scale Diagnostics, LLC.; NeuroRx Research; Neurotrack Technologies; Novartis Pharmaceuticals Corporation; Pfizer Inc.; Piramal Imaging; Servier; Takeda Pharmaceutical Company; and Transition Therapeutics. The Canadian Institutes of Health Research was providing funds to support ADNI clinical sites in Canada. Private sector contributions are facilitated by the Foundation for the National Institutes of Health (www.fnih.org). The grantee organization is the Northern California Institute for Research and Education, and the study is coordinated by the Alzheimer's Therapeutic Research Institute at the University of Southern California. ADNI data are disseminated by the Laboratory for Neuro Imaging at the University of Southern California.

SUPPLEMENTARY MATERIAL

The Supplementary Material for this article can be found online at: https://www.frontiersin.org/articles/10.3389/fnins.2019.00169/full#supplementary-material

REFERENCES

Beall, E. B. (2010). Adaptive cyclic physiologic noise modeling and correction in functional MRI. *J. Neurosci. Methods* 187, 216–228. doi: 10.1016/j.jneumeth.2010.01.013

Beall, E. B., and Lowe, M. J. (2014). SimPACE: generating simulated motion corrupted BOLD data with synthetic-navigated acquisition for the development and evaluation of SLOMOCO: a new, highly effective slicewise motion correction. *Neuroimage* 101, 21–34. doi: 10.1016/j.neuroimage.2014.06.038

Behzadi, Y., Restom, K., Liau, J., and Liu, T. T. (2007). A component based noise correction method (CompCor) for BOLD and perfusion based fMRI. *Neuroimage* 37, 90–101. doi: 10.1016/j.neuroimage.2007.04.042

Bianciardi, M., Fukunaga, M., van Gelderen, P., Horovitz, S. G., de Zwart, J. A., Shmueli, K., et al. (2009). Sources of functional magnetic resonance imaging signal fluctuations in the human brain at rest: a 7 T study. *Magn. Reson. Imaging* 27, 1019–1029. doi: 10.1016/j.mri.2009.02.004

Blondel, V. D., Guillaume, J.-L., Lambiotte, R., and Lefebvre, E. (2008). Fast unfolding of communities in large networks. *J. Stat. Mech.* 2008:10008.

Caballero-Gaudes, C., and Reynolds, R. C. (2017). Methods for cleaning the BOLD fMRI signal. *Neuroimage* 154, 128–149. doi: 10.1016/j.neuroimage.2016.12.018

Ciric, R., Wolf, D. H., Power, J. D., Roalf, D. R., Baum, G. L., Ruparel, K., et al. (2017). Benchmarking of participant-level confound regression strategies for the control of motion artifact in studies of functional connectivity. *Neuroimage* 154, 174–187. doi: 10.1016/j.neuroimage.2017.03.020

Courtemanche, M. J., Sparrey, C. J., Song, X., MacKay, A., and D'arcy, R. C. (2018). Detecting white matter activity using conventional 3 Tesla fMRI: an evaluation of standard field strength and hemodynamic response function. *Neuroimage* 169, 145–150. doi: 10.1016/j.neuroimage.2017.12.008

Friston, K. J., Williams, S., Howard, R., Frackowiak, R. S., and Turner, R. (1996). Movement-related effects in fMRI time-series. *Magn. Reson. Med.* 35, 346–355. doi: 10.1002/mrm.1910350312

Gawryluk, J. R., Mazerolle, E. L., Beyea, S. D., and D'Arcy, R. C. (2014). Functional MRI activation in white matter during the symbol digit modalities test. *Front. Hum. Neurosci.* 8:589. doi: 10.3389/fnhum.2014.00589

Glorot, X., and Bengio, Y. (2010). "Understanding the difficulty of training deep feedforward neural networks," in *Proceedings of the Thirteenth International Conference on Artificial Intelligence and Statistics*, Vol. 9, eds Y. W. Teh and M. Titterington (Sardinia: Chia Laguna Resort), 249–256.

Glover, G. H., Li, T. Q., and Ress, D. (2000). Image-based method for retrospective correction of physiological motion effects in fMRI: RETROICOR. *Magn. Reson. Med.* 44, 162–167. doi: 10.1002/1522-2594(200007)44:1<162::AID-MRM23>3.0.CO;2-E

Griffanti, L., Salimi-Khorshidi, G., Beckmann, C. F., Auerbach, E. J., Douaud, G., Sexton, C. E., et al. (2014). ICA-based artefact removal and accelerated fMRI acquisition for improved resting state network imaging. *Neuroimage* 95, 232–247. doi: 10.1016/j.neuroimage.2014.03.034

Hodgson, K., Poldrack, R. A., Curran, J. E., Knowles, E. E., Mathias, S., Göring, H. H., et al. (2016). Shared genetic factors influence head motion during MRI and body mass index. *Cereb. Cortex* 27, 5539–5546. doi: 10.1093/cercor/bhw321

Jiang, A., Kennedy, D. N., Baker, J. R., Weisskoff, R. M., Tootell, R. B., Woods, R. P., et al. (1995). Motion detection and correction in functional MR imaging. *Hum. Brain Mapp.* 3, 224–235. doi: 10.1002/hbm.460030306

Kim, Y. (2014). "Convolutional neural networks for sentence classification," in *Proceedings of the 2014 Conference on Empirical Methods in Natural Language Processing (EMNLP)* (Doha, Qatar: Association for Computational Linguistics), 1746–1751.

Kingma, D., and Ba, L. (2015). Adam: a method for stochastic optimization. *arXiv* [Preprint]. arXiv:1412.6980

Kong, X.-Z., Zhen, Z., Li, X., Lu, H.-H., Wang, R., Liu, L., et al. (2014). Individual differences in impulsivity predict head motion during magnetic resonance imaging. *PLoS One* 9:e104989. doi: 10.1371/journal.pone.0104989

Krizhevsky, A., Sutskever, I., and Hinton, G. E. (2012). Imagenet classification with deep convolutional neural networks. *Adv. Neural Inf. Process. Syst.* 25, 1097–1105.

Kundu, P., Inati, S. J., Evans, J. W., Luh, W.-M., and Bandettini, P. A. (2012). Differentiating BOLD and non-BOLD signals in fMRI time series using multi-echo EPI. *Neuroimage* 60, 1759–1770. doi: 10.1016/j.neuroimage.2011.12.028

Lemieux, L., Salek-Haddadi, A., Lund, T. E., Laufs, H., and Carmichael, D. (2007). Modelling large motion events in fMRI studies of patients with epilepsy. *Magn. Reson. Imaging* 25, 894–901. doi: 10.1016/j.mri.2007.03.009

Liang, M., and Hu, X. (2015). "Recurrent convolutional neural network for object recognition," in *Proceedings of the IEEE Conference on Computer Vision and Pattern Recognition*, (Piscataway, NJ: IEEE), 3367–3375. doi: 10.1109/CVPR.2015.7298958

Macey, P. M., Macey, K. E., Kumar, R., and Harper, R. M. (2004). A method for removal of global effects from fMRI time series. *Neuroimage* 22, 360–366. doi: 10.1016/j.neuroimage.2003.12.042

Marcus, D. S., Harms, M. P., Snyder, A. Z., Jenkinson, M., Wilson, J. A., Glasser, M. F., et al. (2013). Human Connectome Project informatics: quality control, database services, and data visualization. *Neuroimage* 80, 202–219. doi: 10.1016/j.neuroimage.2013.05.077

Moeller, S., Yacoub, E., Olman, C. A., Auerbach, E., Strupp, J., Harel, N., et al. (2010). Multiband multislice GE-EPI at 7 tesla, with 16-fold acceleration using partial parallel imaging with application to high spatial and temporal whole-brain fMRI. *Magn. Reson. Med.* 63, 1144–1153. doi: 10.1002/mrm.22361

Murphy, K., Birn, R. M., and Bandettini, P. A. (2013). Resting-state fMRI confounds and cleanup. *Neuroimage* 80, 349–359. doi: 10.1016/j.neuroimage.2013.04.001

Murphy, K., Birn, R. M., Handwerker, D. A., Jones, T. B., and Bandettini, P. A. (2009). The impact of global signal regression on resting state correlations: are anti-correlated networks introduced? *Neuroimage* 44, 893–905. doi: 10.1016/j.neuroimage.2008.09.036

Nair, V., and Hinton, G. E. (2010). "Rectified linear units improve restricted boltzmann machines," in *Proceedings of the 27th International conference on machine learning (ICML-10)*, eds J. Fürnkranz and T. Joachims (New York, NY: ACM), 807–814.

Patel, A. X., Kundu, P., Rubinov, M., Jones, P. S., Vértes, P. E., Ersche, K. D., et al. (2014). A wavelet method for modeling and despiking motion artifacts from resting-state fMRI time series. *Neuroimage* 95, 287–304. doi: 10.1016/j.neuroimage.2014.03.012

Power, J. D., Barnes, K. A., Snyder, A. Z., Schlaggar, B. L., and Petersen, S. E. (2012). Spurious but systematic correlations in functional connectivity MRI networks arise from subject motion. *Neuroimage* 59, 2142–2154. doi: 10.1016/j.neuroimage.2011.10.018

Power, J. D., Cohen, A. L., Nelson, S. M., Wig, G. S., Barnes, K. A., Church, J. A., et al. (2011). Functional network organization of the human brain. *Neuron* 72, 665–678. doi: 10.1016/j.neuron.2011.09.006

Power, J. D., Mitra, A., Laumann, T. O., Snyder, A. Z., Schlaggar, B. L., and Petersen, S. E. (2014). Methods to detect, characterize, and remove motion artifact in resting state fMRI. *Neuroimage* 84, 320–341. doi: 10.1016/j.neuroimage.2013.08.048

Power, J. D., Plitt, M., Gotts, S. J., Kundu, P., Voon, V., Bandettini, P. A., et al. (2018). Ridding fMRI data of motion-related influences: removal of signals with distinct spatial and physical bases in multiecho data. *Proc. Natl. Acad. Sci. U.S.A.* 115, E2105–E2114. doi: 10.1073/pnas.1720985115

Power, J. D., Schlaggar, B. L., and Petersen, S. E. (2015). Recent progress and outstanding issues in motion correction in resting state fMRI. *Neuroimage* 105, 536–551. doi: 10.1016/j.neuroimage.2014.10.044

Pruim, R. H., Mennes, M., van Rooij, D., Llera, A., Buitelaar, J. K., and Beckmann, C. F. (2015). ICA-AROMA: a robust ICA-based strategy for removing motion artifacts from fMRI data. *Neuroimage* 112, 267–277. doi: 10.1016/j.neuroimage.2015.02.064

Saad, Z. S., Gotts, S. J., Murphy, K., Chen, G., Jo, H. J., Martin, A., et al. (2012). Trouble at rest: how correlation patterns and group differences become distorted after global signal regression. *Brain Connect.* 2, 25–32. doi: 10.1089/brain.2012.0080

Satterthwaite, T. D., Elliott, M. A., Gerraty, R. T., Ruparel, K., Loughead, J., Calkins, M. E., et al. (2013). An improved framework for confound regression and filtering for control of motion artifact in the preprocessing of resting-state functional connectivity data. *Neuroimage* 64, 240–256. doi: 10.1016/j.neuroimage.2012.08.052

Satterthwaite, T. D., Wolf, D. H., Loughead, J., Ruparel, K., Elliott, M. A., Hakonarson, H., et al. (2012). Impact of in-scanner head motion on multiple measures of functional connectivity: relevance for studies of neurodevelopment

in youth. *Neuroimage* 60, 623–632. doi: 10.1016/j.neuroimage.2011.12.063

Smyser, C. D., Inder, T. E., Shimony, J. S., Hill, J. E., Degnan, A. J., Snyder, A. Z., et al. (2010). Longitudinal analysis of neural network development in preterm infants. *Cereb. Cortex* 20, 2852–2862. doi: 10.1093/cercor/bhq035

Van Dijk, K. R., Sabuncu, M. R., and Buckner, R. L. (2012). The influence of head motion on intrinsic functional connectivity MRI. *Neuroimage* 59, 431–438. doi: 10.1016/j.neuroimage.2011.07.044

Weissenbacher, A., Kasess, C., Gerstl, F., Lanzenberger, R., Moser, E., and Windischberger, C. (2009). Correlations and anticorrelations in resting-state functional connectivity MRI: a quantitative comparison of preprocessing strategies. *Neuroimage* 47, 1408–1416. doi: 10.1016/j.neuroimage.2009.05.005

Wilke, M. (2012). An alternative approach towards assessing and accounting for individual motion in fMRI timeseries. *Neuroimage* 59, 2062–2072. doi: 10.1016/j.neuroimage.2011.10.043

Yan, C.-G., Cheung, B., Kelly, C., Colcombe, S., Craddock, R. C., Di Martino, A., et al. (2013). A comprehensive assessment of regional variation in the impact of head micromovements on functional connectomics. *Neuroimage* 76, 183–201. doi: 10.1016/j.neuroimage.2013.03.004

Zeng, L.-L., Wang, D., Fox, M. D., Sabuncu, M., Hu, D., Ge, M., et al. (2014). Neurobiological basis of head motion in brain imaging. *Proc. Natl. Acad. Sci. U.S.A.* 111, 6058–6062. doi: 10.1073/pnas.1317424111

Conflict of Interest Statement: The authors declare that the research was conducted in the absence of any commercial or financial relationships that could be construed as a potential conflict of interest.

frontiers in Neuroscience

METHODS
published: 18 March 2019
doi: 10.3389/fnins.2019.00204

Phase fMRI Reveals More Sparseness and Balance of Rest Brain Functional Connectivity Than Magnitude fMRI

Zikuan Chen[1]*, *Zening Fu*[1] and *Vince Calhoun*[1,2]

[1] The Mind Research Network and LBERI, Albuquerque, NM, United States, [2] Department of Electrical and Computer Engineering, University of New Mexico, Albuquerque, NM, United States

Conventionally, brain function is inferred from the magnitude data of the complex-valued fMRI output. Since the fMRI phase image (unwrapped) provides a representation of brain internal magnetic fieldmap (by a constant scale difference), it can also be used to study brain function while providing a more direct representation of the brain's magnetic state. In this study, we collected a cohort of resting-state fMRI magnitude and phase data pairs from 600 subjects (age from 10 to 76, 346 males), decomposed the phase data by group independent component analysis (pICA), calculated the functional network connectivity (pFNC). In comparison with the magnitude-based brain function analysis (mICA and mFNC), we find that the pFNC matrix contains fewer significant functional connections (with *p*-value thresholding) than the mFNC matrix, which are sparsely distributed across the whole brain with near/far interconnections and positive/negative correlations in rough balance. We also find a few of brain rest sub-networks within the phase data, primarily in subcortical, cerebellar, and visual regions. Overall, our findings offer new insights into brain function connectivity in the context of a focus on the brain's internal magnetic state.

Keywords: magnitude and phase fMRI, independent component analysis (ICA), functional network connectivity (FNC), functional connectivity sparseness, functional connectivity balance

OPEN ACCESS

Edited by:
Nanyin Zhang,
Pennsylvania State University,
United States

Reviewed by:
Jean Chen,
University of Toronto, Canada
Sadia Shakil,
Institute of Space Technology,
Pakistan

***Correspondence:**
Zikuan Chen
zchen@mrn.org

Specialty section:
This article was submitted to Brain Imaging Methods, a section of the journal Frontiers in Neuroscience

Received: *20 November 2018*
Accepted: *21 February 2019*
Published: *18 March 2019*

Citation:
Chen Z, Fu Z and Calhoun V (2019) Phase fMRI Reveals More Sparseness and Balance of Rest Brain Functional Connectivity Than Magnitude fMRI. Front. Neurosci. 13:204. doi: 10.3389/fnins.2019.00204

INTRODUCTION

Phase functional magnetic resonance imaging (fMRI) is an MRI technique dedicated to fMRI phase data acquisition and post-acquisition processing and analysis. In principle, an fMRI study produces a timeseries of complex-valued images consisting of pairwise magnitude and phase components; therefore, the fMRI phase data are generated together with the magnitude data in an fMRI experiment (at no extra cost). Since the complex-valued fMRI data (magnitude and phase images in pairs) are formed from the same magnetic source (the internal inhomogeneous magnetic fieldmap) through intravoxel dephasing signal detection and subsequent complex modulo/argument calculations (Chen and Calhoun, 2015b), both are useful for brain function depiction with different representations (in different measurements). In theory, the fMRI phase data are more suitable for brain function analysis since phase imaging represents the brain magnetic state seen in internal magnetic fieldmaps.

There is a body of reports on the exploration and exploitation of phase fMRI for brain function study (Rowe, 2005, 2009; Arja et al., 2009; Feng et al., 2009; Balla et al., 2014; Bianciardi et al., 2014; Chen and Calhoun, 2016b; Ozbay et al., 2016). Under linear imaging conditions, an fMRI phase image represents the brain internal magnetic field distribution captured at a timepoint (Chen and Calhoun, 2015b; Chen et al., 2018b). This portrays a brain magnetic state (a magnetization state in a main field B_0, in preparation for MRI scanning) during brain activity (Shmueli et al., 2009; Li et al., 2011; Chen and Calhoun, 2013, 2015a; Wang and Liu, 2015).

In theory, the fMRI magnitude signal is calculated from the complex signal by a nonnegative nonlinearity (e.g., $|\pm 1| = 1$) that fails to represent the source of an internal fieldmap (e.g., degenerating the signs associated with the bipolar-valued field distribution). In comparison, the fMRI phase signal is calculated from the complex MRI signal through a trigonometric operation, $arctan(\varphi)$, which can be linearly approximated by $arctan(\varphi) \approx \varphi$ for $|\varphi| < 1$ (φ denotes a phase signal, measured in units of radian, related to the field value by a constant scale γT_E). Therefore, a phase image is linearly related to the magnetic field in linear phase fMRI (Haacke et al., 1999; Chavhan et al., 2009; Chen and Calhoun, 2015b, 2016b). We may infer the internal fieldmap source from an fMRI phase image under linear approximation; however, such inverse mapping is not available from fMRI magnitude data (due to an irreversible magnitude nonlinearity like $|\pm 1| = 1$).

The trigonometric $arctan(\varphi)$ gives a good linearization for a very small φ, as mathematically defined by $arctan(\varphi) = \varphi$ for $|\varphi| << 1$. In order to maximally reduce the nonlinearity associated with $arctan(\varphi)$, we adopt an additive perturbation model, $\varphi(t) = \varphi_0 \pm \delta\varphi(t)$, to extract the BOLD-only phase signal (the perturbation term $\delta\varphi(t)$) from a timeseries of BOLD phase signals through complex division (a Hilbert inner product) (Chen and Calhoun, 2016b; Chen et al., 2018b). The BOLD-only phase signal $\delta\varphi$ results in good linear mapping of the source of BOLD-only magnetic field perturbation by reducing the nonlinearity associated with $arctan(\varphi)$.

Given a timeseries of fMRI images, we can break down brain function into a collection of brain subfunctions (subnetworks) through an independent component analysis (ICA) method (Calhoun et al., 2001; McKeown et al., 2003; Guo and Pagnoni, 2008; Calhoun and Adali, 2012). Taking advantage of data-driven multivariate statistics, the ICA method has been successfully extended to allow population-level group data analysis (a technique of group ICA) (Calhoun et al., 2001; Beckmann et al., 2005; Guo and Pagnoni, 2008; Calhoun and Adali, 2012). Accordingly, we can apply group ICA to magnitude and phase data separately for brain function decompositions, as denoted by mICA and pICA (Chen et al., 2018a). For comparison of mICA and pICA in correspondence, we constrain the pICA with the magnitude-inferred group information and implement group-information-guided (GIG) pICA (Du and Fan, 2013).

Using mICA and pICA, we then calculate their functional network connectivity (FNC) matrices (denoted by mFNC and pFNC) based on the temporal correlation of mICA and pICA timecourses (Jafri et al., 2008; Arbabshirani and Calhoun, 2011). For larger population data analysis, we may discard the insignificant functional connections based on statistical significance (based on p-value assessment). For example, a p-value thresholding ($<10^{-10}$) removes insignificant connections in mFNC, enhancing identification of significant whole-brain connections such as sparsity, balance, and near and far couplings.

We have recently reported on a method of comparing magnitude and phase-based brain functional connectivity in the resting state via statistical analysis over 100 subjects (Chen et al., 2018a). This revealed interesting similarities and distinctions between mFNC and pFNC. Here, we used a larger cohort of subject data ($N = 600$) to analyze the brain functional connectivity patterns in mFNC and pFNC matrices. We addressed the following aspects: intra-domain (short-range, near) and inter-domain (long-range, far) connections, positive and negative connections, sparseness and nonuniformity of connection distribution, and robustness and significance of group-level connections.

METHODS

Data Collection

A collection of 600 subject datasets (in pairs of magnitude and phase images) were acquired from a cohort of participants (age: 10–76 years, 346 male/254 female) by subject scanning in a Siemens TrioTim 3T scanner at the Mind Research Network. Informed consent was obtained for each subject and the subject scanning protocol was approved by the IRB at the University of New Mexico. The data were gained from the subjects anonymously prior to group analysis.

The fMRI experiments were performed with the following parameter settings: 12-channel coil, GRE-EPI sequence, T_E = 29 ms, T_R = 2 s, flip angle = 75°, field of view = 240 cm × 240 cm, matrix size = 64 × 64, voxel size = 3.75 mm × 3.75 mm × 4.55 mm, slice thickness = 3.5 mm, slice gap = 1.05 mm, total slices 33, acquisition time (T_A) = 5 min, and total volumes 150. Subjects were instructed to keep their eyes open during the scanning and fixate on a foveally presented cross. We obtained two groups of fMRI data, using magnitude and phase images in pairs, with each in a 4D format (64 × 64 × 33 × 150, 3D spatial and 1D temporal in dimension).

Data Processing

Preprocessing the fMRI magnitude images included removing the first two timepoints to avoid T1 equilibration effects; realignment using INRIalign; slice-timing correction using the middle slice as the reference frame; spatial normalization into MNI space with resampled isotropic voxels (3 × 3 × 3 mm); and spatial smoothing with a Gaussian kernel (FWHM = 9 mm). Through data processing, each 4D subject data (magnitude and

Abbreviations: BOLD, blood oxygenation level dependent; fMRI, functional magnetic resonance imaging; mICA, magnitude data independent component analysis (ICA); pICA, phase data ICA; mFNC magnitude-depicted function network connectivity (FNC); pFNC, phase-depicted FNC.

phase separately) in 64 × 64 × 33 × 150 format was converted to 53 × 63 × 46 × 148. For fMRI magnitude image preprocessing, we used the SPM8 automated pipeline (Chen et al., 2018a) as reported (http://www.fil.ion.ucl.ac.uk/spm/software/spm8/).

Extracting BOLD-Only Phase Signals

The raw phase images were first converted to a range in radian ($-\pi$, π) and denoted by φ (bipolarly valued). Then, the phase series images were subjected to spatial realignment through the 3D affine transformation using the motion correction parameters (4 × 4 affine transformation) as derived from the magnitude image realignment in the corresponding magnitude timeseries. Upon phase timeseries image realignment, a complex division (Equation A2 in **Appendix**) was used to extract the temporal phase changes (BOLD-only phase response) with respect to the middle frame at the middle timepoint in the series (Chen et al., 2018b), as denoted by $\delta\varphi$ (bipolarly valued). This calculation is a time-domain phase-unwrapping technique that can extract the small temporal phase changes ($<< \pi$) buried in phase-wrapped timeseries signals (Chen and Calhoun, 2016b). Using the phase image processing, we obtained a 4D phase data $\delta\varphi(\mathbf{r},t)$ for each subject in a format of 53 × 63 × 46 × 148.

Group mICA and GIG-pICA

The SPM-processed magnitude data were decomposed into functional networks using a group-level spatial ICA as illustrated (Chen et al., 2018a) and implemented in the GIFT toolbox (http://mialab.mrn.org/software/gift/). We decomposed the group magnitude data into a number of 100 brain subfunctions (a relatively high model order brain functional ICA), denoted by mICA. The Infomax spatial ICA algorithm was repeated 10 times in ICASSO (http://www.cis.hut.fi/projects/ica/icasso). The aggregate spatial maps were estimated as modes of spatiotemporal ICA($\mathbf{r}$, t). Subject-specific spatial maps $\{mICA^{j}(\mathbf{r})\}$ and timecourses $\{mICA^{j}(t))\}$ (j = 1, 2, …, 600) were estimated using a back-reconstruction method (Calhoun et al., 2001; Erhardt et al., 2011). Then, we selected a subset of 50 components (intrinsic connectivity networks) from the 100 plenary by excluding mICAs obviously affected by physiological, motion, and imaging artifacts as characterized by noncortical activation in spatial maps and high-frequency fluctuations in timecourses (Beckmann et al., 2005; Allen et al., 2011, 2014).

The timecourses mICA(t) underwent postprocessing that included (1) detrending, (2) removing outliers, and (3) low-pass filtering with a cutoff frequency at 0.15 Hz. Finally, the postprocessed mICA(t) were normalized to have a unit variance such that the covariance matrices correspond to correlation matrices (Allen et al., 2014).

Considering the mICA as the brain functional template for group information guidance, we conducted brain functional decomposition on the group phase data $\delta\varphi$ using the GIG-ICA method (Du and Fan, 2013), thus implementing GIG-pICA. We use the GIG-ICA method for phase data decomposition for two reasons: (1) facilitating mICA and pICA correspondence and comparison; and (2) in comparison with the direct ICA phase data decomposition (in our previous 100-subejct experiment Chen et al., 2018a) to show the convergence in phase-inferred features; for example, both pICA methods produce functional cliques in subcortical region.

The pICA timecourses were then postprocessed in ways similar to the mICA timecourse postprocessing. As a result, we obtained a set of 50 pICA components in counterpart to the 50 mICA components.

Group mFNC and Group pFNC Matrices

According to brain structure and functional organization, we classified the 50 selected mICA components roughly into seven brain domains based on spatial activation locations, as ordered by subcortical region (SC(4)), auditory (AUD(2)), sensorimotor (SM(8)), vision (VIS(10)), cognitive control (CC(14)), default mode network (DMN(9)), and cerebellum (CB(3)).

An aggregate ICA timecourse was back-reconstructed using data from 600 subjects to generate the same number of individual subject ICA timecourses. For each subject, we calculated a temporal correlation matrix (i.e., producing a subject-specific FNC matrix). In the results, we obtained 600 single-subject $\{mFNC^{j}\}$ and $\{pFNC^{j}\}$ matrices, j = 1, 2, …, 600, for magnitude and phase data, respectively. We converted the entries in $\{mFNC^{j}(n_1, n_2)\}$ and $\{pFNC^{j}(n_1, n_2)\}$ matrices (in size of 50×50×600) to Fisher z-scores (via a Matlab routine *atanh*(*x*)). By averaging the assemblies, we obtained group-level mFNC and pFNC matrices (in size of 50×50).

Null-Hypothesis Tests on Group mFNC and pFNC

An entry at (n_1, n_2) in mFNC(n_1, n_2) matrix represents a specific functional connection between subfunction $mICA_{n1}$ and subfunction $mICA_{n2}$, for $n_1, n_2 = 1, 2, \ldots, 50$. All the entry values collected from the 600 subject-specific connections constitute an assembly of 600 samples. Through a one-sample *t*-test (on the null hypothesis that an entry at (n_1, n_2) in the group-level mFNC matrix assumes a zero-mean distribution across the 600 samples $\{mFNC^{j}\}$), we obtained a *p*-value and an H-rest value. From all of the *t*-tests on the assembly $\{mFNC^{j}(n_1, n_2)$, j = 1, 2,…, 600, n_1, n_2 = 1, 2,…,50}, we obtained a *p*-value matrix P^{mFNC} (n_1, n_2) in a value range [0,1] and a H-test matrix $H^{mFNC}(n_1, n_2)$ (binary valued {1,0}), in size of 50 × 50. In the same procedure, we obtained a *p*-value matrix P^{pFNC} and an H-test matrix H^{pFNC} from the phase data assembly $\{pFNC^{j}\}$. Each entry of the *p*-value matrix was calculated from a statistic *t*-test over the 600 subject-specific FNCs with a confidence interval. The confidence intervals associated with the *p*-value matrix calculation may vary from entry to entry, which may assume different bounds delimited by positive and negative values.

The statistical hypothesis test may mistakenly produce some rejections of null hypothesis (zero mean), which we can control using the false discovery rate (FDR) through a FDR correction procedure (Benjamini and Hochberg, 1995; Benjamini and Yekutieli, 2001, 2005). This is a more powerful method for correcting FDR for multiple comparisons than the standard Bonferroni correction. It offers a strong control of the family-wise error rate (i.e., the probability that one or more null hypotheses are mistakenly rejected). The FDR correction leads to adjusted

p-values. We made FDR corrections on P^{mFNC} and P^{pFNC} for a specified desirable FDR (default $p = 0.05$).

Based on the binary $H^{mFNC}(n_1, n_2)$ (H = 1 for zero-mean rejection, H = 0 for zero-mean accepted at the 5% level), we excluded the functional connections that have zero-mean distributions (entries with H = 0). We focused on the connections in $mFNC(n_1,n_2)$ whose entries take on nonzero-mean distributions (determined by H = 1). We edited $pFNC(n_1, n_2)$ based on the binary $H^{pFNC}(n_1, n_2)$.

Numerical Characteristics of mFNC and pFNC

Based on the FDR-corrected p-value matrices, P^{mFNC} and P^{pFNC}, we assessed the significance and robustness of the functional connections through a p-value thresholding as given by

$$mFNC^{<}(n_1, n_2) = \begin{cases} mFNC(n_1, n_2), & P^{mFNC}(n_1, n_2) < p_{thresh} \\ 0, & \text{else} \end{cases} \quad (1a)$$

$$pFNC^{<}(n_1, n_2) = \begin{cases} pFNC(n_1, n_2), & P^{pFNC}(n_1, n_2) < p_{thresh} \\ 0, & \text{else} \end{cases} \quad (1b)$$

where p_{thresh} denotes a specified p-value ($p_{thresh} = 0.05$ for the default statistics significance) and the superscript "<" denotes a smaller-than p-value thresholding. As p_{thresh} decreases, the p-value thresholding produces a smaller number of survival entries ($\neq$ 0) in $mFNC^{<}$ and $pFNC^{<}$ matrices, representing the sparsity of higher significant functional connections; high significant connections are also strong connections.

For comparative pattern analysis of matrices $mFNC^{<}$ and $pFNC^{<}$, we expect the following characteristics:

(1) Statistically significant connections through p-value thresholding in **Eq. (1a,1b)** with a span of $p_{thresh} = \{0.05, 10^{-10}, 10^{-50}, 10^{-100}, 10^{-150}, 10^{-200}\}$.
(2) Positive/negative connections and connectivity balance in terms of *mean*(FNC) ± *std*(FNC) (Chen et al., 2018a). The connectivity balance can be also be characterized by the entry number difference between positive count (denoted by #(+)) and negative count (denoted by #(-1)) of signs in $mFNC^{<}$ or $pFNC^{<}$.
(3) Intra-domain (near, in a diagonal block) and inter-domain (far, in an off-diagonal submatrix) connections.
(4) Sparseness and nonuniformity of significant connections. The sparsity can be numerically characterized by the small fractions #(+)/1225 and #(-)/1225, where 1225 = 50(50-1)/2 is the number of total entries in a symmetrical 50 × 50 matrix excluding the self-connections on the diagonal line. The nonuniformity is visibly inspected in $mFNC^{<}$ and $pFNC^{<}$ as some submatrices disappear while some other submatrices persist during the p-value thresholding.

RESULTS

Group mFNC and pFNC

Considering ICA components as coherent brain functional networks, we calculated the functional network connectivity matrix by the temporal correlations (Pearson correlations) among the ICA timecourses. In **Figures 1A,B** are shown the magnitude and phase-depicted mFNC and pFNC matrices (in size 50 × 50), as calculated by the average over the subject-specific $\{mFNC^j(n_1, n_2)\}$and $\{pFNC^j(n_1, n_2)\}$ matrices, respectively. Note the 50 mICA components were arranged in seven domains: SC(4), AUD(2), SM(8), VIS(10), CC(14), DMN(9), and CB(3), as shown at the left vertical labels in **Figure 1A**. Correspondingly, the 50 pICA components were arranged with the same labels in **Figure 1B**.

The ICA-decomposed brain subfunctions are distributed over the brain geometrical space partitioned in seven domains. In general, the intra-domain connections are short connections, whereas the inter-domain connections are always long connections (except for rare inter-domain connections at the domain boundary). In an FNC matrix, an intra-domain short-range (near) connection constitutes the on-diagonal blocks and an inter-domain long-range (far) connection is located in the off-diagonal regions. In **Figure 1,** the magnitude data show strong positive near couplings in the on-diagonal blocks (**Figure 1A**), which differs from the phase-depicted loose connections (**Figure 1B**).

One Sample *t*-tests of Group-Level mFNC and pFNC

The group-level mFNC and pFNC matrices were calculated using an average from assemblies $\{mFNC^j\}$ and $\{pFNC^j\}$, respectively. The t-test on the mFNC matrix gives rise an H-test matrix H^{mFNC} and a p-value matrix P^{mFNC} (in size of 50 × 50), as shown in **Figures 2A,C**. The averaged confidence interval for P^{mFNC} is [0.02, 0.06]. Meanwhile, the pFNC t-test gives rise to H^{pFNC} and P^{pFNC}, as shown in **Figures 2B,D**. The averaged confidence interval for P^{pFNC} is [−0.02, 0.02]. Note that the p-value matrices were displayed in a magnification by log10. The binary H-test matrices were interpreted as H = 1 for rejecting null hypothesis (nonzero mean distributions) and H = 0 for true null hypothesis (zero mean distributions).

In **Figure 2C**, there are 1,119 entries (H = 1 for significant connection) and 106 entries (H = 0 for noisy or random connection) in the H-test matrix H^{mFNC} (50 × 50, with a total number of 1,225 entries in the upper triangle). In **Figure 2D**, there are 1,092 entries (H = 1) and 133 entries (H = 0) in the H-test matrix H^{pFNC}. The entries with H = 0 usually take on small values in mFNC and pFNC matrices, which we consider as noise and omit accordingly (by resetting them to zeros).

Thresholding mFNC and pFNC

We assessed the statistical significance of the functional connections in FNC matrices based on p-value thresholding in Equations (1a,b). In **Figure 3,** the thresholded matrices ($mFNC^{<}$) are drawn from p-value thresholding with $p_{thresh} = \{0.05, 10^{-10}, 10^{-50}, 10^{-100}, 10^{-150}, 10^{-200}\}$ using the upper

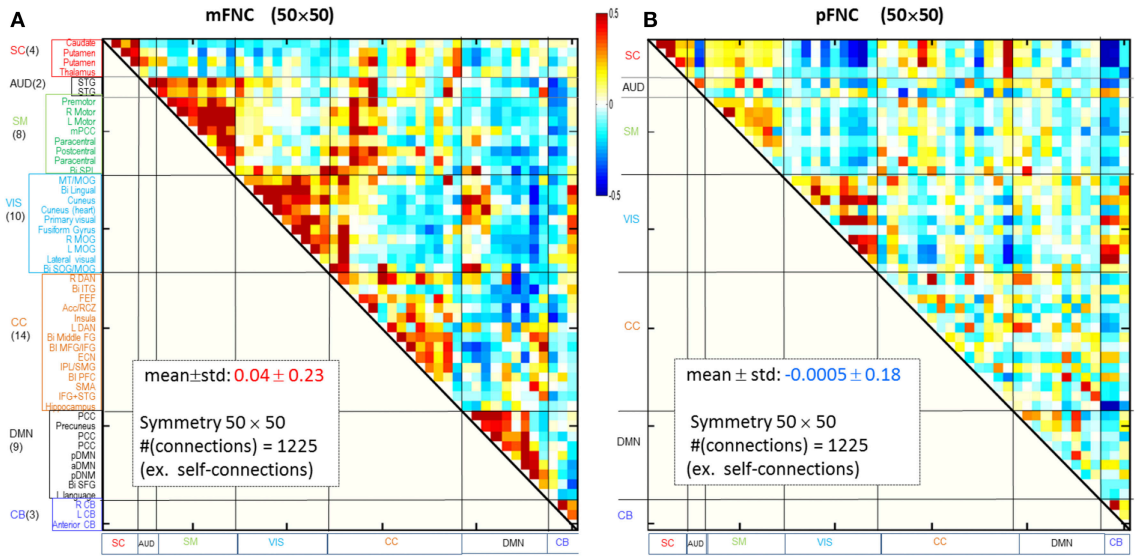

FIGURE 1 | Brain resting-state subfunction arrangement and functional network connectivity. **(A)** Magnitude data depiction: a set of 50 mICA components are classified into seven (7) brain domains {SC(4), AUD(2), MOT(8), VIS(10), CC(14), DMN(9), and CB(3)} and the mFNC matrix (*mean* ± *std*: 0.04 ± 0.23); **(B)** Phase data depiction: the pICA components are classified into 7 domains and the pFNC matrix (*mean* ± *std*: −0.0005 ± 0.18).

triangle portions of the symmetric matrices. For each mFNC$^<$ matrix (after FDR correction), we calculated the following characteristics: *mean* ± *std*, the number of positive couplings (#(+)), the sum of positive couplings ($\sum(+)$), the number of negative couplings (#(−)) and the sum of negative couplings ($\sum(-)$). The connectivity balance can be characterized as *mean*(mFNC$^<$). We can also quantify the functional connectivity imbalance by the quantity #(+) − #(−) in mFNC$^<$ or alternatively by $\sum(+) - \sum(-)$.

Correspondingly, in **Figure 4** we show the thresholded pFNC matrices using the same *p*-value thresholdings and numerical characterizations {#(+), #(−), $\sum(+)$, $\sum(-)$} as used for mFNC. In **Figure 4E,** the subcortical nuclei (SC) reveal significant negative couplings with VIS and CB, along with significant positive couplings with CC ($p < 10^{-150}$).

In **Figure 5,** we present the magnitude- and phase-depicted whole-brain connectivity behaviors for significant connections as determined by *p*-value thresholding. Specifically, we show the plots on the numerical characteristics (in terms of *mean*, counts of positive and negative connections (#(+), #(−)), and sums of positive and negative connections ($\sum(+)$, $\sum(-)$) of mFNC$^<$ and pFNC$^<$ matrices under *p*-value thresholding with $p_{\text{thresh}} = \{0.05, 10^{-10}, 10^{-50}, 10^{-100}, 10^{-150}, 10^{-200.}\}$. In **Figure 5A,** we show the whole-brain connection balance in terms of *mean*(mFNC$^<$) and *mean*(pFNC$^<$), in which a large *mean* value indicates a connection imbalance (deviation from balance 0). In **Figure 5B,** we use the average of whole-brain connection strength in terms of *mean*(|mFNC$^<$|) and *mean*(|pFNC$^<$|), in which a large value indicates a strong connection. It is noted that for small *mean*(mFNC) and *mean*(pFNC) values (close to 0), we may use the *std*(mFNC) and *std*(pFNC) values to quantify connection strengths instead what was used in (Chen et al., 2018a). In **Figures 5C,D,** we show the positive and negative numbers (#(+) vs. #(−)) in mFNC$^<$ and pFNC$^<$ matrices with respect to the *p*-value thresholding, where the difference #(+) − #(−) can be used to quantify the whole-brain connection imbalance. In **Figures 5E,F,** we also the show the positive and negative connections in terms of $\sum(+)$ and $\sum(-)$ with respect to p_{thresh}, where the difference $\sum(+) - \sum(-)$ can also be used to evaluate the connection imbalance. Overall, our experimental results in **Figure 5** show in comparison with fMRI magnitude data usage that the fMRI phase data reveal more connection balance (*mean*(pFNC$^<$) < *mean*(mFNC$^<$)) in **Figure 5A**, higher connection strength (*mean*(|pFNC$^<$|) > *mean*(|mFNC$^<$|)) in **Figure 5B**, and more balance in positive and negative distributions as determined by a smaller #(+) − #(−) in **Figures 5C,D**. and a smaller $\sum(+) - \sum(-)$ in **Figures 5E,F**.

Significant Couplings in mFNC

We used *p*-value thresholding on mFNC to examine robustness and significance of the magnitude-depicted brain functional connections for whole brain space in resting state (**Figure 3**). Here, in **Figure 6**, we see significant connections survived in a very strong *p*-value thresholding ($p < 10^{-200}$, **Figure 3F**). Specifically, we show in **Figure 6A** the functional connections across the seven domains (MOT(8), CC(14), AUD(2), DMN(9), SC(4), CB(3), VIS(10) in an arrangement around a circle) along with links of intra-domain (all are positive, in bright red), positive inter-domain (in dim red), and negative inter-domain (in blue). We observed the following aspects: (1) there are 60 positive connections and 1 negative connection; (2) the domains (MOT, VIS, DMN) each contain dense intra-domain connections; (3) there is no inter-domain connection between (MOT, VIS), (DMN,CC), (DMN, AUD), (DMN, SC), (DMN, CB), (SC, CB), (AUD, SC), and (AUD, CB); and (4) there is no intra-domain link in CB. In **Figure 6B**, we displayed the only

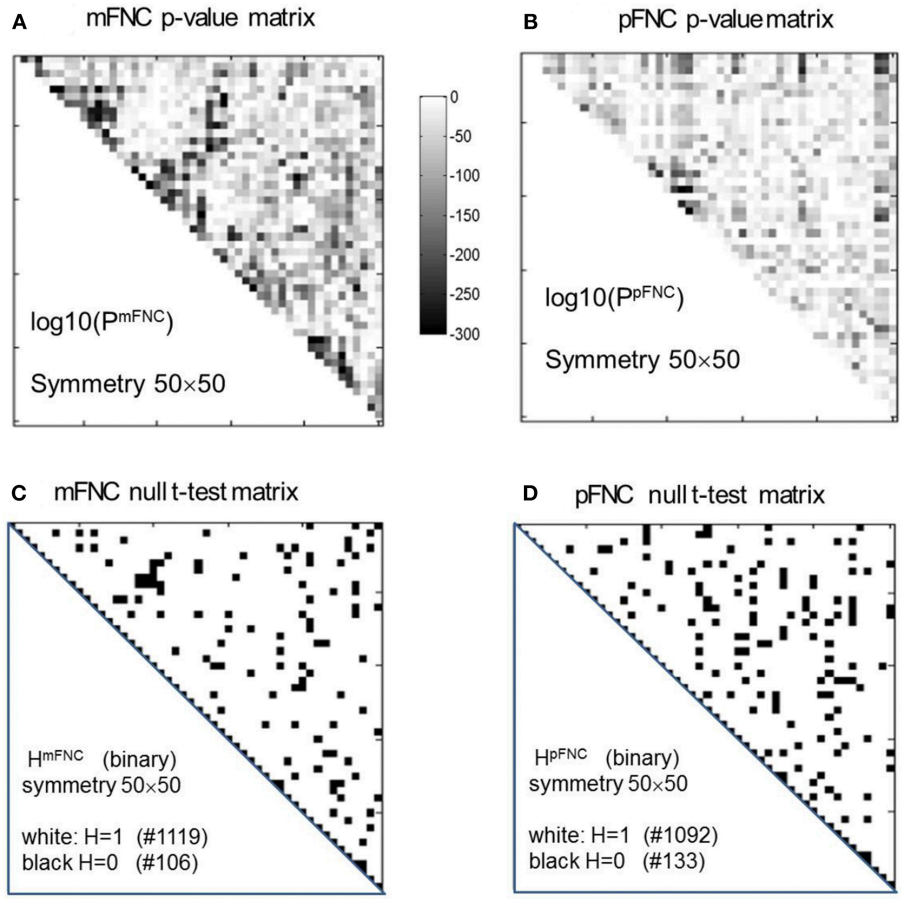

FIGURE 2 | One-sample *t*-tests for the assemblies {mFNC$_n$} and {pFNC$_n$} ($n = 1,2,\ldots,600$). **(A,B)** The *t*-test *p*-value matrices (displayed by a log10 magnification) using $P^{mFNC}(50,50)$ for {mFNC$_n$} and $P^{pFNC}(50,50)$ for {pFNC$_n$}; **(C,D)** The null-hypothesis test results (the entries with H = 1 were used for connection significance analysis).

negative connection survived in $p < 10^{-200}$ during brain resting state, which shows the inter-domain connection between (CC, CB) in a connection strength 0.41 ($p = 2 \times 10^{-209}$). Obviously, the magnitude depicted high significant connections in **Figure 6** ($p < 10^{-200}$) in resting brain state are nonuniformly distributed over the brain space: dense connections in VIS, MOT, and DMN, sparse connections in CC and SC, and no connections within CB.

Significant Couplings in pFNC

In comparison with the most significant connections in mFNC in **Figure 6**, we scrutinize the phase-depicted significant connections in mFNC under the same *p*-value thresholding (*p*-value $< 10^{-200}$) in **Figure 7**. We observed the following aspects: (1) there are a few connections survived in *p*-value $< 10^{-200}$ (10 positive connections and 2 negative connections); (2) there is no intra-domain connections in MOT,CC, AUD, DMN; (3) there are 2 negative far inter-domain connections between (CB, SC); (4) there is 1 positive far inter-domain connection between (CC, SC); (5) there are no inter-domain connections among {MOT, CC, AUD, DMN, VIS, CB}; and (6) only SC has inter-domain connections (1 with CC, 2 with CB). In **Figure 7B**, we displayed the connections among {SC1(pICA1),SC3(pICA3),CB1(pICA48)}, which assume 2 negative far inter-domain connections and 1 positive near intra-domain connection. The subcortical subfunction SC1(pFNC1) is strongly coupled with SC3(pFNC3) with pFNC(1,3) = 0.80 and a high significance (*p*-value = 8×10^{-250}), which constitutes a functional clique in the subcortical nuclei. It seems plausible for the phase data analysis to show that the subcortical nuclei (consisting of basal ganglia and thalamus) form a functional clique that acts as a hub in couplings with other cortical subfunctions in the resting state. This observation is consistent with our previous report on the functional subcortical clique observed from a 100-subject rest fMRI experiment (Chen et al., 2018a).

DISCUSSION

Inferring BOLD-Only Internal Magnetic Field Perturbation From Phase MRI

The rationale of phase fMRI for brain function study lies in the fact that we can infer the brain internal magnetic

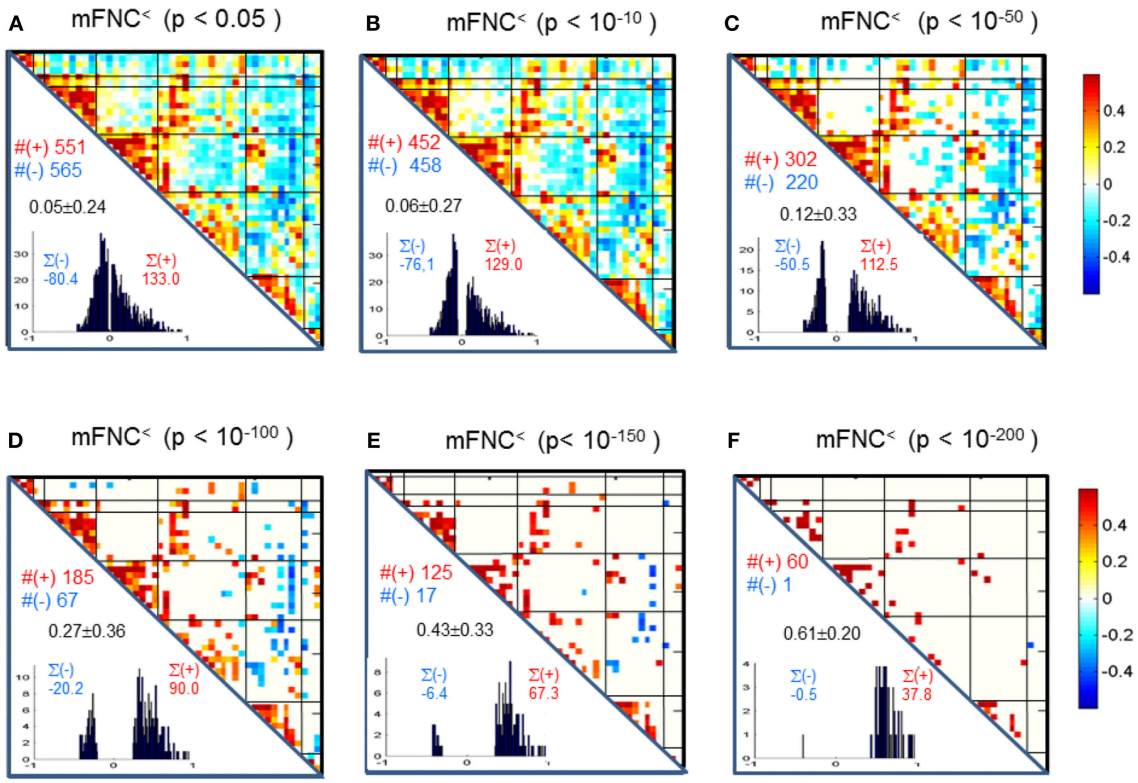

FIGURE 3 | (A–F) Significant connections in group mFNC matrix under *p*-value thresholding with $p_{thresh} = \{0.05, 10^{-10}, 10^{-50}, 10^{-100}, 10^{-150}, 10^{-200}\}$. The numbers of positive and negative connections (denoted by #(+) and #(–) respectively), and the sums of positive and negative connections (denoted by $\sum(+)$ and $\sum(-)$ respectively) were calculated from the survival entries in the p_{thresh}-thresholded matrices ($mFNC^{<}$).

field distribution from an fMRI phase image under linear approximation (a small phase angle condition). For reference convenience, we provide the approximation theory of phase-to-field inverse mapping in the **Appendix**. An fMRI phase image represents a snapshot capture of the brain magnetic state (in terms of magnetic field distribution) under linear phase fMRI approximation. A voxel phase signal represents an intravoxel-average magnetic field value.

As seen in Equation (A3), phase fMRI procures a phase image φ from the MRI quadrature detection by a trigonometric operation, $arctan(\varphi)$, which is nonlinear in a general setting. Mathematically, we have a linear approximation, $arctan(\varphi) = \varphi$ for $|\varphi| << 1$ radian (a small phase angle condition). Numerical simulation (Chen and Calhoun, 2015b) has shown that the phase fMRI nonlinearity ($arctan(\varphi)$) is weak for large phase angles ($|\varphi| \sim \pi$ rad). In reality, an fMRI phase image always has phase wrapping due to the dominant phase background ($|\varphi_0| > \pi$ radian). In practice, an unwrapped phase image is always assumed to represent the internal magnetic fieldmap with the associated nonlinearity of large phase angles ($|\varphi^{unwrap}| > \pi$).

For fMRI data analysis, we extract the dynamic phase perturbations ($\delta\varphi$) using a complex-division approach in Equation (A8), which are considered the BOLD-only phase response signals during a brain activity. Then we infer the BOLD-only magnetic field perturbation (δb) by a linear scaling mapping in Equation (A9). The small phase perturbation (typically $|\delta\varphi| < 0.2$ radian) ensures a good linear approximation: $arctan(\delta\varphi) = \delta\varphi$ for $|\delta\varphi| << 1$. Note that we cannot infer the brain magnetic fieldmap from magnitude fMRI due to irreversible nonlinearity.

Bipolar-Valued Brain Magnetic Field Distribution

A magnetic field may assume positive and negative values. For brain fMRI study, the brain internal magnetic field is from a brain tissue magnetization in a main field B_0. Specifically, this brain tissue magnetic susceptibility property (denoted by χ) undergoes a dipole-convolved magnetization in B_0 to establish an inhomogeneous magnetic fieldmap. Due to the spatial derivative property of the dipole kernel, even a nonnegative susceptibility distribution ($\chi \geq 0$) could induce a bipolar-valued fieldmap (Chen et al., 2018b). The negative signs in a χ-induced fieldmap are maintained during the forward phase fMRI, which result in the fieldmap reconstruction by an inverse mapping from phase to fieldmap. In comparison, the negative signs are completely suppressed (inverted) in the fMRI magnitude signals due to its nonnegativeness (Chen and Calhoun, 2011). In this sense, the phase fMRI provides a direct, accurate representation of the brain magnetic state for bipolar-valued magnetic fieldmaps. Nevertheless, the magnetic fieldmap still differs from the underlying brain tissue magnetic

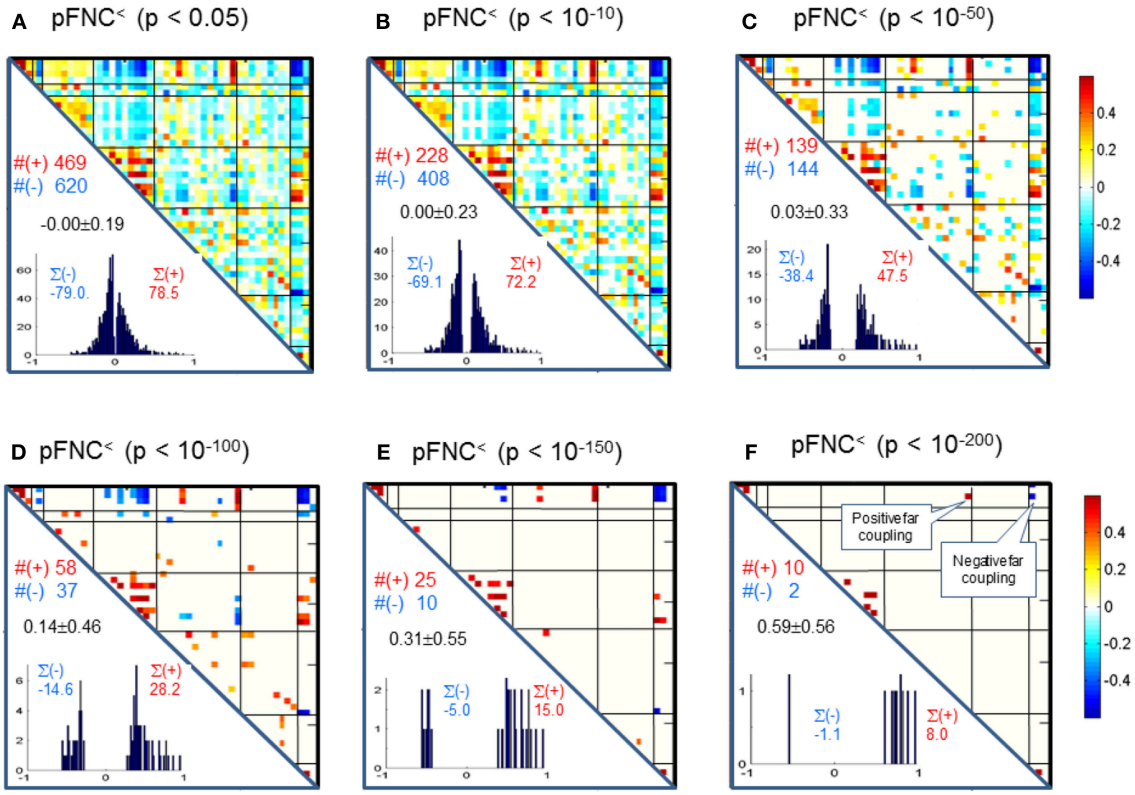

FIGURE 4 | (A–F) Significant connections in group pFNC matrix under *p*-value thresholding with p_{thresh} ={0.05, 10^{-10}, 10^{-50}, 10^{-100}, 10^{-150}, 10^{-200}}. The numbers of positive and negative connections (denoted by #(+) and #(–) respectively), and sums of positive and negative connections (denoted by $\sum(+)$ and $\sum(-)$ respectively) were calculated from the survival entries in the p_{thresh}-thresholded matrices (pFNC$^<$).

susceptibility map using a 3D dipole convolution (Chen and Calhoun, 2013), which in principle can be completely resolved through functional quantitative susceptibility mapping (fQSM) or functional susceptibility mapping (Balla et al., 2014; Chen and Calhoun, 2015a, 2016a,c). More accurate brain functional connectivity analysis using original magnetic susceptibility source data is an important research in future.

Positive and Negative Functional Connections

Research has shown positive and negative functional connections exist among ICA-decomposed brain networks (subfunctions) (Xu, 2015; Xu et al., 2015), either in the resting state or in task performance. Most reports on balanced connectivity (Marino et al., 2005; Fox et al., 2009; Murphy et al., 2009; Litwin-Kumar and Doiron, 2012; Liu et al., 2015) were based on fMRI magnitude data analysis in which the negative magnitude connections (anticorrelations) were reported as a result of a "de-mean" preprocessing that is prone to artifactual negative connections. Using bipolar-valued fMRI phase data, we found more negative connections that cancel the positive connection(s) to make a balanced network for the whole-brain functional connectivity without a de-mean preprocessing (Chen et al., 2018a).

Overall, the phase-depicted balanced brain functional connectivity draws from the bipolarity of phase signals (**Figure 1B**), while magnitude-depicted positively-biased connectivity stems from the nonnegative magnitude signals (**Figure 1A**). These observations are consistent with our previous report with a 100-subject experiment data analysis (Chen et al., 2018a). Since the linear inverse mapping from fMRI phase to magnetic fieldmap maintains the negative signs, the δb-depicted negative connections come from negative phase signals and anti-correlations.

Near and Far Functional Connections

The magnitude-based brain functional connectivity study (Rosenbaum et al., 2017) has shown that nearby neurons are positively correlated, pairs at intermediate distances are negatively correlated, and distant pairs are weakly correlated. We found similar connection patterns in mFNC (**Figure 1A**): the on-diagonal positive blocks indicate strong near (intra-domain) connections, while off-diagonal blocks have negative and small values indicating weak far (inter-domain) connections.

In comparison, the phase-based brain function connectivity in pFNC (in **Figure 1B**) reveals some different patterns. **Figure 1B** reveals negative near connections within domains VIS, CC, and DMN in small and negative entries in the on-diagonal

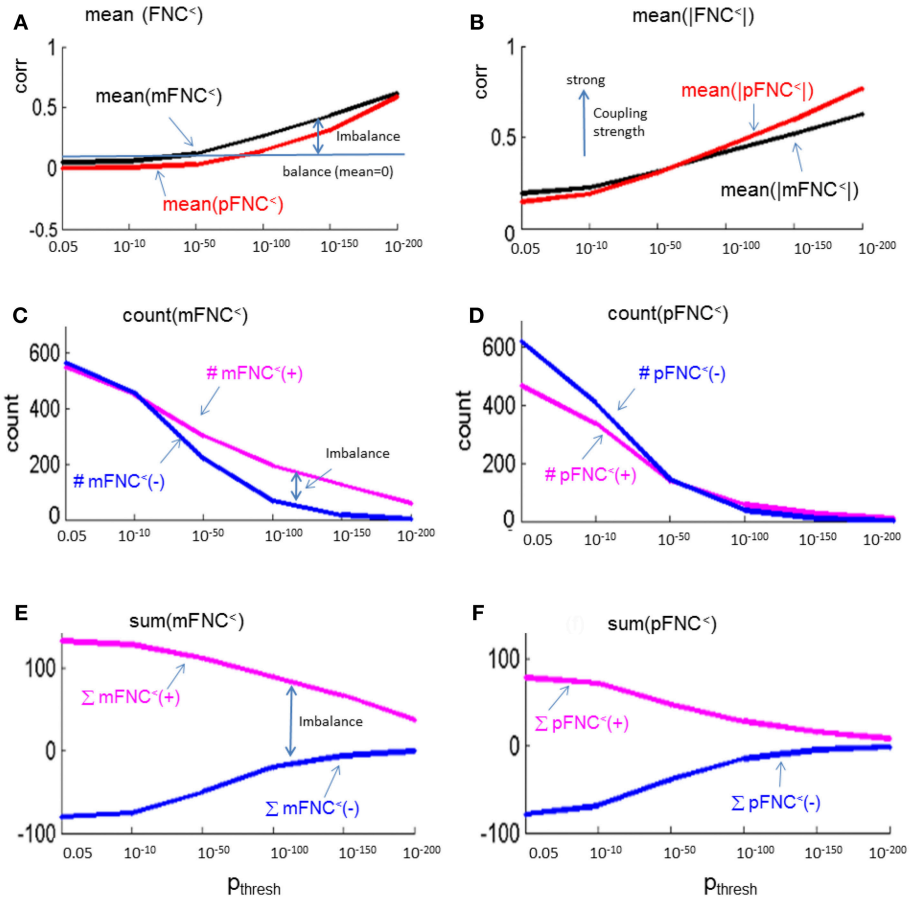

FIGURE 5 | Numerical characteristics of mFNC and pFNC under *p*-value thresholding. **(A)** *mean*(mFNC$^<$) and *mean*(pFNC$^<$) whole-brain network balance; **(B)** *mean*(|mFNC$^<$|) and *mean*(|pFNC$^<$|) whole-brain network coupling strength; **(C)** Counts of positive and negative couplings in mFNC$^<$; **(D)** Counts of positive and negative couplings in pFNC$^<$; **(E)** Sums of positive and negative couplings in pFNC$^<$; and **(F)** Sums of positive and negative couplings in pFNC$^<$.

blocks; also seen are off-diagonal negative and positive blocks indicating strong far (inter-domain) connections. In particular, the subcortical subfunctions (SC(4)) show strong negative connections with both the visual subfunctions (VIS(10)) and the cerebellum subfunctions (CB(3)), while the VIS(10) are generally positively connected with CB(3).

Sparseness and Nonuniformity of Brain FNC

Given a set of ICA-decomposed brain subfunctions, the whole-brain functional connectivity is numerically characterized in an FNC matrix (e.g., mFNC from magnitude data and pFNC from phase data). An entry value in the FNC matrix represents the correlation between two subfunctions in a range $[-1, 1]$: a large value ($\sim$1) indicates a synchrony and a negative sign an anti-correlation. The entries with small values ($\sim$0) are largely due to noise (randomness and instability). For brain function connectivity depiction, we are concerned with the strong connections (negative or positive) over the brain space (near or far connections). By omitting the entries in small values (i.e., via thresholding like Equation 1), we have a small number of survival entries in the FNC matrix showing the sparseness (counting entries in a thresholded FNC matrix) and nonuniformity of their distribution over the brain space.

In our experiment, we had a large number of subject data ($N = 600$) for statistical brain function study. Based on the FNC assemblies $\{\text{mFNC}^j\}$ and $\{\text{pFNC}^j\}$, we conducted *t*-tests on the group-level functional connections to obtain *p*-value matrices, P^{mFNC} and P^{pFNC}, and H-test matrices, H^{mFNC} and H^{pFNC}, respectively. We omitted the entries in mFNC on the condition of $\text{H}^{\text{mFNC}} = 0$, whereby we suppress the small insignificant connection values. By using *p*-value thresholding in Equation (1a), we see significant connections as determined by the *p*-value thresholds ($\text{p}_{\text{thresh}} = \{0.05, 10^{-10}, 10^{-50}, 10^{-100}, 10^{-150}, 10^{-200.}\}$)shown in mFNC$^<$ (see **Figure 3**).There are sparse (in terms of positive and negative counts) and nonuniform connections (in dense and sporadic links) in the brain space as p_{thresh} increases (as seen in **Figure 6),** for the most significant connections ($\text{p}_{\text{thresh}} = 10^{-200}$). Similar sparsity and nonuniformity of phase-depicted connectivity occurs in pFNC$^<$ (**Figures 4**, **7**). Under a specific *p*-value thresholding, the pFNC$^<$ is sparser than mFNC$^<$ (as

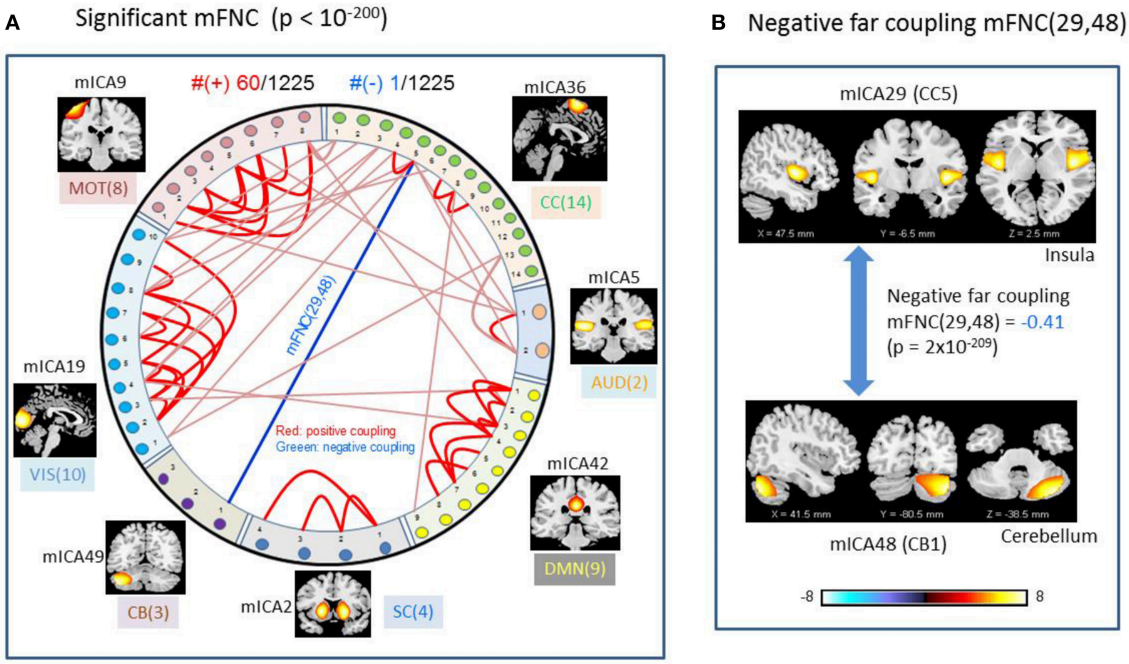

FIGURE 6 | Illustrations of the most significant couplings in mFNC$^{<}$ ($p < 10^{-200}$). **(A)** There are 36 intra-domain positive couplings (near, in bright red color) and 18 inter-domain positive couplings (far, in soft red color), and 1 inter-domain negative coupling (far, in blue color). **(B)** Features of the negative interdomain coupling mFNC(29, 48).

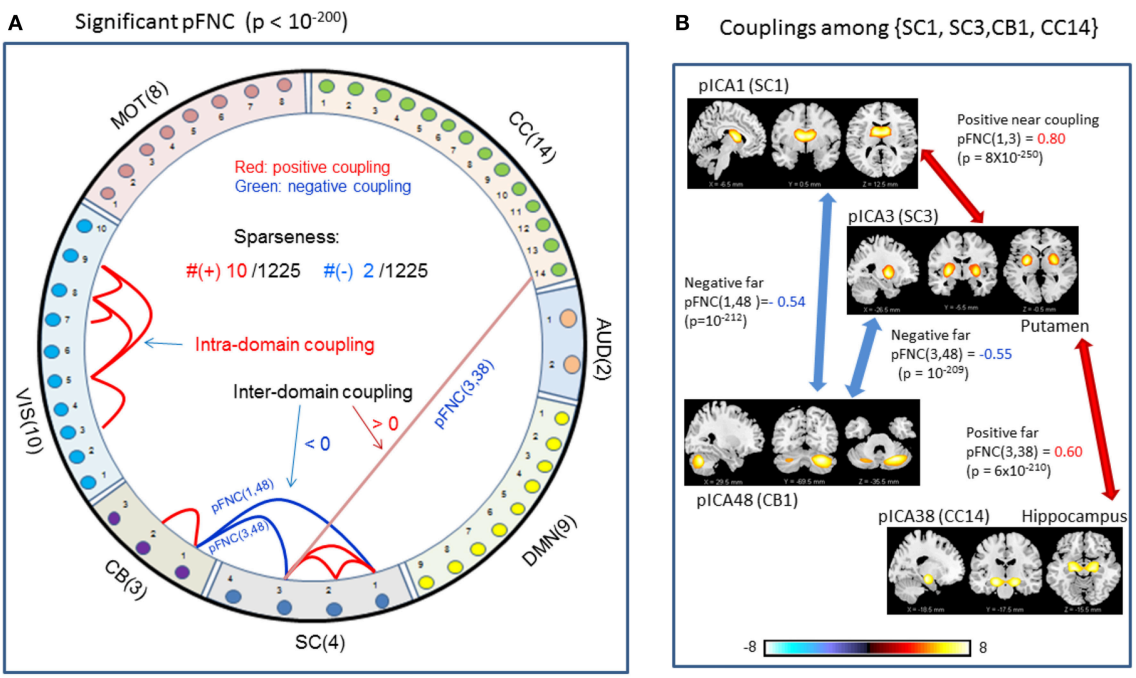

FIGURE 7 | Illustrations of the most significant couplings in pFNC$^{<}$ ($p < 10^{-200}$). **(A)** There are nine (9) intra-domain positive couplings (near, in bright red color) and one (1) inter-domain positive coupling (far, in soft red color), and two (2) inter-domain negative couplings (far, in blue color). **(B)** Features of the two negative interdomain couplings pFNC(1,48) and pFNC(3, 48).

indicated in #(pFNC$^<$ $\neq$ 0) < #(mFNC$^<$ $\neq$ 0); for p_{thresh} < 10^{-50}, pFNC$^<$ is more balance than mFNC$^<$ in terms of |#(pFNC$^<$(+) – #(pFNC$^<$(–)| < |#(mFNC$^<$(+) – #(mFNC$^<$(–)| or |$\sum$(pFNC$^<$(+) – $\sum$(pFNC$^<$(–)| < |$\sum$(mFNC$^<$(+) – $\sum$(mFNC$^<$(–)| (see **Figure 3** through **Figure 5**).

We conclude the subcortical nuclei make a functional clique (with strong intra-domain couplings) that is negatively coupled with VIS and CB subfunctions (**Figure 4**) while positively joined with the strongest couplings.

Significant connections are survived from *p*-value thresholding in Equations (1a,b) with a significance level specified by p_{thresh}. For connection balance analysis in this particular 600-subject experiment, we suggest the use of a p_{thresh} < 10^{-10} (in **Figures 3**, **4**). For connection sparseness analysis, we may use a very small p_{thresh} to examine a few number of high significant connections, as demonstrated in **Figures 6**, **7** for the extreme scenarios with $p_{thresh} = 10^{-200}$. Comparing mFNC$^<$ (**Figure 3**) and pFNC$^<$ (**Figure 4**), the pFNC contains a smaller number of significant connections than mFNC and that the connections in pFNC are more balanced than those in the mFNC. In pFNC analysis, the brain resting state contains two strong negative connections between subcortical nuclei (SC) and cerebellum (CB) and the sparse intra-domain connections. Thus, basal ganglia in the SC domain have the strongest and most significant function connections with CB during brain resting state. We found one strong negative connection between CB and CC and other massive intra-domain connections (specifically #(+) = 60) from the mFNC analysis.

In neuroscience, it is well-established (Alexander et al., 1986; Amos, 2000; Stocco et al., 2010) that the central subcortex (primarily basal ganglia and thalamus) plays a "relay station" for brain functional information traffic, acting as a cohesive functional unit with strong connections to the cerebral cortex and other brain areas. Experimental data analysis (Bell and Shine, 2016) suggests the basal ganglia and thalamus are functional hubs with a core circuit supporting large-scale integration. Our 600-subject experimental results (reported herein) show strong subcortical functional cliques in the whole-brain resting state, which agree with the centralized subcortical hubs concept (Bell and Shine, 2016; Sherman, 2016; Hwang et al., 2017).

CONCLUSION

Our rationale of using fMRI phase data for brain function study is based on the fact that fMRI phase imaging (unwrapped) represents the brain internal magnetic field distribution (the magnetic source for fMRI complex signal formation, the brain magnetic state at a stage prior to MRI scan and detection). We can extract the BOLD-only phase perturbation in small phase change values through calculations of the timeseries of phase images, thus ensuring a linear scale mapping to BOLD-only magnetic field perturbation (magnetic source of fMRI). Using an fMRI dataset from the cohort of 600, we compared the phase-depicted brain functional connectivity (pFNC) and the magnitude-depicted connectivity (mFNC) in terms of measures of positive and negative connections; near and far connections; sparsity and nonuniformity; and statistical significance (based one *p*-value thresholding).

Our experiments (600-subject resting-state phase fMRI) show the phase fMRI data has a smaller number of significant whole-brain connections (sparse connection) in the brain resting state than the magnitude data depiction. Perhaps, the reduced number of significant connections in phase fMRI is largely due to the positive and negative cancellation of linear phase signals. We found the basal ganglia networks (in subcortical nuclei) have strong negative connections with other brain regions in a few of the significant connections in the resting state. These findings are different from the magnitude-depicted functional connectivity in prevailing positive connections. Although we cannot prove or disprove due to a lack of *in vivo* brain function connection truth, we cannot completely confirm our findings from phase fMRI data analysis, but can justify the phase usefulness within the context of linear phase fMRI.

DATA AVAILABILITY

The datasets generated for this study are available on request to the corresponding author.

AUTHOR CONTRIBUTIONS

All authors listed have made a substantial, direct and intellectual contribution to the work, and approved it for publication.

ACKNOWLEDGMENTS

The authors would like to acknowledge the funding supports from NIH grants (2R01EB005846, P20GM103472, R01EB020407).

SUPPLEMENTARY MATERIAL

The Supplementary Material for this article can be found online at: https://www.frontiersin.org/articles/10.3389/fnins.2019.00204/full#supplementary-material

REFERENCES

Alexander, G. E., DeLong, M. R., and Strick, P. L. (1986). Parallel organization of functionally segregated circuits linking basal ganglia and cortex. *Annu. Rev. Neurosci.* 9, 357–381. doi: 10.1146/annurev.ne.09.030186.002041

Allen, E. A., Damaraju, E., Plis, S. M., Erhardt, E. B., Eichele, T., and Calhoun, V. D. (2014). Tracking whole-brain connectivity dynamics in the resting state. *Cereb. Cortex* 24, 663–676. doi: 10.1093/cercor/bhs352

Allen, E. A., Erhardt, E. B., Damaraju, E., Gruner, W., Segall, J. M., Silva, R. F., et al. (2011). A baseline for the multivariate comparison

of resting-state networks. *Front. Syst. Neurosci.* 5:2. doi: 10.3389/fnsys.2011.00002

Amos, A. (2000). A computational model of information processing in the frontal cortex and basal ganglia. *J. Cogn. Neurosci.* 12, 505–519. doi: 10.1162/089892900562174

Arbabshirani, M. R., and Calhoun, V. D. (2011). Functional network connectivity during rest and task: comparison of healthy controls and schizophrenic patients. *Conf. Proc. IEEE Eng. Med. Biol. Soc.* 2011, 4418–4421. doi: 10.1109/IEMBS.2011.6091096

Arja, S. K., Feng, Z., Chen, Z., Caprihan, A., Kiehl, K. A., Adali, T., et al. (2009). Changes in fMRI magnitude data and phase data observed in block-design and event-related tasks. *Neuroimage* 59, 3748–3761. doi: 10.1016/j.neuroimage.2009.10.087

Balla, D. Z., Sanchez-Panchuelo, R. M., Wharton, S. J., Hagberg, G. E., Scheffler, K., Francis, S. T., et al. (2014). Functional quantitative susceptibility mapping (fQSM). *Neuroimage* 100, 112–124. doi: 10.1016/j.neuroimage.2014.06.011

Beckmann, C. F., DeLuca, M., Devlin, J. T., and Smith, S. M. (2005). Investigations into resting-state connectivity using independent component analysis. *Philos. Trans. R. Soc. Lond. B Biol. Sci.* 360, 1001–1013. doi: 10.1098/rstb.2005.1634

Bell, P. T., and Shine, J. M. (2016). Subcortical contributions to large-scale network communication. *Neurosci. Biobehav. Rev.* 71, 313–322. doi: 10.1016/j.neubiorev.2016.08.036

Benjamini, Y., and Hochberg, Y. (1995). Controlling the false discovery rate: a practical and powerful approach to multiple testing. *J. R. Stat. Soc. Series B Stat. Methodol.* 57, 269–300. doi: 10.1111/j.2517-6161.1995.tb02031.x

Benjamini, Y., and Yekutieli, D. (2001). The control of the false discovery rate in multiple testing under dependency. *Ann. Stat.* 29, 1165–1188. doi: 10.2307/2674075

Benjamini, Y., and Yekutieli, D. (2005). False discovery rate?adjusted multiple confidence intervals for selected parameters. *J. Am. Stat. Assoc.* 100, 71–81. doi: 10.1198/016214504000001907

Bianciardi, M., van Gelderen, P., and Duyn, J. H. (2014). Investigation of BOLD fMRI resonance frequency shifts and quantitative susceptibility changes at 7 T. *Hum. Brain Mapp.* 35, 2191–2205. doi: 10.1002/hbm.22320

Calhoun, V. D., and Adali, T. (2012). Multisubject independent component analysis of fMRI: a decade of intrinsic networks, default mode, and neurodiagnostic discovery. *IEEE Rev. Biomed. Eng.* 5, 60–73. doi: 10.1109/RBME.2012.2211076

Calhoun, V. D., Adali, T., Pearlson, G. D., and Pekar, J. J. (2001). A method for making group inferences from functional MRI data using independent component analysis. *Hum. Brain Mapp.* 14, 140–151. doi: 10.1002/hbm.1048

Chavhan, G. B., Babyn, P. S., Thomas, B., Shroff, M. M., and Haacke, E. M. (2009). Principles, techniques, and applications of T2*-based MR imaging and its special applications. *Radiographics* 29, 1433–1449. doi: 10.1148/rg.295095034

Chen, Z., and Calhoun, V. (2012a). Computed inverse resonance imaging for magnetic susceptibility map reconstruction. *J. Comput. Assist. Tomogr.* 36, 265–274. doi: 10.1097/RCT.0b013e3182455cab

Chen, Z., and Calhoun, V. (2012b). Volumetric BOLD fMRI simulation: from neurovascular coupling to multivoxel imaging. *BMC Med. Imaging* 12:8. doi: 10.1186/1471-2342-12-8

Chen, Z., and Calhoun, V. (2013). Understanding the morphological mismatch between magnetic susceptibility source and T2* image. *Magn. Reson. Insights* 6, 65–81. doi: 10.4137/MRI.S11920

Chen, Z., and Calhoun, V. (2015a). Intrinsic functional mapping in reconstructed 4D magnetic susceptibility data space. *J. Neurosci. Methods* 241, 85–93. doi: 10.1016/j.jneumeth.2014.12.014

Chen, Z., and Calhoun, V. (2015b). Nonlinear magnitude and linear phase behaviors of T2* imaging: theoretical approximation and Monte Carlo simulation. *Magn. Reson. Imaging* 33, 390–400. doi: 10.1016/j.mri.2015.01.016

Chen, Z., and Calhoun, V. (2016a). *Inverse MRI for Tomographic Magentic Susceptibility Reconstrucion*. Computed Tomogaphy (www.smgebooks.com). Dover, DE: SM Group Open Access eBooks.

Chen, Z., and Calhoun, V. (2016b). T2* phase imaging and processing for magnetic susceptibility mapping. *Biomed. Phys. Eng. Express*.

Chen, Z., and Calhoun, V. D. (2011). Two pitfalls of BOLD fMRI magnitude-based neuroimage analysis: non-negativity and edge effect. *J. Neurosci. Methods* 199, 363–369. doi: 10.1016/j.jneumeth.2011.05.018

Chen, Z., and Calhoun, V. D. (2016c). Task-evoked brain functional magnetic susceptibility mapping by independent component analysis (chiICA). *J. Neurosci. Methods* 261, 161–171. doi: 10.1016/j.jneumeth.2016.01.007

Chen, Z., Caprihan, A., Damaraju, E., Rachakonda, S., and Calhoun, V. (2018a). Functional brain connectivity in resting-state fMRI using phase and magnitude data. *J. Neurosci. Methods* 293, 299–309. doi: 10.1016/j.jneumeth.2017.10.016

Chen, Z., Robinson, J., and Calhoun, V. (2018b). Brain functional BOLD perturbation modelling for forward fMRI and inverse mapping. *PLoS ONE* 13:e0191266. doi: 10.1371/journal.pone.0191266

Du, Y., and Fan, Y. (2013). Group information guided ICA for fMRI data analysis. *Neuroimage* 69, 157–197. doi: 10.1016/j.neuroimage.2012.11.008

Erhardt, E. B., Rachakonda, S., Bedrick, E. J., Allen, E. A., Adali, T., and Calhoun, V. D. (2011). Comparison of multi-subject ICA methods for analysis of fMRI data. *Hum. Brain Mapp.* 32, 2075–2095. doi: 10.1002/hbm.21170

Feng, Z., Caprihan, A., Blagoev, K. B., and Calhoun, V. D. (2009). Biophysical modeling of phase changes in BOLD fMRI. *Neuroimage* 47, 540–548. doi: 10.1016/j.neuroimage.2009.04.076

Fox, M. D., Zhang, D., Snyder, A. Z., and Raichle, M. E. (2009). The global signal and observed anticorrelated resting state brain networks. *J. Neurophysiol.* 101, 3270–3283. doi: 10.1152/jn.90777.2008

Guo, Y., and Pagnoni, G. (2008). A unified framework for group independent component analysis for multi-subject fMRI data. *Neuroimage* 42, 1078–1093. doi: 10.1016/j.neuroimage.2008.05.008

Haacke, E. M., Brown, R., Thompson, M., and Venkatesan, R. (1999). *Magnetic Resonance Imaging Physical Principles and Sequence Design*. New York, NY: John Wiley and Sons, Inc.

Haacke, E. M., Liu, S., Buch, S., Zheng, W., Wu, D., and Ye, Y. (2015). Quantitative susceptibility mapping: current status and future directions. *Magn. Reson. Imaging* 33, 1–25. doi: 10.1016/j.mri.2014.09.004

Hwang, K., Bertolero, M. A., Liu, W. B., and D'Esposito, M. (2017). The Human thalamus is an integrative hub for functional brain networks. *J. Neurosci.* 37, 5594–5607. doi: 10.1523/JNEUROSCI.0067-17.2017

Jafri, M. J., Pearlson, G. D., Stevens, M., and Calhoun, V. D. (2008). A method for functional network connectivity among spatially independent resting-state components in schizophrenia. *Neuroimage* 39, 1666–1681. doi: 10.1016/j.neuroimage.2007.11.001

Li, W., Wu, B., and Liu, C. (2011). Quantitative susceptibility mapping of human brain reflects spatial variation in tissue composition. *Neuroimage* 55, 1645–1656. doi: 10.1016/j.neuroimage.2010.11.088

Litwin-Kumar, A., and Doiron, B. (2012). Slow dynamics and high variability in balanced cortical networks with clustered connections. *Nat. Neurosci.* 15, 1498–1505. doi: 10.1038/nn.3220

Liu, Y., Huang, L., Li, M., Zhou, Z., and Hu, D. (2015). Anticorrelated networks in resting-state fMRI-BOLD data. *Biomed. Mater. Eng.* 26 (Suppl. 1), S1201–S1211. doi: 10.3233/BME-151417

Marino, J., Schummers, J., Lyon, D. C., Schwabe, L., Beck, O., Wiesing, P., et al. (2005). Invariant computations in local cortical networks with balanced excitation and inhibition. *Nat. Neurosci.* 8, 194–201. doi: 10.1038/nn1391

McKeown, M. J., Hansen, L. K., and Sejnowsk, T. J. (2003). Independent component analysis of functional MRI: what is signal and what is noise? *Curr. Opin. Neurobiol.* 13, 620–629. doi: 10.1016/j.conb.2003.09.012

Murphy, K., Birn, R. M., Handwerker, D. A., Jones, T. B., and Bandettini, P. A. (2009). The impact of global signal regression on resting state correlations: are anti-correlated networks introduced? *Neuroimage* 44, 893–905. doi: 10.1016/j.neuroimage.2008.09.036

Ozbay, P. S., Warnock, G., Rossi, C., Kuhn, F., Akin, B., Pruessmann, K. P., et al. (2016). Probing neuronal activation by functional quantitative susceptibility mapping under a visual paradigm: a group level comparison with BOLD fMRI and PET. *Neuroimage* 137, 52–60. doi: 10.1016/j.neuroimage.2016.05.013

Rosenbaum, R., Smith, M. A., Kohn, A., Rubin, J. E., and Doiron, B. (2017). The spatial structure of correlated neuronal variability. *Nat. Neurosci.* 20, 107–114. doi: 10.1038/nn.4433

Rowe, D. B. (2005). Modeling both the magnitude and phase of complex-valued fMRI data. *Neuroimage* 25, 1310–1324. doi: 10.1016/j.neuroimage.2005.01.034

Rowe, D. B. (2009). Magnitude and phase signal detection in complex-valued fMRI data. *Magn. Reson. Med.* 62, 1356–1360. doi: 10.1002/mrm.21882

Sherman, S. M. (2016). Thalamus plays a central role in ongoing cortical functioning. *Nat. Neurosci*. 19, 533–541. doi: 10.1038/nn.4269

Shmueli, K., de Zwart, J. A., van Gelderen, P., Li, T. Q., Dodd, S. J., and Duyn, J. H. (2009). Magnetic susceptibility mapping of brain tissue in vivo using MRI phase data. *Magn. Reson. Med.* 62, 1510–1522. doi: 10.1002/mrm.22135

Stocco, A., Lebiere, C., and Anderson, J. R. (2010). Conditional routing of information to the cortex: a model of the basal ganglia's role in cognitive coordination. *Psychol. Rev*. 117, 541–574. doi: 10.1037/a0019077

Wang, Y., and Liu, T. (2015). Quantitative susceptibility mapping (QSM): decoding MRI data for a tissue magnetic biomarker. *Magn. Reson. Med*. 73, 82–101. doi: 10.1002/mrm.25358

Xu, J. (2015). Implications of cortical balanced excitation and inhibition, functional heterogeneity, and sparseness of neuronal activity in fMRI. *Neurosci. Biobehav. Rev*. 57, 264–270. doi: 10.1016/j.neubiorev.2015.08.018

Xu, J., Calhoun, V. D., Worhunsky, P. D., Xiang, H., Li, J., Wall, J. T., et al. (2015). Functional network overlap as revealed by fMRI using sICA and its potential relationships with functional heterogeneity, balanced excitation and inhibition, and sparseness of neuron activity. *PLoS ONE* 10:e0117029. doi: 10.1371/journal.pone.0117029

Conflict of Interest Statement: The authors declare that the research was conducted in the absence of any commercial or financial relationships that could be construed as a potential conflict of interest.

frontiers in Neuroscience

ORIGINAL RESEARCH
published: 01 May 2019
doi: 10.3389/fnins.2019.00434

Application of Convolutional Recurrent Neural Network for Individual Recognition Based on Resting State fMRI Data

*Lebo Wang[1], Kaiming Li[2], Xu Chen[3] and Xiaoping P. Hu[1,2,3]**

[1] Department of Electrical and Computer Engineering, University of California, Riverside, Riverside, CA, United States, [2] Department of Bioengineering, University of California, Riverside, Riverside, CA, United States, [3] Center for Advanced Neuroimaging, University of California, Riverside, Riverside, CA, United States

In most task and resting state fMRI studies, a group consensus is often sought, where individual variability is considered a nuisance. None the less, biological variability is an important factor that cannot be ignored and is gaining more attention in the field. One recent development is the individual identification based on static functional connectome. While the original work was based on the static connectome, subsequent efforts using recurrent neural networks (RNN) demonstrated that the inclusion of temporal features greatly improved identification accuracy. Given that convolutional RNN (ConvRNN) seamlessly integrates spatial and temporal features, the present work applied ConvRNN for individual identification with resting state fMRI data. Our result demonstrates ConvRNN achieving a higher identification accuracy than conventional RNN, likely due to better extraction of local features between neighboring ROIs. Furthermore, given that each convolutional output assembles in-place features, they provide a natural way for us to visualize the informative spatial pattern and temporal information, opening up a promising new avenue for analyzing fMRI data.

Keywords: functional magnetic resonance imaging, individual identification, recurrent neural network, convolutional neural network, visualization

OPEN ACCESS

Edited by:
Amir Shmuel,
McGill University, Canada

Reviewed by:
Wenqin Wang,
Tianjin Polytechnic University, China
Xiaoyun Liang,
Australian Catholic University, Australia
Hanbo Chen,
Tencent Holdings Limited, China

***Correspondence:**
Xiaoping P. Hu
xhu@engr.ucr.edu

Specialty section:
This article was submitted to Brain Imaging Methods, a section of the journal Frontiers in Neuroscience

Received: *09 December 2018*
Accepted: *15 April 2019*
Published: *01 May 2019*

Citation:
Wang L, Li K, Chen X and Hu XP (2019) Application of Convolutional Recurrent Neural Network for Individual Recognition Based on Resting State fMRI Data. Front. Neurosci. 13:434. doi: 10.3389/fnins.2019.00434

INTRODUCTION

Mainstream fMRI studies have been focusing on deriving population consensuses using group analysis. A group analysis in neuroimaging, albeit important, commonly neglects individual-to-individual variations. The importance of individual variability in neurobiological research has drawn increasing attention (Mohr and Nagel, 2010). Using task-fMRI, significant individual differences in brain activation were identified, reflecting alterations in cognitive function and behavior (Barch et al., 2013). Individual variability in functional connectivity (FC) has been successfully used to identify subjects from a large group. More specifically, static connectivity patterns throughout the brain were shown to be subject specific and distinctive across scan sessions and conditions, providing powerful features for individual identification (Finn et al., 2015). Therefore, exploring the individual uniqueness of the brain connectivity points to a new avenue to study the brain.

Although the static FC achieved decent accuracy, it required a sufficiently long data set (600 frames, 7.2 min) and considered only the spatial pattern through the temporal correlation without

taking temporal features into full account. The performance degraded with short clips of fMRI data, probably due to temporal variability (or dynamics) in the resting-state fMRI data, which leads to high variability in the FC derived from a short window. On the other hand, the dynamic information of resting state activity, if taken into account, could provide additional features for individual identification, improving the accuracy with the short time series.

In the application of time sequence modeling, recurrent neural networks (RNNs) have shown outstanding promise in a broad range of applications, including video classification, machine translation, and biomedical image segmentation (Sharma et al., 2015; Chen et al., 2016; Vaswani et al., 2017; Gao et al., 2018). For fMRI data analysis, RNN was able to model the dynamics of brain activity in response to sensory stimuli, providing accurate estimates of hemodynamic response with temporal dynamics (Güçlü and van Gerven, 2017). RNNs have also been implemented to incorporate temporal information along with spatial features from resting-state fMRI data instead of merely spatial pattern in the connectome (Dvornek et al., 2017; Chen and Hu, 2018). Furthermore, a convolution-based RNN was introduced to make full use of features in both spatial and temporal domains, consistently outperforming fully connected RNNs (Shi et al., 2015). Therefore, combining the local features between adjacent ROIs by the convolutional structure and sequence modeling capability of RNN may lead to a better approach to extract spatiotemporal features for individual identification on resting-state fMRI data.

In the meantime, it is also valuable to visualize the underlying features in the trained convolutional models. Although deep learning is becoming a panacea in almost every domain, it has been criticized due to its poor interpretability as being a black-box. While many attempts have been made to provide an interpretation and an intuitive understanding of trained networks, our understanding of how these networks work and what is important behind their performance have not kept up with the pace of the development of neural networks. While dedicated deep learning models have achieved amazing performance by end-to-end learning through huge volumes of data, better comprehension of the success of these models can uncover fundamental principles of deep neural networks and reveal important features within the data.

In this work, we adopted convolutional RNN or ConvRNN for individual identification using resting-state fMRI data. The convolutional recurrent model was able to achieve individual identification with shared convolutional weights capturing local coactivation features. In-place visualization of the informative area by ConvRNN also opened up a new avenue for understanding fMRI data based on individual differences.

MATERIALS AND METHODS

Dataset and Preprocessing

The resting-state fMRI data for 100 subjects from the Human Connectome Project (HCP) (54 females, age: 22–36, and TR = 0.72 s) was used in this work. Each subject had four resting-state fMRI sessions, 1200 volumes for each session, leading to 4800 volumes per subject in total (Van Essen et al., 2013). The fMRI data was preprocessed by the HCP minimal preprocessing pipeline (Glasser et al., 2013) and denoised by ICA-FIX (Salimi-Khorshidi et al., 2014), for the removal of spatial artifact/distortion and motion-related fluctuations. Surface-based registration was performed with the MSM-ALL template (Robinson et al., 2014). To decrease the computation complexity, two hundred and thirty-six regions of interest (ROIs) over the cerebral cortex, as shown in **Figure 1** based on meta-analysis (Power et al., 2011), were used for subsequent analysis. BOLD signals within each ROI (10 mm diameter sphere) were averaged spatially. We ordered our ROIs-based data in a 1D array and preserved the order of ROIs according to the Power Atlas, where ROIs having similar functional connectivities are close to each other. They were also demeaned and scaled to unit variance over the temporal axis. For each fMRI session, fMRI data with 1200 volumes was divided into twelve 100-frame clips as inputs of ConvRNN. Data from Day 1 was used as the training dataset. The two sessions from Day 2 were used as validation and testing datasets, respectively. The best model was decided based on the validation dataset and the final performance was assessed on the testing dataset.

Convolutional Recurrent Neural Network

The architecture of the ConvRNN is given in **Figure 2**, along with its unrolling version. In contrast to conventional RNN, convolution was applied in both the input-to-state and state-to-state transitions, in place of the Hadamard product. There were two stacked convolutional layers, with the first convolutional layer containing 8 filters and the second convolutional layer having 16 filters. The kernel size of all convolutional filters was 2. Padding was used in all convolutional layers such that the outputs from each layer had the same spatial dimension as the original input, which is very important for the subsequent visualization of the in-place features. Batch normalization layers were used before the non-linear activation layers of Rectified linear unit (ReLU) to reshape the distribution of convolutional layer outputs in order for better convergence and easy training

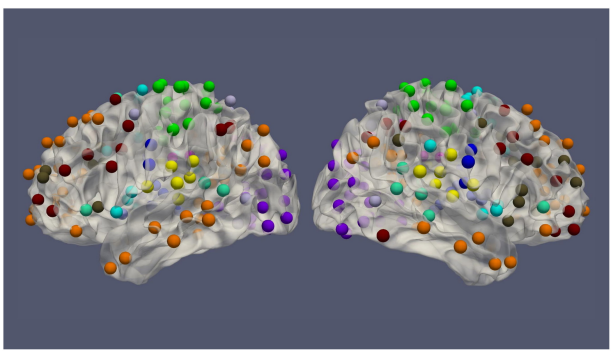

FIGURE 1 | The spatial distribution of 236 ROIs over the cerebral cortex. Voxels within the 10 mm diameter sphere were averaged to get the value for each ROI.

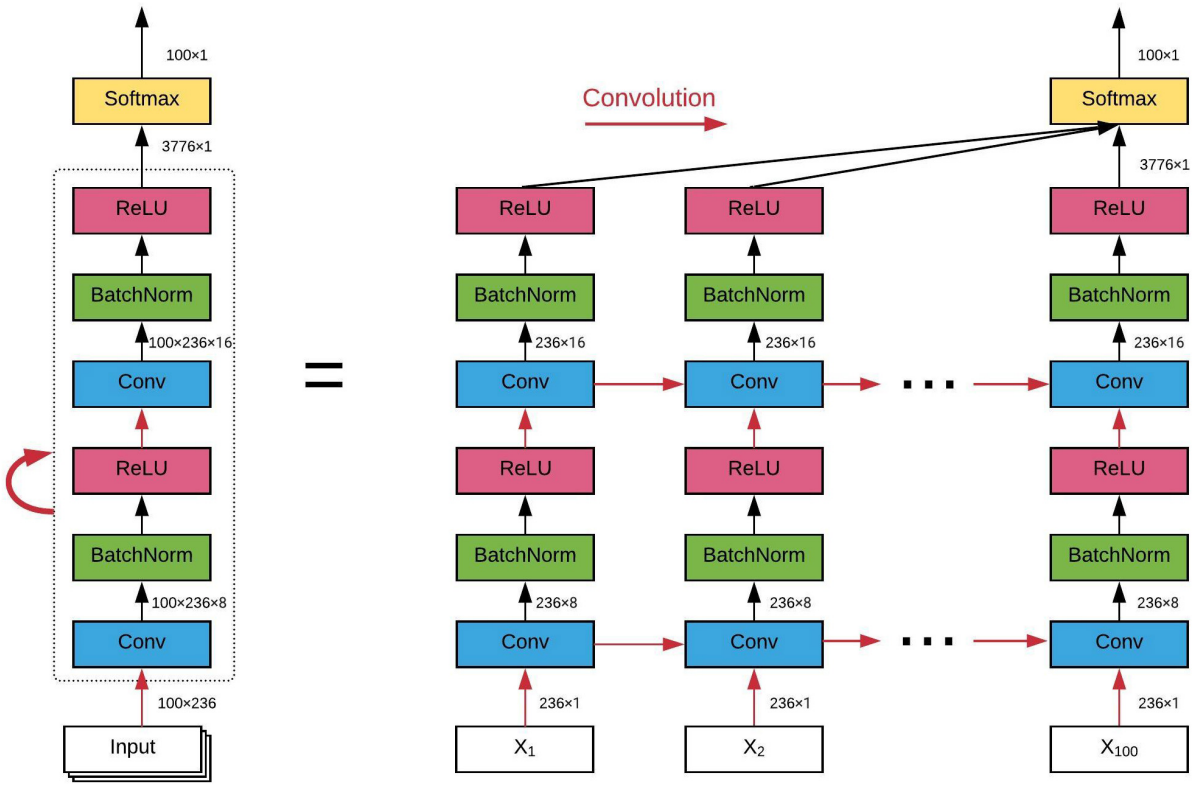

FIGURE 2 | The architecture of our convolutional recurrent neural network and its unrolling version over time. All red arrows represent the convolutional operations between each input-to-state and state-to-state transitions. Batch normalization and ReLU as the non-linear activation are utilized after each convolutional layer. Final classification is based on all hidden states on average. The dimension of the data flow through the diagram is also labeled.

(Ioffe and Szegedy, 2015). The final Softmax layer with 100-category outputs was used for classification based on averaged outputs from all hidden states. No temporal or spatial pooling layer was employed to keep the spatial and temporal resolutions of the original fMRI data. All kernel weights were initialized by the Xavier uniform initializer (Glorot and Bengio, 2010), and recurrent weights were initialized as random orthogonal matrices (Saxe et al., 2013).

Training of the Neural Network

Our implementation of ConvRNN was carried out in Keras (Chollet, 2015) with the Tensorflow backend (Abadi et al., 2016). Considering the limited number of frames for each subject, we chose 100 frames of fMRI data as inputs during training and validation, which is the tradeoff between the number of fMRI clips and the number of frames for each clip. Shuffled minibatches of training data as inputs were fed into the ConvRNN with the batch size of 128. Adam optimizer (Kingma and Ba, 2014) was applied for training with the initial learning rate set to 0.001, and reduced if the validation accuracy stopped increasing. Dropout layer with 50% was utilized before the final classification to avoid overfitting only during the training (Srivastava et al., 2014). After each training epoch, the model was evaluated on the validation dataset and saved only if better validation accuracy was achieved. Finally, the performance of the best model was measured on the testing dataset, which was never involved during training or validation.

It is well known that RNN is difficult to train properly, even though it is a powerful model for time series modeling. The main reasons are vanishing and exploding gradient issues of Backpropagation Through Time (BPTT) on the unrolling version of RNN (Bengio et al., 1994). Therefore, advanced architectures with gating mechanism to overcome the vanishing and exploding gradient problem, such as the Long short-term memory (LSTM) (Hochreiter and Schmidhuber, 1997) and the Gated recurrent unit (GRU) (Cho et al., 2014), have gained a lot of popularity in practice to model long-term dependencies. In this work, LSTM with convolutional structure was applied. For training techniques, we used L2 regularization for recurrent weights, along with the gradient clipping strategy as a simple and computationally efficient method, effectively addressing the issue of exploding gradients (Pascanu et al., 2013). In the present work, the clipping norm of the gradient was set to 1. Different L2 values (0.1, 0.01, 0.001, and 0.0001) on recurrent kernel weights were tested to achieve the best validation accuracy.

Visualization of the Individual Identification

Our ConvRNN first performed feature extraction through two convolutional recurrent layers and then fed the features into

the Softmax layer for the 100-catergory classification. Original data was projected to a high-dimensional feature space, which was easily separated by the classification layer. In the feature space, fMRI data from the same subject are expected to be close to each other and cluster tightly. In consideration of the single classification layer, the identification accuracy of our ConvRNN relies heavily on the performance of feature extraction by convolutional recurrent layers. In order to ascertain and visualize the performance of convolutional recurrent layers in low dimensional space, t-Distributed Stochastic Neighbor Embedding (t-SNE) (Maaten and Hinton, 2008) was applied to map datapoints in high-dimensional feature space onto a two-dimensional representation.

To visualize and understand informative areas related to individual identification, intermediate outputs from convolutional layers were examined. Output patterns were obtained from convolutional layers after non-linear activation and mapped onto the cortical surface (20 mm radius sphere). As all regions are considered equal in our convolutional model during the training, but they are of different importance to the final classification. We also used the occlusion method to visualize informative areas (Zeiler and Fergus, 2014). More specifically, in order to ascertain the contribution of ROIs with regard to individual identification, input of each ROI was zeroed out, and the subsequent performance decrease with the same model configuration was considered as the contribution of this ROI to the final classification.

TABLE 1 | The accuracy of different models on the testing dataset and their number of model weights.

Architecture	# Parameters (feature extraction)	Test accuracy
RNN (Chen and Hu, 2018)	405K (380K)	94.43%
RNN w/o temporal pooling	405K (380K)	95.33%
ConvRNN	382K (3.8K)	98.50%

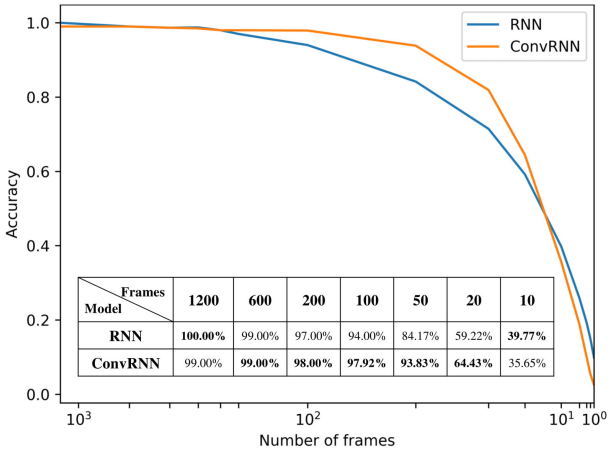

Model \ Frames	1200	600	200	100	50	20	10
RNN	**100.00%**	99.00%	97.00%	94.00%	84.17%	59.22%	**39.77%**
ConvRNN	99.00%	**99.00%**	**98.00%**	**97.92%**	**93.83%**	**64.43%**	35.65%

FIGURE 3 | The relationship between identification accuracy and the window size. We evaluated pre-trained models on testing dataset. Our ConvRNN outperformed RNN except with 1200 frames or with less than 10 frames.

RESULTS

We carried out the supervised classification task to identify each subject from a group of 100 subjects. First, the identification accuracy of different models was assessed on the testing dataset with 100 frames of fMRI data as inputs. As seen in **Table 1**, our ConvRNN model was able to achieve 98.50% accuracy on the testing dataset, where the best performance was obtained with the L2 value of 0.001 during training. The test accuracy for the traditional RNN with average temporal pooling was 94.43% (Chen and Hu, 2018). In order to exclude the influence of temporal averaging, we trained another RNN without the temporal averaging and achieved an identification accuracy of 95.33%. Furthermore, we evaluated the performance of these models using different window sizes on the testing dataset. With the pre-trained models, we adopted different number of frames (from 1200 frames to single frame) as inputs from the testing dataset and evaluated the identification performance. Testing results with different number of frames are plotted in **Figure 3**. As shown in the figure, ConvRNN outperformed conventional RNN (no temporal averaging) in all cases except with 1200 frames or with less than 10 frames. In contrast, FC could achieve over 90% accuracy with 600 frames of fMRI data. But the individual identification accuracy drops to 70% on average when only a short period of fMRI data (100 frames) is used (Finn et al., 2015).

To visualize convolutional outputs on low-dimensional space, we applied t-SNE on intermediate outputs of our ConvRNN before the classification layer. There were 16 convolutional filters in the second convolutional recurrent layer of our ConvRNN. With proper padding, the output of the layer was made to have the same spatial dimension as the input. The feature space with 3776 dimensions was then mapped to a 2D space in **Figure 4**. It is clear that 100 subjects (12 clips with 100 frames for each subject) in the testing dataset appear as non-overlapping cliques in different colors with each clique representing one subject. This figure clearly indicates that spatiotemporal features, capable of individual identification, were successfully obtained by convolutional recurrent layers.

To visualize intermediate outputs of ConvRNN, average patterns from first and second convolutional layers of ConvRNN are shown in **Figures 5**, **6**, respectively. Most patterns from the first convolutional layer were quite similar (except Filter 6) with large distinctive areas, which could be considered as the ubiquitous low-level features from fMRI data. While high-level patterns from the second convolutional layer had diverse informative regions, which were sparse and localized inside the area of those low-level features generated by the first convolutional layer. Meanwhile, when ROIs were individually occluded, performance degradation was observed when some ROIs were occluded, while the occlusion of some ROIs led to negligible degradation of the performance. In **Figure 7**, the absolute value of the performance degradation, normalized to reflect the contribution of each ROI is shown. It is evident that the informative area generated by alternative occlusion was similar as the patterns from first convolutional layer of ConvRNN.

DISCUSSION

While most resting-state fMRI studies have relied on group averages, this study employed individual differences for individual identification. Unlike the first study of individual identification employing static FC (Finn et al., 2015), we incorporated both temporal and spatial features from the fMRI data. As an improvement of our previous work employing the recurrent architecture (Chen and Hu, 2018), we applied a convolutional recurrent neural network which led to a significant improvement in performance and a straightforward means to visualize in-place features. **Figure 3** shows that ConvRNN is better than conventional RNN for the majority of the time windows. The performance of ConvRNN was slightly worse than conventional RNN with 1200 frames, probably due to the small number of testing data when the performance was evaluated on fMRI clips with 1200 frames. On the other hand, since our ConvRNN was trained with the fixed number of frames (i.e., 100), it is not be optimized for short clips of data with less than 10 frames, and its performance with frames less than 10 is therefore worse than that of conventional RNN.

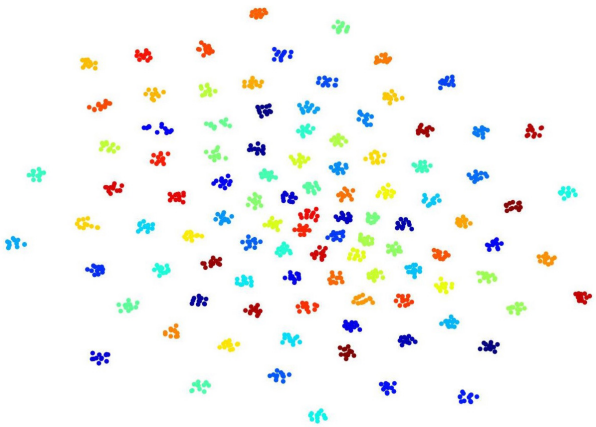

FIGURE 4 | t-Distributed Stochastic Neighbor Embedding (t-SNE) visualization of 2nd convolutional recurrent layer outputs based on 100-subject testing dataset. Twelve hundred 100-frame testing data from 100 subjects were fed into ConvRNN with outputs being obtained before the classification layers and projected to 2D space by t-SNE. Projections for different subjects are in different colors.

Our ConvRNN has the same number of parameters compared with the conventional RNN, indicating that both models have comparable model complexity. Apart from the different types of recurrent unit, our earlier work (Chen and Hu, 2018) employed a temporal pooling layer to reduce the temporal resolution. For a fair comparison with this work, another conventional RNN was applied without the temporal averaging layer. The accuracy of the conventional RNN without the temporal averaging layer was 95.33%, which was 0.9% higher than that with the temporal averaging. This improvement

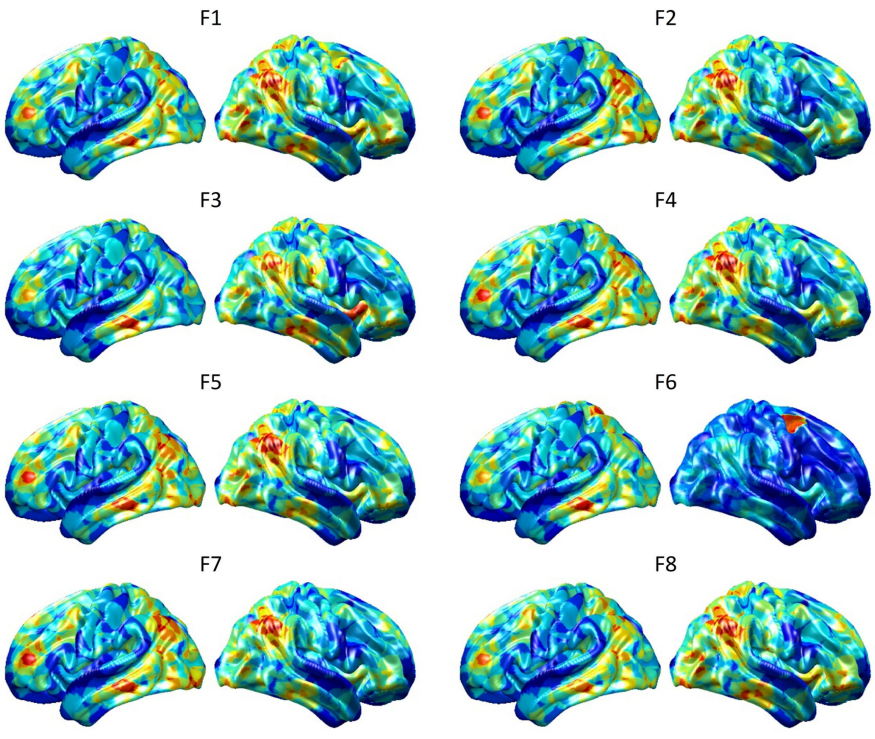

FIGURE 5 | Average output patterns of the first convolutional layer with 8 convolutional kernels. Twelve hundred 100-frame testing data from 100 subjects were fed into the convolutional recurrent model with output patterns generated and averaged from the first non-linear activation layer. Red areas represent large activation values.

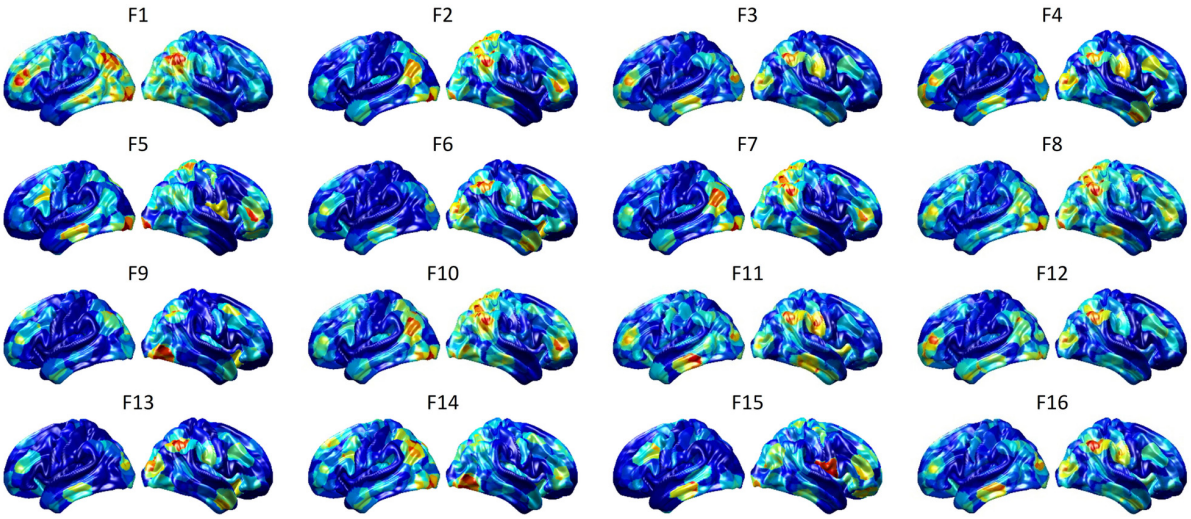

FIGURE 6 | Average output patterns of the second convolutional layer with 16 convolutional kernels. Twelve hundred 100-frame testing data from 100 subjects were fed into the convolutional recurrent model with output patterns generated and averaged from the second non-linear activation layer. Red areas represent large activation values.

due to increased temporal resolution is significantly smaller than the improvement achieved with the adoption of the convolutional structure, indicating that the latter is the main contributor to the performance enhancement. Both the spatial and temporal features were fully utilized by convolutional kernels in the ConvRNN with unprecedented identification accuracy. Also, feature extraction layers of ConvRNN showed strong discriminating power for 100 subjects, where pre-trained layers could be applied for transfer learning on new subjects or semi-supervised learning on partially labeled data. On the other hand, only one hundredths of the parameters in ConvRNN were from the convolutional recurrent layers. Convolution with shared weights in spatial and temporal spans makes it more robust against overfitting during training. Given the reduced number of trainable weights, increasing the depth and width of the model is possible without significantly increasing the model complexity, possibly capturing more sophisticated features in both spatial and temporal domains.

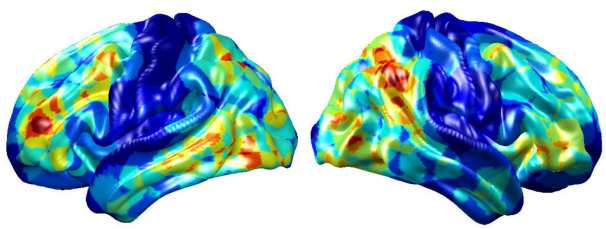

FIGURE 7 | The performance degradation with occlusion. Each ROI was zeroed out separately and evaluated with the pre-trained model of ConvRNN. The performance degradation reflects the contribution of each ROI. Red region reflects large performance degradation if corresponding ROIs were occluded.

Furthermore, convolutional kernels with shared weights sweep across ROIs and frames. Different from the indecomposable matrix multiplication in conventional RNN, ConvRNN generates in-place features with exactly spatial correspondence as the original data. Furthermore, ConvRNN accumulates temporal information related to evolving features in the hidden state. Therefore, it is possible to examine the hidden states to have an in-place visualization and understanding of hidden features from ConvRNN. It is also clear that informative regions from two convolutional layers are totally different, in agreement with the conclusion drawn from convolutional neural networks for image classification (Yosinski et al., 2015). Beside the direct visualization of the hidden state, the occlusion of ROIs served as an indirect method for visualizing significant regions under resting state for identification. Two visualization approaches came to the same conclusion of informative ROIs in term of individual identification using the resting-state fMRI data. In terms of resting state networks (RSNs) in the literature (Holmes et al., 2011; Lee et al., 2012), the informative area identified by our ConvRNN mainly contained frontoparietal network (FPN), default mode network (DMN), as well as visual network (VN). Our result is consistent with a previous study, which concluded that the most distinguishing network was FPN, with significant improvement achieved through the combination of multiple RSNs (Finn et al., 2015). In contrast, occlusion of language network (LN) and somatosensory motor network (SMN) did not cause much reduction in performance. One possible explanation is that there was little explicit or individual-specific language or motor activity during the acquisition of the resting-state fMRI datasets used here.

Although DMN and FPN stood out as the most important networks for individual identification, other networks also contributed to individual identification (Finn et al., 2017). It is likely that contributions from most networks may be

needed with more subjects to be identified. In addition, a hierarchical approach, incorporating all networks, might be the most appropriate and robust approach. Furthermore, a recent study demonstrated that task induced changes in FC provided better prediction of individuals, whereas resting-state fMRI data failed to capture the full range of individual differences (Greene et al., 2018). Such changes in FC could also be incorporated into our model to further improve the identification accuracy.

Several limitations should be noted for further work. First, the present study adopted only 236 ROIs within 10 mm diameter spheres on average, which was enough for an accurate identification for a group of 100 subjects. Inadequate power of identification could be present on new subjects beyond existing subjects. Possible reasons are the limited feature extraction of our model and the high variability of the fMRI data. It is likely that smaller and more ROIs are needed for the identification of more subjects. But more advanced models with good generalization on fMRI data should be explored. Second, current visualization of individual identification depicted in **Figure 7** was based on group average of ROIs' performance. While this highlights areas that are most important for individual identification, it does not explicitly depict individual features. Such features will be the focus of our future studies. Third, visualization of the spatial pattern is easy to understand, but the remarkable performance achieved by RNN suggests that a substantial amount of information is coming from temporal features. Visualizing and understanding temporal features are still necessary to gain a deeper insight into the brain dynamics. Furthermore, other popular architectures (e.g., Siamese network) and pre-trained models should be applied and compared with our approach in terms of classification performance and training efficiency in future work.

CONCLUSION

In this paper, we described the application of the convolutional recurrent neural network for individual identification based on resting-state fMRI data. To explore the dynamics in the resting-state fMRI data, the convolutional architecture with recurrent structure was implemented to extract and incorporate features in both spatial and temporal domains. Compared to conventional RNN model, our ConvRNN model exhibited better identification performance, with local features between neighboring ROIs being modeled by convolutional kernels. Moreover, visualization based on the ConvRNN model provides a direct understanding of the success of identification; this could lead to a promising alternative for analyzing fMRI data.

AUTHOR CONTRIBUTIONS

LW designed and performed experiments and wrote the manuscript. KL analyzed data and reviewed the manuscript. XC collected the data. XH designed research and reviewed the manuscript.

REFERENCES

Abadi, M., Barham, P., Chen, J., Chen, Z., Davis, A., Dean, J., et al. (2016). "TensorFlow: a system for large-scale machine learning," in *OSDI'16 Proceedings of the 12th USENIX conference on Operating Systems Design and Implementation*, (Savannah, GA), 265–283.

Barch, D. M., Burgess, G. C., Harms, M. P., Petersen, S. E., Schlaggar, B. L., Corbetta, M., et al. (2013). Function in the human connectome: task-fMRI and individual differences in behavior. *Neuroimage* 80, 169–189. doi: 10.1016/j.neuroimage.2013.05.033

Bengio, Y., Simard, P., and Frasconi, P. (1994). Learning long-term dependencies with gradient descent is difficult. *IEEE Trans. Neural Netw.* 5, 157–166. doi: 10.1109/72.279181

Chen, J., Yang, L., Zhang, Y., Alber, M., and Chen, D. Z. (2016). "Combining fully convolutional and recurrent neural networks for 3d biomedical image segmentation," in *Proceedings of the Advances in Neural Information Processing Systems*, (Cambridge, MA), 3036–3044.

Chen, S., and Hu, X. P. (2018). Individual identification using functional brain fingerprint detected by recurrent neural network. *Brain Connect.* 8, 197–204. doi: 10.1089/brain.2017.0561

Cho, K., Van Merriënboer, B., Gulcehre, C., Bahdanau, D., Bougares, F., Schwenk, H., et al. (2014). Learning phrase representations using RNN encoder-decoder for statistical machine translation. arXiv:1406.1078 [Preprint].

Chollet, F. (2015). *Keras. GitHub*. Available at: https://github.com/fchollet/keras (accessed March 7, 2018).

Dvornek, N. C., Ventola, P., Pelphrey, K. A., and Duncan, J. S. (2017). "Identifying autism from resting-state fMRI using long short-term memory networks," in *Proceedings of the International Workshop on Machine Learning in Medical Imaging*, (Granada), 362–370. doi: 10.1007/978-3-319-67389-9_42

Finn, E. S., Scheinost, D., Finn, D. M., Shen, X., Papademetris, X., and Constable, R. T. (2017). Can brain state be manipulated to emphasize individual differences in functional connectivity? *Neuroimage* 160, 140–151. doi: 10.1016/j.neuroimage.2017.03.064

Finn, E. S., Shen, X., Scheinost, D., Rosenberg, M. D., Huang, J., Chun, M. M., et al. (2015). Functional connectome fingerprinting: identifying individuals using patterns of brain connectivity. *Nat. Neurosci.* 18:1664. doi: 10.1038/nn.4135

Gao, Y., Phillips, J. M., Zheng, Y., Min, R., Fletcher, P. T., and Gerig, G. (2018). "Fully convolutional structured LSTM networks for joint 4D medical image segmentation," in *Proceedings of the Biomedical Imaging (ISBI 2018), 2018 IEEE 15th International Symposium on*, (Piscataway, NJ), 1104–1108.

Glasser, M. F., Sotiropoulos, S. N., Wilson, J. A., Coalson, T. S., Fischl, B., Andersson, J. L., et al. (2013). The minimal preprocessing pipelines for the Human Connectome Project. *Neuroimage* 80, 105–124. doi: 10.1016/j.neuroimage.2013.04.127

Glorot, X., and Bengio, Y. (2010). "Understanding the difficulty of training deep feedforward neural networks," in *Proceedings of the thirteenth international conference on artificial intelligence and statistics*, (Sardinia), 249–256.

Greene, A. S., Gao, S., Scheinost, D., and Constable, R. T. (2018). Task-induced brain state manipulation improves prediction of individual traits. *Nat. Commun.* 9:2807. doi: 10.1038/s41467-018-04920-3

Güçlü, U., and van Gerven, M. A. (2017). Modeling the dynamics of human brain activity with recurrent neural networks. *Front. Comput. Neurosci.* 11:7. doi: 10.3389/fncom.2017.00007

Hochreiter, S., and Schmidhuber, J. (1997). Long short-term memory. *Neural Comput.* 9, 1735–1780.

Holmes, A. J., Hollinshead, M. O., O'keefe, T. M., Petrov, V. I., Fariello, G. R., Wald, L. L., et al. (2011). The organization of the human cerebral cortex estimated by intrinsic functional connectivity. *Sci. Data* 2:150031.

Ioffe, S., and Szegedy, C. (2015). Batch normalization: accelerating deep network training by reducing internal covariate shift. arXiv:1502.03167 [Preprint].

Kingma, D. P., and Ba, J. (2014). Adam: a method for stochastic optimization. arXiv:1412.6980 [Preprint].

Lee, M. H., Smyser, C. D., and Shimony, J. S. (2012). Resting-state fMRI: a review of methods and clinical applications. *Am. J. Neuroradiol.* 34, 1866–1872. doi: 10.3174/ajnr.a3263

Maaten, L. V. D., and Hinton, G. (2008). Visualizing data using t-SNE. *J. Machine Learn. Res.* 9, 2579–2605.

Mohr, P. N., and Nagel, I. E. (2010). Variability in brain activity as an individual difference measure in neuroscience. *J. Neurosci.* 30, 7755–7757. doi: 10.1523/jneurosci.1560-10.2010

Pascanu, R., Mikolov, T., and Bengio, Y. (2013). "On the difficulty of training recurrent neural networks," in *Proceeedings of the International Conference on Machine Learning*, (Atlanta, GA), 1310–1318.

Power, J. D., Cohen, A. L., Nelson, S. M., Wig, G. S., Barnes, K. A., Church, J. A., et al. (2011). Functional network organization of the human brain. *Neuron* 72, 665–678.

Robinson, E. C., Jbabdi, S., Glasser, M. F., Andersson, J., Burgess, G. C., Harms, M. P., et al. (2014). MSM: a new flexible framework for multimodal surface matching. *Neuroimage* 100, 414–426. doi: 10.1016/j.neuroimage.2014.05.069

Salimi-Khorshidi, G., Douaud, G., Beckmann, C. F., Glasser, M. F., Griffanti, L., and Smith, S. M. (2014). Automatic denoising of functional MRI data: combining independent component analysis and hierarchical fusion of classifiers. *Neuroimage* 90, 449–468. doi: 10.1016/j.neuroimage.2013.11.046

Saxe, A. M., Mcclelland, J. L., and Ganguli, S. (2013). Exact solutions to the nonlinear dynamics of learning in deep linear neural networks. arXiv:1312.6120 [Preprint].

Sharma, S., Kiros, R., and Salakhutdinov, R. (2015). Action recognition using visual attention. arXiv:1511.04119 [Preprint].

Shi, X., Chen, Z., Wang, H., Yeung, D.-Y., Wong, W.-K., and Woo, W.-C. (2015). "Convolutional LSTM network: a machine learning approach for precipitation nowcasting," in *Proceedings of the Advances in Neural Information Processing Systems*, (Cambridge, MA), 802–810.

Srivastava, N., Hinton, G., Krizhevsky, A., Sutskever, I., and Salakhutdinov, R. (2014). Dropout: a simple way to prevent neural networks from overfitting. *J. Machine Learn. Res.* 15, 1929–1958.

Van Essen, D. C., Smith, S. M., Barch, D. M., Behrens, T. E., Yacoub, E., Ugurbil, K., et al. (2013). The WU-Minn human connectome project: an overview. *Neuroimage* 80, 62–79. doi: 10.1016/j.neuroimage.2013.05.041

Vaswani, A., Shazeer, N., Parmar, N., Uszkoreit, J., Jones, L., Gomez, A. N., et al. (2017). "Attention is all you need," in *Proceedings of the Advances in Neural Information Processing Systems*, (Cambridge, MA), 6000–6010.

Yosinski, J., Clune, J., Nguyen, A., Fuchs, T., and Lipson, H. (2015). Understanding neural networks through deep visualization. *arXiv*

Zeiler, M. D., and Fergus, R. (2014). "Visualizing and understanding convolutional networks," in *Proceedings of the European conference on computer vision*, (Munich), 818–833. doi: 10.1007/978-3-319-10590-1_53

Conflict of Interest Statement: The authors declare that the research was conducted in the absence of any commercial or financial relationships that could be construed as a potential conflict of interest.

frontiers in Neuroscience

METHODS
published: 09 July 2019
doi: 10.3389/fnins.2019.00685

Tracking the Main States of Dynamic Functional Connectivity in Resting State

Qunjie Zhou[1†], Lu Zhang[1,2†], Jianfeng Feng[1,2,3,4] and Chun-Yi Zac Lo[2*]*

[1] Shanghai Center for Mathematical Sciences, Fudan University, Shanghai, China, [2] Institute of Science and Technology for Brain Inspired Intelligence, Fudan University, Shanghai, China, [3] Oxford Centre for Computational Neuroscience, Oxford, United Kingdom, [4] Department of Computer Science, University of Warwick, Coventry, United Kingdom

OPEN ACCESS

Edited by:
Xiaoping Philip Hu, University of California, Riverside, United States

Reviewed by:
Mingrui Xia, Beijing Normal University, China
Xiao Liu, National Institute of Neurological Disorders and Stroke (NINDS), United States
Tianming Liu, University of Georgia, United States

***Correspondence:**
Jianfeng Feng
jianfeng64@gmail.com
Chun-Yi Zac Lo
zaclocy@gmail.com

[†] These authors have contributed equally to this work as co-first authors

Specialty section:
This article was submitted to Brain Imaging Methods, a section of the journal Frontiers in Neuroscience

Received: *14 January 2019*
Accepted: *17 June 2019*
Published: *09 July 2019*

Citation:
Zhou Q, Zhang L, Feng J and Lo C-YZ (2019) Tracking the Main States of Dynamic Functional Connectivity in Resting State. Front. Neurosci. 13:685. doi: 10.3389/fnins.2019.00685

Dynamical changes have recently been tracked in functional connectivity (FC) calculated from resting-state functional magnetic resonance imaging (R-fMRI), when a person is conscious but not carrying out a directed task during scanning. Diverse dynamical FC states (dFC) are believed to represent different internal states of the brain, in terms of brain-regional interactions. In this paper, we propose a novel protocol, the signed community clustering with the optimized modularity by two-step procedures, to track dynamical whole brain functional connectivity (dWFC) states. This protocol is assumption free without *a priori* threshold for the number of clusters. By applying our method on sliding window based dWFC's with automated anatomical labeling 2 (AAL2), three main dWFC states were extracted from R-fMRI datasets in Human Connectome Project, that are independent on window size. Through extracting the FC features of these states, we found the functional links in state 1 (WFC-C_1) mainly involved visual, somatomotor, attention and cerebellar (posterior lobe) modules. State 2 (WFC-C_2) was similar to WFC-C_1, but more FC's linking limbic, default mode, and frontoparietal modules and less linking the cerebellum, sensory and attention modules. State 3 had more FC's linking default mode, limbic, and cerebellum, compared to WFC-C_1 and WFC-C_2. With tests of robustness and stability, our work provides a solid, hypothesis-free tool to detect dWFC states for the possibility of tracking rapid dynamical change in FCs among large data sets.

Keywords: community clustering, signed networks, modularity, temporal changes, resting state functional magnetic resonance image

INTRODUCTION

Spontaneous fluctuations are a fundamental mechanism representing neural signals that has been largely explained by functional magnetic resonance imaging (fMRI) data. Resting-state functional connectivity (FC) can demonstrate the intrinsic network organizations of human brain (Friston, 2011). The cognitive activities of high order brain function involve the dynamic interplay of a set of brain circuits rather than a specific region, and the spontaneous activity in rest is also predictive of task and behavior performance (De la Iglesia-Vaya et al., 2013; Reineberg et al., 2015;

Tavor et al., 2016). Accumulating studies have proposed to detect the spatiotemporal organization of dynamic functional connectivity (dFC), and of dynamic whole-brain functional connectivity (dWFC) (Calhoun et al., 2014; Kopell et al., 2014; Preti et al., 2017), showing how brain FC organized over time.

Clustering analysis, particularly k-means is one of the most common methods of categorizing dFC patterns (Calhoun et al., 2014). It partitions n samples in observation space into k clusters, where each sample belongs to the nearest cluster according to its distance from the cluster centroid. However, it requires the pre-defined number of clusters k and is sensitive to initial values that may lead to different results. Hierarchy clustering (HC) aims to building a dendrogram which represents a hierarchy of cluster, and the samples could be attributed to a sub-cluster within a main cluster. Thus, HC is a more flexible method to understand the dFC structures in different levels (Vidaurre et al., 2017). However, it also requires the definition of a specific threshold for cluster separation. Both k-means and HC are not assumption free and need *a priori* knowledge for categorization of the states of brain activity.

The selection of the number of clusters or the threshold may bias or affect the interpretation of the states while lacking comprehensive understanding of the underlying mechanism of dFC. Principal component analysis (PCA) coverts a number of possibly correlated variables into a set of linearly uncorrelated variables, called principal components. It has been used to investigate dynamic brain connectivity patterns, "eigenconnectivities," by ranking and extracting the principal components of dWFC's with higher variability across time and subjects (Leonardi et al., 2013). Though PCA is a powerful tool to detect the different features of dFC, it needs to bear a risk of information loss during the reduction of dimensionality. Other state detection models based on hidden Markov chain also require prior knowledge of the expression form and the number of states (Robinson et al., 2015; Ryali et al., 2016; Vidaurre et al., 2017).

These approaches are able to uncover the similar time-varying recurring connectivity patterns into states, and have revealed the characteristics of dFC linking with the human demographic characterization, cognitive behaviors and diseases (Baker et al., 2014; Calhoun et al., 2014; Karahanoğlu and Van De Ville, 2015; Zhang et al., 2016). However, heterogeneities are widely observed across studies. There is still a lack of reliable methods for the research of dFC networks. In this study, we focused on the co-variation of FCs over time by detecting the state for dWFC's across subjects and time from Human Connectome Project (HCP) data. We proposed the modularity-optimized community clustering algorithm to categorize the dWFC's in an unsupervised and data-driven fashion. This can provide a more appropriate clustering method while little is known in dWFC's states. As the computation for community clustering is computationally expensive and time-consuming, we also proposed a two-steps clustering process to reduce the cost of our proposed algorithm.

MATERIALS AND METHODS

Participants and Data Acquirements

HCP

The dataset used for this study was collected from HCP[1] (WU-Minn Consortium). Our sample includes 812 subjects (ages 22–35 years-old, 450 females) scanned on a 3T Siemens connectome-Skyra scanner. For each subject, a three-dimensional T1 structural image was acquired at 0.7 mm isotropic resolution with 3D MPRAGE acquisition. The four blood-oxygen-level dependent (BOLD) resting state fMRI (R-fMRI) runs were acquired in separate sessions on two different days, each for approximately 15 min (2 mm× 2 mm× 2 mm spatial resolution, TR = 0.72 s, 1200 timepoints, multiband acceleration factor of 8, with eyes open and relaxed fixation on a projected bright cross-hair on a dark background). The WU-Minn HCP Consortium obtained full informed consent from all participants, and research procedures and ethical guidelines were followed in accordance with the Institutional Review Boards (IRB) of Washington University in St. Louis, MO, United States (IRB #20120436). To identify WFC, the whole brain was parcellated into 120 regions according to the automated anatomical labeling (AAL2) atlas (Rolls et al., 2015), with names and abbreviations listed in **Table 1**.

Data Preprocessing

HCP Data

The minimally preprocessed R-fMRI data were used, conducted by HCP Functional Pipeline v2.0 (Glasser et al., 2013), including gradient distortion correction, head motion correction, image distortion correction, and spatial transformation to the Montreal Neurological Institute (MNI) space, with one step spline resampling from the original functional images. The linear trend and quadratic term were removed from these functional images, and several nuisance signals were regressed from the time course of each voxel using multiple linear regression, including cerebrospinal fluid, white matter, and Friston 24 head motion parameters. Finally, temporal band-pass filtering (0.01–0.1 Hz) was performed to reduce the influence of low-frequency drift and the high-frequency physiological noise. The preprocessed time-courses were used for further functional connectivity analyses.

Sliding Window Based Dynamic Functional Connectivity

Either voxel or regional based BOLD signals can be used to calculate FCs. Here, we considered to process the regional based BOLD signals without losing any generality. We denoted time series $\{x_i(t), t = 0, 1, \cdots, N, i = 0, 1, \cdots, M\}$, where t is time and i is the brain region. To characterize the dynamics of FCs, all BOLD signals were segmented into T non-overlapped sliding window with length L (**Figure 1A**). Fisher-z transformed Pearson correlations between all pairs of regional BOLD signal were calculated and normalized in each window as following.

$$FC_{ij}(s) \triangleq \frac{FZ\left(r_{ij}(s)\right) - \mu(s)}{\sigma(s)}$$

[1] http://www.humanconnectomeproject.org/

TABLE 1 | The anatomical regions defined in each hemisphere and their label in the automated anatomical labeling atlas 2 (AAL2, Rolls et al., 2015).

ID	Region description	AAL2	Lobe	Abbreviation
1, 2	Precentral gyrus	Precentral	Sensorimotor	PreCG
3, 4	Superior frontal gyrus, dorsolateral	Frontal_Sup	Frontal	SFG
5, 6	Middle frontal gyrus	Frontal_Mid	Frontal	MFG
7, 8	Inferior frontal gyrus, opercular part	Frontal_Inf_Oper	Frontal	IFGoperc
9, 10	Inferior frontal gyrus, triangular part	Frontal_Inf_Tri	Frontal	IFGtriang
11, 12	IFG pars orbitalis	Frontal_Inf_Orb	Frontal	IFGorb
13, 14	Rolandic operculum	Rolandic_Oper	Frontal	ROL
15, 16	Supplementary motor area	Supp_Motor_Area	Sensorimotor	SMA
17, 18	Olfactory cortex	Olfactory	Frontal	OLF
19, 20	Superior frontal gyrus, medial	Frontal_Sup_Med	Frontal	SFGmedial
21, 22	Superior frontal gyrus, medial orbital	Frontal_Med_Orb	Frontal	PFCventmed
23, 24	Gyrus rectus	Rectus	Frontal	REC
25, 26	Medial orbital gyrus	OFCmed	Frontal	OFCmed
27, 28	Anterior orbital gyrus	OFCant	Frontal	OFCant
29, 30	Posterior orbital gyrus	OFCpost	Frontal	OFCpost
31, 32	Lateral orbital gyrus	OFClat	Frontal	OFClat
33, 34	Insula	Insula	Subcortical	INS
35, 36	Anterior cingulate & paracingulate gyri	Cingulate_Ant	Frontal	ACC
37, 38	Middle cingulate & paracingulate gyri	Cingulate_Mid	Frontal	MCC
39, 40	Posterior cingulate gyrus	Cingulate_Post	Parietal	PCC
41, 42	Hippocampus	Hippocampus	Temporal	HIP
43, 44	Parahippocampal gyrus	ParaHippocampal	Temporal	PHG
45, 46	Amygdala	Amygdala	Subcortical	AMYG
47, 48	Calcarine fissure and surrounding cortex	Calcarine	Occipital	CAL
49, 50	Cuneus	Cuneus	Occipital	CUN
51, 52	Lingual gyrus	Lingual	Occipital	LING
53, 54	Superior occipital gyrus	Occipital_Sup	Occipital	SOG
55, 56	Middle occipital gyrus	Occipital_Mid	Occipital	MOG
57, 58	Inferior occipital gyrus	Occipital_Inf	Occipital	IOG
59, 60	Fusiform gyrus	Fusiform	Temporal	FFG
61, 62	Postcentral gyrus	Postcentral	Sensorimotor	PoCG
63, 64	Superior parietal gyrus	Parietal_Sup	Parietal	SPG
65, 66	Inferior parietal gyrus, excluding supramarginal and angular gyri	Parietal_Inf	Parietal	IPG
67, 68	SupraMarginal gyrus	SupraMarginal	Parietal	SMG
69, 70	Angular gyrus	Angular	Parietal	ANG
71, 72	Precuneus	Precuneus	Parietal	PCUN
73, 74	Paracentral lobule	Paracentral_Lobule	Parietal	PCL
75, 76	Caudate nucleus	Caudate	Subcortical	CAU
77, 78	Lenticular nucleus, Putamen	Putamen	Subcortical	PUT
79, 80	Lenticular nucleus, Pallidum	Pallidum	Subcortical	PAL
81, 82	Thalamus	Thalamus	Subcortical	THA
83, 84	Heschl's gyrus	Heschl	Temporal	HES
85, 86	Superior temporal gyrus	Temporal_Sup	Temporal	STG
87, 88	Temporal pole: superior temporal gyrus	Temporal_Pole_Sup	Temporal	TPOsup
89, 90	Middle temporal gyrus	Temporal_Mid	Temporal	MTG
91, 92	Temporal pole: middle temporal gyrus	Temporal_Pole_Mid	Temporal	TPOmid
93, 94	Inferior temporal gyrus	Temporal_Inf	Temporal	ITG
95, 96	Cerebellum Crus I	Cerebelum_Crus1_L	Cerebellum	CRBLCrus1
97, 98	Cerebellum Crus II	Cerebelum_Crus2_L	Cerebellum	CRBLCrus2
99, 100	Cerebellum lobule III, hemisphere	Cerebelum_3_L	Cerebellum	CRBL3
101, 102	Cerebellum lobule IV V, hemisphere	Cerebelum_4_5_L	Cerebellum	CRBL45

(Continued)

TABLE 1 | Continued

ID	Region description	AAL2	Lobe	Abbreviation
103, 104	Cerebellum lobule VI, hemisphere	Cerebelum_6_L	Cerebellum	CRBL6
105, 106	Cerebellum lobule VII b, hemisphere	Cerebelum_7b_L	Cerebellum	CRBL7b
107, 108	Cerebellum lobule VIII, hemisphere	Cerebelum_8_L	Cerebellum	CRBL8
109, 110	Cerebellum lobule IX, hemisphere	Cerebelum_9_L	Cerebellum	CRBL9
111, 112	Cerebellum lobule X, hemisphere	Cerebelum_10_L	Cerebellum	CRBL10
113	Cerebellum lobule I II, vermis	Vermis_1_2	Cerebellum	Vermis12
114	Cerebellum lobule III, vermis	Vermis_3	Cerebellum	Vermis3
115	Cerebellum lobule IV V, vermis	Vermis_4_5	Cerebellum	Vermis45
116	Cerebellum lobule VI, vermis	Vermis_6	Cerebellum	Vermis6
117	Cerebellum lobule VII b, vermis	Vermis_7	Cerebellum	Vermis7
118	Cerebellum lobule VIII, vermis	Vermis_8	Cerebellum	Vermis8
119	Cerebellum lobule IX, vermis	Vermis_9	Cerebellum	Vermis9
120	Cerebellum lobule X, vermis	Vermis_10	Cerebellum	Vermis10

Column five provides a set of abbreviations for the anatomical descriptions.

$r_{ij}(s)$ is the Pearson correlation between subset of signals $x_i(t_s)$ and $x_j(t_s)$ where $t_s = s, s+1, \cdots, s+L-1$, and FZ$(\cdot)$ is the Fisher r-z transform

$$FZ\left(r_{ij}(s)\right) \triangleq \frac{1}{2}\ln\left(\frac{1+r_{ij}(s)}{1+r_{ij}(s)}\right)$$

$\mu(s)$ and $\sigma(s)$ represent the mean and standard deviation of the total $\frac{M(M-1)}{2}$ different pairs of FZ$(r_{ij}(s))$, separately. Therefore, we obtained N/L dWFC's networks for each subject. Because of the expensive computation, we used a two-steps clustering process to reduce the cost of the clustering algorithm. The dWFC's calculated from all the time windows of each subject are grouped into sub-datasets for community clustering. The similarity matrix was presented by the Pearson correlation coefficient between any pair of dynamic dWFC's for further states detection.

Community Detection of Signed Graph

Each dWFC is considered as a vertex in graph theory. The community clustering algorithm assigns a graph with n vertices into c communities $\sigma_i \in \{1, 2, \ldots, c\}$; i.e., each node was assigned to a community σ_i, where $i = 1, 2, \ldots, n$. Q-modularity of a weighted graph is defined as the edge weights within the community minus the expected edge weights of them (Leicht and Newman, 2008); i.e., $Q = \frac{1}{m}\sum_{i,j}(A_{i,j} - p_{i,j})\,\delta_{i,j}$, where $\delta_{i,j} = 1$ if $\sigma_i = \sigma_j$ and 0 otherwise; $p_{i,j} = k_i k_j / m$ represents the expected edge weight between i and vertex j; m is total the weight of all vertexes. A is adjacent matrix, where $A_{i,j}$ is the exact edge weight between vertex i and vertex j. By maximization of the Q-modularity, the community structure is determined with dense connections as an intra-community feature, while the sparse connections as inter-community features. As declared above, it is natural to use the similarity matrix, calculated from Pearson correlation coefficient of all pairs of dWFC's, as the adjacent matrix in community clustering. In this study, the adjacent matrix A is a signed weighted matrix, and we employ an approach based on an extended signed Q-modularity of the graph (Lu et al., 2017). The graph is divided into two graphs composed by positive edges and negative edges, respectively, represent by A^+ and A^-, where $A^+_{i,j} \geq 0$ and $A^-_{i,j} \leq 0$. The extended signed Q-modularity equals (Lu et al., 2017): (i) the fraction of edge weights, of which both head and tail nodes fall within the same community, minus (ii) the expected value of the edge weights of a random graph that follows the same positive weight degree distribution of the intrinsic graph, plus (iii) the expected value of the edge weights of a random graph that follows the same negative weight degree distribution of this intrinsic graph. This can be formulated as

$$Q = \frac{1}{2m}\sum_{i,j}\left(A_{i,j} - p^+_{i,j} + p^-_{i,j}\right)\delta_{i,j}$$

m is the sum of the absolute values of elements of the matrix A. $p^{\pm}_{i,j}$ stands for the expected coupling probability between vertex i and vertex j based on positive and negative coupling, respectively, represented by $A^{\pm}$. **Figure 2** illustrates the examples of the community structure in the "weighted" and "signed weighted" graph. The fast community detection algorithm (CDA) is used in maximize Q-modularity (Le Martelot and Hankin, 2013). The code from http://www.elemartelot.org/index.php/programming/cd-code was modified for handling of signed weighted edges.

Two-Steps Community Clustering of dWFC's for Large Data-Set

The correlation coefficient for each pair of dWFC's for an individual subject was computed as the similarity index for community detection. Ideally the community detection was performed across all subjects and time. However, the computation is extremely high when the subject population is large. In consideration of reducing the memory footprint and calculation time, this stage was developed in two steps due to the large amount of dWFC's (**Figure 3**). Firstly, all the dWFC's were separated into many sub-groups in chronological order such that each subject assigned a number of dWFC's to each given group, denoted by S. That is, there were S dWFC's from each subject in each group. The number of groups equals to the total number of dWFC's of each subject divided by the amount in each group, i.e., $\frac{N}{LS}$. The clustering algorithm was applied

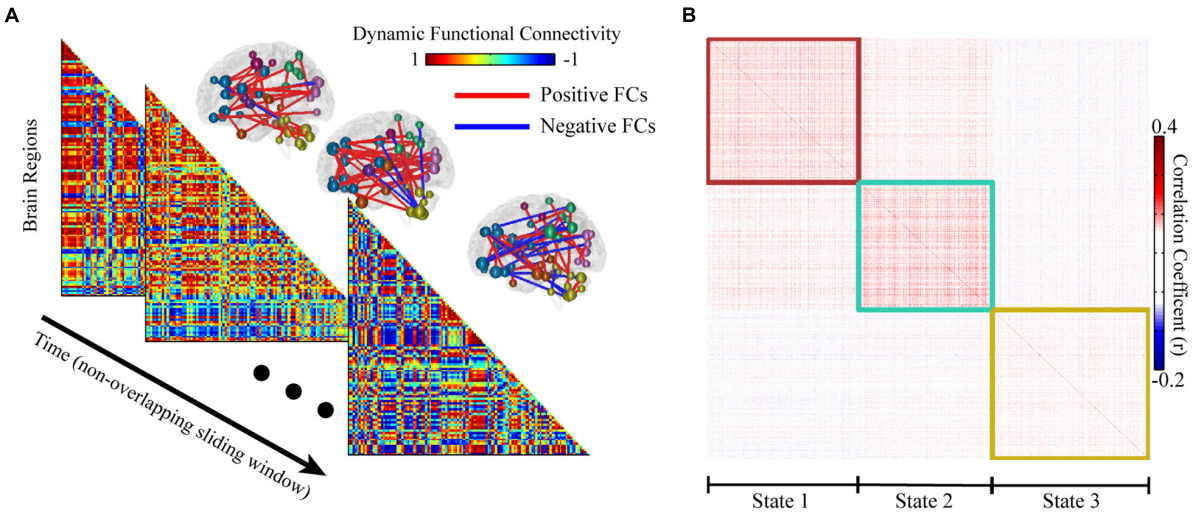

FIGURE 1 | Sliding window based whole functional connectivity (WFC). **(A)** The whole brain dynamic functional connectivity matrix was computed with 14.4 s non-overlapping sliding window (length of 20 time points). The corresponding top 100 significant FCs are shown for illustration at upper right of the matrix. **(B)** An example of the community clustering results across time and subjects. The similar (reoccurred) network patterns were clustered into 3 modules, representing 3 states. The similarity of dynamic functional connectivity was defined as their Pearson correlation coefficient.

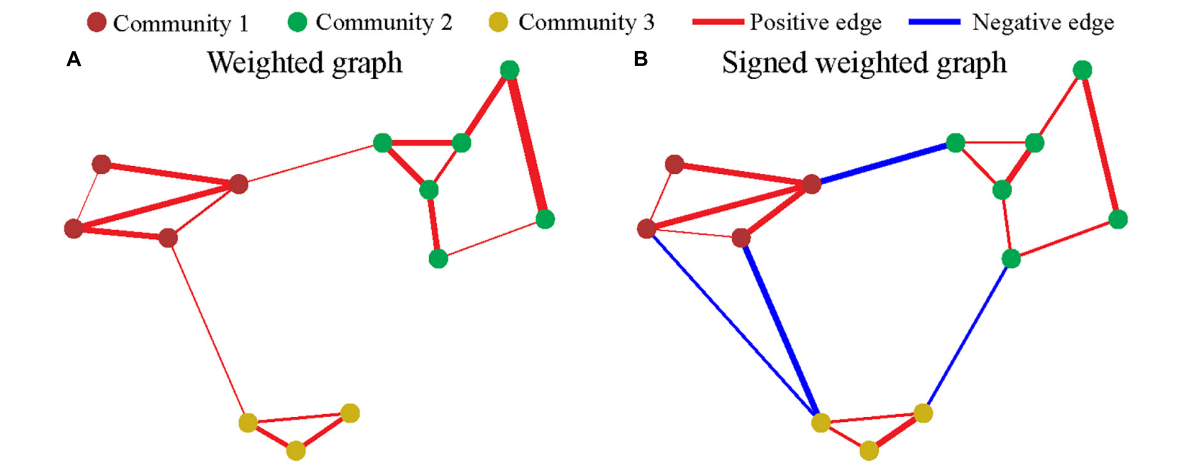

FIGURE 2 | Community in graph. Each dot represents a vertex (node), and the color of nodes represent the community. Each line represents an edge, and the width and color represent the weighting and sign, respectively. **(A)** The community of weighted graph. **(B)** The community of signed weighted graph.

separately in each group, and the cluster centroids (mean of dWFC's within a cluster) were kept. Next, all the cluster centroids extracted from different groups could be further clustered by applying the community detection on the correlation matrix of cluster centroids. We also randomly selected $\frac{N}{LS}$ samples from 194880 dWFC samples (60 windows×4 sessions×812 subjects) into a group for 100 times. To test the stability and similarity of the clustering results from each group, we compared the clustering centroids obtained in random groups with those obtained in chronological groups, regardless of its sampling method (**Figure 4A**). Finally, we used the Davies–Bouldin index (DBI) (Davies and Bouldin, 1979), a well-known clustering quality measure by averaging the maximal similarity between each cluster and all other clusters, as a metric for evaluating the clustering performance both in step 1 (for dWFC's in each group) and step 2 (for centroids from different groups). The smaller the index is, the better the clustering result is. Furthermore, we also used k-means algorithm to compare the rationality of the number of states with our method. For each group, we fixed the number of clusters as K from 1 to 6, and set 100 different initial values to detect the best partition with the minimal intra-class distance.

Detection of Connectivity States

After two step clustering, all of the dWFC's were assigned to the corresponding communities, which we defined the "states" here, according to their cluster centroids. The occurrence, transition rate, and mean lifetime of these states were calculated as dynamic parameters for all WFC's in MR sessions (Ryali et al., 2016). The

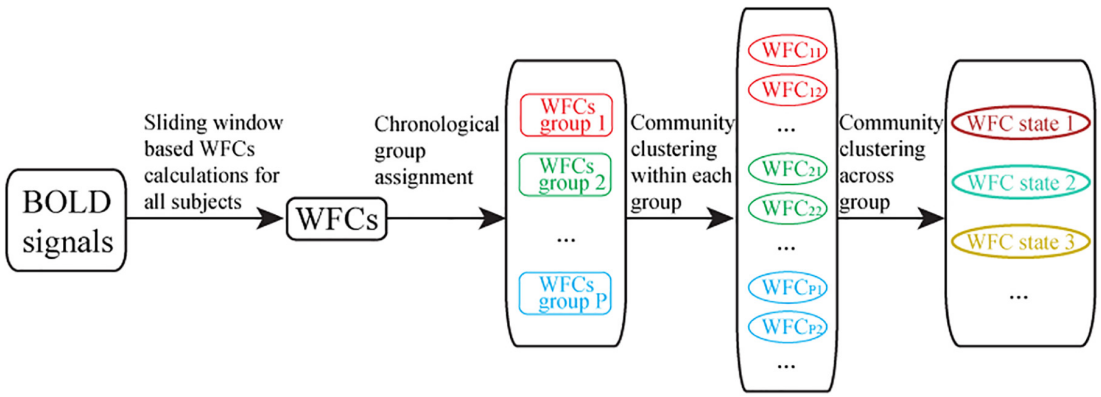

FIGURE 3 | Flowchart of two-steps community clustering of dynamic whole brain function connectivity. (1) The extraction of dynamic whole brain functional connectivity based on sliding window; (2) Random group assignment for community clustering, where each group consists of a number of dWFC's from all subject; (3) Community clustering results within each group, and the cluster centroids (averaged dWFC of the same state in each group) were preserved; (4) Final community clustering for the cluster centroids obtained from groups.

features of corresponding WFC communities were computed by averaging all dynamic WFC's from each community, denoted as WFC-C$_i$. Here we define the "feature score" by computing the correlation coefficient between WFC-C$_i$ and a given WFC, and the highest feature score among the states could predict the corresponding state.

RESULTS

The Three States of Dynamic Whole-Brain Functional Connectivity

We applied our method in R-fMRI data from 812 healthy adults released by HCP to estimate the functional network connectivity states. The AAL2 atlas was considered first so that the number of regions M was 120. The length of the time series N was 4800. We set $L = 20$ and the influence of window length had been illustrated in **Supplementary Figure S1**. We set $S = 5$ due to the large computation consumption and we finally obtained 48 groups (a larger S could help to reduce the inconsistency between groups, see **Supplementary Figure S1**). The WFC's within a community follows a common variation trend (positive correlation, **Figure 1B**) while those from different communities do not, or even follow a reversed variation trend (negative correlation). Noted that cluster centroids extracted in step 1 are distinctly divided into three communities (**Figure 4A**), both for the chronological groups and random groups, which revealed high resemblance of clustering results between groups. Thus, each WFC in a given time window of a given subject could be assigned to one of the three WFC state. The feature of the corresponding WFC community (WFC-C) was calculated by averaging all dynamic WFC's from each community; and we computed the feature score among the three WFC-C's to represent the predicted state for the original WFC's. The distribution of the matching rate between the clustering states and the predicted states was 93.3% on average (**Figure 4D**), which may be helpful to detect the state for an unknown network without performing the clustering. For dynamic parameters, the state 3 showed the highest occurrence, whereas the state 2 showed the lowest occurrence (**Figure 4B**). The transition between state 1 and state 3 showed the most frequent rate (**Figure 4C**). There was no difference in mean lifetime that the three states had an averaged mean lifetime of 24.8 s for state 1, 25.1 s for state 2, and 25.9 s for state 3.

The Evaluation of the Number of States

The k-means algorithm was used to compare with our method (**Figure 5A**). The DBI was used to evaluate the clustering results of both steps. The mean DBI of 48 groups reached to the minimum of 9.58 while $K = 3$ in step 1 (**Figure 5B**), showing a better clustering result for small groups compared to CDA (the mean DBI = 9.74). However, the DBI of k-means centroids of $K = 3$ also achieved the optimal clustering performance in step 2 with the minimum of 0.54 (**Figure 5C**), whereas DBI of community centroids reached a smaller value of 0.52, a better result of overall clustering across groups. Both of the results in two steps indicated that the number of 3 clusters was the best for categorization of dWFC's states.

Features of the Whole-Brain Functional Connection States

The AAL2 regions were assigned to Yeo's seven functional modules according to the top ratio (the percentage of voxels of specific region within each network) (Yeo et al., 2011). Cerebellum and subcortical regions are added as two additional modules. **Figure 6** illustrates the top 200 FC's in the three WFC-C's with functional modules, and the transition rates among states from HCP data. For state 1 (WFC-C$_1$), the highest FC's mainly include functional links both within and across visual, somatomotor, attention and cerebellar (posterior lobe) modules. The highest FC's in WFC-C$_2$ were similar with WFC-C, but FC's linking limbic, default mode and frontoparietal

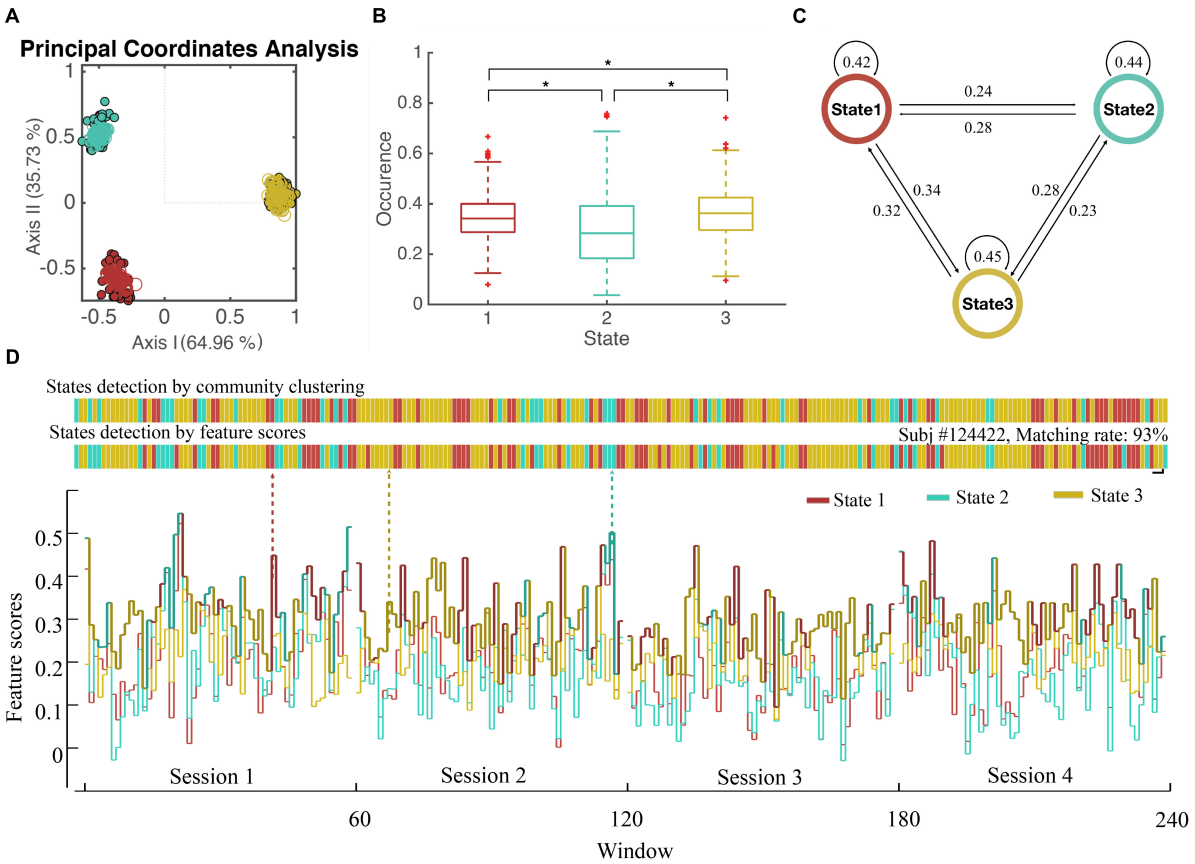

FIGURE 4 | State Detection of Dynamical WFC. **(A)** The scatter plot of WFC's in principal coordinate analysis. Each point represents a cluster centroid (the averaged WFC's of the same community) detected in step 1. (Dots represent centroids in chronological groups and circles represent random groups) Distance between WFC points is defined by 1-correlation$_{wfc-wfc}{}^2$, where principal coordinate analysis projects those WFC points into 2D spaces while preserved the original distance as much as possible. **(B)** The boxplot of the occurrence of three detected states for all subjects and the *p*-value of two-sample *t*-test between the occurrence of different states. **(C)** The transition rate between three detected states. **(D)** The states of dynamic functional connectivity for a single subject (subject #124422 as an example) were detected based on individual community clustering and feature scores. The states show in colors according to the WFC communities in **(A)**.

modules were more involved whereas the cerebellum, sensory and attention modules were less involved. In WFC-C_3, the FC's linking default mode, limbic, and cerebellum were more involved, whereas somatomotor, dorsal, ventral attention, and visual modules were much less so, compared to WFC-C_1 and WFC-C_2.

Robustness of dWFC's States Across Window Lengths

The clustering result is independent of window length (**Supplementary Figure S2**), shown by the detection of dWFC's states with various window lengths among 10, 20, 30, 40, and 50. The averaged dWFC's in the same community had a high level of similarity that their Pearson correlation were close to 1, seen from the diagonal elements of each 3 × 3 matrix (**Supplementary Figure S2B**). Whereas, comparing the off-diagonal elements between correlation matrices of different window size, we still observed a trend that the differences between three averaged dWFC's would reduce as the window length increased.

The Influence of Parcellation Methods

We also detected three communities using dWFC's calculated from two different additional atlases, the Shen-268 atlas (Shen et al., 2013) and Power 264 atlas (Power et al., 2011; **Supplementary Figure S3**). The results showed that the number of dynamic states was independent to the parcellation schemes. However, the detected state in each window was different across atlases. By matching the most overlapping states, the averaged matching rate of states extracted between the AAL2 Shen-268 was 82.7%, and the Power was 66.9%. Besides, we also randomly relocate the state sequence of the samples, the matching rate was significantly lower than the estimated matching rate ($p < 0.0001$), indicating that the states obtained across the atlases were similar but not identical.

DISCUSSION

We proposed a new method to categorize and track time-varying networks in R-fMRI studies. It involves two-step community

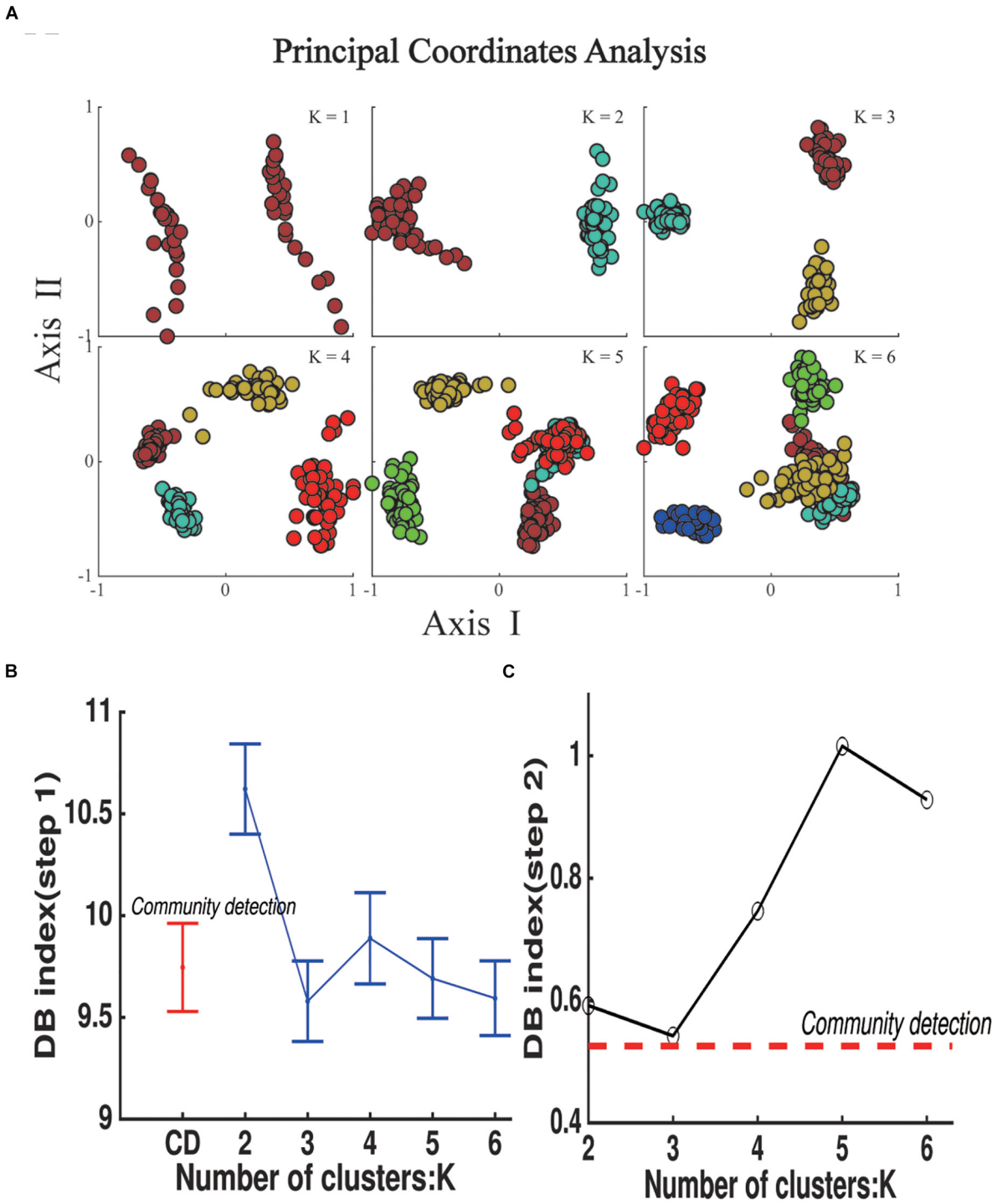

FIGURE 5 | State Detection results using k-means clustering algorithm in step 1. **(A)** The scatter plot of k means centroids obtained in step 1 in principal coordinate analysis, K represents the number of the clusters in each group and N represents the number of communities detected by Modularity-based algorithm in step 2. **(B)** DB index for the clustering results for groups in step 1. Dots represent the mean value for 48 groups and error bars represent standard deviation. **(C)** DB index for the clustering results of k means centroids (blue polygon) and community centroids (red dash line).

detection, which is computing efficient and provides robust results in large data set application. In recent years, various methods were proposed to capture time-varying networks in R-fMRI studies (Pinotsis et al., 2013; Calhoun et al., 2014; Cavanna et al., 2017; Preti et al., 2017). Essentially, it involves two main considerations.

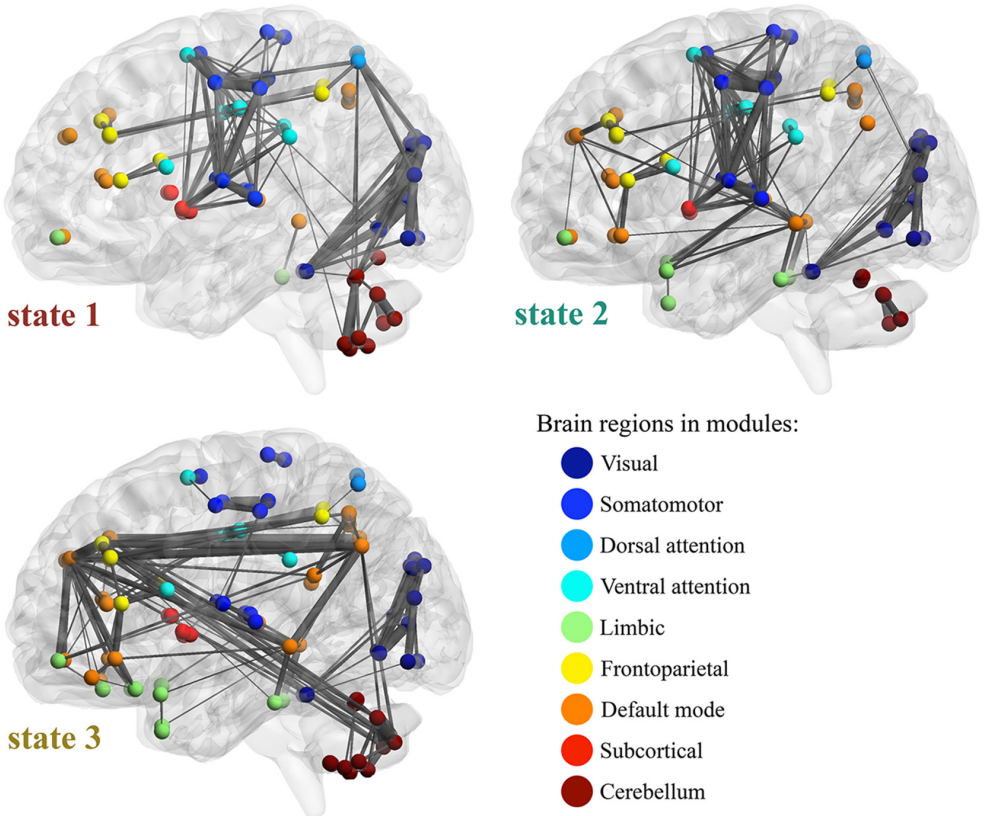

FIGURE 6 | Feature of WFC states. Top 200 functional connections are illustrated in each WFC states, with the Yeo's 7 functional modules, subcortical and cerebellar regions. The width of the connections represents the connectivity strength. The transition rates among states are indicated by the arrows. For state 1 (WFC-C1), the high FCs in mainly includes functional links both within and across visual, somatomotor, attention and cerebellar (posterior lobe) modules. WFC-C2 was similar with WFC-C1 in those high FCs, however, the FCs in WFC-C2 between cerebellum and the sensory and attention modules were decreased, and higher connections within and across limbic, default mode and frontoparietal modules, in which medial temporal gyrus (MTG), Superior temporal gyrus of temporal pole (TPOsup), inferior temporal gyrus (ITG), inferior parietal gyrus (IPG), dorsolateral superior frontal gyrus (SFG) and medial superior frontal gyrus (SFG medial) are highly involved. In WFC-C3, FCs within sensory and attention modules are still active, but FCs across those modules are decreased. Another feature of WFC-C3 high values of FCs in default network modules, as well as FCs across modules including default, limbic and cerebellum networks. MTG, precuneus (PCUN), angular gyrus (ANG), middle frontal gyrus (MFG), superior parietal gyrus (SPG), and Crus1/Crus2 in cerebellum are highly involved.

The first consideration, what is the best feature to represent the time-varying networks. For example, ICA could be used to reveal the spatial-temporal structure of the fMRI signals in either signal subject or group of subjects (Calhoun et al., 2009). Time and frequency decomposition of regional coherence was also calculated through cross wavelet transform (Yaesoubi et al., 2015). However, most common method is sliding window based FCs (Hutchison et al., 2013; Thompson, 2018; Reinen et al., 2018), as brain function are accomplished by the interplay of a set of brain areas rather than a specific region (De la Iglesia-Vaya et al., 2013). A recent study questioned the validity, stability and statistics significance for various dFC pattern detecting method (Hindriks et al., 2016). The optimal window size remains unknown. To track rapid temporal changes in FC, shorter window is necessary for high temporal resolution; while FC calculation requires longer window for robustness and statistics significance. It may need further studies to address this question through our method. We calculated FC the on various window sizes to test the reliability of the results. In our application on HCP data set with high tempo-spatial solution resolution, the three whole-brain dFC states are stable and independent of sessions and window lengths. The robust results suggest that our method could be helpful to establishing the golden standard in dWFC's tracking in R-fMRI analysis (Shakil et al., 2016).

The second consideration is mainly a machine learning problem or a clustering problem. Lacking prior knowledge about the categorization of dynamical brain states, an unsupervised learning method especially clustering analysis is more suitable for detecting dynamical brain states. K-means, a prototype-based clustering method, is the most widely used in clustering analysis for its convenience and computing speed. However, it needs to set the number of states and initial values in advance and requires a relatively balanced data structure for good performance. Though many different methods have been applied, the number of states in the brain still remains unknown. For example, two brain states were revealed as a

within-network state and a between-network state in both healthy and Parkinson disease patients (Kim et al., 2017). Di and Biswal (2015) separated out triple brain states: salience-, default-, and motor- networks. Seven brain states have also been discovered in work by Allen et al. (2014) through group ICA based-FC and k-means clustering. Further, as many as 13 clusters of innovation-driven co-activation patterns were detected in work (Karahanoğlu and Van De Ville, 2015). Another important issue of clustering analysis is the measure of distance or similarity between samples. Euclidean distance is an intuitive and commonly used distance. However, the Euclidean distance of WFC depends largely on the overall level of the functional connectivity, which could be affected by measurements, individual difference. The Pearson correlation induces a distance that remains unchanged and is equivalent to the Euclidean distance after normalization of the data. That is, $1 - corr(x, y) = \| x - y \|^2/2m$, where $x - y$ represents the Euclidean distance between sample x and y and m is the dimension of data. It measures the consistency of the sequence of FCs within the network between two WFC's that will not be influenced by the overall functional connectivity value. Therefore, we used Pearson correlation to measure the similarity but also normalized each dynamical brain network for some following analysis of the detected brain states.

Due to the large sample size, we complete the clustering in two steps that we calculate the cluster centroids in each group and combine these results by clustering all the centroids. But it brings up a problem to select an appropriate state number K for each group and deal with the differences of results caused by different initial values. Hierarchical clustering can detect the hierarchical relationship in the data and it does not need to set the initial values. But it is more impossible to afford the large computation cost, because the computational complexity of hierarchical clustering is at least $O(n^2)$, which n represents the amount of dWFC. Moreover, the two-steps clustering strategy is not suitable for hierarchical clustering for it may break or disrupted the hierarchy of data when dividing samples into several groups and leave a tricky problem of matching samples at the same level from different groups. PCA helps to discover and describe different FC patterns through an appropriate number of PCs called "eigenconnectivities," while it is still a question how to classify dWFC's into different states so that we can track the dynamical changes of whole brain network structure. Hidden Markov chain based methods are usually performed directly on the bold signal time series of the brain rather than functional connectivity structure, they require a pre-given form of the probability distribution of each state as well as the number of states. Lacking a comprehensive understanding of the underlying mechanism of dWFC's states, we categorize the dWFC's through community detection methods based on the similarity of dWFC's pair, working in an unsupervised, data-driven fashion. Finally, by computing the feature score between networks (the similarity), we can easily estimate an unknown state of network into a specific state, without redundant clustering procedures. This is helpful for further studies of the dynamic networks.

By comparison with k-means clustering, our proposed method with two-step of CDA showed better superiority. On the one hand, the DBI showed that the best number of clustering was 3 with k-means, indicating the CDA could detect the optimal number for the states of dWFC's. On the other hand, compared to CDA, although k-means showed a smaller mean value of DBI for all groups in the first step, the larger DBI in the second step indicated longer distances between the centroids among groups, showing the weakness for the overall detection by the two step clustering method. According to the procedure of k-means algorithm, a possible reason might be that the k-means is sensitive to outliers (Hautamäki et al., 2005). When an outlier is added to a given cluster, the center of the cluster will move toward to the outlier, resulting in the change of the criteria to update the members of this cluster. Finally, the members of the cluster are more likely close to the outliers. In contrast, the community clustering showed better robustness than k-means. According to the fast community detection algorithm (Le Martelot and Hankin, 2013), an outlier alone can little influence the update of the community structure in each iteration because of its small degree, and therefore the community among groups had more stable and similar structures, showing its advantage for subdividing a large sample size into several groups of small samples.

By taking advantage of the higher temporal resolution in HCP, we can reduce the window to less than 10 s while maintaining sufficient samples to calculate correlation coefficients. However, it still remains unclear as to what the optimal window for detecting dynamical brain states is. Although community clustering methods are robust for summarizing the generality of dFC's independent of time and subjects; this method might not be sensitive to individual heterogeneities. Further studies are needed to address whether there might be sub states within the three dFC states, i.e., to identify the hierarchical structure of the dynamic FC's. The self-converged community clustering method to detect the connectivity states, does not rely on the appearance of a clear gap between any two individual dFC's from various brain states (Leicht and Newman, 2008). It is a more appropriate clustering method while few are known in dWFC states. Besides, the two-steps community clustering protocol for large R-fMRI data sets is robust and computing efficient. A distinct gap between community centroids of different states, regardless of which groups they come from, showing that our method performed stably in each group. These results revealed that there were three states existed for all the dWFC across subjects and time, with the robustness with various window lengths and parcellations. Of note, the states of dWFC's were not identical across parcellations, because of the location of regions, region size, including/excluding cerebellum, and the extracted time series were different, resulting in different dWFC's across atlases. The parcellation scheme may affect the dWFC's with specific functions (e.g., involving cerebellum or not), and the diversity of states among atlases may be further studied.

ETHICS STATEMENT

The WU-Minn HCP Consortium obtained full informed consent from all participants, and research procedures and ethical guidelines were followed in accordance with the Institutional Review Boards (IRB) of Washington University in St. Louis, MO, United States (IRB #20120436).

AUTHOR CONTRIBUTIONS

LZ and CYL designed the research. QZ and LZ performed the research. QZ, LZ, and CYL analyzed the data. QZ, LZ, CYL, and JF wrote the manuscript.

FUNDING

LZ was supported by the China Postdoctoral Science Foundation (2016M591590). JF was a Royal Society Wolfson Research Merit Award holder. JF was partially supported by the key project of the Shanghai Science and Technology Innovation Plan (Nos. 15JC1400101 and 16JC1420402), the National Natural Science Foundation of China (Grant Nos. 71661167002 and 91630314), and the 111 Project (No. B18015). CYL was partially supported by the National Key Research and Development Program of China (No. 2018YFC0910503), the Young Scientists Fund of the National Natural Science Foundation of China (No. 81801774), and the Natural Science Foundation of Shanghai (No. 18ZR1403700). The research was also partially supported by the Shanghai AI Platform for Diagnosis and Treatment of Brain Diseases, the Projects of Zhangjiang Hi-Tech District Management Committee, Shanghai (Nos. 2016-17), the key project of Shanghai Science and Technology (No. 16JC1420402), the Base for the Introducing Talents of Discipline to Universities (No. B18015), and Shanghai Municipal Science and Technology Major Project (No. 2018SHZDZX01) and ZJLab.

SUPPLEMENTARY MATERIAL

The Supplementary Material for this article can be found online at: https://www.frontiersin.org/articles/10.3389/fnins.2019.00685/full#supplementary-material

REFERENCES

Allen, E. A., Damaraju, E., Plis, S. M., Erhardt, E. B., Eichele, T., and Calhoun, V. D. (2014). Tracking whole-brain connectivity dynamics in the resting state. *Cereb. Cortex* 24, 663–676. doi: 10.1093/cercor/bhs352

Baker, A. P., Brookes, M. J., Rezek, I. A., Smith, S. M., Behrens, T., Probert Smith, P. J., et al. (2014). Fast transient networks in spontaneous human brain activity. *Elife* 3:e01867. doi: 10.7554/eLife.01867

Calhoun, V. D., Liu, J., and Adali, T. (2009). A review of group ICA for fMRI data and ICA for joint inference of imaging, genetic, and ERP data. *Neuroimage* 45, S163–S172. doi: 10.1016/j.neuroimage.2008.10.057

Calhoun, V. D., Miller, R., Pearlson, G., and Adalı, T. (2014). The chronnectome: time-varying connectivity networks as the next frontier in fMRI data discovery. *Neuron* 84, 262–274. doi: 10.1016/j.neuron.2014.10.015

Cavanna, F., Vilas, M. G., Palmucci, M., and Tagliazucchi, E. (2017). Dynamic functional connectivity and brain metastability during altered states of consciousness. *Neuroimage* 180, 383–395. doi: 10.1016/j.neuroimage.2017.09.065

Davies, D. L., and Bouldin, D. W. (1979). A cluster separation measure. *IEEE Trans Pattern Anal. Mach. Intell.* 1, 224–227. doi: 10.1109/tpami.1979.4766909

De la Iglesia-Vaya, M., Molina-Mateo, J., Escarti-Fabra, J. M., Kannan, S. A., and Marti-Bonmati, L. (2013). "Brain connections – resting state fmri functional connectivity," in *Novel Frontiers of Advanced Neuroimaging*, ed. K. N. Fountas (London: InTech).

Di, X., and Biswal, B. B. (2015). Dynamic brain functional connectivity modulated by resting-state networks. *Brain Struct. Funct.* 220, 37–46. doi: 10.1007/s00429-013-0634-633

Friston, K. J. (2011). Functional and effective connectivity: a review. *Brain Connect.* 1, 13–36. doi: 10.1089/brain.2011.0008

Glasser, M. F., Sotiropoulos, S. N., Wilson, J. A., Coalson, T. S., Fischl, B., Andersson, J. L., et al. (2013). The minimal preprocessing pipelines for the human connectome project. *Neuroimage* 80, 105–124. doi: 10.1016/j.neuroimage.2013.04.127

Hautamäki, V., Cherednichenko, S., Kärkkäinen, I., Kinnunen, T., and Fränti, P. (2005). "Improving K-means by outlier removal," in *Image Analysis Lecture Notes in Computer Science*, eds H. Kalviainen, J. Parkkinen, and A. Kaarna (Berlin: Springer), 978–987 doi: 10.1007/11499145_99

Hindriks, R., Adhikari, M. H., Murayama, Y., Ganzetti, M., Mantini, D., Logothetis, N. K., et al. (2016). Can sliding-window correlations reveal dynamic functional connectivity in resting-state fMRI? *Neuroimage* 127, 242–256. doi: 10.1016/j.neuroimage.2015.11.055

Hutchison, R. M., Womelsdorf, T., Allen, E. A., Bandettini, P. A., Calhoun, V. D., Corbetta, M., et al. (2013). Dynamic functional connectivity: promise, issues, and interpretations. *Neuroimage* 80, 360–378. doi: 10.1016/j.neuroimage.2013.05.079

Karahanoğlu, F. I., and Van De Ville, D. (2015). Transient brain activity disentangles fMRI resting-state dynamics in terms of spatially and temporally overlapping networks. *Nat. Comms.* 6:7751. doi: 10.1038/ncomms8751

Kim, J., Criaud, M., Cho, S. S., Díez-Cirarda, M., Mihaescu, A., Coakeley, S., et al. (2017). Abnormal intrinsic brain functional network dynamics in Parkinson's disease. *Brain* 140, 2955–2967. doi: 10.1093/brain/awx233

Kopell, N. J., Gritton, H. J., Whittington, M. A., and Kramer, M. A. (2014). Beyond the connectome: the dynome. *Neuron* 83, 1319–1328. doi: 10.1016/j.neuron.2014.08.016

Le Martelot, E., and Hankin, C. (2013). Fast multi-scale detection of relevant communities in large-scale networks. *Comput. J.* 56, 1136–1150. doi: 10.1093/comjnl/bxt002

Leicht, E. A., and Newman, M. E. J. (2008). Community structure in directed networks. *Phys. Rev. Lett.* 100:118703. doi: 10.1103/PhysRevLett.100.118703

Leonardi, N., Richiardi, J., Gschwind, M., Simioni, S., Annoni, J.-M., Schluep, M., et al. (2013). Principal components of functional connectivity: a new approach to study dynamic brain connectivity during rest. *Neuroimage* 83, 937–950. doi: 10.1016/j.neuroimage.2013.07.019

Lu, W., Chen, B., Jin, Z., Waxman, D., and Feng, J. (2017). "Establishing the community structure of signed interconnected graph in data," in *Proceedings of the 2017 36th Chinese Control Conference*, (Dalian: IEEE), 11127–11132.

Pinotsis, D. A., Hansen, E., Friston, K. J., and Jirsa, V. K. (2013). Anatomical connectivity and the resting state activity of large cortical networks. *Neuroimage* 65, 127–138. doi: 10.1016/j.neuroimage.2012.10.016

Power, J. D., Cohen, A. L., Nelson, S. M., Wig, G. S., Barnes, K. A., Church, J. A., et al. (2011). Functional network organization of the human brain. *Neuron* 72, 665–678. doi: 10.1016/j.neuron.2011.09.006

Preti, M. G., Bolton, T. A., and Van De Ville, D. (2017). The dynamic functional connectome: state-of-the-art and perspectives. *Neuroimage* 160, 41–54. doi: 10.1016/j.neuroimage.2016.12.061

Reineberg, A. E., Andrews-Hanna, J. R., Depue, B. E., Friedman, N. P., and Banich, M. T. (2015). Resting-state networks predict individual differences in common and specific aspects of executive function. *Neuroimage* 104, 69–78. doi: 10.1016/j.neuroimage.2014.09.045

Reinen, J. M., Chen, O. Y., Hutchison, R. M., Yeo, B. T. T., Anderson, K. M., Sabuncu, M. R., et al. (2018). The human cortex possesses a reconfigurable dynamic network architecture that is disrupted in psychosis. *Nat. Commun.* 9:1157. doi: 10.1038/s41467-018-03462-y

Robinson, L. F., Atlas, L. Y., and Wager, T. D. (2015). Dynamic functional connectivity using state-based dynamic community structure: method and application to opioid analgesia. *Neuroimage* 108, 274–291. doi: 10.1016/j.neuroimage.2014.12.034

Rolls, E. T., Joliot, M., and Tzourio-Mazoyer, N. (2015). Implementation of a new parcellation of the orbitofrontal cortex in the automated anatomical labeling atlas. *Neuroimage* 122, 1–5. doi: 10.1016/j.neuroimage.2015.07.075

Ryali, S., Supekar, K., Chen, T., Kochalka, J., Cai, W., Nicholas, J., et al. (2016). Temporal dynamics and developmental maturation of salience, default and central-executive network interactions revealed by variational bayes hidden markov modeling. *PLoS Comput. Biol.* 12:e1005138. doi: 10.1371/journal.pcbi.1005138

Shakil, S., Lee, C.-H., and Keilholz, S. D. (2016). Evaluation of sliding window correlation performance for characterizing dynamic functional connectivity and brain states. *Neuroimage* 133, 111–128. doi: 10.1016/j.neuroimage.2016.02.074

Shen, X., Tokoglu, F., Papademetris, X., and Constable, R. T. (2013). Groupwise whole-brain parcellation from resting-state fMRI data for network node identification. *Neuroimage* 82, 403–415. doi: 10.1016/j.neuroimage.2013.05.081

Tavor, I., Parker Jones, O., Mars, R. B., Smith, S. M., Behrens, T. E., and Jbabdi, S. (2016). Task-free MRI predicts individual differences in brain activity during task performance. *Science* 352, 216–220. doi: 10.1126/science.aad8127

Thompson, G. J. (2018). Neural and metabolic basis of dynamic resting state fMRI. *Neuroimage* 180, 448–462. doi: 10.1016/j.neuroimage.2017.09.010

Vidaurre, D., Smith, S. M., and Woolrich, M. W. (2017). Brain network dynamics are hierarchically organized in time. *Proc. Natl. Acad. Sci. U.S.A.* 114, 12827–12832. doi: 10.1073/pnas.1705120114

Yaesoubi, M., Allen, E. A., Miller, R. L., and Calhoun, V. D. (2015). Dynamic coherence analysis of resting fMRI data to jointly capture state-based phase, frequency, and time-domain information. *Neuroimage* 120, 133–142. doi: 10.1016/j.neuroimage.2015.07.002

Yeo, B. T. T., Krienen, F. M., Sepulcre, J., Sabuncu, M. R., Lashkari, D., Hollinshead, M., et al. (2011). The organization of the human cerebral cortex estimated by intrinsic functional connectivity. *J. Neurophysiol.* 106, 1125–1165. doi: 10.1152/jn.00338.2011

Zhang, J., Cheng, W., Liu, Z., Zhang, K., Lei, X., Yao, Y., et al. (2016). Neural, electrophysiological and anatomical basis of brain-network variability and its characteristic changes in mental disorders. *Brain* 139, 2307–2321. doi: 10.1093/brain/aww143

Conflict of Interest Statement: The authors declare that the research was conducted in the absence of any commercial or financial relationships that could be construed as a potential conflict of interest.

frontiers in Neuroscience

ORIGINAL RESEARCH
published: 23 August 2019
doi: 10.3389/fnins.2019.00803

Dynamics of Segregation and Integration in Directional Brain Networks: Illustration in Soldiers With PTSD and Neurotrauma

D. Rangaprakash[1,2], Michael N. Dretsch[3,4,5], Jeffrey S. Katz[1,5,6,7], Thomas S. Denney Jr.[1,5,6,7] and Gopikrishna Deshpande[1,5,6,7,8,9]**

[1] Department of Electrical and Computer Engineering, AU MRI Research Center, Auburn University, Auburn, AL, United States, [2] Departments of Radiology and Biomedical Engineering, Northwestern University, Chicago, IL, United States, [3] U.S. Army Aeromedical Research Laboratory, Fort Rucker, AL, United States, [4] U.S. Army Medical Research Directorate-West, Walter Reed Army Institute for Research, Joint Base Lewis–McChord, WA, United States, [5] Department of Psychology, Auburn University, Auburn, AL, United States, [6] Alabama Advanced Imaging Consortium, Auburn, AL, United States, [7] Center for Neuroscience, Auburn University, Auburn, AL, United States, [8] Center for Health Ecology and Equity Research, Auburn University, Auburn, AL, United States, [9] Department of Psychiatry, National Institute of Mental Health and Neurosciences, Bengaluru, India

OPEN ACCESS

Edited by:
Nanyin Zhang,
The Pennsylvania State University,
United States

Reviewed by:
Tianming Liu,
University of Georgia, United States
Xin Di,
New Jersey Institute of Technology,
United States
Meiling Li,
Athinoula A. Martinos Center for Biomedical Imaging, Harvard Medical School, United States

***Correspondence:**
D. Rangaprakash
rzd0016@auburn.edu
Gopikrishna Deshpande
gopi@auburn.edu

Specialty section:
This article was submitted to Brain Imaging Methods, a section of the journal Frontiers in Neuroscience

Received: 14 December 2018
Accepted: 17 July 2019
Published: 23 August 2019

Citation:
Rangaprakash D, Dretsch MN, Katz JS, Denney TS Jr and Deshpande G (2019) Dynamics of Segregation and Integration in Directional Brain Networks: Illustration in Soldiers With PTSD and Neurotrauma. Front. Neurosci. 13:803. doi: 10.3389/fnins.2019.00803

Brain functioning relies on various segregated/specialized neural regions functioning as an integrated-interconnected network (i.e., metastability). Various psychiatric and neurologic disorders are associated with aberrant functioning of these brain networks. In this study, we present a novel framework integrating the strength and temporal variability of metastability in brain networks. We demonstrate that this approach provides novel mechanistic insights which enables better imaging-based predictions. Using whole-brain resting-state fMRI and a graph-theoretic framework, we integrated strength and temporal-variability of complex-network properties derived from effective connectivity networks, obtained from 87 U.S. Army soldiers consisting of healthy combat controls (n = 28), posttraumatic stress disorder (PTSD; n = 17), and PTSD with comorbid mild-traumatic brain injury (mTBI; n = 42). We identified prefrontal dysregulation of key subcortical and visual regions in PTSD/mTBI, with all network properties exhibiting lower variability over time, indicative of poorer flexibility. Larger impairment in the prefrontal-subcortical pathway but not prefrontal-visual pathway differentiated comorbid PTSD/mTBI from the PTSD group. Network properties of the prefrontal-subcortical pathway also had significant association (R^2 = 0.56) with symptom severity and neurocognitive performance; and were also found to possess high predictive ability (81.4% accuracy in classifying the disorders, explaining 66–72% variance in symptoms), identified through machine learning. Our framework explained 13% more variance in behaviors compared to the conventional framework. These novel insights and better predictions were made possible by our novel framework using static and time-varying network properties in our three-group scenario, advancing the mechanistic understanding of PTSD and comorbid mTBI. Our contribution has wide-ranging applications for network-level characterization of healthy brains as well as mental disorders.

Keywords: functional MRI, network dynamics, complex network modeling, effective connectivity, dynamic connectivity, posttraumatic stress disorder, mild traumatic brain injury, machine learning

INTRODUCTION

The dynamic abilities of the human brain are attributed to its highly interconnected neural architecture. Functional MRI (fMRI) connectivity modeling is popularly employed to study interrelationships between brain regions at the systems-level. However, fMRI connectivity is limited in that it can characterize only pairwise relationships (i.e., bivariate). To characterize connection ensembles (Rubinov and Sporns, 2010), and not just connection pairs, strategies beyond traditional connectivity modeling, such as complex-network modeling (Rubinov and Sporns, 2010) using graph-theoretic techniques, are useful. This approach makes use of individual connectivity weights as well as the pattern in which these connections coexist, to make various inferences on the network structure.

Functional Segregation

A graph comprises of a set of nodes (brain regions) that are interconnected by edges (connectivity weights), and network measures quantify different characteristics of the topology of such graphs. Rubinov and Sporns (2010) illustrate the applicability and interpretation of several complex-network measures in brain imaging. Among them, *functional segregation*, necessary for optimal specialized processing, informs about dense-connectedness within separate subnetworks. It quantifies whether the regions connected to a given node are connected amongst themselves, thus forming subnetworks wherein majority of the nodes are connected to every other node. For example, during altered consciousness, segregation is reduced, especially in the thalamus (Crone et al., 2013). In the current study, we employed transitivity (global whole-brain-level measure), clustering coefficient and local efficiency (both local node-level measures) to quantify segregation (Rubinov and Sporns, 2010).

Functional Integration

In contrast, functional integration captures the ease of interaction between segregated regions (Rubinov and Sporns, 2010). For example, there is elevated segregation in prefrontal and cerebellar subnetworks in attention-deficit hyperactivity disorder (ADHD), but lower integration between these subnetworks (Lin et al., 2014), indicative of characteristic attentional reaction-time deficits observed in this population. In the current study, we employed global efficiency (global measure), shortest path length, and edge betweenness (both local measures at connection-level) to quantify integration (Rubinov and Sporns, 2010). Although traditional connectivity identifies standalone aberrant connections in clinical groups, these measures of integration identify those connections that are not only important by themselves, but are also important for the rest of the connections in the network.

Graph Measures and Military Population

It has been extensively demonstrated that segregation and integration are disrupted in psychiatric disorders [for example, see (Yu et al., 2013; Rocca et al., 2014)]. Most report a narrow, but balanced relationship between them in healthy populations (called metastability) (Hellyer et al., 2015), which is impaired in neurologic and psychiatric disorders (Yu et al., 2013; Rocca et al., 2014). Using resting-state fMRI and our novel framework, we investigated network-level aberrations in soldiers with posttraumatic stress disorder (PTSD) and post-concussion syndrome (PCS) associated with documented mild traumatic brain injury(s) (mTBI). PCS is an outcome of mTBI, in which the individual presents persistent post-concussive symptoms 3 months' post-injury.

In military populations, there is considerable comorbidity between mTBI and PTSD (Hoge et al., 2008, 2009), often attributed to life-threatening events such as exposure to blast from improvised explosive devices (IEDs), which result in mTBI as well as psychological trauma. With the prevailing clinical approaches focusing on patient reporting, and with substantial overlapping symptoms between PTSD and PCS (Eierud et al., 2014), a better comprehension of the neurobiological-mechanistic basis for PTSD and PCS is imperative for improved diagnosis and treatment outcomes, and for making return-to-duty decisions. Prior fMRI works on comorbid PTSD and mTBI are limited (Spielberg et al., 2015), although its prevalence is considerably high in general society as well as military populations (Veterans, 2015). In the current study, we explored our novel framework involving functional segregation and integration in three groups: soldiers with elevated posttraumatic stress symptoms (PTSD group), PCS + PTSD (comorbid group sustaining both PTSD and PCS), and healthy combat controls. For the sake of disambiguation, we call complex-network modeling as "network-level," while connectivity modeling is termed "connectivity-level" and activation analysis as "region-level." Although several studies have identified region-level and connectivity-level aberrations in specific key prefrontal and subcortical regions in mTBI and PTSD (Simmons and Matthews, 2012), a thorough understanding of the aberrations of directional relationships and associated changes in network structure have not emerged from them. We address this limitation in this study.

Effective Connectivity

Graph-theoretic analysis begins from network graphs constructed using pairwise connections, which can be obtained through connectivity modeling. Although functional connectivity (FC) has been the predominant choice so far, we sought to investigate directional networks with causal relationships instead of co-activation (a non-directional entity). It has not been adequately explored, even though it is an equally important mechanism for network-level interactions. Causal connectivity has been discovered even in fMRI timescales (Roebroeck et al., 2005; Abler et al., 2006; David et al., 2008; Deshpande et al., 2011; Deshpande and Hu, 2012; Ryali et al., 2016; Rangaprakash et al., 2018a), indicating that identifying causal networks in addition to co-activation networks is important for a more extensive characterization. Further, PTSD and PCS are typically considered as prefrontal dysregulation disorders (Simmons and Matthews, 2012), meaning that prefrontal causal connectivity is compromised. This provided the impetus for us to further investigate directional connectivity. To our surprise, there have been hardly any fMRI studies

investigating effective connectivity (EC) in either PTSD or PCS or the comorbid condition.

Granger Causality

Granger causality (GC), an exploratory technique, was employed to quantify EC (Deshpande et al., 2010b). It is the most prevalent technique for deriving causal relationships in natural systems (Kirchgässner et al., 2012). Both recent simulations (Ryali et al., 2011; Wen et al., 2013) and experimental results, including optogenetics and electrophysiology (David et al., 2008; Katwal et al., 2013; Ryali et al., 2016; Wang et al., 2016), demonstrate that GC is reliable for drawing inferences regarding directional relationships between brain regions when used after deconvolving the hemodynamic response function (HRF) from fMRI data (as done in the current study). Several recent fMRI works have also employed this technique (Deshpande et al., 2013; Sathian et al., 2013; Grant et al., 2014; Lacey et al., 2014; Wheelock et al., 2014; Feng et al., 2015; Grant et al., 2015; Hutcheson et al., 2015; Bellucci et al., 2016).

Dynamic Connectivity

Most studies investigating fMRI connectivity assume connectivity as stationary over time, although static connectivity does not capture dynamic variations of connectivity. While an fMRI scan endures for several minutes, mental processes occur within a few milliseconds to a few seconds' time, implying that connectivity varies over the timescales of fMRI scans, and that those variations contain biologically relevant information (Hutchison et al., 2013), which are different from that contained in static connectivity (Jia et al., 2014). Recent works have found connectivity dynamics to be a unique and important marker of brain functioning (Hansen et al., 2015; Jin et al., 2017). Therefore, the current study utilized both static EC (SEC) and dynamic EC (DEC). Brain networks were constructed from strength (SEC) and temporal variability (DEC) of directional connectivity, using which we obtained strength and variability of segregation/integration measures, respectively. Such a characterization of dynamic network properties is one of the important novel contributions of this work. While dynamic connectivity has prevailed in neuroimaging for some time (Hutchison et al., 2013), for the first time we introduce dynamic modeling of segregation and integration in a novel framework.

Lower variability of connectivity over time is associated with both psychiatric and neurologic conditions (Garrett et al., 2013; Jia et al., 2014; Miller et al., 2016; Rashid et al., 2016; Rangaprakash et al., 2017a, 2018a), often corresponding to a lack of cognitive flexibility. Compromised behavioral performance is linked with reduced temporal variance of connectivity in both clinical and non-clinical populations (Sakoğlu et al., 2010; Jia et al., 2014; Rangaprakash et al., 2017a, 2018a). Such reduction is linked to impaired ability in dynamically adjusting to changing conditions (thoughts, behaviors, etc.). A healthy biological system is flexible in response to continual momentary changes within the internal and external milieu of the organism. In those terms, temporally "frozen" connectivity and/or complex-network properties point to compromised brain health. Such a characterization has been done in recent connectivity studies (Jia et al., 2014; Rangaprakash et al., 2017a). Higher variability of connectivity is also considered a marker of greater mental flexibility (Zhang et al., 2016).

Hypotheses

In this work, we extend these concepts to the reduced temporal variability (or rigidity) in network properties instead of individual connection strengths. We hypothesized that *PTSD and mTBI are characterized by altered strength and lower temporal variability of segregation and integration in directional brain networks*. We associated the connections exhibiting suppressed network properties with *deflation*, given that reduced engagement of certain prefrontal-subcortical and prefrontal-cortical pairwise connectivities may be considered as an outcome of impaired regulation from prefrontal regions (Gross, 2014). Similarly, we associated the connections exhibiting elevated network properties with *inflation*, or pathologically enhanced network-level engagement, given that pairwise hyper-connectivity is seen as an outcome of neurological disruption (Hillary et al., 2015), and has been noticed in PTSD (Hayes et al., 2012; Simmons and Matthews, 2012; Cisler et al., 2014). Within this framework, we sought to identify such networks properties which were (i) affected by PTSD but not mTBI (we call this *hypothesis-1*, see **Figure 1A**), and (ii) affected by PTSD as well as comorbid PTSD and mTBI (we call this *hypothesis-2*; see **Figure 1B**). Such dichotomy would enable us to identify both common (*hypothesis-1*) and distinguishing (*hypothesis-2*) network features between PTSD and mTBI, given the high comorbidity and overlapping symptomatology between them (Spielberg et al., 2015). Notably, we tested the hypothesis on whole-brain data, in a data-driven manner without imposition of any priors, using resting-state fMRI, which is not task dependent. With the network properties that fit our hypothesis, we assessed their association with relevant behaviors (neurocognitive functioning, and symptom severity in PTSD and PCS).

Machine Learning

Statistical group separation is the analysis framework for our hypothesis. However, statistical separation does not automatically attribute them with predictive diagnostic ability (Deshpande et al., 2010a) at the individual-subject level. Machine-learning classifiers have been successfully utilized on fMRI data for such diagnostic prediction in disorders like major depression (Deshpande et al., 2009), PTSD (Liu et al., 2015), Parkinson's (Marquand et al., 2013), dementia (Chen et al., 2011), ADHD (Deshpande et al., 2015), prenatal-cocaine-exposure syndrome (Deshpande et al., 2010a), autism (Deshpande et al., 2013; Libero et al., 2015), and many others. However, to the best of our knowledge, there have been no works utilizing complex-network properties in PTSD/mTBI classification. Given the unique high-level information contained in network properties, we expected network measures to possess predictive ability. Neuropsychiatric conditions such as PCS and PTSD are currently diagnosed through clinical observation and self-report, hence classification

FIGURE 1 | Illustration of our hypothesis showing decreasing temporal variability (implying rigidity) of segregation/integration, and either increasing or decreasing segregation/integration (implying *inflation* or *deflation*, respectively) as we move from Control to PTSD to PCS + PTSD. Font and circle sizes are symbolic of the increasing/decreasing trend, with smaller circles/text representing *deflation* and rigidity, and larger circles/text representing *inflation* and flexibility. **(A)** Hypothesis-1: some network properties would be disrupted only in PTSD (significant for Control vs. PTSD and Control vs PCS + PTSD comparisons, but not PTSD vs. PCS + PTSD comparison). **(B)** Hypothesis-2: some network properties would be significantly different between all three groups. Note that *inflation* and *deflation* generally correspond to elevation or suppression of network properties, respectively, and not just connection strengths of individual paths. However, in the special case when local network properties of the paths are considered, *inflation* and *deflation* are referred to the network properties, as well as connection strengths of the paths under consideration.

using neuroimaging-based network signatures can be useful in obtaining more accurate diagnoses in these highly comorbid conditions. Hence, we employed a machine learning technique to identify highly predictive features by recursively eliminating unimportant complex-network features in a data-driven way. In addition, we sought to find an overlap between connections with network properties satisfying our primary hypotheses (**Figure 1**), *and* those possessing high predictive ability. As our secondary hypothesis, we hypothesized that such network properties would predict the diagnostic membership of a new subject better than available non-imaging measures (neurocognitive, behavioral and self-report measures), thus underscoring their relevance to the

underlying neuropathology of mTBI and PTSD. We place special emphasis on network properties having all the desirable qualities assessed in this work: high statistical separation, behavioral relevance and high predictive ability. Our study illustrates the utility of our methodological framework using the PTSD/mTBI cohort as an example.

MATERIALS AND METHODS

A schematic of the entire processing pipeline is available at the end of the methods section (**Figure 4**).

Participants

Active-duty soldiers (aged between 18 and 50 years) were recruited from Fort Benning, GA, United States and Fort Rucker, AL, United States to participate voluntarily in the study. The study was conducted in accordance with the Declaration of Helsinki, and the procedures were approved by Auburn University's Institutional Review Board (IRB) as well as the Headquarters United States Army Medical Research and Materiel Command, IRB (HQ USAMRDC IRB). Written informed consent was obtained from all participants.

Eighty-seven male, active duty U.S. Army soldiers were enrolled in the study, which included 17 with PTSD, 42 with comorbid PCS and PTSD (PCS + PTSD), and 28 combat controls (all groups were matched in age, education and race), all having combat experience in Iraq (Operation Iraqi Freedom, OIF) and/or Afghanistan (Operation Enduring Freedom, OEF). Participants were grouped based on symptom severity in PTSD using the "PTSD Checklist-5" (PCL5) score, post-concussive symptoms using the "Neurobehavioral Symptom Inventory" (NSI) score, clinician referral and medical history. (i) Participants with post-concussive symptoms, clinician referral, history of medically documented mTBI, and scores $\geq$ 38 on the PCL5 and $\geq$ 26 on the NSI were grouped as the comorbid PCS + PTSD group. (ii) Participants with no history of mTBI in the last 5 years, a score $\geq$ 38 on PCL5, and $<$ 26 on NSI and clinician referral were grouped as PTSD. (iii) Participants with score $<$ 38 on PCL5 and $<$ 26 on NSI, no mTBI within the last 5 years, no DSM-IV-TR or DSM-V diagnosis of a psychiatric disorder (based on medical records), and no history of moderate-to-severe TBI were grouped as combat controls. All participants were assessed by a licensed medical practitioner, and reported being deployed to a combat environment. Those with psychotic, mood or substance dependency disorders were excluded.

Measures

A battery of psychological health measures were administered to the participants prior to their MRI scan. The battery consisted of the Brief Traumatic Brain Injury Screen [BTBIS; (Schwab et al., 2007)], PCL-5 (Blevins et al., 2015), NSI (Cicerone and Kalmar, 1995), Life Events Checklist (LEC; (Gray et al., 2004)), Combat Exposure Scale [CES; (Guyker et al., 2013)], Childhood Environment [CE; (King et al., 2003)], Zung Depression Scale [ZDS; (Zung et al., 1965)], Zung Anxiety Scale [ZAS; (Zung, 1971)], Alcohol Use Dependency Identification Test [AUDIT; (Saunders et al., 1993)], and the Epworth Sleepiness Scale [ESS; (Johns, 1991)]. In **Supplementary Section** "Psychological Health Measures," (SI-2.1) we present, in more detail, the measures that were most relevant for this study [PCL5, NSI, and CNS vital signs (CNS-VS]). Neurocognitive composite index (NCI) was derived from CNS-VS domain scores (Gualtieri and Johnson, 2006) as an aggregate measure of neurocognitive functioning.

Procedures

For procedures done prior to the fMRI scans during the scheduled appointment, see **Supplementary Section** "Procedures" (SI-2.2).

fMRI

Participants were scanned in a 3T MAGNETOM Verio scanner (Siemens Healthcare, Erlangen, Germany) using T2* weighted multiband echo-planar imaging (EPI) sequence in resting state (participants would keep their eyes open and fixated on a white cross displayed on a dark background on the screen using an Avotec projection system, and not think of anything specific), with TR = 600 ms, TE = 30 ms, FA = 55°, slice gap = 1 mm, multiband factor = 2, anterior to posterior phase encoding direction, voxel size = 3 mm × 3 mm × 4 mm, and 1000 volumes. Brain coverage was confined to the cerebral cortex, subcortical structures, midbrain and pons (cerebellum was excluded). Two identical but separate scans were performed for every participant and processed independently [more information in the **Supplementary Section** "Procedures" (SI-2.2)].

fMRI Data Pre-processing

Standard resting-state fMRI data pre-processing steps were done including realignment, normalization to MNI space, detrending and regressing out nuisance covariates such as six head-motion parameters, white matter signal and cerebrospinal fluid signal, and band-pass filtering (0.01–0.1 Hz). The largest permitted head motion was half the voxel-size (1.5 mm); no significant group differences were observed in participant head-motion ($p > 0.05$) (also see **Table 1**). Pre-processing was performed using Data Processing Assistant for Resting-State fMRI (DPARSF v1.7) (Chao-Gan and Yu-Feng, 2010), which is based on Statistical Parametric Mapping (SPM8) (Friston et al., 2007) and Resting-State fMRI Data Analysis Toolkit (Song et al., 2011).

Deconvolution was then carried out on voxel-level time series, because confounds arising from spatial and inter-subject variability of the hemodynamic response function (HRF) (Handwerker et al., 2004; Rangaprakash et al., 2017c) could lead to a scenario wherein two fMRI time series show high effective connectivity but the underlying neural signals are not highly connected, and vice versa (refer to **Figure 2** for an illustration) (Rangaprakash et al., 2018b,c). Such phenomena have been specifically found in the case of PTSD and mTBI with functional connectivity (Rangaprakash et al., 2017c). Additionally, causal connections could potentially switch directions in case the underlying HRFs possess different times-to-peak. In this respect, it has been demonstrated that deconvolution results in improved estimation of effective connectivity (David et al., 2008; Ryali et al., 2012, 2016). The viewpoint of cellular neuroscience on BOLD

TABLE 1 | Mean, median and standard deviation of demographics, head motion, psychological measures (PCL5, NSI, and CES), and CNS-VS neurocognitive measures for each of the groups.

Variable		Controls	PTSD	PCS + PTSD
DEMOGRAPHICS AND HEAD MOTION				
Age, years	Mean	32.6	32.2	33.7
	Median	31	32	33
	SD	6.7	7.6	6.8
Education, years	Mean	15.1	14.5	14.1
	Median	16	14	14
	SD	1.9	2.2	1.9
Race	White	18 (66.7%)	11 (64.7%)	26 (66.7%)
	Black	2 (7.4%)	3 (17.6%)	9 (22.0%)
	Hispanic	3 (11.1%)	3 (17.6%)	2 (4.9%)
	Asian	2 (7.4%)	0	1 (2.4%)
	Other	0	0	1 (2.4%)
Head motion (mean frame-wise displacement)	Mean	0.098	0.121	0.111
	Median	0.072	0.076	0.069
	SD	0.082	0.106	0.104
Medication		2 (7.4%)	4 (23.5%)	13 (31.7%)*
Lifetime mTBIs	Mean (Range)	0.3 (2)	1.1 (6)	2.5 (15)*
PSYCHOLOGICAL MEASURES				
Traumatic stress[a]	Mean	23.5	56.6	70.9
	Median	21.5	48.5	70.5
	SD	4.2	17.8	15.2
Post-concussive symptoms[a]	Mean	6.6	25.9	43.4
	Median	5	17.5	41.5
	SD	4.8	19.2	16.1
Combat exposure[a]	Mean	7.2	16.7	28.6
	Median	2.5	15	29
	SD	9.8	11.2	8.6
NEUROCOGNITIVE MEASURES				
Neurocognitive composite index[t,z]	Mean	101.2	94.3	81.7
	Median	100.7	94.6	82.2
	SD	12.9	12.5	20.7
Reaction time	Mean	97.4	95.3	84
	Median	101	92	91
	SD	23	11.9	32.8
Complex attention[t]	Mean	94.2	78.1	70
	Median	99.5	92	80
	SD	23.3	30.9	31.3
Cognitive flexibility[t,z]	Mean	103.6	97.1	80.5
	Median	103	93	86
	SD	16.3	15.2	26.7
Processing speed[t]	Mean	104.8	100.1	89.9
	Median	104	98	92
	SD	20.9	11	20.1
Executive functioning[t,z]	Mean	106	101	84.1
	Median	104.5	104	90
	SD	13.3	13.2	24.8
Verbal memory	Mean	99.6	92.1	83.6
	Median	106.5	103	83
	SD	12.5	9.5	13.9

[a]denotes $p < 0.05$, all three groups; [t]denotes $p < 0.05$, Controls vs. PCS + PTSD, [z]denotes $p < 0.05$, PTSD vs. PCS + PTSD. Traumatic Stress = PCL5; Post-concussive Symptoms = NSI; Combat Exposure = CES.

fMRI presented in a recent paper (Hall et al., 2016) discussed several caveats in the interpretation of fMRI results, wherein careful consideration is warranted based on the underlying cellular mechanisms. Neurovascular dynamics or HRF variability is one such primary issue, about which they comment as follows: "*advances in cellular neuroscience demonstrating differences in this neurovascular relationship in different brain regions, conditions or pathologies are often not accounted for when interpreting BOLD*." They advise employing computational modeling (e.g., deconvolution) to mitigate the issue. We employed a popular blind deconvolution algorithm (Wu et al., 2013). Many recent papers have employed it [see for example (Amico et al., 2014; Lamichhane et al., 2014; Boly et al., 2015; Rangaprakash et al., 2017a,b)]. The deconvolution is blind since both the HRF and underlying latent neural time series are estimated only from the recorded fMRI data. Resting-state fMRI data is modeled as event-related using point processes with randomly occurring events; then, voxel-specific HRFs are estimated using Wiener deconvolution. This technique is date-driven; hence, we do not encounter overfitting issues that often plague model-based approaches.

Since whole-brain fMRI data has high dimensionality, 125 functionally homogeneous brain regions spread out across the cerebral cortex and encompassing it completely, determined using spectral clustering [known as the Craddock-200 atlas (Craddock et al., 2012)], were taken and mean deconvolved time series were obtained from them. All further analyses (carried out on the Matlab® platform) utilized these 125 time series from every participant.

Effective Connectivity Analysis

A precursor to obtaining network-level characterization is to first get the connectivity network itself, which is, computing SEC and DEC matrices from pre-processed fMRI data. Whole-brain SEC and DEC were computed using GC (Deshpande et al., 2010b), which is an exploratory technique used to quantitatively measure directional relationships between brain regions. While SEC uses a multivariate autoregressive (MVAR) model, DEC employs a dynamic MVAR model evaluated in a Kalman filter framework using variable parameter regression (Wheelock et al., 2014).

The concept of Granger causality (GC) is that, if future values of time series "Y2" can, in a mathematical sense, be predicted by the past values of time series "Y1," then a causal influence is inferred from time series Y1 to time series Y2 (Granger, 1969). GC's MVAR model predicts one time series from the other quantitatively, as described briefly next. Given k different time series $Z(t) = [z_1(t), z_2(t), \ldots z_k(t)]$, wherein k corresponds to 125 ROIs of this work, the MVAR model of order p is given by:

$$Z(t) = M(0)\,Z(t) + M(1)\,Z(t-1) + M(2)\,Z(t-2) + \cdots + M(p)\,Z(t-p) + E(t) \quad (1)$$

Here, E(t) is the model error, while $M(0) \ldots M(p)$ are model coefficients. Like in earlier studies (Deshpande et al., 2010b), this formulation included a zero-lag term with coefficient $M(0)$ which would eliminate the contribution of zero-lag cross-correlation between the time series. Since $M(0)$ represents co-variance between time series and not used in GC computation, the effect

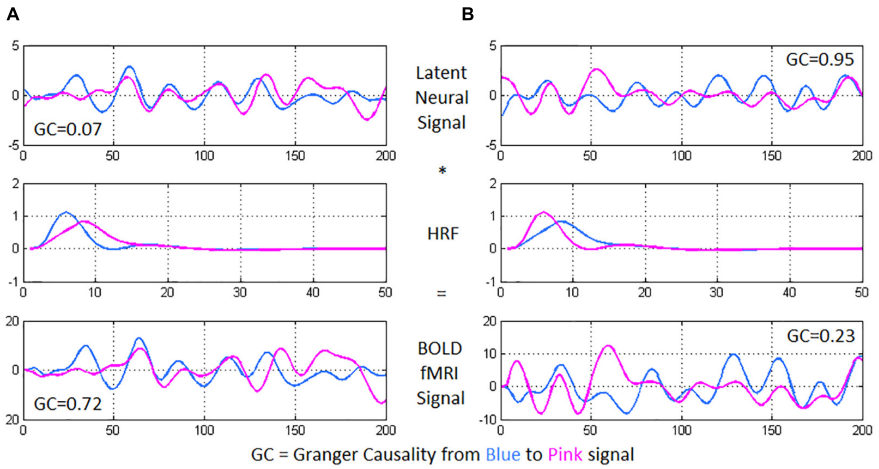

FIGURE 2 | Using two time series from experimental fMRI data, we illustrate the importance of performing hemodynamic deconvolution for effective connectivity modeling. The latent neural signals are convolved with the hemodynamic response function (HRF) to provide the BOLD fMRI time series. Within-subject spatial HRF variability across the brain could often result in a scenario wherein **(A)** the latent neural signals have true low directional connectivity [quantified using Granger causality (GC) from blue to pink signal] while the BOLD fMRI time series show high GC wherein the pink time series seems to follow after the blue time series, and **(B)** the latent neural variables have true high directional connectivity while the BOLD fMRI time series show low GC. In the former case, while the neural signals nearly overlap, the delay in the HRFs causes an observable delay in the BOLD time series, resulting in high GC from the blue to the pink BOLD time series. In the latter case, the delay noticeable in the neural signals (pink signal leads blue) is negated by the delay in the HRFs (blue signal leads pink), resulting in nearly overlapping BOLD time series and a low GC value.

of zero-lag cross-correlation gets ignored in GC. Given that diagonal elements of $M(0)$ are set to zero, we only model the instantaneous cross-correlation, and not the auto-correlation between the time series.

The coefficients were estimated using multivariate least-squares estimation. It computes the set of optimal coefficients with model error being minimized in a least-squares sense. The model order p can either be chosen by utilizing a mathematical principle such as the Bayesian Information Criterion (BIC) (Roebroeck et al., 2005) or based upon the needs of the application being considered. In neuroimaging, causal relationships corresponding to neural delays less than or equal to the TR are of interest (Deshpande et al., 2013), hence we used a first order model. Given that fMRI's temporal resolution is relatively low, a first-order model has been shown to capture the most relevant directional information (Deshpande and Hu, 2012).

The degree to which the past $Z(t\text{-}p)$ is able to predict the present $Z(t)$ is given by the coefficient matrix $M(p)$. The sum of all such coefficients would then correspond to the degree to which the past values put together can predict the present. As in prior works (Kaminski et al., 2001), GC was formally derived, based on the model coefficients, as:

$$GC_{ij} = \sum_{n=1}^{p} m_{ij}(n) \tag{2}$$

Wherein m_{ij} are the elements of matrix M and GC_{ij} refers to the SEC value from ROI i to ROI j. Notably, a single coefficient matrix was computed for the entire duration of the experiment, that is, coefficients are not varying with time. A deeper theoretical rendering of GC can be found here (Deshpande et al., 2010b). GC-based methods have been experimentally validated for fMRI EC analysis (David et al., 2008; Katwal et al., 2013), and they have been extensively utilized for fMRI EC modeling in recent times [see for example (Deshpande et al., 2011, 2015)].

Next, DEC was computed by employing time-varying dynamic Granger causality (DGC), evaluated using a Kalman filter framework. Dynamic multivariate vector autoregressive (dMVAR) model was employed for estimating DGC (Grant et al., 2014; Wheelock et al., 2014). DEC is the underlying time-varying physiological process, while DGC is the mathematical measure that quantifies it. This technique has also been used in several recent studies (Deshpande et al., 2013; Wheelock et al., 2014; Hutcheson et al., 2015). Unlike GC formulation, dMVAR model coefficients $M'(p,t)$ are a function of time, hence the model is "dynamic."

$$\begin{aligned} Z(t) = {} & M'(0,t)\,Z(t) + M'(1,t)\,Z(t-1) \\ & + \cdots + M'(p,t)\,Z(t-p) + E(t) \end{aligned} \tag{3}$$

A Kalman filter framework which uses variable parameter regression (Büchel and Friston, 1998) was used to estimate dynamic model coefficients, which involved imposing a forgetting factor (which was chosen as 1 in our case). DGC was thus computed as:

$$DGC_{ij}(t) = \sum_{n=1}^{p} m_{ij}(n,t) \tag{4}$$

Where m_{ij} are the elements of matrix M and $DGC_{ij}(t)$ is the value of DEC from ROI i to ROI j at a given time point t. Like in GC, zero-lag cross-correlation effects were compensated here also. Further, a forgetting factor of 1 was used to make

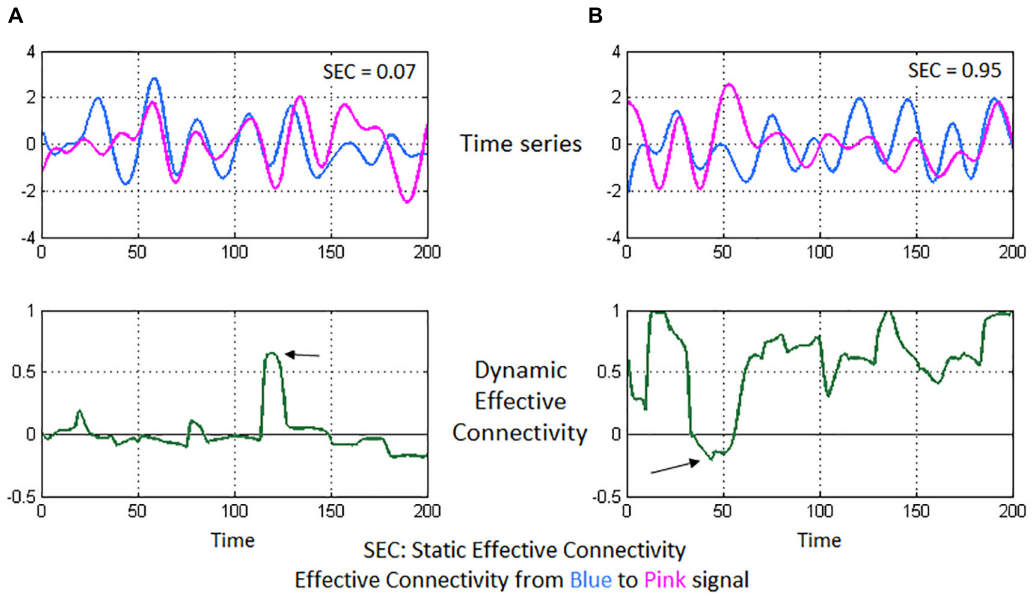

FIGURE 3 | Illustration of static and dynamic effective connectivity (SEC and DEC) from a neuroimaging standpoint using two experimental fMRI time series. In **(A)**, the two time series seem highly correlated and nearly overlapping. However, the variations in the pink time series do not appear to happen after (or before) the variations in blue time series (top-left figure). This poor causal relationship results in a low SEC value (= 0.07). Correspondingly, DEC values hover around the zero-value (bottom-left figure) since a causal relationship does not seem to emerge for most part of time, except for a brief span (marked by the arrow) when there is a visible causal relationship. In **(B)**, the pink time series seems to constantly follow after the blue time series (top-right figure), indicating that the pink signal's associated brain region activates (and deactivates) immediately after the blue signal's region activates (and deactivates), thus a causal relationship and a high SEC value (= 0.95). DEC provides additional insight (bottom-right figure), wherein steady causality is maintained almost for the entire duration except for a brief span (marked by the arrow), wherein DEC dips because of observable lack of causality in the time series' of those sections.

the system well-conditioned so that the coefficients may be estimated accurately.

A 125 × 125 whole-brain SEC matrix was obtained for every participant by computing GC between all combinations of connections between the 125 ROIs. With DEC, the dynamic MVAR model coefficients are a function of time, hence, with our fMRI data having 1000 time points, we obtained a 125 × 125 × 1000 DEC matrix per participant. SEC and DEC matrices were used for further complex-network analysis. To illustrate the concepts of SEC and DEC in the context of neuroimaging, we show a simple illustration using a pair of fMRI time series from our experimental data (see **Figure 3**).

Complex-Network Analysis

We first describe the network measures of segregation and integration, and then explain how they were used in the context of this work. As noted earlier, given the complexity of our hypothesis, we dealt with weighted directed networks in this work. Functional segregation was quantified using transitivity (global measure, one value for whole brain per participant), clustering coefficient and local efficiency (both local measures, one value per node/region per participant). Functional integration was quantified using global efficiency (global measure), shortest path length and edge betweenness (both local measures, one value per connection per participant). We obtained source codes for these measures from the Brain Connectivity Toolbox (April 2014 release) (Rubinov and Sporns, 2010), and implemented the entire pipeline in the Matlab® platform through custom codes. A detailed account of these measures can be found in Rubinov and Sporns (2010). For the benefit of readers, we have explained each of these measures in detail using a simplified example network in **Supplementary Section** "Complex-Network Analysis" (SI-2.3).

Briefly, transitivity is a global measure of overall efficiency of local processing in the brain. Clustering coefficient (*CC*) gives a transitivity-type characterization for every node. Local efficiency (*EffLoc*) is closely related to *CC*, wherein nodes with powerful neighbors that are involved in several shortest paths have higher *EffLoc*, indicating that the node is important in the sub-network for specialized processing. While *CC* and *EffLoc* usually give similar (but not same) results, their interpretations are different. In this work, along with transitivity as the global measure, we employed both *CC* and *EffLoc* as local measures, which are the two popularly used local measures of segregation. We took an overlap (intersection) of the final significant group differences for the two measures, so that the affected nodes had differences in both the measures, thus providing more conservative results with a broader interpretation.

Global efficiency (*EffGlob*) is a global measure indicating the aggregate ease of communication in the entire network. Shortest path length (SPL) is a measure of how easy it is to reach one node from the other, and is analogous to meta-connectivity. Edge betweenness (*EB*) measures the number of

all shortest paths in the entire network that contain the given connection. Like SPL, *EB* is an important network measure because it characterizes the importance of a connectivity path not only through its pairwise connectivity value but also through the significance of the connectivity path for other connectivity paths present in the network. If a connectivity path matters a lot for other paths, i.e., for communication between various other nodes, then the given path would have high integration ability (i.e., *SPL* and EB). Such a characterization can be obtained only through complex-network modeling since traditional pairwise connectivity informs us only about the strength of interaction between just two brain regions. In this work, we employed *EffGlob* as the global measure and both *SPL* and *EB* as local measures of integration. As with segregation, we took an overlap (intersection) of the final significant group differences in the two local measures, so that the affected paths had differences in both measures, thus providing more conservative, but potentially more reliable, results with wider interpretation.

Next, we describe how these six network measures were used in the context of this work. SEC and DEC connectivities were used separately to construct static and time-varying networks with brain regions as nodes and connectivity strengths between them as the weighted directed edges of the network graphs. Absolute value of connectivity was used to construct the network graphs. With SEC, a single network was constructed for the entire duration of time in the data, giving a "connectivity strength" network, which was used to obtain each one of the six complex-network measures for every run of every participant. With DEC, we considered each time point of the DEC time series as a snapshot of the network at that time instant, and then constructed a graph using the nodes and edge values from that snapshot. We computed network measures for that snapshot, and repeated the procedure independently for the rest of DEC time series to obtain a time series of values for each network measure. Then, for each network measure, we computed the variance of the network measure time series to obtain a single value for the entire duration of the data. This gave us a network with paths whose weights corresponded to the temporal variability of complex-network measures. This was obtained for every measure and for every run of every participant, similar to SEC.

Statistically significant differences in these strength and variability networks were obtained, in accordance with our hypothesis ($p < 0.05$, FDR corrected). We corrected for 31250 comparisons: 125 comparisons of segregation (125 ROIs), 15500 comparisons of integration ($125 \times 125 - 125$), each for both static connectivity and variance of dynamic connectivity networks. Differences were controlled for age, race, education, and head-motion [using mean frame-wise displacement, as defined by Power et al. (2012)]. That is, we found significant group differences with both SEC and DEC derived complex-network measures separately for these three pairwise comparisons (thus giving a total of six comparisons per network measure): Control vs PTSD, Control vs. PCS + PTSD, PTSD vs. PCS + PTSD. We then identified the common network measures among four of these comparisons (*hypothesis-1*) which excluded PTSD vs PCS + PTSD comparison, and we also identified common network measures among all the six comparisons (intersection, hypothesis-2), all of which also fit our hypothesis, that is, conformed to the increasing/decreasing trend as we moved from Control to PTSD to PCS + PTSD.

It is notable that we have taken a conservative approach in this work. We opted to look for common differences in pairwise statistical comparisons, rather than performing a single three-way statistical comparison, which is less conservative. We obtained common differences in static as well as dynamic network measures, and we also constrained the differences to conform to a trend as per our hypothesis. Additionally, we computed two local measures in segregation as well as integration, and considered only common differences in them, which added another level of constraints on our findings. In addition to these, we notably discarded any paths which had significant network-level differences in local measures of integration (i.e., SPL and EB), but not significant pairwise effective connectivity differences themselves. That is, we included only those paths which had significantly different SEC and variance of DEC in accordance with the trend set out in our hypothesis ($p < 0.05$, FDR corrected, controlled for age, race, education and head-motion), in addition to having significantly different local measures of integration (i.e., SPL and EB). This was done to ensure that, irrespective of network-level disturbance, the significant connections that emerged in this work would have also cleared whole-brain multiple-comparisons-corrected statistical threshold with traditional static and dynamic effective connectivity like in most other studies. This reassured that our results conformed to multiple layers of validation, verification and statistical standards, and that evidence of network disruption were obtained via multiple analysis approaches, in addition to providing novel insights through network characterization.

Behavioral Relevance of Network Properties

In an effort to assess the behavioral relevance of complex-network measures, we first obtained the association of the strength and variability of complex-network measures (only those which fit our hypothesis) with symptom severity in PCS (NSI score) and PTSD (PCL5 score), as well as neurocognitive functioning (NCI score and subtests). Neurocognitive functioning (e.g., executive functioning, cognitive flexibility) is often impaired in psychiatric disorders such as PTSD and PCS (Simmons and Matthews, 2012), hence identifying such network properties associated with it would be important. We report significant associations between complex-network properties and behavioral/clinical measures.

In order to obtain additional insight into how network properties of the ensemble of identified connections mapped on to the ensemble of behaviors, we performed partial least squares regression (PLSR) analysis (Krishnan et al., 2011), which we employed to predict neurocognitive functioning (NCI and subtests) and symptom severity (PCL5, NSI) from strength and variability of network measures obtained from our prior analysis. We present the percentage variance in behaviors explained by the complex-network measures.

Machine Learning Classification Analysis

For predicting the diagnostic membership of a novel subject based on a novel measurement using the measure, success in hypothesis testing is neither necessary nor sufficient. A mechanism to quantify the predictive ability of the features is not available with the hypothesis testing framework, requiring us to acknowledge what a technique like hypothesis testing can do, and cannot do. Statistically significant network properties necessarily need not have high predictive ability, and vice versa. Hence, those network properties that are both statistically significant (in accordance with our hypothesis) and are top-classifiers (high predictive ability) carry superior importance and relevance. Therefore, we used machine learning techniques to identify such network properties (features) which can accurately classify individuals between controls, PTSD, and PCS + PTSD. A Recursive Cluster Elimination based Support Vector Machine (RCE-SVM) classifier (Deshpande et al., 2010a) was used to classify the participants based on whole-brain network properties (both strength and variability). Notably, findings from prior complex-network analysis were not used to bias the machine learning analysis as whole-brain data was used. A detailed account of this technique can be found in Rangaprakash et al. (2017a), and we have explained it thoroughly in **Supplementary Section** "Machine Learning Classification Analysis" (SI-2.4) to benefit the reader.

Briefly, RCE-SVM iteratively eliminates features to minimize prediction error. The training data is clustered, and upon SVM classification the clusters are scored using testing data. Low-scoring clusters are eliminated (*RCE step*) and the procedure is repeated until only the top-predictive features remain. In this work, we made the following parameter choices. The training set consisted of 80% of the participants, while the testing set consisted of the remaining 20%. We began the algorithm with forty clusters in the first RCE step. Based on performance, the bottom 20% of the clusters were eliminated in every subsequent RCE step. Two clusters containing the top-predictive features remained in the final RCE step. With a hundred random iterations, sixfold cross validation was performed in every iteration, resulting in a total of 600 iterations over the complete execution.

To be conservative, we obtained the worst-case classification accuracy by evaluating the lowest accuracy value gathered from test data among all 600 iterations (sixfolds × 100 repetitions). Statistical significance of the accuracies was computed through estimating p-values using a binomial null distribution $B(\eta,\rho)$, with ρ being the probability of accurate classification and η being the number of participants like in previous studies (Pereira et al., 2009). Only accuracies with $p < 0.05$ (Bonferroni corrected) were taken as statistically significant.

We repeated this procedure and performed classification independently with 32 available non-imaging measures as input features instead of network measures. The 32 measures were: (i) psychological health measures: Perceived Stress Scale, Epworth Sleepiness Scale, Pittsburgh Sleep Quality Index, Zung Depression Scale, and Zung Anxiety Scale; (ii) behavioral measures: all CNS-VS measures including the NCI score; (iii) exposure/injury descriptives: CES, lifetime concussions, and Life Events Checklist. Worst-case accuracies and top-classifying features were obtained, with them being compared with the results obtained by using complex-network measures.

Machine Learning Regression (Dimensional) Analysis

Network properties having statistical significance in accordance with our hypothesis, having behavioral relevance as well as having high predictive ability were attributed distinctive importance in this study. Using such features, we finally performed support vector regression (SVR) to predict PTSD and PCS symptom severity, in order to assess those features dimensionally. Similar to the classification analysis, we performed sixfold cross-validated linear SVR over one million iterations. Specifically, in each iteration, the regression model was developed using 5/6th of the randomly chosen participants. The model used features described above as inputs and learned the underlying function which maps onto the PCL5 and NSI scores. Subsequently, the model was used to predict PCL5 and NSI scores in the remaining 1/6th participants. Our machine learning classification and regression analyses involved no hyperparameter optimization. We report correlation (R^2) between predicted and measured symptom severity scores.

Figure 4 summarizes the processing pipeline of all the methods.

RESULTS

Demographics

The demographics (for the three groups) are presented in **Table 1**. There were no significant group differences in age, $p = 0.70$, or education, $p = 0.15$. The results indicated a difference in the frequency of reported psychotropic use between the groups, $\tau b = 0.24$, $p = 0.01$, with the highest percentage of medicated participants being in the comorbid group. The number of reported lifetime mTBIs also had significant group differences specifically between control group and the PCS + PTSD group [$F(2,171) = 5.81$, $p = 0.004$], but not the control versus PTSD groups or PTSD versus PCS + PTSD groups, $p > 0.05$.

Psychological Health and Neurocognitive Function

The results revealed significant differences between the three groups in posttraumatic symptoms (PCL5), [$F(2,81) = 101.65$, $p < 0.001$], post-concussive symptoms (NSI), [$F(2,78) = 49.79$, $p < 0.001$], and CES, $F(2,79) = 40.69$, $p < 0.001$. All p-values remained significant after corrections for multiple comparisons. As observed in **Table 1**, the PCS + PTSD group had the highest scores out of the three groups on these respective measures.

The results indicated that, after corrections for multiple comparisons, the control group displayed significantly higher scores than the PCS + PTSD group on all neurocognitive measures, $p < 0.05$, except for reaction time and verbal memory, $p > 0.05$. The PCS + PTSD group also had significantly lower

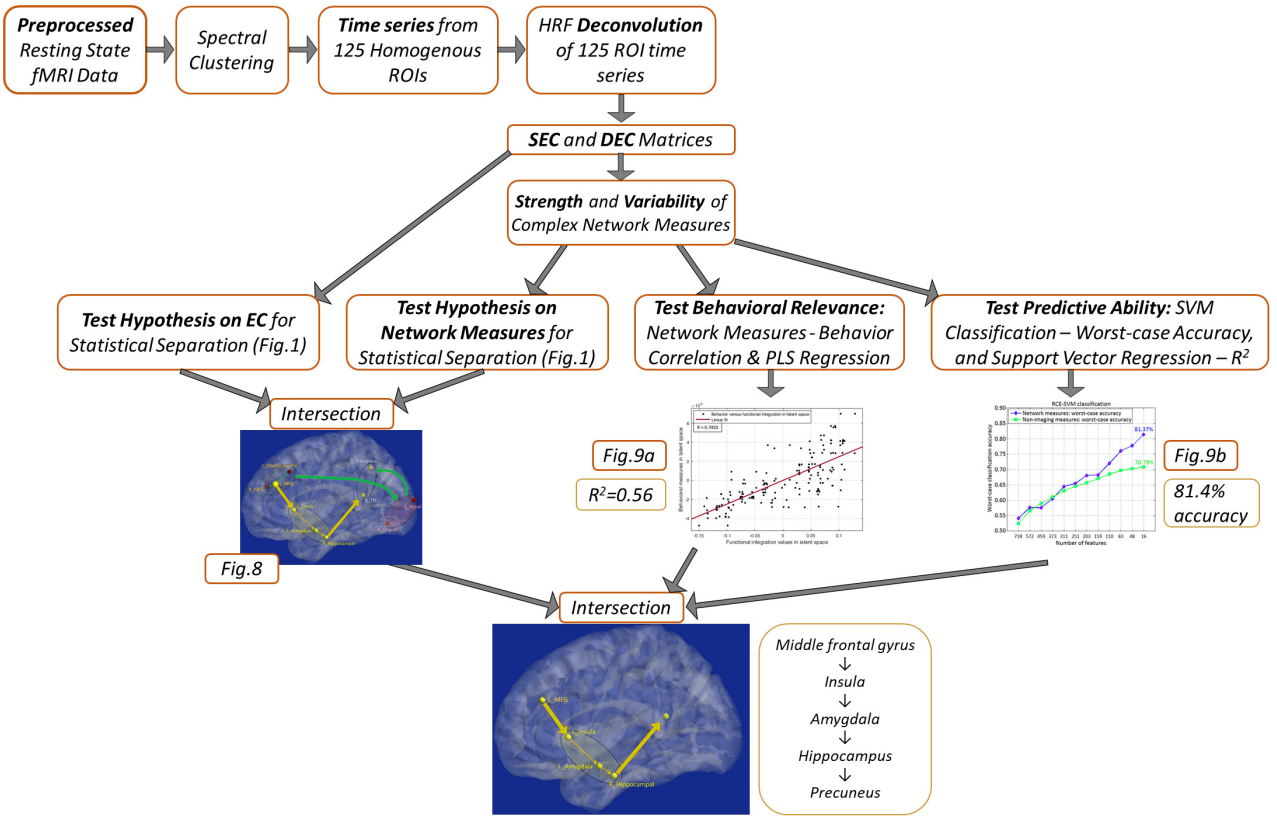

FIGURE 4 | Schematic of the complete processing pipeline executed in this study. Results corresponding to different analyses are summarized, which can be viewed in more detail by referring to the corresponding figures.

scores in executive functioning, cognitive flexibility, and the NCI compared to the PTSD group, $p < 0.05$. The findings suggest that both the PTSD and PCS + PTSD groups display lower scores than controls, but also, the comorbid group had greater impairments than the PTSD group (see **Table 1**).

Complex-Network Analysis Using Effective Connectivity

We used SEC and DEC connectivity matrices to compute six complex-network measures (two global and four local measures). With global measures (**Figure 5**), we found significantly lower strength and variability of both segregation and integration in PTSD and PCS + PTSD compared to controls. Our finding indicates that both specialized processing and efficient communication are compromised in the disorders at the whole brain level. However, no significant differences were found between PTSD and PCS + PTSD groups, indicating that PTSD might contribute to global aberrations whereas the effect of mTBI might be more localized.

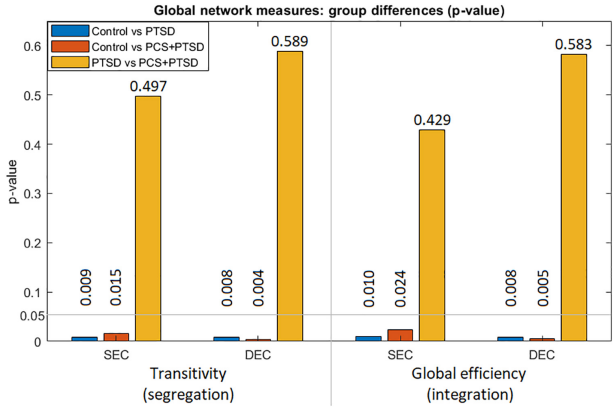

FIGURE 5 | Group differences (*p*-values) for the two global measures (transitivity and global efficiency) obtained from both SEC and DEC matrices. We observe that whole-brain differences were driven by PTSD, while mTBI likely did not cause whole-brain-level changes.

Local Measures

Further granularity was obtained with local measures. Altered segregation was mainly observed in prefrontal and occipital regions (**Figure 6A**). None of the occipital regions were statistically different between the PTSD and PCS + PTSD groups, while the majority of the remaining identified regions were significantly different. While these results were obtained using a strict statistical threshold, we noticed that when a liberal threshold was used (not shown here), more prefrontal nodes

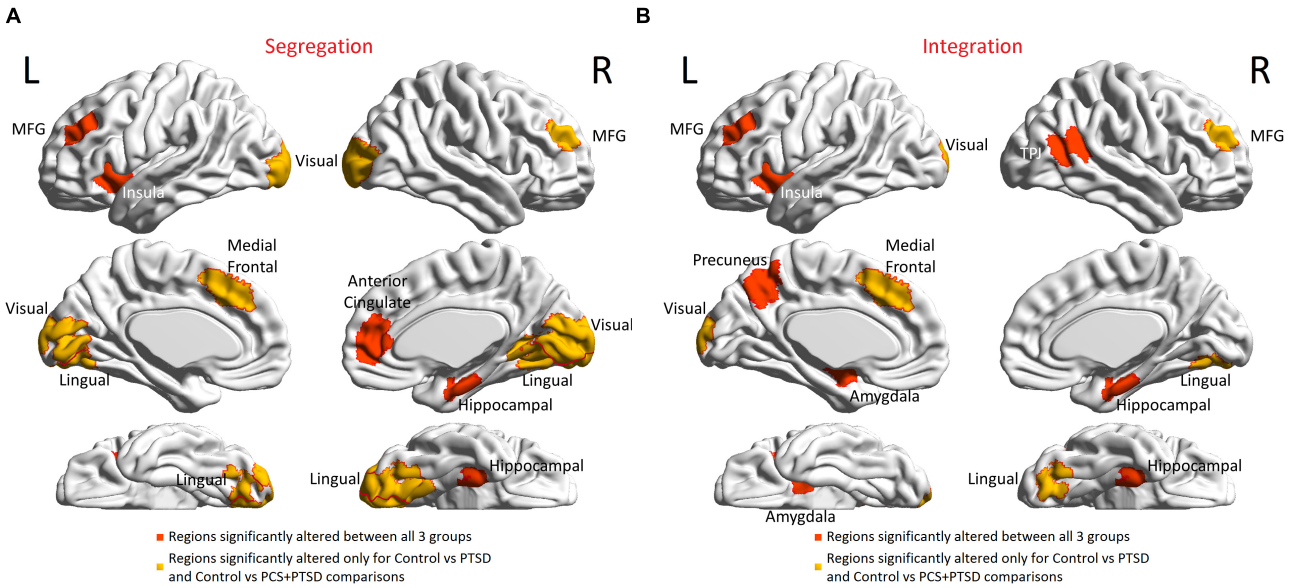

FIGURE 6 | Brain regions with altered functional segregation and/or integration across groups. **(A)** Regions-of-interest (ROIs) associated with significantly disrupted functional segregation. **(B)** ROIs associated with significantly disrupted functional integration. The ROIs were defined by the Craddock-200 atlas (Craddock et al., 2012). MFG, middle frontal gyrus; TPJ, temporo-parietal junction.

were affected compared to parietal/occipital nodes, which were all characterized by lower segregation. This might explain why we observed lower transitivity (global segregation) in PTSD and PCS + PTSD compared to controls.

Generally, the terms "*inflation*" and "*deflation*" (**Figure 1**) correspond to elevation (increased value) or suppression (decreased value) of static network properties, respectively, and not just connection strengths of individual paths. Similarly, "rigidity" corresponds to lower temporal variability of dynamic network properties. However, in the special case when local network properties of paths (i.e., integration) were considered, these terms referred to network properties as well as connection strengths of the paths under consideration.

Next, aberrant local measures of integration were found along two distinct pathways (see **Figure 6B** for the affected ROIs), which we present as two subnetworks for clarity: (i) fronto-visual subnetwork (**Figure 7A**), and (ii) parietal-*inflation* subnetwork (**Figure 7B**). The fronto-visual subnetwork showed prefrontal *deflation* of secondary visual areas and lingual gyrus, i.e., lower strength/variance of network properties (SPL and EB) of paths connecting certain prefrontal regions to certain visual regions. This subnetwork was, however, not significantly different between the PTSD and PCS + PTSD groups, indicating that it might not be affected by an mTBI (since one difference between these groups is a history of significant prior mTBI(s) in the PCS + PTSD group). Notably, all paths here also exhibited lower SEC/vDEC connectivity values in addition to lower strength and variability of integration.

The parietal-*inflation* subnetwork (see **Figure 7B**) showed that the visual areas affected in the fronto-visual subnetwork were driving two key parietal regions [precuneus, temporo-parietal-junction (TPJ)]. Additionally, we observed fronto-subcortical disinhibition resulting in rigid *inflation* (increased strength but lower variance of network properties SPL and EB) of key subcortical areas (amygdala, hippocampus) and anterior insula, which subsequently resulted in the *inflation* of the same key parietal regions (precuneus, TPJ). Interestingly, this fronto-subcortical-parietal subnetwork was significantly different between all three groups, indicating that both PTSD and mTBI affect this subnetwork, while the occipital part was not significantly different between PTSD and PCS + PTSD (see **Figure 7C**). This is a potentially important finding.

Schematic of the entire network (**Figure 8**) shows that the left middle frontal gyrus (MFG), which largely overlaps with the dorsolateral prefrontal cortex (DLPFC), is the likely source of the network-level disruption, whose *deflation* (suppressed network properties) results in *inflation* (elevated network properties) of downstream subcortical and visual pathways, culminating in parietal *inflation*. **Figures 6–8** were visualized using BrainNet Viewer (Xia et al., 2013). In **Supplementary Information**, we provide observations from additional supplemental analysis performed by us (i) using a different brain parcellation instead of Craddock-200 [see **Supplementary Section** "Observations Using a Different Brain Parcellation Instead of Craddock-200" (SI-3.1)], (ii) using eigenvariate time series data instead of mean time series [see **Supplementary Section** "Observations Using Eigenvariate Time Series Data Instead of Mean Time Series" (SI-3.2)], and (iii) using ROI-level deconvolved data instead of voxel-level deconvolved data [see **Supplementary Section** "Observations Using ROI-Level Deconvolved Data Instead of Voxel-level

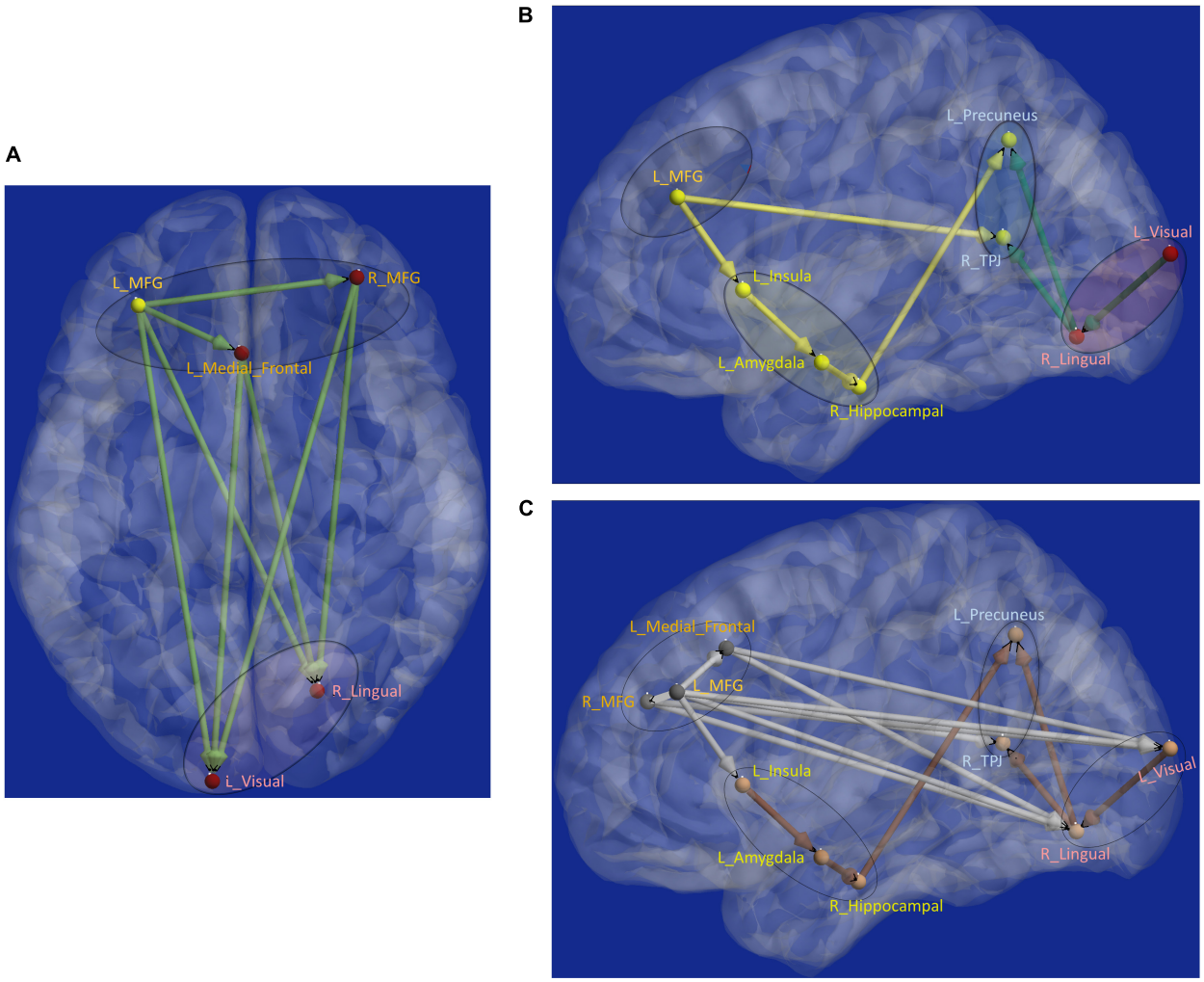

FIGURE 7 | Functional segregation/integration (metastability) results. **(A)** The network of integration was broken down into two sub-networks. **(A)** Shows the first of the two sub-networks, the fronto-visual sub-network that exhibited lower strength of integration and lower temporal variation of integration, which was significant for control vs. PTSD and control vs. PCS + PTSD comparisons (but not PTSD vs. PCS + PTSD comparison). The yellow node had altered segregation between all three groups, while the red nodes were different except for the PTSD vs. PCS + PTSD comparison. This sub-network likely represents reduced prefrontal inhibition of visual memory processing and retrieval. **(B)** Second of the two sub-networks, the parietal *inflation* sub-network that exhibited altered strength of integration and lower temporal variation of integration. Yellow paths were significantly different for all group-wise comparisons. Green paths were altered except for the PTSD vs. PCS + PTSD comparison. This sub-network showed parietal-*inflation* caused by subcortical and visual network disruptions, which were in-turn driven by the left middle frontal gyrus (MFG). **(C)** The entire network of disruption found in the work, showing nodes/paths in gray which were on a rigid deflated regime (lower strength and temporal variability of segregation/integration; as well as lower strength and variability of effective connectivity, marking hypo-connected inflexible connectivity), and nodes/paths in brown, which were on a rigid *inflation* regime (higher strength of segregation/integration and lower variation of segregation/integration over time; as well as higher strength and lower variability of effective connectivity, marking hyper-connected inflexible connectivity). Noticeably, all prefrontal nodes and prefrontal-originating paths exhibited a deflated regime, while the rest (those not associated with prefrontal regions) exhibit an inflated regime. Such a lucid dichotomy is interesting. It is clearly observable that *deflation* originates in the prefrontal cortex, which subsequently results in the *inflation* of parietal regions through two routes, subcortical and visual. MFG, middle frontal gyrus; TPJ, temporo-parietal junction.

Deconvolved Data" (SI-3.3)]. Our results remained consistent across different choices.

Behavioral Relevance of Network Properties

Strength and temporal variability of functional integration values of four paths, which were significantly different between all three groups (the yellow connections in **Figure 8**), as well as the strength and temporal variability of functional segregation of MFG and Insula (**Figure 6A**) showed significant associations ($p < 0.05$ Bonferroni corrected) with neurocognitive functioning (NCI) and severity of both PTSD symptoms (PCL5-score) and post-concussive symptoms (NSI-score), thus highlighting their relevance to the underlying pathophysiology (see **Table 2**). Notably the associations followed the expected trend: increase

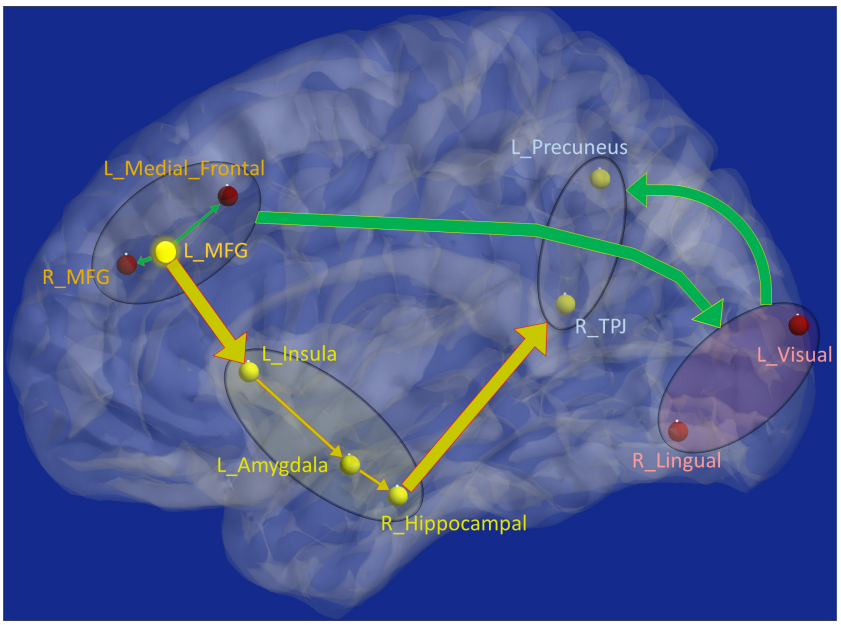

FIGURE 8 | Schematic of the entire network: Yellow nodes/paths were significantly different for all three group-wise comparisons. Green paths (and red nodes) were significantly different except for the PTSD vs. PCS + PTSD comparison. Thick lines correspond to connections between major sub-networks while thin lines correspond to connections within sub-networks. The prefrontal sub-network consisted of MFG and medial frontal, the parietal sub-network consisted of TPJ and precuneus, the visual sub-network consisted of lingual and primary visual areas while the emotion-memory sub-network consisted of sub-cortical regions such as amygdala and hippocampus and cortical regions such as the insula. Disrupted left-MFG causes *deflation* of emotion-memory regions and visual memory-related regions, culminating in parietal-*inflation* causing heightened symptoms often observed in PTSD and PCS.

in symptom severity and decrease in behavioral performance corresponded to higher strength of integration in inflated paths and lower in deflated paths, and lower variability (i.e., rigidity) in integration in all paths (similarly with segregation). However, those connections which were not different between PTSD and PCS + PTSD (green paths in **Figure 8**), as well as other nodes in **Figure 6A** and global complex-network measures had no significant associations with symptoms and neurocognitive performance.

Since multitude of network paths and nodes had relevant associations with multiple measures of symptoms and neurocognitive performance (which we will now refer to as neurobehavioral indices), it would be interesting to measure how much variance in the neurobehavioral indices could be explained by those set of network measures. This was accomplished using PLSR (Krishnan et al., 2011), which finds the combined ability of the strength and variability of functional integration of the four connections and functional segregation of two nodes to predict neurobehavior. We found that the strength of network measures could explain 48.95% variance in the neurobehavioral indices, while the temporal variability of network measures could explain 57.17% variance. When both were combined, they could explain 61.74% variance in the neurobehavioral indices. A significantly large association between these network measures and neurobehavior (R^2 = 0.56, R = 0.75, p = 3.5 × 10^{-32}) was observed in the latent space (see **Figure 9A** for linear fit). The latent space consists of categorical variables that represent all network measures and all neurobehavioral indices included into the model, so that their relationship in the latent space could be considered the effective association of all the included network measures with all the neurobehaviors. As such, the latent space variables contain more "information" in them than the individual variables themselves, consequently explaining more variance than individual measures. For this reason, our finding of higher R^2-value must not be surprising (Vul et al., 2009), and this is fundamental to the multivariate nature of PLS, as elaborated by Krishnan et al. (2011). Our finding reiterates that the strength and variability of functional integration of the four paths and that of segregation of the two nodes identified in this work are behaviorally relevant.

One a side note, head motion [mean frame-wise displacement (Power et al., 2012)] was not significantly correlated with behavioral measures in latent space (R = 0.049, p = 0.52), complex network measures in latent space (R = 0.056, p = 0.46), PCL5 (R = 0.047, p = 0.54) or NSI (R = 0.015, p = 0.84) symptom severity scores. This enhanced our confidence in the results.

Machine Learning Classification Results

Top predictors are those that, among all network measures, possess the highest ability in predicting the diagnostic membership of a novel subject. To identify the top-predictors, we performed RCE-SVM classification (Deshpande et al., 2010a). Classification was done with two different paradigms: (i) classification using the 32 non-imaging measures (NIMs), and (ii) classification using strength and temporal variability

TABLE 2 | Association of strength and variability of complex-network measures with the NCI score and symptom severity in PTSD (PCL5 score) and PCS (NSI score).

Complex network measure	Path (Integration) or node (Segregation)	Symptom severity score		Behavioral measure
		PCL5 score (PTSD)	*NSI score (PCS)*	*Neurocognitive Composite Index (NCI)*
Static functional integration measures				
Shortest path length	L_MFG → L_Insula	−0.6902	−0.6756	0.6589
	L_Insula → L_Amygdala	0.6822	0.6759	−0.6298
	L_Amyg → R_Hippocampus	0.6535	0.6930	−0.6389
	R_Hippocampus → L_Precuneus	0.6990	0.6580	−0.3545
Edge betweenness	L_MFG → L_Insula	−0.6704	−0.6853	0.5871
	L_Insula → L_Amygdala	0.7370	0.6868	−0.5303
	L_Amyg → R_Hippocampus	0.7080	0.6372	−0.3956
	R_Hippocampus → L_Precuneus	0.7156	0.6669	−0.4193
Variance of dynamic functional integration				
Shortest path length	L_MFG → L_Insula	−0.7532	−0.7327	0.6704
	L_Insula → L_Amygdala	−0.7579	−0.7382	0.6748
	L_Amyg → R_Hippocampus	−0.7541	−0.7358	0.6709
	R_Hippocampus → L_Precuneus	−0.8520	−0.7737	0.4579
Edge betweenness	L_MFG → L_Insula	−0.7330	−0.7287	0.6672
	L_Insula → L_Amygdala	−0.7358	−0.7260	0.6586
	L_Amyg → R_Hippocampus	−0.7326	−0.7264	0.6590
	R_Hippocampus → L_Precuneus	−0.8513	−0.7776	0.4619
Static functional segregation measures				
Clustering Coefficient	L_MFG	−0.6859	−0.6685	0.6245
Local Efficiency	L_MFG	−0.7013	−0.6990	0.6826
	L_Insula	0.6527	0.6550	−0.6290
Dynamic functional segregation measures				
Clustering Coefficient	L_MFG	−0.7478	−0.7271	0.6538
	L_Insula	−0.7412	−0.7204	0.6533
Local Efficiency	L_MFG	−0.7524	−0.7324	0.6692

Table presents the correlation values (R-value), which were significant with $p < 0.05$ Bonferroni corrected.

of network measures taken from the entire brain (all data, nothing left out). Results showed that classification using network measures provided significantly better accuracy (approximately 10% more, $p < 0.05$ Bonferroni-corrected) than classification using NIMs (**Figure 9B**). This result indicates that network measures have superior predictive ability in identifying individuals with PCS and PTSD as compared to NIMs.

Table 3 shows the worst-case accuracies and top predictive features (for average accuracy, please see **Supplementary Section** "Supplemental Machine Learning Classification Results" (SI-3.4) and **Supplementary Figure S3**). Also of considerable interest are the top-predictors that resulted in highest classification accuracy. For classification using network measures, strength, and temporal variability of functional integration of the following four paths were the top predictive features: L_MFG → L_Insula, L_Insula → L_Amygdala, L_Amygdala → R_Hippocampus and R_Hippocampus → L_Precuneus). Coincidentally these four paths also showed statistically significant differences in static as well as time-varying network properties (the yellow paths in **Figure 8**, which were significantly different between all three groups). Also, coincidentally, these were the same four paths whose network measures had significant associations with neurocognitive functioning and symptom severity. To expand upon this, our findings revealed that, in addition to behavioral relevance and statistical separation, these paths also possessed the highest predictive ability, all obtained in a data-driven fashion from whole-brain complex-network data.

Machine Learning Regression Results

Finally, using these network properties (the yellow paths in **Figure 8**), we performed SVR to predict PCL5 (and NSI) scores. Over one million iterations, we found that predicted and measured PCL5 scores were significantly correlated ($R^2 = 0.72 \pm 0.05$, $R = 0.85 \pm 0.03$, $P = 3 \times 10^{-7} \pm 10^{-6}$), as also were predicted and measured NSI scores ($R^2 = 0.66 \pm 0.04$, $R = 0.81 \pm 0.03$, $P = 7 \times 10^{-7} \pm 10^{-6}$). With such high predictive ability (i.e., 66–72% variance explained in symptom severity), these network properties assume considerable importance in the context of PTSD and PCS + PTSD pathology. **Figure 4** summarizes the processing pipeline of our entire work, along with corresponding results.

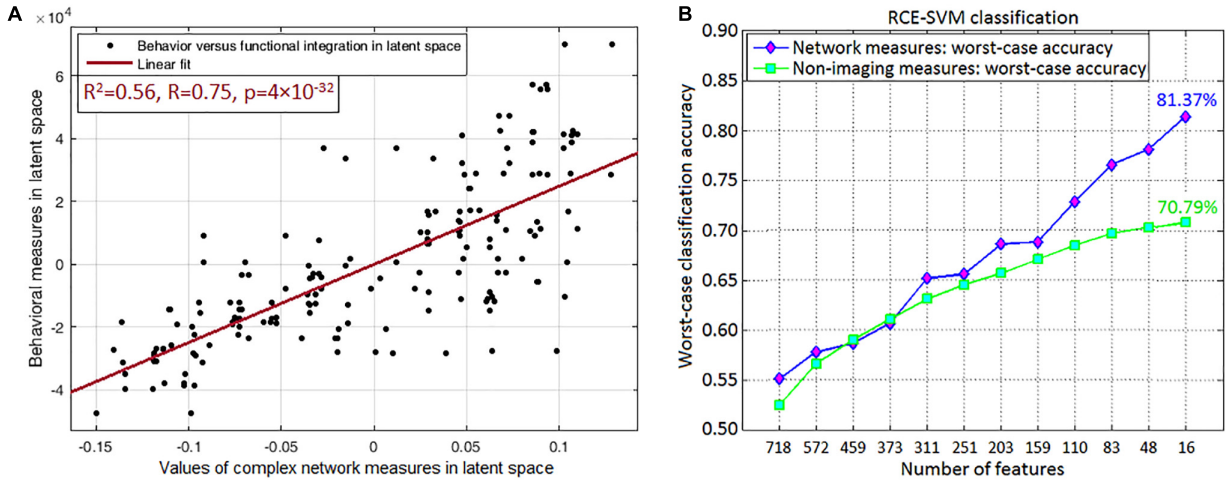

FIGURE 9 | Association and prediction results. **(A)** Partial least squares regression maps independent (all included network measures combined) and dependent (all neurobehaviors combined) variables into a latent space to find an aggregate relationship between them. The regression displayed in the figure is performed in the latent space, which contains categorical variables representing all included network measures of the four integration paths (MFG → Insula, Insula → Amygdala, Amygdala → Hippocampus, Hippocampus → Precuneus) and two functional segregation nodes (MFG, Insula) (both of which fit our hypothesis), and the neurobehaviors in latent space. Their association in the latent space could be considered as the net association of all these network measures with all the neurobehaviors. **(A)** Shows the linear fit in latent space (R^2 = 0.56, R = 0.75, p = 3.5 × 10^{-32}). **(B)** Machine learning classification result, which was obtained through recursive cluster elimination based support vector machine (RCE-SVM) classifier, to classify between control, PTSD and PCS + PTSD groups. **(B)** Shows worst-case classification accuracies obtained using recursively reducing number of discriminative features (poorer features are successively eliminated). Classification was independently performed with both complex-network measures obtained from the entire brain and non-imaging measures (NIMs). We observed that network measures outperformed NIMs, with approximately 10% superior performance in the final RCE step using top-predictive features of network measures.

DISCUSSION

In the current study, we successfully employed a novel complex-network modeling framework to understand network-level impairments in PTSD with and without mTBI. With the evidence that the healthy brain is characterized by a balance between functional segregation and integration, we sought to identify aberrations in segregation and integration in these disorders. We hypothesized that *PTSD and mTBI are characterized by altered strength and lower temporal variability of segregation and integration in directional brain networks*. Specifically, we sought to identify networks that were affected by PTSD but not mTBI (hypothesis-1), as well as those affected by both PTSD and mTBI (PTSD and PCS + PTSD group) (hypothesis-2). We found evidence to support both hypotheses. This is the first fMRI study utilizing EC network modeling in either PTSD or PCS or the comorbid condition; the first study aiming to classify PTSD from comorbid PTSD/mTBI based on resting-state network properties using machine learning techniques; and the first study to examine network properties using both static and time-varying methods.

TABLE 3 | Machine learning classification was performed using recursive cluster elimination based support vector machine (RCE-SVM), to classify between controls, PTSD and PCS + PTSD groups.

	Worst-case accuracy	Top-predictive features
Non-imaging measures	70.79%	Epworth sleepiness scale and Zung depression scale
Complex network measures	81.37%	Strength and variability of functional integration of the four yellow paths in **Figure 8**
p-value for row-wise comparison	7.81 × 10^{-28}	

Table presents the obtained worst-case classification accuracies along with top-predictive features.

With global measures, we found that segregation and integration were significantly different for control vs PTSD and control vs PCS + PTSD comparisons only. This implies that the clinical groups had aberrations at the whole-brain level compared to controls, which is expected. However, the PTSD and comorbid groups do not exhibit any differences at the whole-brain level, suggesting that mTBI might result in more localized aberrations not detectable by network modeling at the whole-brain level. To further investigate discrete group differences, we used local measures of segregation and integration.

In accordance with our hypothesis (**Figure 1**), group differences in local segregation measures showed a clear dichotomy between prefrontal and occipital regions (**Figure 6A**); with all identified prefrontal nodes having lower segregation and all identified occipital and subcortical nodes having higher segregation. This indicates disruptive reduction in specialized local processing in the prefrontal cortex, especially in the MFG and medial prefrontal regions. This disruption had a negative relationship with the occipital and subcortical nodes, which showed disruptive increase in local processing. In addition, none of the occipital nodes were significantly different between

PTSD and PCS + PTSD, implying that those regions might not differentiate between PTSD and PCS + PTSD.

With local integration measures, we found a clear dichotomy along two distinct pathways. The fronto-visual-parietal pathway (**Figure 7A**) was not significantly different between PTSD and PCS + PTSD groups, indicating that mTBI likely does not have a significant impact on this part of the network. Neither these paths (either connectivities or integration measures) nor the associated occipital nodes (segregation) exhibited any significant association with symptom severity (PCL5 and NSI) or neurocognitive functioning, hence we inferred that this part of the network does not play a significant role in symptom expression, but it might act as a supportive backend for other neural processes causing the symptoms. The other pathway (fronto-subcortical-parietal, **Figure 7A**) was significantly different between all the three groups, and network properties of the paths and associated nodes also showed significant associations with symptom severity and neurocognitive functioning. Thus, we inferred that disruption of this part of the network contributes to symptom expression, and is likely implicated in mTBI pathology. This dichotomy provides novel insights into our understanding of both common and distinguishing network characteristics in PTSD and mTBI, which has largely plagued the field, given the high comorbidity and overlapping symptomatology between them (Simmons and Matthews, 2012).

Another clear dichotomy arises in the strength of network properties across groups. All prefrontal nodes and the paths associated with them showed lower segregation/integration in PTSD and PCS + PTSD compared to controls, suggesting a strong effect of disruptive *deflation* prevalent in the prefrontal cortex. All the subcortical, parietal and occipital nodes showed higher segregation, and all paths associated with them not involving prefrontal regions showed higher integration in PTSD and PCS + PTSD compared to controls, a clear indication of disruptive *inflation* in these regions. Notably, these trends were also replicated in the raw effective connectivity values. We argue that this is definitive evidence for impaired prefrontal top-down regulation causing reduced control over limbic structures and other regions responsible for symptom-expression. Such unambiguous dichotomy clearly delineates the distinct functionality between the prefrontal cortex and the rest of the brain, and highlights its relevance to PTSD and mTBI.

Such dichotomy was not observed in the temporal variability of network properties, in that all nodes/paths showed lower variance, indicating some degree of pathological "frozen" state (in accordance with our hypothesis). In other words, paths with lower strength of network properties (*deflation*) tended to remain in that state over the duration of the scan, potentially suggesting impaired ability to increase the connectivity and the values of complex-network measures. Similarly, paths with higher strength of network properties (*inflation*) tended to remain inflated, also indicating impaired ability to decrease the connectivity and the values of complex-network measures. In total, we identified 15 nodes (segregation) and 16 paths (integration) which were significantly different with the control vs. PTSD and control vs PCS + PTSD comparisons, while only four nodes and five paths were significantly different between all the three groups. It is noteworthy that all the other nodes, with the exception of the amygdala and parietal regions, involved in the connections with affected functional integration also had altered segregation, implying segregation-integration imbalance in these regions. This observation corroborates with prior works, which have found evidence for a fine balance between segregation and integration (or metastability) in healthy individuals (Hellyer et al., 2015), which is disrupted in neurologic and psychiatric disorders (Yu et al., 2013; Rocca et al., 2014).

The networks were obtained with resting-state fMRI data; hence, they represent the differences in baseline state between the groups. Based on the prior knowledge regarding the neural mechanisms underlying cognitive emotion regulation (Gross, 2014), we propose that our network (**Figure 8**) corresponds to an aberrant emotion regulation system, with impaired prefrontal control leading to an insufficient control over emotionally intensive traumatic memories, which might underpin trauma re-experiencing, flashbacks, hyperarousal and other symptoms in soldiers with PTSD and PCS + PTSD.

Functions of the individual nodes/regions that were identified as having aberrations in the complex-network properties provides interesting insights into the neuropathology underpinning PTSD and mTBI. The MFG has been implicated in cognitive control (Emmert et al., 2016), which includes emotion regulation. It plays a pivotal role in the initiation of voluntary regulation of emotion (Gross, 2014). All of the network-level aberrations in our results could be traced back to the MFG (by tracing the directional connections), leading us to the conclusion that the MFG is the origin of network disruption in these disorders. Several earlier works have speculated about the MFG to be the likely origin of network disruption in PTSD (White et al., 2014; Kennis et al., 2015), including a recent meta-analysis (Simmons and Matthews, 2012). However, direct evidence for such a hypothesis has not been found so far. We provide novel evidence that supports this explanation. In fact, a recent meta-analysis presented evidence from numerous findings that repetitive transcranial magnetic stimulation (rTMS) applied to the MFG may be effective as a treatment for PTSD (Berlim and Van Den Eynde, 2014). Corroborating this, we discovered the network of disturbance caused by the impairment of MFG, wherein MFG is the source of disruptions. Taken together, the MFG likely plays a key role in the initiation of cognitive control necessary for emotion regulation, which when compromised, likely contributes to the maintenance of symptoms associated with PTSD and PCS + PTSD.

We noticed prefrontal top-down *deflation* of functional integration driven by the MFG, resulting in the *inflation* of functional integration in sub-cortical structures via the insula as well as parietal memory-related and sensory association regions. The anterior insula plays a major role in mediating prefrontal control over subcortical regions, and is thus found to be involved in emotion regulation and dysregulation (Thayer and Lane, 2000; Gross, 2014). It is structurally well connected with the amygdala through white-matter tracts (Oishi et al., 2015), and also plays a key role in subjective emotional experiences (feelings), integrating emotionally relevant information through multiple sources, and possibly representing them as one of the many complex emotions (Thayer and Lane, 2000). We found that prefrontal *deflation* of the insula causes inflated

functional integration in the amygdala, which then results in inflated local functional integration in the hippocampus. *Inflation* of the hippocampus, a region crucial for declarative memories, might imply elevated explicit traumatic memory retrieval. It is well documented that both the hippocampus and the amygdala play a vital role in mTBI and PTSD (Simmons and Matthews, 2012; Costanzo et al., 2014). Since traumatic memories are unique in the intensity of associated negative emotions, emotion and memory share deep interconnection in PTSD (Vasterling et al., 2009).

The precuneus plays an important role in the generation of the experience of visual memories, whereas the TPJ is necessary for higher-level audio-visual verbalization and information processing (Gross, 2014). The path from the MFG leading to these regions was characterized by reduced strength and variance of functional integration. Thus, the memory-related and sensory association network comprising the precuneus and TPJ may translate to subcortical *inflation* and lack of prefrontal control, contributing to the perseveration of traumatic memories as observed in soldiers with PTSD.

There was a robust finding of disruption in the occipital regions in our results. While the majority of the nodes and paths were associated with the occipital region, none of them were significantly different between PTSD and PCS + PTSD groups, and none of them had behavioral relevance (through associations with symptom severity and neurocognitive performance). Hence, we inferred that this part of the network does not play a significant role in symptom generation, but might act as a supportive backend for the other fronto-subcortical-parietal processes, which do appear to contribute to the symptoms (owing to their association with symptom severity). This inference is justifiable, given that the visual imagery aspect of traumatic memories dominates the experience of vivid imagery associated with traumatic memory perseveration in PTSD (Hayes et al., 2012). It is known that the secondary visual regions, including the lingual gyrus, largely enables visual imagery (Thompson et al., 2009). In addition, the degree of activation in visual areas during imagery is directly proportional to the visual intensity of the object being imagined (Carpenter et al., 1999). Hence, it is likely that this measure is not sensitive to discriminate between PTSD and PCS + PTSD groups. This could provide substantiation for our inference that the occipital part of the network might be a backend process providing "imagery support." Thus, it appears more likely that symptom severity can be attributed to the disruptions originating in the MFG, as illustrated by significant associations with neurocognitive performance and symptom scores.

There has been little success in addressing diagnostic limitations associated with homogeneity of symptoms and high comorbidity between PTSD and mTBI in military personnel (Costanzo et al., 2014). It is acknowledged that the additional burden of an mTBI in comorbid PCS + PTSD results in increased symptom severity (Vasterling et al., 2009). In the current study, we provide a mechanistic basis that might distinguish the underlying neurologic disruptions contributing to symptoms reported by PTSD cases from those reported by comorbid PTSD/mTBI cases. It is unclear as to whether the differences between the PTSD and PCS + PTSD groups are driven by higher symptom severity of the PCS + PTSD group or by impairments in white-matter integrity caused by an mTBI. A recent study found diffused white-matter tracts between the hippocampus and striatum to be the cause of corresponding functional connectivity differences between PTSD and comorbid PTSD/mTBI conditions (Rangaprakash et al., 2017a), yet it is unclear whether they can be extended to our findings. The network pathways that seem to differentiate, based on the strength of associations with neurocognitive measures, between the PTSD and comorbid PTSD/mTBI cases (PCS + PTSD) were the MFG, insula, amygdala, hippocampus, and precuneus.

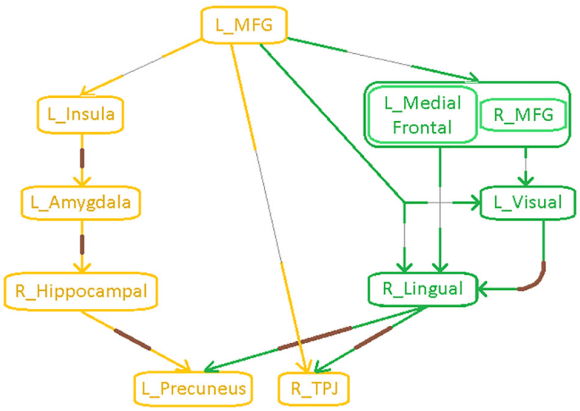

FIGURE 10 | Flowchart illustrating an integrated model of connectivity and network-level aberrations in PTSD and mTBI. Paths with thin gray lines correspond to lower strength of network properties and connectivity (SEC) and lower temporal variability of network properties (i.e., rigidity) and connectivity (vDEC) in the clinical groups compared to healthy controls, indicative of breakdown in prefrontal top-down modulation. Paths with thick brown lines correspond to higher strength and lower temporal variability (i.e., rigidity) of network properties and connectivity, indicative of *inflation* in subcortical limbic and parietal memory-related regions. Yellow paths were significantly different between all the three groups, while the green paths were significantly different only for the control vs. PTSD and control vs. PCS + PTSD comparisons.

Our results are significant given that regions identified here have been implicated (albeit inconsistently) in earlier studies (Hayes et al., 2012; Simmons and Matthews, 2012; Eierud et al., 2014) to be involved in both PTSD and mTBI; however, a precise understanding of the underlying mechanisms, network structure, and their subsequent causal relationships has not emerged from them. With the help of a novel framework involving complex-network modeling with static and dynamic EC networks, we identified the nodes and network paths associated with the disorders, and detailed their directional relationships. We also highlighted the commonalities and differences in the PTSD and PCS + PTSD networks. Our characterization corroborates with behavioral manifestations of PTSD and PCS + PTSD, thus substantiating the utility and fidelity of our approach. **Figure 10** summarizes our network-level findings with a flowchart.

Additionally, functional integration of four specific paths had significant associations with neurocognitive performance and symptom severity (MFG → insula, insula → amygdala,

amygdala → hippocampus, hippocampus → precuneus), as also did functional segregation of two nodes (MFG and insula), highlighting their relevance to the underlying neurobehavior and symptomatology. These paths and nodes were the same as those which were identified as significantly different between all the three groups (**Figure 8**). In the PLS regression model, the aforementioned network measures explained approximately 62% variance in neurobehavioral measures.

Finally, we employed supervised machine learning classification to identify top predictors that could diagnose a novel subject. Literature is highly limited on the application of machine learning to the classification of either PTSD or mTBI [see notable recent works (Liu et al., 2015; Vergara et al., 2016)]. Additionally, there have been no studies to have employed machine learning to classify comorbid PTSD and mTBI. A notable contribution of our work is that we performed machine learning classification, and found that accuracies obtained using network measures were significantly higher (∼10% more) than non-imaging measures. Interestingly, we found that the network measures of the same four aforementioned paths (MFG → insula, insula → amygdala, amygdala → hippocampus, hippocampus → precuneus) resulted in the highest classification accuracy. They were identified to be the top features of diagnostic prediction, in addition to being identified as statistically significant in accordance with our hypothesis, as also being behaviorally relevant through associations with neurocognitive and symptom scores. Each of these attributes were determined in a data-driven fashion from network properties of the entire brain, without imposing any priors or biases. In addition, SVR analysis showed that PCL5 and NSI scores predicted using these network properties could explain 72% and 66% variance in measured symptom severity, respectively. These observations demonstrate that these network-level markers have potential as high-quality biomarkers of the neurobehavioral characteristics of PTSD and PCS. Our network-level features satisfy three out of four conditions posited by Woo and Wager (2015) as necessary to be a good biomarker (diagnosticity, deployability, and interpretability). With regard to the fourth condition (generalizability), based on suggestions by Woo and Wager (2015), we issue an open call for researchers to share clinical data with us for validating our classifier using their data.

Our work presents some notable methodological contributions. While modeling of dynamic connectivity has been prevalent for a while (Hutchison et al., 2013), the modeling of dynamic properties of complex-network measures is in its nascent stages. Graph theoretic measures provide additional characterization of the connectomic brain, which is not available through pairwise connectivity modeling (Rubinov and Sporns, 2010), hence the development and advancement of dynamic complex-network modeling (similar to dynamic connectivity modeling) is important and necessary for brain imaging. A few studies have probed on this topic. Zalesky et al.'s (2014) work was one of the first major studies on dynamics of graph metrics, wherein they introduced the modeling of time-varying graph measures. Liao et al. (2015) later explored the structural substrates of time-varying graph metrics, whereas Chiang et al. (2016) presented a technique for studying temporal stationarity of graph metrics. Chen et al. (2016) took forward these developments to study the dynamics of the salience network's spatiotemporal organization, while Betzel et al. (2016) studied the correspondence between dynamics of connectivity and dynamics of modularity. These studies have demonstrated the use of time-varying graph metrics in different ways; however, as Preti et al. (2016) have pointed out in their review, prior studies have focused on only two metrics, efficiency and modularity. None of these studies integrates information from both static and time-varying graph metrics, nor have they probed into the dynamics of graph metrics obtained from directional connectivity. Our study is an advancement over these prior works, in that we present a technique to compute time-varying global, nodal as well as connection-level metrics of segregation and integration from effective connectivity networks, additionally presenting a novel framework for integrating the variability in dynamic network information with static network information to study three different cohorts (two psychiatric populations and a control group). In our opinion, this is a notable advancement in the field. Our contribution is broad and robust to accommodate the specific requirements of different varieties of brain imaging studies.

This study integrates several dimensions within a single framework, as follows: (i) Connectivity modeling as well as complex network modeling, (ii) segregation (node-level) as well as integration (connection-level), (iii) static as well as dynamic connectivity, (iv) EC modeling, especially dynamic EC being a recent advancement, (v) PTSD as well as comorbid PCS + PTSD, and (vi) statistical analysis as well as machine-learning based predictive analysis. It is notable that this is the first fMRI study to utilize either effective connectivity or dynamic connectivity or static/dynamic complex-network modeling based on effective connectivity in either PTSD or PCS or the comorbid condition; and one among a few studies to have utilized machine learning in either of these disorders. Additionally, since our findings were based on an overlap/intersection of results with the PTSD and the PCS + PTSD groups, the observations and conclusions are also relevant to the characterization of PTSD alone. We intend to convey that our novel framework is relevant to the study of any cognitive domain, psychiatric or neurologic condition. We urge researchers to employ this framework for enhancing the understanding other disorders and cognitive domains.

Finally, we present several caveats and limitations of our work, demanding careful interpretation of the findings, as also providing suggestions for future works: (1) Participants sustaining an added burden of PCS in addition to PTSD displayed higher symptom severity in comparison to those with PTSD alone. Though there is limited imaging literature on comorbid PTSD and PCS, we speculate that: (i) PTSD-related brain aberrations that were already prevalent before developing PCS would be aggravated by the added burden of a prior mTBI, *or*, (ii) alleviated functional neural aberrations corresponding to elevated symptom severity would be a consequence of the participants sustaining an mTBI with subsequently or concomitantly being exposed to a traumatic

experience, in comparison to participants who were exposed to psychological trauma alone. Untangling the underlying cause-effect relationships in comorbid PTSD and PCS could be an aim of future experimental designs, in order to confirm either of the two scenarios. (2) Though we compare and discus the common and distinguishing neural phenotypes of PTSD and mTBI, it must be noted that our study population did not consist of a pure mTBI/PCS group; rather it consisted of a group with elevated PTSD symptoms (pure PTSD group) and a comorbid group diagnosed with both mTBI/PCS and PTSD, using which the common and distinguishing neural phenotypes of PTSD and mTBI/PCS were derived through our novel framework (**Figure 1**). (3) Military participants with CES were part of our study cohort. This is an invaluable strength of our work since it provides a more representative control group. Recent works have found differences between healthy civilians and healthy combat personnel with resting-state fMRI connectivity (Kennis et al., 2015), "potentially due to military training, deployment, and/or trauma exposure." Hence, future studies could verify if our findings are equally applicable to civilian or non-combat-related PTSD and PCS. (4) With only male soldiers being considered in this study, our findings are not directly generalizable to female soldiers. (5) During RCE-SVM classification, our entire dataset was split into training (80%) and testing/validation (20%) data sets, resulting in about seventeen participants (20% of 87 participants) in the testing set. This is not a relatively large number for an fMRI connectivity study. (6) Given the heterogeneous patterns in PTSD and mTBI, the number of subjects used in this study is relatively small, which raises concerns about the reproducibility of our results. Our findings must thus be interpreted with certain degree of caution. Additionally, we invite researchers to replicate our study design in larger sample sizes to assess reproducibility of our findings. To determine clinical utility of the findings for diagnosis, the findings must be replicated on a larger sample that is representative of the target population in terms of ethnicity, gender, etc. (7) Given the uncontrolled nature of resting state (Hurlburt et al., 2015), it is not possible to determine whether resting-state connectivity differences between groups are driven by differences in the "type of mind wandering" exhibited by controls versus those with disorder, rather than an inherent "baseline" difference. It is possible that the scanning session had captured the brain while being engaged in the symptomatic state itself rather than, or perhaps in addition to, capturing the underlying physiological weaknesses that putatively caused the symptoms. This issue could be specific to only some clinical populations like ours, where symptoms often manifest during periods of idle thought. It is not possible to completely untangle this problem with the data we have. However, future studies could employ methods such as "descriptive experience sampling" (Hurlburt et al., 2015) in order to characterize the "type of mind wandering" in PTSD versus controls so as to ascertain whether such differences might underlie alterations in resting state connectivity. (8) With our fMRI data being cross-sectional, there is scope for longitudinal studies to develop similar hypotheses over the advancement, recovery and rehabilitation phases of the clinical groups. In addition, it would be an appropriate test for validating the four pivotal network paths underlying information integration (L_MFG → L_Insula, L_Insula → L_Amygdala, L_Amyg → R_Hippocampus, R_Hippocampus → L_Precuneus) as candidate imaging biomarkers for PTSD, and comorbid PCS and PTSD.

ETHICS STATEMENT

This study was conducted in accordance with the Declaration of Helsinki, and the procedures were approved by the Auburn University's Institutional Review Board (IRB) as well as the Headquarters United States Army Medical Research and Materiel Command, IRB (HQ USAMRDC IRB). Written informed consent was obtained from all the participants. Material has been reviewed by the Walter Reed Army Institute of Research. There is no objection to its presentation and/or publication. The opinions or assertions contained herein are the private views of the author, and are not to be construed as official, or as reflecting true views of the Department of the Army or the Department of Defense. The investigators have adhered to the policies for protection of human subjects as prescribed in AR 70–25.

AUTHOR CONTRIBUTIONS

DR, MD, JK, TD, and GD conceived the work and wrote the manuscript. DR, MD, JK, and GD developed the methodology. TD and GD provided the resources and supervised the entire work. MD was the project PI.

FUNDING

All authors acknowledge financial support for this work from the United States Army Medical Research and Materiel Command (MRMC) (Grant # 00007218). The funders had no role in study design, data collection and analysis, decision to publish, or preparation of the manuscript.

ACKNOWLEDGMENTS

All authors thank the personnel at the TBI Clinic and Behavioral Health Clinic, Fort Benning, GA, United States and the U.S. Army Aeromedical Research Laboratory, Fort Rucker, AL, United States, and most of all, the soldiers who participated in the study. The authors also thank Julie Rodiek and Wayne Duggan for facilitating data acquisition. Contents of this study have appeared in DR's doctoral thesis (Rangaprakash, 2016).

SUPPLEMENTARY MATERIAL

The Supplementary Material for this article can be found online at: https://www.frontiersin.org/articles/10.3389/fnins.2019.00803/full#supplementary-material

REFERENCES

Abler, B., Roebroeck, A., Goebel, R., Höse, A., Schönfeldt-Lecuona, C., Hole, G., et al. (2006). Investigating directed influences between activated brain areas in a motor-response task using fMRI. *Magn. Reson. Imaging* 24, 181–185. doi: 10.1016/j.mri.2005.10.022

Amico, E., Gomez, F., Di Perri, C., Vanhaudenhuyse, A., Lesenfants, D., Boveroux, P., et al. (2014). Posterior cingulate cortex-related co-activation patterns: a resting state FMRI study in propofol-induced loss of consciousness. *PLoS One* 9:e100012. doi: 10.1371/journal.pone.0100012

Bellucci, G., Chernyak, S., Hoffman, M., Deshpande, G., Monte, O., Knutson, K., et al. (2016). Effective connectivity of brain regions underlying third party punishment: functional MRI and granger causality evidence. *Soc. Neurosci.* 12, 124–134. doi: 10.1080/17470919.2016.1153518

Berlim, M. T., and Van Den Eynde, F. (2014). Repetitive transcranial magnetic stimulation over the dorsolateral prefrontal cortex for treating posttraumatic stress disorder: an exploratory meta-analysis of randomized, double-blind and sham-controlled trials. *Can. J. Psychiatry* 59, 487–496. doi: 10.1177/070674371405900905

Betzel, R., Fukushima, M., He, Y., Zuo, X., and Sporns, O. (2016). Dynamic fluctuations coincide with periods of high and low modularity in resting-state functional brain networks. *Neuroimage* 127, 287–297. doi: 10.1016/j.neuroimage.2015.12.001

Blevins, C., Weathers, F., Davis, M., Witte, T., and Domino, J. (2015). The posttraumatic stress disorder checklist for DSM-5 (PCL-5): development and initial psychometric evaluation. *J. Trauma Stress.* 28, 489–498. doi: 10.1002/jts.22059

Boly, M., Sasai, S., Gosseries, O., Oizumi, M., Casali, A., Massimini, M., et al. (2015). Stimulus set meaningfulness and neurophysiological differentiation: a functional magnetic resonance imaging study. *PLoS One* 10:e0125337. doi: 10.1371/journal.pone.0125337

Büchel, C., and Friston, K. (1998). Dynamic changes in effective connectivity characterized by variable parameter regression and Kalman filtering. *Hum. Brain Mapp.* 6, 403–408. doi: 10.1002/(sici)1097-0193(1998)6:5/6<403::aid-hbm14>3.3.co;2-0

Carpenter, P. A., Just, M. A., Keller, T. A., Eddy, W., and Thulborn, K. (1999). Graded functional activation in the visuospatial system with the amount of task demand. *J. Cogn. Neurosci.* 11, 9–24. doi: 10.1162/089892999563210

Chao-Gan, Y., and Yu-Feng, Z. (2010). DPARSF: a MATLAB toolbox for pipeline data analysis of resting-state fMRI. *Front. Syst. Neurosci.* 4:13. doi: 10.3389/fnsys.2010.00013

Chen, G., Ward, D., Xie, C., Li, W., Wu, Z., Jones, J. L., et al. (2011). Classification of Alzheimer disease, mild cognitive impairment, and normal cognitive status with large-scale network analysis based on resting-state functional MR imaging. *Radiology* 259, 213–221. doi: 10.1148/radiol.10100734

Chen, T., Cai, W., Ryali, S., Supekar, K., and Menon, V. (2016). Distinct global brain dynamics and spatiotemporal organization of the salience network. *PLoS Biol.* 14:e1002469. doi: 10.1371/journal.pbio.1002469

Chiang, S., Cassese, A., Guindani, M., Vannucci, M., Yeh, H., Haneef, Z., et al. (2016). Time-dependence of graph theory metrics in functional connectivity analysis. *Neuroimage* 125, 601–615. doi: 10.1016/j.neuroimage.2015.10.070

Cicerone, K. D., and Kalmar, K. (1995). Persistent postconcussion syndrome: the structure of subjective complaints after mild traumatic brain injury. *J. Head Trauma Rehabil.* 10, 1–17.

Cisler, J., Steele, J., Lenow, J., Smitherman, S., Everett, B., Messias, E., et al. (2014). Functional reorganization of neural networks during repeated exposure to the traumatic memory in posttraumatic stress disorder: an exploratory fMRI study. *J. Psychiatr. Res.* 48, 47–55. doi: 10.1016/j.jpsychires.2013.09.013

Costanzo, M. E., Chou, Y. Y., Leaman, S., Pham, D. L., Keyser, D., Nathan, D. E., et al. (2014). Connecting combat-related mild traumatic brain injury with posttraumatic stress disorder symptoms through brain imaging. *Neurosci. Lett.* 577, 11–15. doi: 10.1016/j.neulet.2014.05.054

Craddock, R., James, G., Holtzheimer, P. I., Hu, X., and Mayberg, H. (2012). A whole brain fMRI atlas generated via spatially constrained spectral clustering. *Hum. Brain Mapp.* 33, 1914–1928. doi: 10.1002/hbm.21333

Crone, J. S., Soddu, A., Höller, Y., Vanhaudenhuyse, A., Schurz, M., Bergmann, J., et al. (2013). Altered network properties of the fronto-parietal network and the thalamus in impaired consciousness. *Neuroimage Clin.* 4, 240–248. doi: 10.1016/j.nicl.2013.12.005

David, O., Guillemain, I., Saillet, S., Reyt, S., Deransart, S., Segebarth, C., et al. (2008). Identifying neural drivers with functional MRI: an electrophysiological validation. *PLoS Biol.* 6:e315. doi: 10.1371/journal.pbio.0060315

Deshpande, G., and Hu, X. (2012). Investigating effective brain connectivity from fMRI data: past findings and current issues with reference to Granger causality analysis. *Brain Connect.* 2, 235–245. doi: 10.1089/brain.2012.0091

Deshpande, G., James, G., Craddock, R., Mayberg, H. S., and Hu, X. P. (2009). "Predicting Treatment in Patients with Major Depression Using Granger-Based Connectivity and Support Vector Machines," in *Proceedings of ISMRM 17th Scientific Meeting*, Honolulu, HI.

Deshpande, G., Li, Z., Santhanam, P., Coles, C. L. M., Hamann, S., and Hu, X. (2010a). Recursive cluster elimination based support vector machine for disease state prediction using resting state functional and effective brain connectivity. *PLoS One* 5:e14277. doi: 10.1371/journal.pone.0014277

Deshpande, G., Sathian, K., and Hu, X. (2010b). Assessing and compensating for zero-lag correlation effects in time-lagged Granger causality analysis of FMRI. *IEEE Trans. Biomed. Eng.* 57, 1446–1456. doi: 10.1109/TBME.2009.2037808

Deshpande, G., Libero, L., Sreenivasan, K., Deshpande, H., and Kana, R. (2013). Identification of neural connectivity signatures of autism using machine learning. *Front. Hum. Neurosci.* 17:670. doi: 10.3389/fnhum.2013.00670

Deshpande, G., Santhanam, P., and Hu, X. (2011). Instantaneous and causal connectivity in resting state brain networks derived from functional MRI data. *Neuroimage* 54, 1043–1052. doi: 10.1016/j.neuroimage.2010.09.024

Deshpande, G., Wang, P., Rangaprakash, D., and Wilamowski, B. (2015). Fully connected cascade artificial neural network architecture for attention deficit hyperactivity disorder classification from functional magnetic resonance imaging data. *IEEE Trans. Cybernatics* 45, 2668–2679. doi: 10.1109/TCYB.2014.2379621

Eierud, C., Craddock, R., Fletcher, S., Aulakh, M., King-Casas, B., Kuehl, D., et al. (2014). Neuroimaging after mild traumatic brain injury: review and meta-analysis. *Neuroimage Clin.* 4, 283–294. doi: 10.1016/j.nicl.2013.12.009

Emmert, K., Kopel, R., Sulzer, J., Brühl, A. B., Berman, B. D., Linden, D. E. J., et al. (2016). Meta-analysis of real-time fMRI neurofeedback studies using individual participant data: how is brain regulation mediated? *Neuroimage* 124(Pt A), 806–812. doi: 10.1016/j.neuroimage.2015.09.042

Feng, C., Deshpande, G., Liu, C., Gu, R., Luo, Y.-J., and Krueger, F. (2015). Diffusion of responsibility attenuates altruistic punishment: a functional magnetic resonance imaging effective connectivity study. *Hum. Brain Mapp.* 37, 663–677. doi: 10.1002/hbm.23057

Friston, K. J., Ashburner, J., Kiebel, S. J., Nichols, T. E., and Penny, W. D. (2007). *Statistical Parametric Mapping: The Analysis of Functional Brain Images*. Cambridge, MA: Academic Press.

Garrett, D., Samanez-Larkin, G., MacDonald, S., Lindenberger, U., McIntosh, A., and Grady, C. (2013). Moment-to-moment brain signal variability: a next frontier in human brain mapping? *Neurosci. Biobehav. Rev.* 37, 610–624. doi: 10.1016/j.neubiorev.2013.02.015

Granger, C. (1969). Investigating causal relations by econometric models and cross-spectral methods. *Econometrica* 37, 424–438.

Grant, M., White, D., Hadley, J., Hutcheson, N., Shelton, R., Sreenivasan, K., et al. (2014). Early life trauma and directional brain connectivity within major depression. *Hum. Brain Mapp.* 35, 4815–4826. doi: 10.1002/hbm.22514

Grant, M., Wood, K., Sreenivasan, K., Wheelock, M., White, D., Thomas, J., et al. (2015). Influence of early life stress on intra- and extra-amygdaloid causal connectivity. *Neuropsychopharmacology* 40, 1782–1793. doi: 10.1038/npp.2015.28

Gray, M., Litz, B., Hsu, J., and Lombardo, T. (2004). Psychometric properties of the life events checklist. *Assessment* 11, 330–341. doi: 10.1177/1073191104269954

Gross, J. J. (2014). *Handbook of Emotion Regulation*. New York, NY: The Guilford Press.

Gualtieri, C. T., and Johnson, L. G. (2006). Reliability and validity of a computerized neurocognitive test battery, CNS Vital Signs. *Arch. Clin. Neuropsychol.* 21, 623–643. doi: 10.1016/j.acn.2006.05.007

Guyker, W., Donnelly, K., Donnelly, J., Dunnam, M., Warner, G., Kittleson, J., et al. (2013). Dimensionality, reliability, and validity of the combat

experiences scale. *Mil. Med.* 178, 377–384. doi: 10.7205/MILMED-D-12-00223

Hall, C., Howarth, C., Kurth-Nelson, Z., and Mishra, A. (2016). Interpreting BOLD: towards a dialogue between cognitive and cellular neuroscience. *Philos. Trans. R. Soc. Lond. B.* 371:20150348. doi: 10.1098/rstb.2015.0348

Handwerker, D. A., Ollinger, J. M., and D'Esposito, M. (2004). Variation of BOLD hemodynamic responses across subjects and brain regions and their effects on statistical analyses. *Neuroimage* 21, 1639–1651. doi: 10.1016/j.neuroimage.2003.11.029

Hansen, E., Battaglia, D., Spiegler, A., Deco, G., and Jirsa, V. (2015). Functional connectivity dynamics: modeling the switching behavior of the resting state. *Neuroimage* 105, 525–535. doi: 10.1016/j.neuroimage.2014.11.001

Hayes, J., Vanelzakker, M., and Shin, L. (2012). Emotion and cognition interactions in PTSD: a review of neurocognitive and neuroimaging studies. *Front. Integr. Neurosci.* 6:89. doi: 10.3389/fnint.2012.00089

Hellyer, P., Scott, G., Shanahan, M., Sharp, D., and Leech, R. (2015). Cognitive flexibility through metastable neural dynamics is disrupted by damage to the structural connectome. *J. Neurosci.* 35, 9050–9063. doi: 10.1523/JNEUROSCI.4648-14.2015

Hillary, F., Roman, C., Venkatesan, U., Rajtmajer, S. M., Bajo, R., and Castellanos, N. D. (2015). Hyperconnectivity is a fundamental response to neurological disruption. *Neuropsychology* 29, 59–75. doi: 10.1037/neu0000110

Hoge, C. W., Castro, C., Messer, S. C., McGurk, D., Cotting, D. I., and Koffman, R. L. (2008). Mild traumatic brain injury in U.S. soldiers returning from Iraq. *N. Engl. J. Med.* 358, 453–463. doi: 10.1056/NEJMoa072972

Hoge, C. W., Goldberg, H. M., and Castro, C. A. (2009). Care of war veterans with mild traumatic brain injury: flawed perspectives. *N. Engl. J. Med.* 360, 1588–1591. doi: 10.1056/nejmp0810606

Hurlburt, R., Alderson-Day, B., Fernyhough, C., and Kühn, S. (2015). What goes on in the resting-state? A qualitative glimpse into resting-state experience in the scanner. *Front. Psychol.* 6:1535. doi: 10.3389/fpsyg.2015.01535

Hutcheson, N. L., Sreenivasan, K. R., Deshpande, G., Reid, M. A., Hadley, J., White, D. M., et al. (2015). Effective connectivity during episodic memory retrieval in schizophrenia participants before and after antipsychotic medication. *Hum. Brain Mapp.* 36, 1442–1457. doi: 10.1002/hbm.22714

Hutchison, R., Womelsdorf, T., Allen, E., Bandettini, P., Calhoun, V., Corbetta, M., et al. (2013). Dynamic functional connectivity: promise, issues, and interpretations. *Neuroimage* 80, 360–378. doi: 10.1016/j.neuroimage.2013.05.079

Jia, H., Hu, X., and Deshpande, G. (2014). Behavioral relevance of the dynamics of the functional brain connectome. *Brain Connect.* 4, 741–759. doi: 10.1089/brain.2014.0300

Jin, C., Jia, H., Lanka, P., Rangaprakash, D., Li, L., Liu, T., et al. (2017). Dynamic brain connectivity is a better predictor of PTSD than static connectivity. *Hum. Brain Mapp.* 38, 4479–4496. doi: 10.1002/hbm.23676

Johns, M. (1991). A new method for measuring daytime sleepiness: the epworth sleepiness scale. *Sleep* 14, 540–545. doi: 10.1093/sleep/14.6.540

Kaminski, M., Ding, M., Truccolo, W., and Bressler, S. (2001). Evaluating causal relations in neural systems: granger causality, directed transfer function and statistical assessment of significance. *Biol. Cybern.* 85, 145–157. doi: 10.1007/s004220000235

Katwal, S. B., Gore, J. C., Gatenby, J. C., and Rogers, B. P. (2013). Measuring relative timings of brain activities using fMRI. *Neuroimage* 66, 436–448. doi: 10.1016/j.neuroimage.2012.10.052

Kennis, M., Rademaker, A. R., van Rooij, S. J., Kahn, R. S., and Geuze, E. (2015). Resting state functional connectivity of the anterior cingulate cortex in veterans with and without post-traumatic stress disorder. *Hum. Brain Mapp.* 36, 99–109. doi: 10.1002/hbm.22615

King, D., King, L., and Vogt, D. (2003). *Manual for the Deployment Risk and Resilience Inventory (DRRI): A Collection of Measures for Studying Deployment-Related*. Boston, MA: National Center for PTSD.

Kirchgässner, G., Wolters, J., and Hassler, U. (2012). *Introduction to Modern Time Series Analysis*. New York, NY: Springer.

Krishnan, A., Williams, L., McIntosh, A., and Abdi, H. (2011). Partial least squares (PLS) methods for neuroimaging: a tutorial and review. *Neuroimage* 56, 455–475. doi: 10.1016/j.neuroimage.2010.07.034

Lacey, S., Stilla, R., Sreenivasan, K., Deshpande, G., and Sathian, K. (2014). Spatial imagery in haptic shape perception. *Neuropsychologia* 60, 144–158. doi: 10.1016/j.neuropsychologia.2014.05.008

Lamichhane, B., Adhikari, B. M., Brosnan, S. F., and Dhamala, M. (2014). The neural basis of perceived unfairness in economic exchanges. *Brain Connect.* 4, 619–630. doi: 10.1089/brain.2014.0243

Liao, X., Yuan, L., Zhao, T., Dai, Z., Shu, N., Xia, M., et al. (2015). Spontaneous functional network dynamics and associated structural substrates in the human brain. *Front. Hum. Neurosci.* 9:478. doi: 10.3389/fnhum.2015.00478

Libero, L., DeRamus, T., Lahti, A., Deshpande, G., and Kana, R. (2015). Multimodal neuroimaging based classification of autism spectrum disorder using anatomical, neurochemical, and white matter correlates. *Cortex* 66, 46–59. doi: 10.1016/j.cortex.2015.02.008

Lin, P., Sun, J., Yu, G., Wu, Y., Yang, Y., Liang, M., et al. (2014). Global and local brain network reorganization in attention-deficit/hyperactivity disorder. *Brain Imaging Behav.* 8, 558–569. doi: 10.1007/s11682-013-9279-3

Liu, F., Xie, B., Wang, Y., Guo, W., Fouche, J. P., Long, Z., et al. (2015). Characterization of post-traumatic stress disorder using resting-state fMRI with a multi-level parametric classification approach. *Brain Topogr.* 28, 221–237. doi: 10.1007/s10548-014-0386-2

Marquand, A. F., Filippone, M., Ashburner, J., Girolami, M., Mourao-Miranda, J., Barker, G. J., et al. (2013). Automated, high accuracy classification of parkinsonian disorders: a pattern recognition approach. *PLoS One* 8:e69237. doi: 10.1371/journal.pone.0069237

Miller, R., Yaesoubi, M., Turner, J., Mathalon, D., Preda, A., Pearlson, G., et al. (2016). Higher dimensional meta-state analysis reveals reduced resting fMRI connectivity dynamism in schizophrenia patients. *PLoS One* 11:e0149849. doi: 10.1371/journal.pone.0149849

Oishi, K., Faria, A., Hsu, J., Tippett, D., Mori, S., and Hillis, A. (2015). Critical role of the right uncinate fasciculus in emotional empathy. *Ann. Neurol.* 77, 68–74. doi: 10.1002/ana.24300

Pereira, F., Mitchell, T., and Botvinick, M. (2009). Machine learning classifiers and fMRI: a tutorial overview. *Neuroimage* 45, S199–S209. doi: 10.1016/j.neuroimage.2008.11.007

Power, J. D., Barnes, K. A., Snyder, A. Z., Schlaggar, B. L., and Petersen, S. E. (2012). Spurious but systematic correlations in functional connectivity MRI networks arise from subject motion. *Neuroimage* 59, 2142–2154. doi: 10.1016/j.neuroimage.2011.10.018

Preti, M., Bolton, T., and Van De Ville, D. (2016). The dynamic functional connectome: state-of-the-art and perspectives. *Neuroimage* 160, 41–54. doi: 10.1016/j.neuroimage.2016.12.061

Rangaprakash, D. (2016). *Brain Connectivity Modeling in Soldiers with Mild-Traumatic Brain Injury and Posttraumatic Stress Disorder*. Ph.D. thesis, Auburn University, Auburn, AL.

Rangaprakash, D., Deshpande, G., Daniel, T., Goodman, A., Robinson, J., Salibi, N., et al. (2017a). Compromised hippocampus-striatum pathway as a potential imaging biomarker of mild traumatic brain injury and posttraumatic stress disorder. *Hum. Brain Mapp.* 38, 2843–2864. doi: 10.1002/hbm.23551

Rangaprakash, D., Dretsch, M. N., Yan, W., Katz, J. S., Denney, T. S., and Deshpande, G. (2017b). Hemodynamic response function parameters obtained from resting-state functional MRI data in soldiers with trauma. *Data Brief* 14, 558–562. doi: 10.1016/j.dib.2017.07.072

Rangaprakash, D., Dretsch, M. N., Yan, W., Katz, J. S., Denney, T. S., and Deshpande, G. (2017c). Hemodynamic variability in soldiers with trauma: implications for functional MRI connectivity studies. *Neuroimage Clin.* 16, 409–417. doi: 10.1016/j.nicl.2017.07.016

Rangaprakash, D., Dretsch, M., Venkatraman, A., Katz, J., Denney, T., and Deshpande, G. (2018a). Identifying disease foci from static and dynamic effective connectivity networks: illustration in soldiers with trauma. *Hum. Brain Mapp.* 39, 264–287. doi: 10.1002/hbm.23841

Rangaprakash, D., Wu, G.-R., Marinazzo, D., Hu, X., and Deshpande, G. (2018b). Hemodynamic response function (HRF) variability confounds resting-state fMRI functional connectivity. *Mag. Reson. Me.* 80, 1697–1713. doi: 10.1002/mrm.27146

Rangaprakash, D., Wu, G.-R., Marinazzo, D., Hu, X., and Deshpande, G. (2018c). Parameterized hemodynamic response function data of healthy individuals obtained from resting-state functional MRI in a 7T MRI scanner. *Data Brief* 17, 1175–1179. doi: 10.1016/j.dib.2018.01.003

Rashid, B., Arbabshirani, M., Damaraju, E., Cetin, M., Miller, R., Pearlson, G., et al. (2016). Classification of schizophrenia and bipolar patients using static and dynamic resting-state fMRI brain connectivity. *Neuroimage* 134, 645–657. doi: 10.1016/j.neuroimage.2016.04.051

Rocca, M. A., Valsasina, P., Meani, A., Falini, A., Comi, G., Filippi, M., et al. (2014). Impaired functional integration in multiple sclerosis: a graph theory study. *Brain Struct. Funct.* 221, 115–131. doi: 10.1007/s00429-014-0896-4

Roebroeck, A., Formisano, E., and Goebel, R. (2005). Mapping directed influence over the brain using Granger causality and fMRI. *Neuroimage* 25, 230–242. doi: 10.1016/j.neuroimage.2004.11.017

Rubinov, M., and Sporns, O. (2010). Complex network measures of brain connectivity: uses and interpretations. *Neuroimage* 52, 1059–1069. doi: 10.1016/j.neuroimage.2009.10.003

Ryali, S., Chen, T., Supekar, K., and Menon, V. (2012). Estimation of functional connectivity in fMRI data using stability selection-based sparse partial correlation with elastic net penalty. *Neuroimage* 59, 3852–3861. doi: 10.1016/j.neuroimage.2011.11.054

Ryali, S., Shih, Y., Chen, T., Kochalka, J., Albaugh, D., Fang, Z., et al. (2016). Combining optogenetic stimulation and fMRI to validate a multivariate dynamical systems model for estimating causal brain interactions. *Neuroimage* 132, 398–405. doi: 10.1016/j.neuroimage.2016.02.067

Ryali, S., Supekar, K., Chen, T., and Menon, V. (2011). Multivariate dynamical systems models for estimating causal interactions in fMRI. *Neuroimage* 54, 807–823. doi: 10.1016/j.neuroimage.2010.09.052

Sakoğlu, U., Pearlson, G., Kiehl, K., Wang, Y., Michael, A., and Calhoun, V. (2010). A method for evaluating dynamic functional network connectivity and task-modulation: application to schizophrenia. *MAGMA* 23, 351–366. doi: 10.1007/s10334-010-0197-8

Sathian, K., Deshpande, G., and Stilla, R. (2013). Neural changes with tactile learning reflect decision level reweighting of perceptual readout. *J. Neurosci.* 33, 5387–5398. doi: 10.1523/JNEUROSCI.3482-12.2013

Saunders, J., Aasland, O., Babor, T., de la Fuente, J., and Grant, M. (1993). Development of the alcohol use disorders identification test (AUDIT): WHO collaborative project on early detection of persons with harmful alcohol consumption–II. *Addiction* 88, 791–804. doi: 10.1111/j.1360-0443.1993.tb02093.x

Schwab, K., Ivins, B., Cramer, G., Johnson, W., Sluss-Tiller, M., Kiley, K., et al. (2007). Screening for traumatic brain injury in troops returning from deployment in Afghanistan and Iraq: initial investigation of the usefulness of a short screening tool for traumatic brain injury. *J. Head Trauma Rehabil.* 22, 377–389. doi: 10.1097/01.htr.0000300233.98242.87

Simmons, A. N., and Matthews, S. (2012). Neural circuitry of PTSD with or without mild traumatic brain injury: a meta-analysis. *Neuropharmacology* 62, 598–606. doi: 10.1016/j.neuropharm.2011.03.016

Song, X. W., Dong, Z. Y., Long, X. Y., Li, S. F., Zuo, X. N., Zhu, C. Z., et al. (2011). REST: a toolkit for resting-state functional magnetic resonance imaging data processing. *PLoS One* 6:e25031. doi: 10.1371/journal.pone.0025031

Spielberg, J. M., McGlinchey, R. E., Milberg, W. P., and Salat, D. H. (2015). Brain network disturbance related to posttraumatic stress and traumatic brain injury in veterans. *Biol. Psychiatry* 78, 210–216. doi: 10.1016/j.biopsych.2015.02.013

Thayer, J. F., and Lane, R. D. (2000). A model of neurovisceral integration in emotion regulation and dysregulation. *J. Affect. Disord.* 61, 201–216. doi: 10.1016/s0165-0327(00)00338-4

Thompson, W. L., Slotnick, S. D., Burrage, M. S., and Kosslyn, S. M. (2009). Two forms of spatial imagery: neuroimaging evidence. *Psychol. Sci.* 20, 1245–1253. doi: 10.1111/j.1467-9280.2009.02440.x

Vasterling, J. J., Verfaellie, M., and Sullivan, K. D. (2009). Mild traumatic brain injury and posttraumatic stress disorder in returning veterans: perspectives from cognitive neuroscience. *Clin. Psychol. Rev.* 29, 674–684. doi: 10.1016/j.cpr.2009.08.004

Vergara, V., Mayer, A., Damaraju, E., Kiehl, K., and Calhoun, V. (2016). Detection of mild traumatic brain injury by machine learning classification using resting state functional network connectivity and fractional anisotropy. *J. Neurotrauma* 34, 1045–1053. doi: 10.1089/neu.2016.4526

Veterans (2015). *Veterans Statistics: PTSD, Depression, TBI, Suicide*. Available at: http://www.veteransandptsd.com/PTSD-statistics.html. (accessed November 2015).

Vul, E., Harris, C., Winkielman, P., and Pashler, H. (2009). Puzzlingly high correlations in fMRI studies of emotion, personality, and social cognition. *Perspect. Psychol. Sci.* 4, 274–290. doi: 10.1111/j.1745-6924.2009.01129.x

Wang, Y., Katwal, S., Rogers, B., Gore, J., and Deshpande, G. (2016). Experimental validation of dynamic granger causality for inferring stimulus-evoked Sub-100 ms timing differences from fMRI. *IEEE Trans. Neural. Syst. Rehabil. Eng.* 25, 539–546. doi: 10.1109/TNSRE.2016.2593655

Wen, X., Rangarajan, G., and Ding, M. (2013). Is granger causality a viable technique for analyzing fMRI data? *PLoS One* 8:e67428. doi: 10.1371/journal.pone.0067428

Wheelock, M. D., Sreenivasan, K. R., Wood, K. H., Ver Hoef, L. W., Deshpande, G., and Knight, D. C. (2014). Threat-related learning relies on distinct dorsal prefrontal cortex network connectivity. *Neuroimage* 102, 904–912. doi: 10.1016/j.neuroimage.2014.08.005

White, S. F., Costanzo, M. E., Blair, J. R., and Roy, M. J. (2014). PTSD symptom severity is associated with increased recruitment of top-down attentional control in a trauma-exposed sample. *Neuroimage Clin.* 7, 19–27. doi: 10.1016/j.nicl.2014.11.012

Woo, C., and Wager, T. (2015). Neuroimaging-based biomarker discovery and validation. *Pain* 156, 1379–1381. doi: 10.1097/j.pain.0000000000000223

Wu, G., Liao, W., Stramaglia, S., Ding, J., Chen, H., and Marinazzo, D. (2013). A blind deconvolution approach to recover effective connectivity brain networks from resting state fMRI data. *Med. Image Anal.* 17, 365–374. doi: 10.1016/j.media.2013.01.003

Xia, M., Wang, J., and He, Y. (2013). BrainNet viewer: a network visualization tool for human brain connectomics. *PLoS One* 8:e68910. doi: 10.1371/journal.pone.0068910

Yu, Q., Sui, J., Kiehl, K. A., Pearlson, G., and Calhoun, V. D. (2013). State-related functional integration and functional segregation brain networks in schizophrenia. *Schizophr. Res.* 150, 450–458. doi: 10.1016/j.schres.2013.09.016

Zalesky, A., Fornito, A., Cocchi, L., Gollo, L., and Breakspear, M. (2014). Time-resolved resting-state brain networks. *Proc. Natl. Acad. Sci. U.S.A* 111, 10341–10346. doi: 10.1073/pnas.1400181111

Zhang, J., Cheng, W., Liu, Z., Zhang, K., Lei, X., Yao, Y., et al. (2016). Neural, electrophysiological and anatomical basis of brain-network variability and its characteristic changes in mental disorders. *Brain* 139, 2307–2321. doi: 10.1093/brain/aww143

Zung, W. (1971). A rating instrument for anxiety disorders. *Psychosomatics* 12, 371–379. doi: 10.1016/s0033-3182(71)71479-0

Zung, W., Richards, C., and Short, M. (1965). Self-rating depression scale in an outpatient clinic. Further validation of the SDS. *Arch. Gen. Psychiatry* 13, 508–515.

Conflict of Interest Statement: The authors declare that the research was conducted in the absence of any commercial or financial relationships that could be construed as a potential conflict of interest.

frontiers in Neuroscience

PERSPECTIVE
published: 05 November 2019
doi: 10.3389/fnins.2019.01190

Arousal Contributions to Resting-State fMRI Connectivity and Dynamics

*Yameng Gu[1], Feng Han[1] and Xiao Liu[1,2]**

[1] Department of Biomedical Engineering, The Pennsylvania State University, University Park, PA, United States, [2] Institute for CyberScience, The Pennsylvania State University, University Park, PA, United States

Resting-state functional magnetic resonance imaging (rsfMRI) is being widely used for charting brain connectivity and dynamics in healthy and diseased brains. However, the resting state paradigm allows an unconstrained fluctuation of brain arousal, which may have profound effects on resting-state fMRI signals and associated connectivity/dynamic metrics. Here, we review current understandings of the relationship between resting-state fMRI and brain arousal, in particular the effect of a recently discovered event of arousal modulation on resting-state fMRI. We further discuss potential implications of arousal-related fMRI modulation with a focus on its potential role in mediating spurious correlations between resting-state connectivity/dynamics with physiology and behavior. Multiple hypotheses are formulated based on existing evidence and remain to be tested by future studies.

Keywords: resting-state fMRI, brain dynamics, arousal, global signal, connectivity

OPEN ACCESS

Edited by:
Federico Giove, Centro Fermi – Museo storico della fisica e Centro studi e ricerche Enrico Fermi, Italy

Reviewed by:
Thomas T. Liu, University of California, San Diego, United States
Ali Golestani, University of Toronto, Canada

***Correspondence:**
Xiao Liu
xxl213@engr.psu.edu

Specialty section:
This article was submitted to Brain Imaging Methods, a section of the journal Frontiers in Neuroscience

Received: *14 January 2019*
Accepted: *21 October 2019*
Published: *05 November 2019*

Citation:
Gu Y, Han F and Liu X (2019) Arousal Contributions to Resting-State fMRI Connectivity and Dynamics. Front. Neurosci. 13:1190. doi: 10.3389/fnins.2019.01190

INTRODUCTION

The advent of resting-state functional magnetic resonance imaging (fMRI) (Biswal et al., 1995; Fox and Raichle, 2007) has revolutionized our understanding of large-scale brain networks, including their intrinsic organization (Fox et al., 2005), developmental and aging profiles (Fair et al., 2007; Stevens et al., 2008), state-dependent re-organization (Horovitz et al., 2009; Barttfeld et al., 2014), genetic basis (Wiggins et al., 2012), and most importantly their modulations in various brain diseases (Zhang and Raichle, 2010). The majority of studies in this research field has been focused on inferring functional brain connectivity with fMRI correlations. The majority of these studies estimated functional connectivity based on an entire session of typical 5–10 min, which implicitly assumes stationary relationships between different brain regions and ignores temporal brain dynamics at finer time scales of seconds. Recently, the non-stationary nature of resting-state fMRI (rsfMRI) became a hot topic of this research field (Chang and Glover, 2010) and a set of methods/metrics has been proposed to extract and quantify time-varying information in rsfMRI data, which is expected to provide information supplementary to those stationary analyses (Hutchison et al., 2013; Preti et al., 2017).

The approaches for quantifying rsfMRI dynamics can be divided into multiple categories. The most straightforward class is sliding window approaches, which quantify rsfMRI connectivity within short time windows of 1–2 min and then examine its temporal variability accordingly.

The connectivity metrics could be either conventional correlation/coherence (Chang and Glover, 2010; Allen et al., 2012) or more sophisticated metrics, such as network parameters from graph-theory based quantifications (Braun et al., 2015; Shine et al., 2016). A group of single-volume resolved methods has also been proposed to quantify rsfMRI dynamics. These methods treat fMRI volumes at single time points as basic units of analyses and try to identify repeated patterns of brain co-activations using different algorithms, including the temporal functional mode (TFM) extracted with temporal independent component analysis (ICA) (Smith et al., 2012), the co-activation patterns (CAP) identified by clustering (Liu and Duyn, 2013b; Liu et al., 2013), and the brain states defined using hidden Markov model (HMM) (Chen et al., 2016; Vidaurre et al., 2017). Subsequent quantification can then be applied to quantify temporal dynamics, such as occurrence rate and transitioning probabilities, of these single-volume fMRI events. The third category of dynamic approaches expands the second type by focusing on spatiotemporal structures in rsfMRI signals. Different algorithms were employed to derive quasi-periodic patterns (QPP) (Thompson et al., 2014) and lag threads (Mitra et al., 2015a) from rsfMRI data that may represent propagating activities of the brain.

These dynamic approaches have been applied to rsfMRI data to quantify brain dynamics and investigate its associations with behavior (Vidaurre et al., 2017) and modulations under pathological conditions (Mitra et al., 2015b). A very consistent observation across studies and species is the sensitivity of fMRI dynamics to brain states showing distinct arousal levels (Barttfeld et al., 2014; Tagliazucchi and Laufs, 2014; Liang et al., 2015; Mitra et al., 2015c; Ma et al., 2016; Laumann et al., 2017). The brain arousal is conventionally defined as a transient intrusion of being awake into sleep stages or an abrupt temporary increase of the vigilance level (Atlas Task Force, 1992; Halász et al., 2004), and the sleep and anesthesia conditions are known to show distinct arousal levels. In particular, the application of a wake-sleep classifier trained based on dynamic functional connectivity of a small EEG-fMRI data set to a large cohort of 1,147 rsfMRI datasets has found that 30% subjects actually fell asleep within 3 min into resting-state scanning (Tagliazucchi and Laufs, 2014). These findings not only suggest an important role of arousal in generating/modulating rsfMRI signals and thus connectivity/dynamics measures derived from it, but also imply its prevalent influence on human rsfMRI studies. Consistent with these observations, a characteristic neurophysiological event signifying a transient arousal modulation was identified recently and shown to have profound effect on concurrently acquired fMRI signals (Liu et al., 2015, 2018), which give us an opportunity of further looking into the relationship between the arousal and rsfMRI signals. In this perspective, we will first review the relationship between the brain arousal and global rsfMRI signal and a recently discovered neurophysiological event that may underlie this relationship. We will then discuss potential implications of these findings on different aspects of rsfMRI research (**Figure 1**), including the motion-rsfMRI, physiology-rsfMRI, and disease-rsfMRI relationships in different sections.

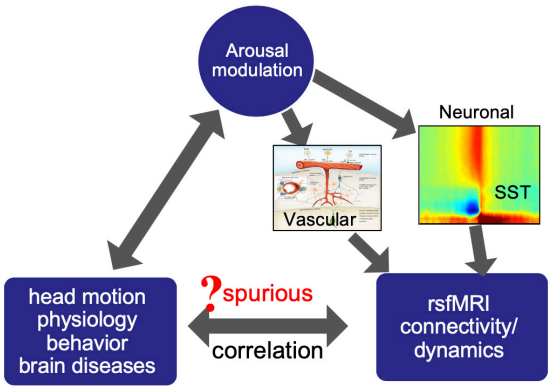

FIGURE 1 | Arousal modulations may introduce spurious correlations between rsfMRI connectivity/dynamics and other measures by modulating both.

A NEUROPHYSIOLOGICAL EVENT UNDERLYING THE GLOBAL RSFMRI SIGNAL

The global rsfMRI signal averaged over the entire brain and spatially non-specific fMRI correlations it induces have been found highly sensitive to brain arousal state (Matsuda et al., 2002; Schölvinck et al., 2010). The transition into the light sleep is characterized by a large increase in this global rsfMRI signal (Fukunaga et al., 2006; Horovitz et al., 2008; Larson-Prior et al., 2009), and a similar but smaller change was also observed from an alert eyes-open condition to a sleep-conducive eyes-closed condition (Wong et al., 2013; Xu et al., 2014; Wei et al., 2018; Agcaoglu et al., 2019). Caffeine can effectively reduce the global rsfMRI signal and corresponding EEG vigilance index (Wong et al., 2013), whereas several hypnotic drugs (Kiviniemi et al., 2005; Saper et al., 2005; Greicius et al., 2008; Licata et al., 2013) and sleep deprivation (Yeo et al., 2015) had the opposite effects. It is also worth noting that multiple studies also showed the connectivity changes of the default mode network (DMN) under various states of consciousness (Yan et al., 2009; Vanhaudenhuyse et al., 2010; Heine et al., 2012; Demertzi et al., 2015). These studies provided convincing evidence for a close relationship between the arousal and rsfMRI, particularly its global component, but the neural basis underlying this relationship had remained unknown until very recently.

The first clue for the neural basis of the global rsfMRI signal came from the study of rsfMRI dynamics. It has been suggested that the rsfMRI connectivity and its dynamics are actually caused by brain co-activations at different time points that can be captured by CAPs (Liu and Duyn, 2013b; Liu et al., 2013; Matsui et al., 2018). Applying the CAP decomposition to rsfMRI data with and without removing the global signal showed distinct effects on two types of CAPs. Whereas the global signal regression (GSR) procedure has very limited effect on higher-order CAPs, e.g., those related to the DMN, it dramatically changes sensory CAPs involving the sensorimotor and visual cortices (Liu and Duyn, 2013a; Liu et al., 2013; Nalci et al., 2017). The finding

not only confirmed that the global signal is largely driven by global rsfMRI co-activations occurring only at a proportion of time points, but also implied the neuronal origin of this fMRI co-activation since it occurs preferentially with sensory networks rather than randomly. These results are consistent with another series of research work on the temporal heterogeneity of the global rsfMRI signal (He and Liu, 2012; Nalci et al., 2017). With these findings, the search for the neurophysiological correlate of the global rsfMRI signal was shifted to the event type of neuronal processes.

An electrophysiological event signifying a transient arousal modulation was recently discovered and suggested to underlie the global rsfMRI signal (Liu et al., 2015, 2018). This sequential spectral transition (SST) event was first observed in the global signal of a large-scale electrocorticography (ECoG) recording from monkeys, showing as a stereotypic time-frequency pattern of sequential power changes at three distinct frequency bands: a large, sudden reduction in the middle-frequency (9–21 Hz) power is followed by an increased broad-band high-frequency gamma power (>42 Hz) and then a burst of low-frequency delta waves (1–4 Hz). The SST lasts 10–20 s and shows similar state-dependency as the global rsfMRI signal (Liu et al., 2015). Concurrent fMRI-electrophysiology recordings from another group of monkeys confirmed that the SST induces widespread fMRI increases, i.e., the global rsfMRI co-activation, shown as a large peak in the global signal (Liu et al., 2018). In addition to such one-to-one correspondence between the SST and global rsfMRI peak, their relationship was further confirmed from the other two aspects. First, the global rsfMRI co-activation demonstrated a much larger amplitude in sensory regions, i.e., the sensorimotor, auditory, and visual cortices, and this sensory-dominant pattern is consistent with the spatial pattern of the high-frequency gamma (40–90 Hz) power increase at the SST event. Second, the global co-activations are associated with very specific de-activations at subcortical arousal-promoting areas, i.e., the Nucleus Basalis (NB) at the basal forebrain and the midline thalamus in the non-specific arousal pathway, in accordance with a transient arousal drop suggested by the middle-to-low frequency spectral transition at SST events (Liu et al., 2018). Consistent with this finding, the inactivation of the NB in one brain hemisphere of monkeys resulted in a significant reduction of the global rsfMRI signal in the ipsilateral side (Turchi et al., 2018). Overall, the finding of the SST event and its relationship with fMRI signals provide a neurophysiological understanding of the relationship between the brain arousal states and rsfMRI connectivity/dynamics.

Arousal-related fMRI changes can have potential implications in many aspects of rsfMRI research. The sensory-dominant pattern of SST-induced fMRI changes is expected to introduce very systematic changes in rsfMRI correlations, which could be easily misinterpreted as meaningful modulations of functional brain connectivity. The transient nature of the SST (10–20 s) will also have profound effects on rsfMRI dynamics at the time scale of interest to most of dynamic rsfMRI studies. More importantly, the perils of the arousal-related fMRI component can go beyond its direct effects on rsfMRI connectivity/dynamics by potentially introducing their spurious correlations with other subject measures of physiology, behavior, and pathology. Arousal state is known to have profound effects on physiology (Trinder et al., 2001) and also able to affect behavioral performance (Teigen, 1994) or even head motions (Van Den Berg, 2006). Many brain diseases, including Alzheimer's disease (Musiek et al., 2015), Parkinson's disease (Breen et al., 2014), and autism spectrum disorders (ASD) (Cohen et al., 2014), are known to concur with disrupted sleep and circadian rhythms (Wulff et al., 2010), and many medications for these diseases are also known to affect brain arousal state. Together with the profound effects of arousal modulation on rsfMRI signals, these may lead to spurious relationships between rsfMRI connectivity/dynamics and various physiological and behavioral measurements (**Figure 1**). The remaining part of this perspective will have detailed discussions regarding the role of arousal modulations in mediating the relationship of rsfMRI with different types of subject measurements.

THE POTENTIAL ROLE OF AROUSAL MODULATIONS IN MOTION-RSFMRI RELATIONSHIP

The correlation has been found between the rsfMRI connectivity and head motions in both intra- and inter-subject analyses (Power et al., 2012; van Dijk et al., 2012; Yan et al., 2013). Specifically, more head motions are associated with increased local but reduced long-range rsfMRI connectivity. This motion-connectivity association has been interpreted as a causal relationship with assuming that the head motion affects fMRI signals and thus their correlations. However, there are observations inconsistent with this interpretation. First, the motion-associated rsfMRI signal/correlation change persists or even reaches its peaks 10 s after motion ceases (Power et al., 2014; Byrge and Kennedy, 2018). This temporal feature cannot be caused by the spin-history artifact, which should have a much short delay to the motion according to simulation and also monotonically decay over time (Yancey et al., 2011). Instead, this time delay is in a similar time scale as the typical hemodynamic delay. Secondly, the associated rsfMRI connectivity changes showed systematic spatial patterns that are unexpected from relatively random head motions. Thirdly, the same amount of head motions causes significant rsfMRI connectivity changes across subjects but not between different sessions of the same subjects (Zeng et al., 2014). For these reasons, the motion-connectivity relationship may not be causal, but actually mediated by a third factor. We propose that the arousal modulation could be a candidate that mediates this relationship for the following reasons. First, a widely used motion index, differentiated signal variance (DVARS), detects large fMRI changes, including large global signal peaks that have been linked to the SST event of arousal modulation. Secondly, the motion-fMRI correlations also show a sensory-dominant pattern similar to that of the global co-activations and SST gamma power (Yan et al., 2013). Thirdly, sleepiness has been shown to be associated with more head motions (Van Den Berg, 2006). Transient sleep structures, such as

microsleep and/or microarousal, and associated physiological modulations might be direct causes of head motions. Indeed, a transient respiratory modulation was found to concur with head motions detected by fMRI changes (Byrge and Kennedy, 2018). For all these reasons, we hypothesize that transient arousal modulations induce spurious correlations between the head motion and rsfMRI connectivity, which account for a significant proportion of the observed motion-rsfMRI relationships. The key to validating this hypothesis is to differentiate the head motions of arousal relevance from those caused by discomfort, general fidgetiness, and other factors, as well as their effects on rsfMRI signals. It is worth noting that the framewise displacement (FD), another widely used motion index calculated directly from image alignment parameters (Yoo et al., 2005), might better serve this purpose, compared with DVARS, with less contamination from the arousal-related global signals.

THE POTENTIAL ROLE OF AROUSAL MODULATIONS IN PHYSIOLOGY-RSFMRI RELATIONSHIP

Physiological signals, including respiratory volume and cardiac pulse rate, were also shown to have strong correlations with rsfMRI signals (Birn et al., 2006; Shmueli et al., 2007; Chang et al., 2016b; Özbay et al., 2018), which has been regarded as evidence of non-neuronal contributions to rsfMRI signal fluctuation. A recent study combing fMRI, physiology, and electroencephalogram (EEG) provided further insight into this physiology-rsfMRI relationship (Yuan et al., 2013). It first confirmed the correlation between the physiology and rsfMRI but further suggested that they both are also correlated with the alpha-band EEG power, which is an indicator of brain vigilance and also shows a large modulation at the SST. Moreover, this study further showed the physiology-rsfMRI correlation is dependent on brain states and significant only during the sleep-conducive eyes-closed condition but not under an alert eyes-open condition. It is worth noting that the correlations between rsfMRI and physiological signals also appear to be much stronger in the sensory regions than the rest of the brain (Birn, 2006; Shmueli et al., 2007; Yuan et al., 2013; Özbay et al., 2018). All these findings strongly suggest an involvement of the arousal in this physiology-rsfMRI relationship. We thus hypothesize that the physiology-rsfMRI relationship is partly caused by their co-modulations at transient arousal events, such as the SST. Given the potential involvement of physiology, we want to also emphasize that the arousal modulation may cause fMRI changes via two different routes. It can modulate neural activities across the cortex via the ascending arousal pathways, and thus fMRI signal changes through local neuro-vascular coupling. The SST event and associated global rsfMRI co-activation are likely evidence for this type of arousal-fMRI connections. In addition, the brain stem arousal centers are also able to directly modulate vascular tone, for example, through sympathetic innervations of the arteries in the brain pial surface (Hamel, 2005; Özbay et al., 2018), and thus cause global rsfMRI changes of vascular origin. Large white-matter fMRI changes associated with cardiac signal changes likely originate from this type of vascular modulations (Özbay et al., 2018). Differentiating the contributions from these two mechanisms remains a challenge for future research.

THE POTENTIAL ROLE OF AROUSAL MODULATIONS IN DISEASE-RSFMRI RELATIONSHIPS

Resting-state fMRI connectivity and dynamics have also been extensively studied under pathological conditions, and significant modulations were reported in a wide range of neurological disorder and psychiatric diseases, including the Alzheimer's disease, ASD, and major depression (Zhang and Raichle, 2010). Given that these brain diseases are often associated with disrupted sleep and circadian rhythms (Wulff et al., 2010), it is reasonable to suspect that the arousal difference may, at least partly, account for rsfMRI connectivity modulations observed in certain brain diseases. A survey of existing literatures indeed found the evidence for the modulation of the global rsfMRI signal under certain pathological conditions. A simple example is schizophrenia. Whereas an early study had suggested that schizophrenia patients showed hyperconnectivity in the default network compared with their first-degree relatives and healthy controls (Whitfield-Gabrieli et al., 2009), it was found later that these changes may actually arise from an enhanced global signal in schizophrenia (Yang et al., 2014). A computational model was also employed to demonstrate that increased neuronal coupling can indeed enhance the global signal (Yang et al., 2014). However, based on the evidence we reviewed so far regarding the relationship between the global rsfMRI signal and arousal, we argue that the distinct arousal state could be an alternative explanation for the global rsfMRI signal seen in the schizophrenia patients.

The global signal could affect rsfMRI findings in a rather implicit way. Using rsfMRI data from the Autism Brain Imaging Data Exchange (ABIDE) initiative, a previous study has shown that interhemispheric rsfMRI connectivity shows a much larger inter-subject variability in high-functioning ASD adults than matched healthy controls, and this finding has been interpreted as idiosyncratic distortions of ASD brains (Hahamy et al., 2015). The interhemispheric rsfMRI connectivity often shows a sensory-dominant pattern due to strong bilateral correlations in sensory regions. Given the sensory-dominant pattern of the global rsfMRI co-activations of arousal relevance (Liu et al., 2018), the presence of a strong global signal is also expected to enhance this pattern and thus its cross-subject similarity. We therefore hypothesize that the difference in the global rsfMRI signal is responsible for the interhemispheric connectivity difference between the ASD and control groups. To test this hypothesis, we examined ABIDE datasets from three different sites (**Figure 2**). For two datasets (CAL: 19 ASD and 19 controls; PBG: 30 ASD and 27 controls) that previously showed a large contrast between the ASD and control groups, rsfMRI data were actually acquired under the sleep-conducive eyes-closed condition (**Figures 2A–C**, top and middle). Moreover, the control group shows a much

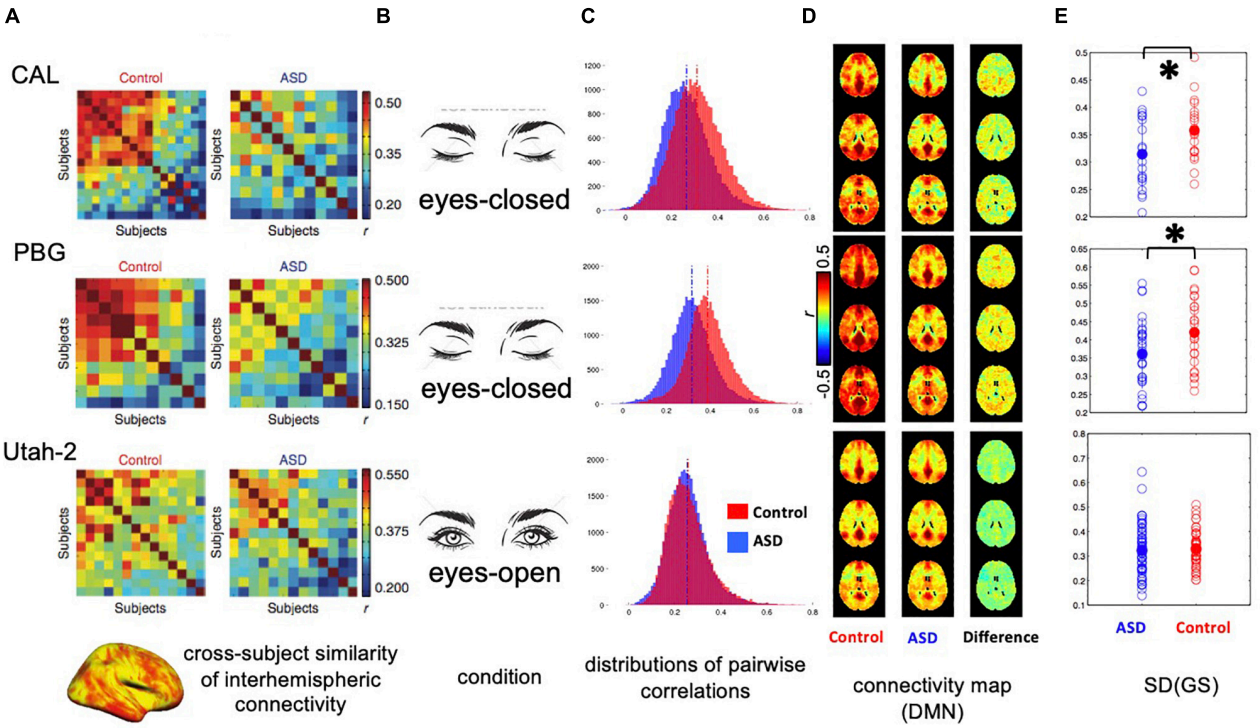

FIGURE 2 | Distinct global signal in ASD patients may have implicit impact on interhemispheric rsfMRI connectivity. **(A)** Correlation matrices showing the inter-subject similarity of interhemispheric rsfMRI connectivity pattern for three datasets collected at different sites. The data from the first two sites, i.e., CAL and PBG show a big difference between the ASD and control groups with controls showing much higher cross-subject similarities. **(B)** Conditions for rsfMRI experiments. The first two sites collected rsfMRI data under sleep-conducive eyes-closed condition. **(C)** Histograms showing the distribution of all pairwise rsfMRI connectivity. In the first two datasets, the control groups show overall stronger rsfMRI connectivity compared with the ASD groups. However, this difference was not observed in the third dataset. **(D)** RsfMRI connectivity maps with respect to a seed region at the posterior cingulate cortex (PCC) showing the DMN network. In the first two datasets, the control groups show larger spatially non-specific correlations compared with the ASD groups, presumably due to a larger global signal. **(E)** Standard deviation of the global rsfMRI signal. The control groups of the first two datasets are characterized by significantly larger global signal than the ASD groups, whereas the global signal is smaller and not different in the two groups for the third dataset. *$0.01 < p < 0.05$.

stronger global signal and rsfMRI connectivity than the ASD group ($p = 0.036$ for CAL and $p = 0.022$ for PBG, 2-sample t-test; **Figures 2D,E,** top and middle). In contrast, the Utah dataset (58 ASD versus 43 controls) not showing much group difference in the previous study was acquired under a more alert eyes-open condition and their global signals are not significantly different ($p = 0.735$; **Figures 2A–C**, bottom). Correspondingly, the global signal is low in both ASD and control groups for this dataset (**Figures 2D,E**, bottom). These preliminary results clearly suggest that the ASD groups are characterized by the global rsfMRI signal distinct from healthy controls, especially under the sleep-conducive eyes-closed condition, which might be attributed to their abnormal sleep patterns (Devnani and Hegde, 2015).

Arousal might also mediate the correlation between rsfMRI connectivity/dynamics and certain behavioral measures within the healthy population in a similar way. Even though the arousal itself describes a brain state that varies over time, the ability of regulating arousal could be an individual trait that is stable within but varies across individuals. If the healthy population contains subgroups that not only have distinct ability of regulating arousal but also differ significantly in certain cognitive functions, rsfMRI connectivity and dynamics could be spuriously linked to behavioral measures of cognitive functions via arousal-related rsfMRI changes. Although this is purely a conjecture to be tested by future studies, caution needs to be exercised before completely excluding this possibility.

CONCLUDING REMARKS AND FUTURE RESEARCH

Here we reviewed the current understanding of the relationship between the brain arousal and resting-state fMRI, in particular a newly discovered neurophysiological event underlying the global rsfMRI signal. We then discussed potential implications of the arousal-related modulation on rsfMRI research, i.e., its role in affecting rsfMRI connectivity/dynamics and mediating their spurious correlations with physiological and behavioral measures. We also formulated multiple testable hypotheses based on existing evidence. Future research ought to validate these hypotheses, which are important not only for proper interpretations of rsfMRI results but also for better quantifications of brain connectivity and dynamics using rsfMRI

with properly dealing with the arousal confounding effects, i.e., removing or retaining the arousal-related component based on research purposes. Before the validation of these hypothesis, one should be cautious about large global signal and sensory-dominant pattern in rsfMRI results, which are indicative of arousal involvement. Researchers may also consider to reduce the potential arousal influence at the stage of data collection, for example, by acquiring data at the eye-open state or breaking down a long scan into multiple shorter ones. The profound arousal effect on rsfMRI presents additional challenges to rsfMRI-based measures of brain connectivity/dynamics. But on the bright side, this would enable fMRI-based arousal measures (Chang et al., 2016a; Falahpour et al., 2018; Liu et al., 2018), which may provide new opportunities for understanding the arousal's role in affecting brain function and dysfunction, especially with big neuroimaging data acquired recently from healthy and diseased populations. It is, however, worth noting that the performance of these template-based arousal measures could be dependent on the presence of the SST events and thus the general vigilance state (Falahpour et al., 2018). It remains a challenge for future studies to improve the fMRI-based arousal measure by better understanding arousal-related fMRI changes.

AUTHOR CONTRIBUTIONS

YG and XL designed the study and performed the analyses. YG, XL, and FH wrote the manuscript.

FUNDING

This research was supported by the National Institutes of Health (NIH) Pathway to Independence Award (K99/R00) 5R00NS092996-03.

REFERENCES

Agcaoglu, O., Wilson, T. W., Wang, Y. P., Stephen, J., and Calhoun, V. D. (2019). Resting state connectivity differences in eyes open versus eyes closed conditions. *Hum. Brain Mapp.* 40, 2488–2498. doi: 10.1002/hbm.24539

Allen, E. A., Damaraju, E., Plis, S. M., Erhardt, E. B., Eichele, T., and Calhoun, V. D. (2012). Tracking whole-brain connectivity dynamics in the resting state. *Cereb. cortex* 24, 663–676. doi: 10.1093/cercor/bhs352

Atlas Task Force (1992). EEG arousals: scoring rules and examples: a preliminary report from the sleep disorders atlas task force of the American sleep disorders association. *Sleep* 15, 173–184.

Barttfeld, P., Uhrig, L., Sitt, J. D., Sigman, M., Jarraya, B., and Dehaene, S. (2014). Signature of consciousness in the dynamics of resting-state brain activity. *Proc. Natl. Acad. Sci. U.S.A.* 112, 887–892. doi: 10.1073/pnas.1418031112

Birn, A. E. (2006). [The national-international nexus in public health: Uruguay and the circulation of child health and welfare policies, 1890-1940]. *Hist. Cienc. Saude Manguinhos* 13, 675–708.

Birn, R. M., Diamond, J. B., Smith, M. A., and Bandettini, P. A. (2006). Separating respiratory-variation-related fluctuations from neuronal-activity-related fluctuations in fMRI. *Neuroimage* 31, 1536–1548. doi: 10.1016/j.neuroimage.2006.02.048

Biswal, B., Yetkin, F. Z., Haughton, V. M., and Hyde, J. S. (1995). Functional connectivity in the motor cortex of resting human brain using echo-planar MRI. *Magn. Reson. Med.* 34, 537–541. doi: 10.1002/mrm.1910340409

Braun, U., Schäfer, A., Walter, H., Erk, S., Romanczuk-Seiferth, N., Haddad, L., et al. (2015). Dynamic reconfiguration of frontal brain networks during executive cognition in humans. *Proc. Natl. Acad. Sci. U. S. A.* 112, 11678–11683. doi: 10.1073/pnas.1422487112

Breen, D. P., Vuono, R., Nawarathna, U., Fisher, K., Shneerson, J. M., Reddy, A. B., et al. (2014). Sleep and circadian rhythm regulation in early Parkinson disease. *JAMA Neurol.* 71, 589–595. doi: 10.1001/jamaneurol.2014.65

Byrge, L., and Kennedy, D. P. (2018). Identifying and characterizing systematic temporally-lagged BOLD artifacts. *Neuroimage* 171, 376–392. doi: 10.1016/j.neuroimage.2017.12.082

Chang, C., and Glover, G. H. (2010). Time-frequency dynamics of resting-state brain connectivity measured with fMRI. *Neuroimage* 50, 81–98. doi: 10.1016/j.neuroimage.2009.12.011

Chang, C., Leopold, D. A., Scholvinck, M. L., Mandelkow, H., Picchioni, D., Liu, X., et al. (2016a). Tracking brain arousal fluctuations with fMRI. *Proc. Natl. Acad. Sci. U.S.A.* 113, 4518–4523. doi: 10.1073/pnas.1520613113

Chang, C., Raven, E. P., and Duyn, J. H. (2016b). Brain-heart interactions: challenges and opportunities with functional magnetic resonance imaging at ultra-high field. *Philos. Trans. A. Math. Phys. Eng. Sci.* 374:20150188. doi: 10.1098/rsta.2015.0188

Chen, S., Langley, J., Chen, X., and Hu, X. (2016). Spatiotemporal modeling of brain dynamics using resting-state functional magnetic resonance imaging with gaussian hidden markov model. *Brain Connect.* 6, 326–334. doi: 10.1089/brain.2015.0398

Cohen, S., Conduit, R., Lockley, S. W., Rajaratnam, S. M., and Cornish, K. M. (2014). The relationship between sleep and behavior in autism spectrum disorder (ASD): a review. *J. Neurodev. Disord.* 6:44. doi: 10.1186/1866-1955-6-44

Demertzi, A., Antonopoulos, G., Heine, L., Voss, H. U., Crone, J. S., De Los Angeles, C., et al. (2015). Intrinsic functional connectivity differentiates minimally conscious from unresponsive patients. *Brain* 138, 2619–2631. doi: 10.1093/brain/awv169

Devnani, P., and Hegde, A. (2015). Autism and sleep disorders. *J. Pediatr. Neurosci.* 10, 304–307. doi: 10.4103/1817-1745.174438

Fair, D. A., Dosenbach, N. U. F., Church, J. A., Cohen, A. L., Brahmbhatt, S., Miezin, F. M., et al. (2007). Development of distinct control networks through segregation and integration. *Proc. Natl. Acad. Sci. U.S.A.* 104, 13507–13512. doi: 10.1073/pnas.0705843104

Falahpour, M., Chang, C., Wong, C. W., and Liu, T. T. (2018). Template-based prediction of vigilance fluctuations in resting-state fMRI. *Neuroimage* 174, 317–327. doi: 10.1016/j.neuroimage.2018.03.012

Fox, M. D., and Raichle, M. E. (2007). Spontaneous fluctuations in brain activity observed with functional magnetic resonance imaging. *Nat. Rev. Neurosci.* 8, 700–711. doi: 10.1038/nrn2201

Fox, M. D., Snyder, A. Z., Vincent, J. L., Corbetta, M., Van Essen, D. C., and Raichle, M. E. (2005). The human brain is intrinsically organized into dynamic, anticorrelated functional networks. *Proc. Natl. Acad. Sci. U.S.A.* 102, 9673–9678. doi: 10.1073/pnas.0504136102

Fukunaga, M., Horovitz, S. G., van Gelderen, P., de Zwart, J. A., Jansma, J. M., Ikonomidou, V. N., et al. (2006). Large-amplitude, spatially correlated fluctuations in BOLD fMRI signals during extended rest and early sleep stages. *Magn. Reson. Imaging* 24, 979–992. doi: 10.1016/j.mri.2006.04.018

Greicius, M. D., Kiviniemi, V., Tervonen, O., Vainionpää, V., Alahuhta, S., Reiss, A. L., et al. (2008). Persistent default-mode network connectivity during light sedation. *Hum. Brain Mapp.* 29, 839–847. doi: 10.1002/hbm.20537

Hahamy, A., Behrmann, M., and Malach, R. (2015). The idiosyncratic brain: distortion of spontaneous connectivity patterns in autism spectrum disorder. *Nat. Neurosci.* 18, 302–309. doi: 10.1038/nn.3919

Halász, P., Terzano, M., Parrino, L., and Bódizs, R. (2004). The nature of arousal in sleep. *J. Sleep Res.* 13, 1–23. doi: 10.1111/j.1365-2869.2004.00388.x

Hamel, E. (2005). Perivascular nerves and the regulation of cerebrovascular tone. *J. Appl. Physiol.* 100, 1059–1064. doi: 10.1152/japplphysiol.00954.2005

He, H., and Liu, T. T. (2012). A geometric view of global signal confounds in resting-state functional MRI. *Neuroimage* 59, 2339–2348. doi: 10.1016/j.neuroimage.2011.09.018

Heine, L., Soddu, A., Gómez, F., Vanhaudenhuyse, A., Tshibanda, L., Thonnard, M., et al. (2012). Resting state networks and consciousness Alterations of multiple resting state network connectivity in physiological, pharmacological, and pathological consciousness states. *Front. Psychol.* 3:295. doi: 10.3389/fpsyg.2012.00295

Horovitz, S. G., Braun, A. R., Carr, W. S., Picchioni, D., Balkin, T. J., Fukunaga, M., et al. (2009). Decoupling of the brain's default mode network during deep sleep. *Proc. Natl. Acad. Sci. U.S.A.* 106, 11376–11381. doi: 10.1073/pnas.0901435106

Horovitz, S. G., Fukunaga, M., De Zwart, J. A., Van Gelderen, P., Fulton, S. C., Balkin, T. J., et al. (2008). Low frequency BOLD fluctuations during resting wakefulness and light sleep: a simultaneous EEG-fMRI study. *Hum. Brain Mapp.* 29, 671–682. doi: 10.1002/hbm.20428

Hutchison, R. M., Womelsdorf, T., Allen, E. A., Bandettini, P. A., Calhoun, V. D., Corbetta, M., et al. (2013). Dynamic functional connectivity: promise, issues, and interpretations. *Neuroimage* 80, 360–378. doi: 10.1016/j.neuroimage.2013.05.079

Kiviniemi, V. J., Haanpää, H., Kantola, J. H., Jauhiainen, J., Vainionpää, V., Alahuhta, S., et al. (2005). Midazolam sedation increases fluctuation and synchrony of the resting brain BOLD signal. *Magn. Reson. Imaging* 23, 531–537. doi: 10.1016/j.mri.2005.02.009

Larson-Prior, L. J., Zempel, J. M., Nolan, T. S., Prior, F. W., Snyder, A., and Raichle, M. E. (2009). Cortical network functional connectivity in the descent to sleep. *Proc. Natl. Acad. Sci. U.S.A.* 106, 4489–4494. doi: 10.1073/pnas.0900924106

Laumann, T. O., Snyder, A. Z., Mitra, A., Gordon, E. M., Gratton, C., Adeyemo, B., et al. (2017). On the stability of BOLD fMRI correlations. *Cereb. Cortex* 27, 4719–4732. doi: 10.1093/cercor/bhw265

Liang, Z., Liu, X., and Zhang, N. (2015). Dynamic resting state functional connectivity in awake and anesthetized rodents. *Neuroimage* 104, 89–99. doi: 10.1016/j.neuroimage.2014.10.013

Licata, S. C., Nickerson, L. D., Lowen, S. B., Trksak, G. H., MacLean, R. R., and Lukas, S. E. (2013). The hypnotic zolpidem increases the synchrony of BOLD signal fluctuations in widespread brain networks during a resting paradigm. *Neuroimage* 70, 211–222. doi: 10.1016/j.neuroimage.2012.12.055

Liu, X., Chang, C., and Duyn, J. H. (2013). Decomposition of spontaneous brain activity into distinct fMRI co-activation patterns. *Front. Syst. Neurosci.* 7:101. doi: 10.3389/fnsys.2013.00101

Liu, X., De Zwart, J. A., Schölvinck, M. L., Chang, C., Ye, F. Q., Leopold, D. A., et al. (2018). Subcortical evidence for a contribution of arousal to fMRI studies of brain activity. *Nat. Commun.* 9, 395. doi: 10.1038/s41467-017-02815-3

Liu, X., and Duyn, J. H. (2013a). "Resting-State fMRI Signal Anti-Correlation Exists in Absence of Global Signal Regression," in *Proceedings of the 21st ISMRM Annual Meeting*, Salt Lake City, UT, 2251.

Liu, X., and Duyn, J. H. (2013b). Time-varying functional network information extracted from brief instances of spontaneous brain activity. *Proc. Natl. Acad. Sci. U.S.A.* 110, 4392–4397. doi: 10.1073/pnas.1216856110

Liu, X., Yanagawa, T., Leopold, D. A., Chang, C., Ishida, H., Fujii, N., et al. (2015). Arousal transitions in sleep, wakefulness, and anesthesia are characterized by an orderly sequence of cortical events. *Neuroimage* 116, 222–231. doi: 10.1016/j.neuroimage.2015.04.003

Ma, Y., Hamilton, C., and Zhang, N. (2016). Dynamic connectivity patterns in conscious and unconscious brain. *Brain Connect.* 7, 1–12. doi: 10.1089/brain.2016.0464

Matsuda, T., Matsuura, M., Ohkubo, T., Ohkubo, H., Atsumi, Y., Tamaki, M., et al. (2002). Influence of arousal level tor functional magnetic resonance imaging (fMRI) study: simultaneous recording of fMRI and electroencephalogram. *Psychiatry Clin. Neurosci.* 56, 289–290. doi: 10.1046/j.1440-1819.2002.01016.x

Matsui, T., Murakami, T., and Ohki, K. (2018). Neuronal origin of the temporal dynamics of spontaneous BOLD activity correlation. *Cereb. Cortex* 29, 1496–1508. doi: 10.1093/cercor/bhy045

Mitra, A., Snyder, A. Z., Blazey, T., and Marcus, E. (2015a). Lag threads organize the brain's intrinsic activity. *Proc. Natl. Acad. Sci. U.S.A.* 112, E2235–E2244. doi: 10.1073/pnas.1523893113

Mitra, A., Snyder, A. Z., Constantino, J. N., and Raichle, M. E. (2015b). The lag structure of intrinsic activity is focally altered in high functioning adults with autism. *Cereb. Cortex* 27:bhv294. doi: 10.1093/cercor/bhv294

Mitra, A., Snyder, A. Z., Tagliazucchi, E., Laufs, H., and Raichle, M. E. (2015c). Propagated infra-slow intrinsic brain activity reorganizes across wake and slow wave sleep. *eLife* 4:e10781. doi: 10.7554/eLife.10781.001

Musiek, E. S., Xiong, D. D., and Holtzman, D. M. (2015). Sleep, circadian rhythms, and the pathogenesis of Alzheimer disease. *Exp. Mol. Med.* 47:e148. doi: 10.1038/emm.2014.121

Nalci, A., Rao, B. D., and Liu, T. T. (2017). Global signal regression acts as a temporal downweighting process in resting-state fMRI. *Neuroimage* 152, 602–618. doi: 10.1016/j.neuroimage.2017.01.015

Özbay, P. S., Chang, C., Picchioni, D., Mandelkow, H., Moehlman, T. M., Chappel-Farley, M. G., et al. (2018). Contribution of systemic vascular effects to fMRI activity in white matter. *Neuroimage* 176, 541–549. doi: 10.1016/j.neuroimage.2018.04.045

Power, J. D., Barnes, K. A., Snyder, A. Z., Schlaggar, B. L., and Petersen, S. E. (2012). Spurious but systematic correlations in functional connectivity MRI networks arise from subject motion. *Neuroimage* 59, 2142–2154. doi: 10.1016/j.neuroimage.2011.10.018

Power, J. D., Mitra, A., Laumann, T. O., Snyder, A. Z., Schlaggar, B. L., and Petersen, S. E. (2014). Methods to detect, characterize, and remove motion artifact in resting state fMRI. *Neuroimage* 84, 320–341. doi: 10.1016/j.neuroimage.2013.08.048

Preti, M. G., Bolton, T. A., and Van De Ville, D. (2017). The dynamic functional connectome: state-of-the-art and perspectives. *Neuroimage* 160, 41–54. doi: 10.1016/j.neuroimage.2016.12.061

Saper, C. B., Scammell, T. E., and Lu, J. (2005). Hypothalamic regulation of sleep and circadian rhythms. *Nature* 437, 1257–1263. doi: 10.1038/nature04284

Schölvinck, M. L., Maier, A., Ye, F. Q., Duyn, J. H., Leopold, D. A., Scholvinck, M. L., et al. (2010). Neural basis of global resting-state fMRI activity. *Proc. Natl. Acad. Sci. U.S.A* 107, 10238–10243. doi: 10.1073/pnas.0913110107

Shine, J. M., Bissett, P. G., Bell, P. T., Koyejo, O., Balsters, J. H., Gorgolewski, K. J., et al. (2016). The dynamics of functional brain networks: integrated network states during cognitive task performance. *Neuron* 92, 544–554. doi: 10.1016/j.neuron.2016.09.018

Shmueli, K., van Gelderen, P., de Zwart, J. A., Horovitz, S. G., Fukunaga, M., Jansma, J. M., et al. (2007). Low-frequency fluctuations in the cardiac rate as a source of variance in the resting-state fMRI BOLD signal. *Neuroimage* 38, 306–320. doi: 10.1016/j.neuroimage.2007.07.037

Smith, S. M., Miller, K. L., Moeller, S., Xu, J., Auerbach, E. J., Woolrich, M. W., et al. (2012). Temporally-independent functional modes of spontaneous brain activity. *Proc. Natl. Acad. Sci. U.S.A.* 109, 3131–3136. doi: 10.1073/pnas.1121329109

Stevens, W. D., Hasher, L., Chiew, K. S., and Grady, C. L. (2008). A neural mechanism underlying memory failure in older adults. *J. Neurosci.* 28, 12820–12824. doi: 10.1523/JNEUROSCI.2622-08.2008

Tagliazucchi, E., and Laufs, H. (2014). Decoding wakefulness levels from typical fmri resting-state data reveals reliable drifts between wakefulness and sleep. *Neuron* 82, 695–708. doi: 10.1016/j.neuron.2014.03.020

Teigen, K. H. (1994). Yerkes-dodson: a law for all seasons. *Theory Psychol.* 4, 525–547. doi: 10.1177/0959354394044004

Thompson, G. J., Pan, W. J., Magnuson, M. E., Jaeger, D., and Keilholz, S. D. (2014). Quasi-periodic patterns (QPP): large-scale dynamics in resting state fMRI that correlate with local infraslow electrical activity. *Neuroimage* 84, 1018–1031. doi: 10.1016/j.neuroimage.2013.09.029

Trinder, J., Padula, M., Berlowitz, D., Kleiman, J., Breen, S., Rochford, P., et al. (2001). Cardiac and respiratory activity at arousal from sleep under controlled ventilation conditions. *J. Appl. Physiol.* 90, 1455–1463. doi: 10.1152/jappl.2001.90.4.1455

Turchi, J., Chang, C., Ye, F. Q., Russ, B. E., Yu, D. K., Cortes, C. R., et al. (2018). The basal forebrain regulates global resting-state fMRI fluctuations. *Neuron* 97, 940–952.e4. doi: 10.1016/j.neuron.2018.01.032

Van Den Berg, J. (2006). Sleepiness and head movements. *Ind. Health* 44, 564–576. doi: 10.2486/indhealth.44.564

van Dijk, K. R. A., Sabuncu, M. R., and Buckner, R. L. (2012). The influence of head motion on intrinsic functional connectivity MRI. *Neuroimage* 59, 431–438. doi: 10.1016/j.neuroimage.2011.07.044

Vanhaudenhuyse, A., Noirhomme, Q., Tshibanda, L. J. F., Bruno, M. A., Boveroux, P., Schnakers, C., et al. (2010). Default network connectivity reflects the level

of consciousness in non-communicative brain-damaged patients. *Brain* 133, 161–171. doi: 10.1093/brain/awp313

Vidaurre, D., Smith, S. M., and Woolrich, M. W. (2017). Brain network dynamics are hierarchically organized in time. *Proc. Natl. Acad. Sci. U.S.A.* 114, 12827–12832. doi: 10.1073/pnas.1705120114

Wei, J., Chen, T., Li, C., Liu, G., Qiu, J., and Wei, D. (2018). Eyes-open and eyes-closed resting states with opposite brain activity in sensorimotor and occipital regions: multidimensional evidences from machine learning perspective. *Front. Hum. Neurosci.* 12:422. doi: 10.3389/fnhum.2018.00422

Whitfield-Gabrieli, S., Thermenos, H. W., Milanovic, S., Tsuang, M. T., Faraone, S. V., McCarley, R. W., et al. (2009). Hyperactivity and hyperconnectivity of the default network in schizophrenia and in first-degree relatives of persons with schizophrenia. *Proc. Natl. Acad. Sci. U. S. A.* 106, 1279–1284. doi: 10.1073/pnas.0809141106

Wiggins, J. L., Bedoyan, J. K., Peltier, S. J., Ashinoff, S., Carrasco, M., Weng, S. J., et al. (2012). The impact of serotonin transporter (5-HTTLPR) genotype on the development of resting-state functional connectivity in children and adolescents: a preliminary report. *Neuroimage* 59, 2760–2770. doi: 10.1016/j.neuroimage.2011.10.030

Wong, C. W., Olafsson, V., Tal, O., and Liu, T. T. (2013). The amplitude of the resting-state fMRI global signal is related to EEG vigilance measures. *Neuroimage* 83, 983–990. doi: 10.1016/j.neuroimage.2013.07.057

Wulff, K., Gatti, S., Wettstein, J. G., and Foster, R. G. (2010). Sleep and circadian rhythm disruption in psychiatric and neurodegenerative disease. *Nat. Rev. Neurosci.* 11, 589–599. doi: 10.1038/nrn2868

Xu, P., Huang, R., Wang, J., Van Dam, N. T., Xie, T., Dong, Z., et al. (2014). Different topological organization of human brain functional networks with eyes open versus eyes closed. *Neuroimage* 90, 246–255. doi: 10.1016/j.neuroimage.2013.12.060

Yan, C., Cheung, B., Kelly, C., Colcombe, S., Craddock, R. C., Di, A., et al. (2013). NeuroImage A comprehensive assessment of regional variation in the impact of head micromovements on functional connectomics. *Neuroimage* 76, 183–201. doi: 10.1016/j.neuroimage.2013.03.004

Yan, C., Liu, D., He, Y., Zou, Q., Zhu, C., Zuo, X., et al. (2009). Spontaneous brain activity in the default mode network is sensitive to different resting-state conditions with limited cognitive load. *PLoS One* 4:e0005743. doi: 10.1371/journal.pone.0005743

Yancey, S. E., Rotenberg, D. J., Tam, F., Chiew, M., Ranieri, S., Biswas, L., et al. (2011). Spin-history artifact during functional MRI: potential for adaptive correction. *Med. Phys.* 38, 4634–4646. doi: 10.1118/1.3583814

Yang, G. J., Murray, J. D., Repovs, G., Cole, M. W., Savic, A., Glasser, M. F., et al. (2014). Altered global brain signal in schizophrenia. *Proc. Natl. Acad. Sci. U.S.A.* 111, 7438–7443. doi: 10.1073/pnas.1405289111

Yeo, B. T. T., Tandi, J., and Chee, M. W. L. (2015). Functional connectivity during rested wakefulness predicts vulnerability to sleep deprivation. *Neuroimage* 111, 147–158. doi: 10.1016/j.neuroimage.2015.02.018

Yoo, S. S., Choi, B. G., Juh, R., Pae, C. U., and Lee, C. U. (2005). Head motion analysis during cognitive fMRI examination: application in patients with schizophrenia. *Neurosci. Res.* 53, 84–90. doi: 10.1016/j.neures.2005.06.004

Yuan, H., Zotev, V., Phillips, R., and Bodurka, J. (2013). Correlated slow fluctuations in respiration, EEG, and BOLD fMRI. *Neuroimage* 79, 81–93. doi: 10.1016/j.neuroimage.2013.04.068

Zeng, L.-L., Wang, D., Fox, M. D., Sabuncu, M., Hu, D., Ge, M., et al. (2014). Neurobiological basis of head motion in brain imaging. *Proc. Natl. Acad. Sci. U.S.A.* 111, 6058–6062. doi: 10.1073/pnas.1317424111

Zhang, D., and Raichle, M. E. (2010). Disease and the brain's dark energy. *Nat. Rev. Neurol.* 6, 15–28. doi: 10.1038/nrneurol.2009.198

Conflict of Interest: The authors declare that the research was conducted in the absence of any commercial or financial relationships that could be construed as a potential conflict of interest.

frontiers in Neuroscience

ORIGINAL RESEARCH
published: 28 April 2020
doi: 10.3389/fnins.2020.00258

Diagnosis of Autism Spectrum Disorder Using Central-Moment Features From Low- and High-Order Dynamic Resting-State Functional Connectivity Networks

*Feng Zhao[1,2], Zhiyuan Chen[1,2], Islem Rekik[3], Seong-Whan Lee[4] and Dinggang Shen[5,4]**

[1] School of Computer Science and Technology, Shandong Technology and Business University, Yantai, China, [2] Shandong Co-Innovation Center of Future Intelligent Computing, Yantai, China, [3] BASIRA Lab, CVIP Group, Computing, School of Science and Engineering, University of Dundee, Dundee, United Kingdom, [4] Department of Brain and Cognitive Engineering, Korea University, Seoul, South Korea, [5] Department of Radiology and Biomedical Research Imaging Central, University of North Carolina at Chapel Hill, Chapel Hill, NC, United States

OPEN ACCESS

Edited by:
Xiaoping Philip Hu, University of California, Riverside, United States

Reviewed by:
Liang Wang, Institute of Psychology (CAS), China
Delin Sun, Duke University, United States
Jun Shi, Shanghai University, China
Mingli Zhang, Mcgill University, Canada

***Correspondence:**
Dinggang Shen
dgshen@med.unc.edu

Specialty section:
This article was submitted to Brain Imaging Methods, a section of the journal Frontiers in Neuroscience

Received: *07 December 2019*
Accepted: *09 March 2020*
Published: *28 April 2020*

Citation:
Zhao F, Chen Z, Rekik I, Lee S-W and Shen D (2020) Diagnosis of Autism Spectrum Disorder Using Central-Moment Features From Low- and High-Order Dynamic Resting-State Functional Connectivity Networks. Front. Neurosci. 14:258. doi: 10.3389/fnins.2020.00258

The sliding-window-based dynamic functional connectivity networks (D-FCNs) derived from resting-state functional magnetic resonance imaging (rs-fMRI) are effective methods for diagnosing various neurological diseases, including autism spectrum disorder (ASD). However, traditional D-FCNs are low-order networks based on pairwise correlation between brain regions, thus overlooking high-level interactions across multiple regions of interest (ROIs). Moreover, D-FCNs suffer from the temporal mismatching issue, i.e., subnetworks in the same temporal window do not have temporal correspondence across different subjects. To address the above problems, we first construct a novel high-order D-FCNs based on the principle of "correlation's correlation" to further explore the higher level and more complex interaction relationships among multiple ROIs. Furthermore, we propose to use a central-moment method to extract temporal-invariance properties contained in either low- or high-order D-FCNs. Finally, we design and train an ensemble classifier by fusing the features extracted from conventional FCN, low-order D-FCNs, and high-order D-FCNs for the diagnosis of ASD and normal control subjects. Our method achieved the best ASD classification accuracy (83%), and our results revealed the features extracted from different networks fingerprinting the autistic brain at different connectional levels.

Keywords: autism spectrum disorder, dynamic functional connectivity networks, resting-state functional MRI, central-moment features, conventional FC network

INTRODUCTION

Autism spectrum disorder (ASD) is a serious childhood neurodevelopmental disease, characterized by the impairment in social interaction, communication, and many other behavioral and cognitive functions in varying degrees (Geschwind and Levitt, 2007). According to the 2018 community report from the Centers for Disease Control and Prevention (CDCP)[1], about 1 in 59 American

[1]https://www.cdc.gov/ncbddd/autism/data.html.

children has been identified with some form of ASD, with about four times more common among boys than among girls. Thus, accurate early diagnosis and timely intervention of ASD, especially for the infants under 12 months old, may have pivotal importance in preventing the progression of detrimental symptoms (Jin et al., 2015). However, ASD is a very complex and highly heterogeneous neurological disorder, which affects many higher-level brain functions and sometimes whole-brain structures, making it challenging for accurate diagnosis. To address this, extensive research efforts (Geschwind and Levitt, 2007; Anagnostou and Taylor, 2011; Jin et al., 2015; Wang et al., 2018) have been dedicated to analyzing the neuroimaging data with different modalities, including structural magnetic resonance imaging (s-MRI) (Wee et al., 2013), functional MRI (fMRI) (Zhao et al., 2018), diffusion tensor imaging (DTI) (Deshpande et al., 2013), and positron emission tomography (PET) (Zürcher et al., 2015), to investigate ASD-related biological or neurological mechanisms. In this way, the respective biomarkers could be identified for characterizing ASD.

Recently, resting-state fMRI (rs-fMRI) uses blood-oxygenation-level-dependent (BOLD) signals to probe brain activity, which has shown great potential in exploring the *in vivo* neuronal underpinnings of ASD (Fornito et al., 2015; Liu et al., 2016; Huang et al., 2018; Zhao et al., 2018). Since BOLD signals are sensitive to the spontaneous and intrinsic neural activities within the brain, re-fMRI can be used as an efficient and noninvasive way for investigating neuropathological substrates of many neurological and psychiatric disorders at a whole-brain system level (Admon et al., 2012; Ganella et al., 2017; Li et al., 2017). Temporal correlation of the BOLD signals between different pairs of brain regions of interest (ROIs) is often used to define brain functional connectivity (FC), which can be used to explore how brain ROIs interact with each other. In practice, FC is often modeled as a FC network (FCN), with each specific brain ROI as a node in the network, and the strength of FC between a pair of brain ROIs as an edge (or link). In terms of both topological structures and connection strength, the differences between normal and disrupted FCN caused by certain pathological attacks reveal potential biomarkers to understand pathological underpinnings of ASD. Therefore, FCN has charted out a promising research direction to investigate the brain's functional differences between control and disease groups (Zhang et al., 2015, 2016; Qiao et al., 2018).

To date, researchers have developed many FCN models to capture rich information exchange across ROIs so that functional neurological biomarkers can be reliably identified for ASD diagnosis (Jie et al., 2014; Ha et al., 2015a; Plitt et al., 2015). The most commonly adopted FCN, namely, conventional FCN (C-FCN), is usually rooted in the assumption that the strength of FC is temporally stationary in the entire rs-fMRI scan duration (Achard, 2006; Zhao et al., 2018). Under such an assumption, FC is quantified with the correlation (e.g., Pearson's correlation) between a pair of rs-fMRI time series from two ROIs. As a result, C-FCN captures the functional connectivity between two ROIs in a *static* manner, which unfortunately overlooks the *dynamic* interaction between brain ROIs during the scan period.

In fact, recent studies have demonstrated that the dynamic changes of FC throughout the entire scan time may be an intrinsic property of brain function (Damaraju et al., 2014a; Kudela et al., 2017). Given the increasing evidence that dynamic FC during the entire scan time is very important for understanding the fundamental properties of brain network and the underpinnings of disordered brain connectivity changes, different studies have resorted to dynamic FC networks (D-FCNs) to characterize dynamic changes of FC, as well as the association of these dynamic changes with brain diseases (Damaraju et al., 2014b; Wee et al., 2015; Guo et al., 2017).

The most commonly used strategy of constructing D-FCNs is the sliding-window approach (Hutchison et al., 2013). The detailed contracture process of D-FCNs [i.e., low-order dynamic functional connectivity networks (Lo-D-FCNs), which will be discussed in the following section) is shown in **Figure 1**. Specifically, the entire rs-fMRI time series from a subject were segmented into multiple overlapping subseries by a sliding window with prefixed window length and step size between two successive windows (**Figure 1A1**). For each subseries, a FC subnetwork is constructed by calculating the short-term correlation between different ROIs, which is similar to the construction of C-FCN. As an example, the construction process of the second subnetwork is shown in **Figures 1A2,B2**, where x_i and x_j, respectively, denote the average rs-fMRI time series across all voxels within the ith and the jth ROIs, and their correlation $\rho_{ij}(2)$ is computed as the FC strength between the ith and the jth ROIs. In such a way, we can obtain a FC subnetwork (**Figure 1B2**), which reflects a short-term FC relationship between two ROIs. Repeating the above process, we can obtain a temporal FC subnetwork series, which is called dynamic FC networks (D-FCNs, i.e., Lo-D-FCNs) (**Figure 1B1**). Obviously, the correlation series (e.g., $[\rho_{ij}(1), \rho_{ij}(2), \cdots, \rho_{ij}(K)]$ in **Figure 1B1**) along the scanning time between a pair of ROIs can represent the temporal change of FC between the two ROIs, which indicates that D-FCNs can capture the dynamic properties of FC throughout the scan time and can provide rich discriminative information for ASD diagnosis.

While D-FCNs opens a new avenue for us to comprehensively understand brain activities, it still has the following two issues need to be addressed.

First, D-FCNs cannot reveal the potentially much complex and high-level relationship among multiple ROIs. Similar to C-FCN, D-FCNs is also based on computing pairwise correlation between neural signals, such as Pearson's correlation and partial correlation, between a pair of rs-fMRIs from two ROIs to estimate the FC strength (**Figure 1A2**). Although such simple FC network representation has been widely utilized for examining brain functional activity, it dramatically ignores much complex and high-level interactions across multiple ROIs. In such a sense, C-FCN and D-FCNs are referred to as the low-order FCN, and thus, D-FCNs also will be named as Lo-D-FCNs in this paper. Recently, emerging connectomic studies have demonstrated that examining more complex interactions involving multiple ROIs can provide more valuable insights into brain disease fingerprinting and diagnosis (Chen et al., 2016; Zhang et al., 2016, 2017a,b,c; Guo et al., 2017;

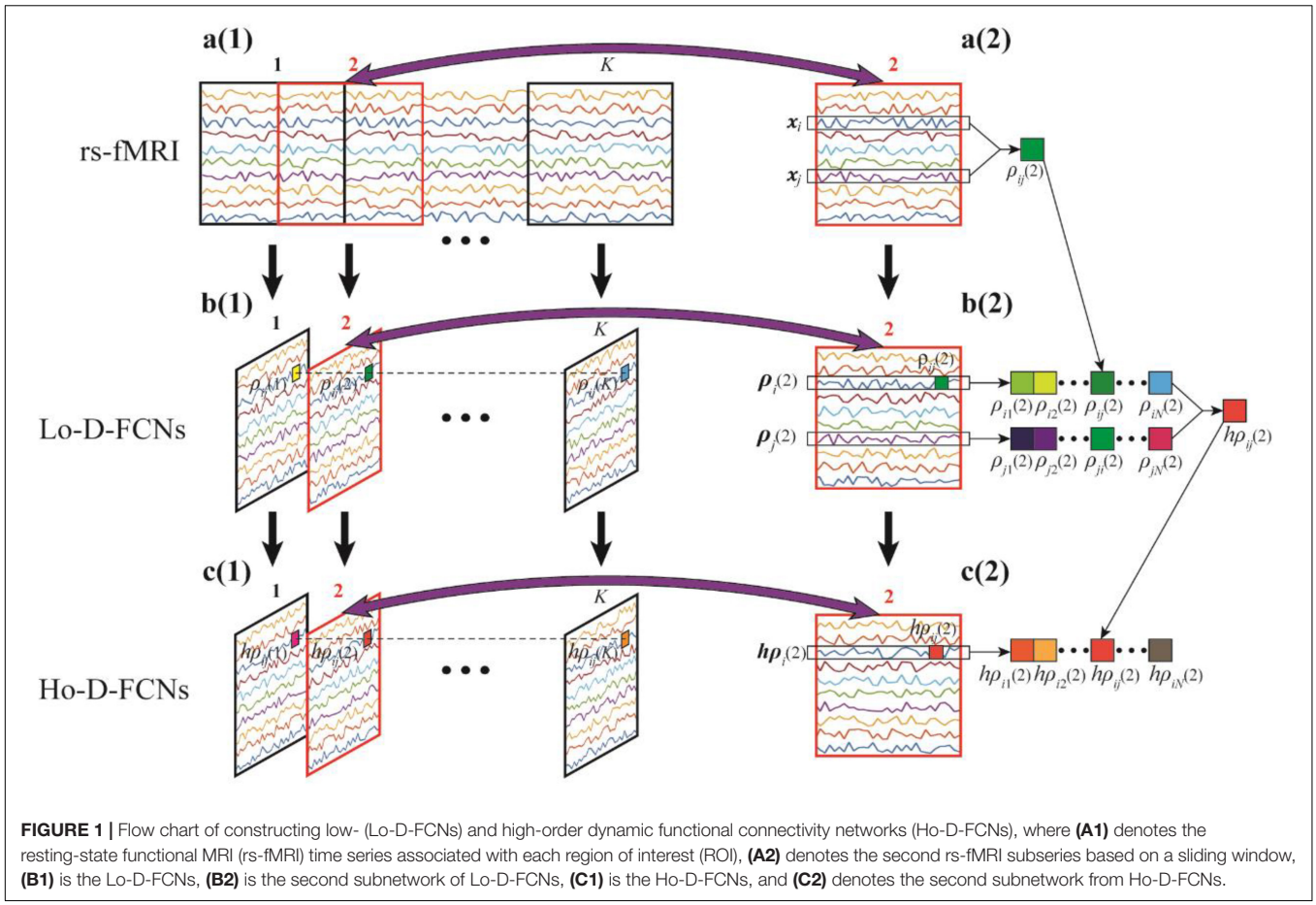

FIGURE 1 | Flow chart of constructing low- (Lo-D-FCNs) and high-order dynamic functional connectivity networks (Ho-D-FCNs), where **(A1)** denotes the resting-state functional MRI (rs-fMRI) time series associated with each region of interest (ROI), **(A2)** denotes the second rs-fMRI subseries based on a sliding window, **(B1)** is the Lo-D-FCNs, **(B2)** is the second subnetwork of Lo-D-FCNs, **(C1)** is the Ho-D-FCNs, and **(C2)** denotes the second subnetwork from Ho-D-FCNs.

Morris and Rekik, 2017; Soussia and Rekik, 2018; Zhao et al., 2018). Correspondingly, those FCNs, reflecting complex interactions across multiple ROIs, are referred as the high-order FCN (Ho-FCN).

By far, much attention has been dedicated to construct Ho-FCN models for exploring the interactions among multiple ROIs. For instance, Chen et al. (2016) constructed a Ho-FCN model based on the correlations between each pair of dynamic FC time series from sliding-window-based Lo-D-FCNs. Guo et al. (2017) modeled a Ho-FCN using a minimum spanning tree for Alzheimer's disease (AD) classification. Based on a more simple and intuitive way, i.e., correlation's correlation strategy, a new Ho-FCN was developed by Zhang et al. (2016) for more sensitive early AD detection. Different from Lo-FCN or Lo-D-FCNs, Ho-FCN presented by Zhang et al. defines another correlation between two brain regions based on their FC profiles, rather than BOLD signals. Here, the FC profile of a brain region means the traditional low-order FC of this region. In such a way, the correlation's correlation is able to reveal some interesting information; for example, some brain regions may exhibit stronger correlation with each other in a feature space (defined by FC profile) than the raw neural signal space. Consequently, Ho-FCN is able to provide another source of information for diagnosis (Zhang et al., 2016).

Inspired from the principle of the correlation's correlation, we construct a novel high-order dynamic FCNs (Ho-D-FCNs) for exploring the high-order dynamic FC relationships among multiple ROIs. **Figures 1C1,C2** display the flowchart of constructing Ho-D-FCNs. For each subnetwork from the Lo-D-FCNs, such as the second one shown in **Figure 1B2**, we regard the correlations series between a ROI and all other ROIs as its short-time FC profile, which reflects the FC relationship between this ROI and all other ROIs in a short scanning time. For example, $\rho_i(2)$ is the short-time FC profile of the ith ROI and $\rho_j(2)$ is that of the jth ROI (**Figure 1B2**). Then, the high-order correlation is computed for each pair of ROI based on the associated short-time FC profiles, such as $hp_{ij}(2)$ shown in **Figure 1C2**. Intuitively, such correlation reflects the relatively shorter time resemblance between a pair of FC profiles from two ROIs (i.e., correlation's correlation) and thus involves multiple ROIs. By doing so, we can obtain a corresponding high-order subnetwork (e.g., **Figure 1C2**) from each low-order subnetwork (e.g., **Figure 1B2**), which reflects how the low-order temporal correlations between different brain ROIs interact with each other during a short scan time. Accordingly, the high-order subnetwork series (**Figure 1C1**) is referred as Ho-D-FCNs and utilized to reveal some new characteristics for biomarker detection. In fact, the experimental result in *The Most Discriminative Features for ASD Diagnosis* shows

that Ho-D-FCNs can provide complementary information to C-FCN and Lo-D-FCNs.

Second, Lo-D-FCNs is sensitive to the chronological order of its subnetworks, which limits its use in comparative studies. Specifically, due to the unconstrained mental activity during the brain resting state, we cannot establish the temporal correspondence among these FC subnetworks from the same temporal window across different subjects. Therefore, the subnetwork series concatenated along scanning time (i.e., Lo-D-FCNs) might be dynamically mismatched across different subjects, which somewhat hinders the investigation and comparison of dynamic FC at a population level. It is noteworthy that Ho-D-FCNs presented in previous section also faces the same problem. By far, no method is proved to be effective in addressing this issue (Zhang et al., 2017a).

Statistical moment methods, including central, Hu, Zernike moments, and so on, have been broadly used in many areas for detecting and deriving various invariant properties of random signals (Hu, 1962; Hung et al., 2006). For the processing of a one-dimensional random sequence generated from a random variable, central-moment method owns the following merits: (Geschwind and Levitt, 2007) although central moment of different order partly characterizes some dynamic properties of a random sequence from its distinct view, their integration can provide a comprehensive characterization of the fluctuation properties of this sequence. (Jin et al., 2015) Most of central-moment features have the clear mathematical interpretability, e.g., for a sequence, its first-order central moment (i.e., mean) can reflect the fluctuation central; second-order central moment (i.e., variance) can reflect the fluctuation level; third-order central moment can reflect the skewness; and the fourth-order central moment can reflect the kurtosis. In theory, the change characteristics of a random sequence can be better represented by central-moment features. Usually, these central-moment features with the range from first- to seventh order are enough for us to analyze and describe the wave profile distribution of a random variable implicated in the sequence (Anagnostou and Taylor, 2011). More importantly, central-moment features are invariant to the temporal order of a sequence. In other words, as one expressional form of a random variable's probability distribution, central-moment features of a random sequence are immune to the order of its elements (in a mathematical sense).

To clarify the characteristic of central moment, we show the calculated central-moment values of four sequences Y1–Y4 in **Figure 2**, where the values in the parentheses following each sequence (Y1–Y4) sequentially denote the mean, variance, and third- and forth-order central moment. In **Figure 2A**, Y1 and Y2 denote two sequences with reversed order. We can see that Y1 and Y2 have the same values of central moment, demonstrating the invariance of central-moment features with respect to the sequence order. In **Figure 2B**, Y3 and Y4 are two symmetric sequences with identical symmetry axis but rather different fluctuating range. From the calculated central moments for Y3 and Y4, we can see that, except for the mean, the other central moments have noticeable difference, which means that central-moment features are able to reflect the dynamic change of a sequence. Based on the analysis of **Figure 2**, we can see that the central-moment features is invariant to sequence order and is able to capture the dynamic variation of a sequence.

Inspired by the advantages of central-moment method, we put forward a new approach that employs central-moment technique to excavate the temporal-invariance discriminative features of Lo-D-FCNs. Specifically, we treat each FC correlation time series of a pair of ROIs in a Lo-D-FCNs (such as $[\rho_{ij}(1), \rho_{ij}(2), \cdots, \rho_{ij}(K)]$ in **Figure 1B1**), which reflects the temporal changes of FC between two ROIs, as a one-dimensional random sequence that is generated from a random variable, and then, we extract the central-moment features of the sequence for further classification. Similarly, for Ho-D-FCNs, we regard the connection strength (i.e., the connection weight of an edge) series along the scanning time (such as$[h\rho_{ij}(1), h\rho_{ij}(2), \cdots, h\rho_{ij}(K)]$ in **Figure 1C1**) as a one-dimensional sequence and extract corresponding central-moment features.

Using the central-moment features, we can summarize the dynamic variation of either low- or high-order FC among multiple ROIs along the scanning time and give a general physiological interpretation to some extent. For example, if the value of the first-order central moment (i.e., mean value) from the FC correlation time series between a pair of ROIs in Lo-D-FCNs or among multiple ROIs in Ho-D-FCNs is relatively large, these ROIs may have strong functional correlation with each other. Similarly, if the value of the second-order central moment (i.e., variance value) is relatively large, it means that the correlations among the corresponding ROIs is very unstable during the whole scanning time; in other words, the periods of high correlation among all the corresponding ROIs may alternate with the periods of low correlation. Contrarily, such an interpretation is very hard to be obtained by directly analyzing Lo-D-FCNs or Ho-D-FCNs due to the large-scale and dynamic network structure.

In summary, there are three parts of contribution in this paper: (Geschwind and Levitt, 2007) proposing new Ho-D-FCNs (never used in previous ASD diagnosis) to reflect high-level connectivity information across multiple ROIs; (Jin et al., 2015) utilizing a central-moment method to capture FC properties derived from Lo-D-FCNs or Ho-D-FCNs without performing chronological time matching; (Anagnostou and Taylor, 2011) employing three multilevel FCN models (i.e., C-FCN, Lo-D-FCNs, and Ho-D-FCNs) to comprehensively investigate complex and multilevel functional associations among brain ROIs.

MATERIALS AND PREPROCESSING

Subjects

The rs-fMRI dataset used in this paper was downloaded from a publicly available Autism Brain Imaging Data Exchange (ABIDE) database (Di Martino et al., 2013). To alleviate data heterogeneity, we only consider the rs-fMRI data acquired from 45 ASD patients and 47 normal controls (NCs) with ages ranging from 7- to 15 years old, scanned at New York University Langone Medical Center. All these considered subjects had no excessive head motion with a displacement of <1.5 mm or an angular rotation of <1.5° in any of three directions.

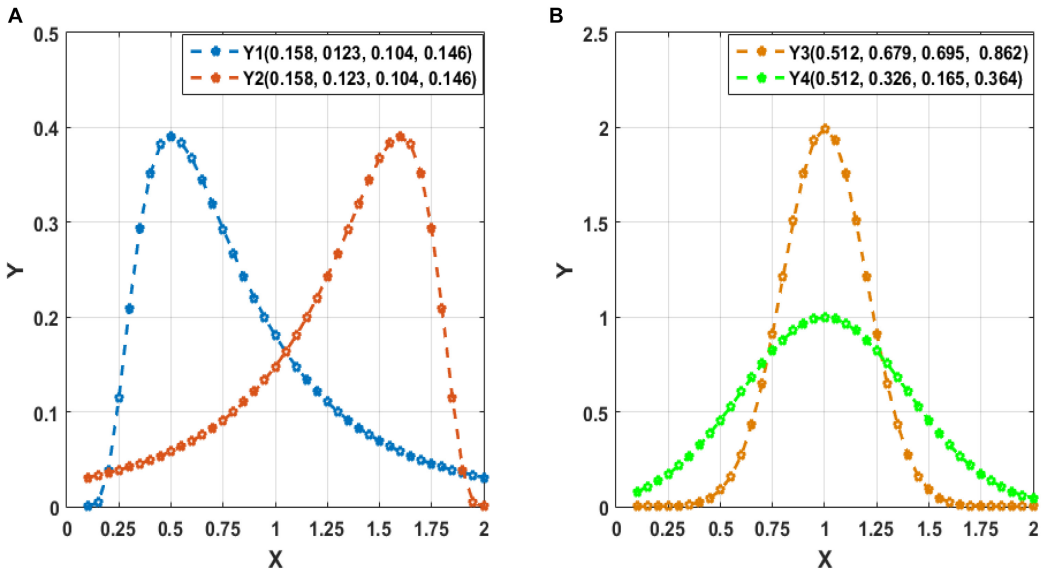

FIGURE 2 | Illustration of the calculated mean, variance, and third- and forth-order central moment (sequentially denoted in the corresponding parentheses) for four sequences Y1–Y4. **(A)** Two sequences (Y1 and Y2) with reversed order. **(B)** Two symmetric sequences (Y3 and Y4) with identical symmetry axis but different fluctuating range.

The detailed demographic information of these subjects is summarized in **Table 1**. As shown in **Table 1**, there were no significant differences ($p > 0.05$) in gender, age, and FIQ between two groups. ASD subjects were diagnosed based on the autism criteria in Diagnostic and Statistical Manual of Mental Disorders, 4th Edition, Text Revision (DSM-IV-TR) (American Psychiatric Association, 2000). More details on the data collection, exclusion criteria, and scan parameters can be obtained from the ABIDE website[2].

Data Acquisition and Preprocessing

All included subjects were scanned using a 3-T Siemens Allegra scanner at the NYU Langone Medical Center. During the 6 min rs-fMRI scan procedure, most subjects were instructed to relax with their eyes and stare at a white fixation cross at the center of the black screen. Their eye statuses were monitored by an eye tracker. The mean framewise displacement (FD) was computed to describe head motion for each individual. The individuals were excluded if their mean FD is >1 mm (Lin et al., 2015; Ray et al., 2015). On the other hand, head motion effect was further corrected with the Friston 24-parameter model in the following process. The main scanning parameters used in this dataset include the flip angle = 90, 33 slices, TR/TE = 2,000/15 ms, 180 volumes, and voxel thickness = 4 mm.

For rs-fMRI data preprocessing, we used the Statistical Parametric Mapping (SPM8) software[3]. Specifically, the first 10 rs-fMRI volumes were removed to ensure magnetization stabilization. Then, all rs-fMRI volumes were normalized to the Montreal Neurological Institute (MNI) space with the resolution of $3 \times 3 \times 3$ mm^3. Subsequently, ventricle, global signals were regressed out as nuisance signals, while head motion was corrected with the Friston 24-parameter model (i.e., 6 head motion parameters, 6 head motion parameters from the previous time point, and the 12 corresponding squared items) for decreasing head motion effects (Satterthwaite et al., 2013; Yan et al., 2013). Furthermore, the band-pass filtering (0.01–0.08 Hz) and signal detrending were also performed to avoid physiological noise (Cordes et al., 2001), measurement error (Achard et al., 2008), and magnetic field drifts of the scanner (Tomasi and Volkow, 2010). Finally, the brain was parcellated into 116 brain ROIs using the Automated Anatomical Labeling (AAL) atlas (Tzourio-Mazoyer et al., 2002). Next, the average rs-fMRI time series was calculated for each brain ROI and then represented in a data matrix $X \in R^{170 \times 116}$, where 170 denotes the total number of temporal image volumes and 116 denotes the total number of all brain ROIs.

[2]http://fcon_1000.projects.nitrc.org/indi/abide/abide_I.html.

[3]http://www.fil.ion.ucl.ac.uk/spm/software/spm8/.

TABLE 1 | Demographic information of the subjects.

	ASD	NC	*p*-values
Gender (M/F)	36/9	36/11	0.2135[a]
Age (mean ± SD)	11.1 ± 2.3	11.0 ± 2.3	0.773[b]
FIQ (mean ± SD)	106.8 ± 17.4	113.3 ± 14.1	0.0510[b]
ADI-R (mean ± SD)	32.2 ± 14.3[c]	–	–
ADOS (mean ± SD)	13.7 ± 5.0	–	–

ASD, autism spectrum disorders; NC, normal control; M, male; F, female; FIQ, Full Intelligence Quotient; ADI-R, Autism Diagnostic Interview-Revised; ADO, autism diagnostic observation schedule. [a]The p value was obtained by χ^2-test. [b]The p-value was obtained by two-sample two-tailed t-test. [c]Two patients do not have the ADI-R score.

METHOD

In this section, we mainly detail how to construct our Ho-D-FCNs based on the "correlation's correlation" principle. As mathematical notations, we use uppercase bold letters (e.g., ***G***, ***C***) to denote FC networks or matrices, lowercase bold letters (e.g., ***x***) to denote vectors, and lower case letters (e.g., *i*, *j*) to denote scalars.

Figure 3 displays the flowchart of our proposed classification framework, including the following four steps: ① constructing various FC networks, including C-FCN, Lo-D-FCNs, and Ho-D-FCNs; ② extracting the central-moment features, ranging from the first- to the seventh-order, from Lo-D-FCNs and Ho-D-FCNs (central-moment extracted from Lo-D-FCNs and Ho-D-FCNs can be regarded as the network feature since each of its elements is derived from a correlation time series of a pair of ROIs); ③ selecting the most discriminative features in a two-stage feature selection process for reducing feature dimensionality and eliminating irrelevant features to the target classification task; and ④ classification fusion. We construct an ensemble classifier with three linear support vector machines (SVM) classifiers (Cortes and Vapnik, 1995), each being trained with a specific type of FC features. The classification scores by all SVM classifiers are finally fused, by weighted averaging, to predict the target class label (ASD or NC) for a given testing subject.

Multilevel FC Networks Construction

A network structure can be modeled as a graph comprising a set of vertexes and edges linking them. Let ***G*** denote a FC network where each vertex represents a specific ROI, and each edge is weighted by the strength of FC between its end vertices (i.e., ROIs). Let ***C*** denote the connectivity matrix of ***G***, where each column (resp. row) denotes a specific ROI, and each element of ***C*** denotes the strength of FC between two ROIs. The structure of ***G*** is encoded in ***C***. Next, we will detail how the corresponding connectivity matrices of C-FCN, Lo-D-FCNs, and Ho-D-FCNs are constructed.

C-FCN Construction

For each subject, let $x_i = (x_{i1}, x_{i2}, \cdots, x_{iM})(i = 1, 2, \cdots, N)$ denote the average rs-fMRI time series across all voxels within the *i*th ROI, where *M* denotes the total number of temporal image volumes, and *N* denotes the total number of all ROIs. We can generate the conventional correlation-based FC network (C-FCN) G_C by a symmetric matrixC_C , defined as:

$$C_C = (\rho_{ij})_{1 \le i,j \le N}, \tag{1}$$

where ρ_{ij} denotes the Pearson's correlation between the average rs-fMRI time series from the *i*th and the *j*th ROIs, defined as:

$$\rho_{ij} = \mathrm{corr}(x_i, x_j), \tag{2}$$

It can be seen from Equation (1) that each row or column of C_C denotes the Pearson correlation series between a specific ROI and all other ROIs. Notably, G_C encodes the static interactions between any pair of ROIs during the entire scanning duration, which fails to capture the dynamic nature of neural activity.

Lo-D-FCNs Construction

To encode the nonstationary interactions between different ROIs, we adopt the sliding-window strategy to generate Lo-D-FCNs. Specifically, suppose that the length of the sliding window is *T* and the step size between two successive windows is *S*, thus the entire rs-fMRI time series $x_i = (x_{i1}, x_{i2}, \cdots, x_{iM})(i = 1, 2, \cdots, N)$ corresponding to the *i*th ROI are partitioned into *K* overlapping segments with a predefined sliding window, where $K = [(M - T)/S] + 1$.

Letting $x_i(k) = \left[x_{i1}\left(k\right), x_{i2}\left(k\right), \cdots, x_{iT}\left(k\right)\right](k = 1, 2, \cdots, K)$ denote the *k*th time subseries of x_i , we can calculate the *k*th submatric $C_{\mathrm{Lo-D}}(k)$ as Equation (1).

$$C_{\mathrm{Lo-D}}\left(k\right) = \left[\rho_{ij}\left(k\right)\right]_{1 \le i,j \le N} \quad \left(k = 1, 2, \cdots, K\right) \tag{3}$$

where $\rho_{ij}\left(k\right)$ is computed as:

$$\rho_{ij}\left(k\right)\rho_{ij}\left(k\right) = \mathrm{corr}\left[x_i\left(k\right), x_j\left(k\right)\right] \tag{4}$$

Obviously, $C_{\mathrm{Lo-D}}(k)$ reflects the interaction between two ROIs during a relatively shorter time period. The submatrix series $\left\{C_{\mathrm{Lo-D}}\left(k\right)\right\}_{k=1}^{K}$ along the scanning time describes the temporal change of the connectivity strength for all ROI pairs. The corresponding FCN of $\left\{C_{\mathrm{Lo-D}}\left(k\right)\right\}_{k=1}^{K}$ is called Lo-D-FCNs and denoted as$C_{\mathrm{Lo-D}}(k)$ (see **Figure 3**).

Ho-D-FCNs Construction

To fully capture high-order functional interactions across brain ROIs, we adopt the "correlation's correlation" principle (Zhang et al., 2016; Morris and Rekik, 2017; Soussia and Rekik, 2018; Zhao et al., 2018) to generate Ho-D-FCNs. Specifically, for the *i*th ROI of a subject, we can get a correlation series $\rho_i\left(k\right) = \left[\rho_{i1}\left(k\right), \rho_{i2}\left(k\right), \ldots, \rho_{iN}\left(k\right)\right]$ from the *k*th submatrix$C_{\mathrm{Lo-D}}(k)$ (see Equation 3). Mathematically, $\rho_i\left(k\right)$ denotes the *i*th row or column of the symmetric matrix$C_{\mathrm{Lo-D}}(k)$. We regard $\rho_i\left(k\right)$ as the short-time FC profile of the *i*th ROI on the *k*th time subseries, reflecting the correlations between the *i*th ROI and all other ROIs during the *k*th time section. Then, the correlation is computed between the short-time FC profile $\rho_i\left(k\right)$ of the *i*th ROI and the short-time FC profile $\rho_j\left(k\right)$ of the *j*th ROI as follows:

$$h\rho_{ij}\left(k\right) = \mathrm{corr}\left[\rho_i\left(k\right), \rho_j(k)\right], \tag{5}$$

Obviously, $h\rho_{ij}\left(k\right)$ denotes the "correlation's correlation" between the *i*th ROI and the *j*th ROI in the *k*th time section, quantifying how the correlation series $\rho_i\left(k\right)$ [i.e., the FC profiles $\rho_i\left(k\right)$ between the *i*th ROI and all other ROIs resemble the correlation series $\rho_i\left(k\right)$[i.e., the FC profiles $\rho_j\left(k\right)$] between the *j*th ROI and all other ROIs. As a result, $h\rho_{ij}\left(k\right)$ can reveal more complex relationship between the FC profiles $\rho_i\left(k\right)$ and$\rho_j\left(k\right)$, not just the original rs-fMRI time series $x_i\left(k\right)$ and $x_j\left(k\right)$. Thus, the correlation coefficient $h\rho_{ij}\left(k\right)$ can characterize more complex and abstract interactions among multiple ROIs, which occur in a relatively shorter time period. We further define a submatrix $C_{\mathrm{Ho-D}}\left(k\right)$ in the *k*th time section as follows:

$$C_{\mathrm{Ho-D}}\left(k\right) = \left[\rho h_{ij}\left(k\right)\right]_{1 \le i,j \le N}, \tag{6}$$

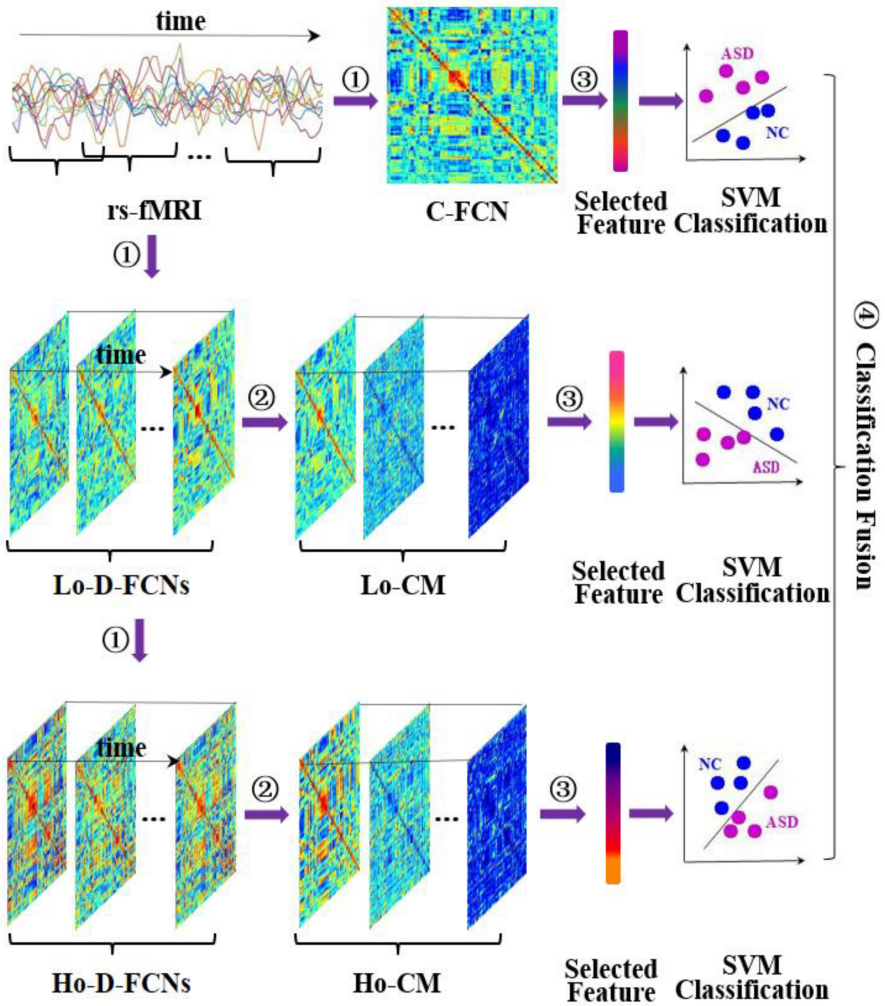

FIGURE 3 | Overview of our proposed classification framework, including four main steps: ① constructing multiple functional connectivity networks (FCNs), ② extracting central-moment features, ③ feature selection, and ④ classification fusion. Lo-CM denotes the central-moment features from low-order dynamic functional connectivity networks (Lo-D-FCNs), and Ho-CM is from high-order dynamic functional connectivity networks (Ho-D-FCNs). The means of other symbols are the same with those presented in *Introduction*.

Based on Equation (6), we can construct a Ho-D-FCNs, denoted as$C_{\mathrm{Ho-D}}(k)$, where the submatrices series $\{C_{\mathrm{Ho-D}}(k)\}_{k=1}^{K}$ is regarded as the associated dynamic FC of $C_{\mathrm{Ho-D}}(k)$ along the scanning time. Obviously, $C_{\mathrm{Ho-D}}(k)$ can capture high-level interactions across multiple ROIs while preserving the dynamic aspect of brain functional activity. Similar to $G_{\mathrm{Lo-D}}$, **Figure 3** displays the main steps for constructing $G_{\mathrm{Ho-D}}(k)$.

Feature Extraction and Selection

With the above-mentioned methods in *Multilevel FC Networks Construction*, three different types of FCN, i.e., G_C, $G_{\mathrm{Lo-D}}$ and $G_{\mathrm{Lo-D}}$, are obtained to form multilevel representations of functional interactions across multiple ROIs. In this section, we mainly introduce how to extract and select features from these FCNs.

Central-Moment Feature Extraction

We note that both FC networks $G_{\mathrm{Lo-D}}$ and $G_{\mathrm{Ho-D}}$ are out of temporal synchrony across different subjects. In other words, the kth time subseries, $\rho_{ij}^{l}(k)$ $(k = 1, 2, \cdots, K)$ [or $h\rho_{ij}^{l}(k)$] from the lth subject may be inconsistent with $\rho_{ij}^{r}(k)$ [or $h\rho_{ij}^{r}(k)$] from the rth subject due to the unconstrained mental activities during resting state. To extract *consistent* dynamic connectomic features across subjects, we propose to extract the central-moment features of $G_{\mathrm{Lo-D}}$ and carry out the same procedure for $G_{\mathrm{Ho-D}}$. Specifically, we first construct a FC time series ρ_{ij} between the ith ROI and the jth ROI by concatenating the elements $\rho_{ij}(k)$ (see Equation 3) as follows:

$$\rho_{ij} = [\rho_{ij}(1), \rho_{ij}(2), \cdots \rho_{ij}(k), \cdots, \rho_{ij}(K)](1 \le i, j \le N,\ 1 \le k \le K), \quad (7)$$

where ρ_{ij} reflects the FC dynamic changes along the scanning time between the ith ROI and the jth ROI. We calculate its dth order central-moment $m_{ij}(d)$ of ρ_{ij}as follows:

$$m_{ij}\left(d\right) = \sqrt[d]{\frac{\sum_{k=1}^{K}\left[\rho_{ij}\left(k\right) - \bar{\rho}_{ij}\right]^{d}}{K}} (d = 1, 2, \cdots D), \quad (8)$$

where D denotes the highest order. We further get a central-moment matrix series $\left\{M_{\mathrm{Lo-D}}(d)\right\}_{d=1}^{D}$ from $G_{\mathrm{Lo-D}}$ [i.e., $\{C_{\mathrm{Lo-D}}\left(k\right)\}_{k=1}^{K}$] by the following definition:

$$M_{\mathrm{Lo-D}}\left(d\right) = \left[m_{ij}\left(d\right)\right]_{1\le i,j\le N} (d = 1, 2, \cdots D), \quad (9)$$

It can be seen from Equation (8) that $m_{ij}\left(d\right)$ is invariant to the element order of $\rho_{ij} = [\rho_{ij}(1), \rho_{ij}(2), \cdots \rho_{ij}\left(k\right), \cdots, \rho_{ij}(K)]$. Thus, $\left\{M_{\mathrm{Lo-D}}(d)\right\}_{d=1}^{D}$ is insensitive to temporal asynchrony across subject.

We use the same strategy to derive central-moment matrix series $\left\{M_{Ho-D}(d)\right\}_{d=1}^{D}$ of $G_{\mathrm{Ho-D}}$ [i.e., $\{C_{\mathrm{Ho-D}}\left(k\right)\}_{k=1}^{K}$] using the following formula:

$$M_{\mathrm{Ho-D}}\left(d\right) = \left[hm_{ij}\left(d\right)\right]_{1\le i,j\le N} (d = 1, 2, \cdots D), \quad (10)$$

where $hm_{ij}\left(d\right)$ is computed as follows:

$$hm_{ij}\left(d\right) = \sqrt[d]{\frac{\sum_{k=1}^{K}\left[h\rho_{ij}\left(k\right) - \overline{h\rho}_{ij}\right]^{d}}{K}} (d = 1, 2, \cdots D), \quad (11)$$

$h\rho_{ij}\left(k\right)$ denotes the "correlation's correlation" between the ith ROI and the jth ROI in the kth time section (see Equation 5). We also give a brief illustration of $M_{\mathrm{Lo-D}}(d)$ and $M_{\mathrm{Ho-D}}\left(d\right)$ construction in **Figure 3**.

Feature Selection Using a Two-Stage Approach

For the lth subject, we obtain three types of raw features, i.e., the features $C_C^{(l)}$ of C-FCN, the central-moment features $M_{\mathrm{Lo-D}}^{(l)}\left(d\right)$ of Lo-D-FCNs, and the central-moment features $M_{\mathrm{Ho-D}}^{(l)}\left(d\right)$ of Ho-D-FCNs, each of which is a $N \times N$ symmetric matrix. Here, N denotes the number of ROIs, and $N = 116$ is set in our case. Since each matrix is symmetric, we only vectorize their lower off-diagonal triangular part to define the feature vector set$\left\{y_0^{(l)}, y_1^{(l)}, y_2^{(l)}\right\}$, for representing the lth subject, where $y_0^{(l)}$, $y_1^{(l)}$, and $y_2^{(l)}$ denote the vectorization of $C_C^{(l)}$, $M_{\mathrm{Lo-D}}^{(l)}\left(d\right)$, and $M_{\mathrm{Ho-D}}^{(l)}\left(d\right)$, respectively. The dimensionality of $y_c^{(l)}$ $(0 \le c \le 2)$ is$\frac{N(N-1)}{2}$, and it is 6,670 in our case, where c denotes the type of feature vector. Obviously, the feature dimensionality is much larger than the total number of subjects. More importantly, many features may be irrelevant to ASD diagnosis.

To remove the redundant features while preserving a small subset of discriminative features that are most likely relevant to ASD pathology, we design a two-stage feature selection strategy. Specifically, in the first stage, for each feature from $y_c^{(l)}$ $(0 \le i \le 2)$, we perform a two-sample t-test between NC and ASD subjects, due to its simplicity and efficiency. Then, we select the features only with their p-values smaller than a certain threshold. In such a way, we can get a preliminary set of features that are highly correlated with the class label, while the rest features not correlated with classification well be eliminated. However, some feature may be still correlated to each other, thus causing feature redundancy. Therefore, to further remove features from these correlated features, we adopt the L_1-norm regularized least squares regression, known as LASSO (Tibshirani, 1996), to further optimize the feature subset in the second stage. Note that the t-test is performed on each feature individually, while LASSO regression considers all features jointly such that the correlation between features can be taken into account. Specifically, let $\bar{y}_c^{(l)}$ $(0 \le c \le 2)$ denote the features selected by the t-test. $I^{(l)}$ is the class labels of $\bar{y}_c^{(l)}$, where $I^{(l)} = 1$ if the lth subject is ASD and $I^{(l)} = -1$ if the lth subject is NC. Let w_c represent the weight vector for the feature selection task. Mathematically, the LASSO model can be formalized as energy functional to optimize (Tibshirani, 1996):

$$\min \frac{1}{2}\sum_{l=1}^{L}\left\|I^{(l)} - < y_c^{(l)}, W_c > \right\|^2 + \lambda\|W_c\|_1 \quad (12)$$

where $\langle \bullet, \bullet \rangle$ denotes the inner operator, L denotes the number of subjects, and λ is a parameter, controlling the model's sparsity based on the L_1-norm regularization. The larger the value of λ , the sparser the model is. In this way, we can jointly achieve sparse feature selection. In other words, those features with nonzero elements of w_i were eventually retained. Let $\bar{\bar{y}}_c^{(l)}$ $(0 \le c \le 2)$ denote the final selected set of feature from the original pool of feature vectors $y_c^{(l)}$ $(0 \le c \le 2)$.

Classifier Learning and Fusing

After selecting the most important features by the two-stage approach, we use SVM with linear kernel for ASD classification. Considering these features $\bar{\bar{y}}_c^{(l)}$ $(0 \le c \le 2)$ are generated from three FCNs with different level, we train an SVM classifier for each type of features $\bar{\bar{y}}_c^{(l)}$ $(0 \le c \le 2)$. SVM seeks a maximum margin hyper-plane to separate the samples from two different classes. The empirical risk on the training data and the complexity of the model can be balanced by the hyperparameter γ, thus ensuring good generalization ability on the unseen data. Finally, we can fuse these three SVM classifiers together for making the final result. Specifically, each type of features $\bar{\bar{y}}_c^{(l)}$ are used to train a specific classifier. Then, for a test subject, each SVM will output an associated decision score, indicating the probability of that subject belonging to a class. Finally, to obtain classification result, we calculate the weighted average of the three decision scores from these SVM models with weight α tuned for each SVM, which reflects the reliability of corresponding decision score. In **Figure 3**, we provide a brief illustration of the classifier learning and fusing.

EXPERIMENTAL ANALYSIS

For evaluating the performance of our proposed method, we adopted a sixfold cross-validation (CV) strategy to perform experiments. For example, all training subjects were randomly partitioned into six subsets (each subset with a roughly equal number of samples), and each time the samples within one subset are selected as the testing dataset, while the remaining samples within the other five subsets are combined together as the training dataset for feature selection and classifier training. For evaluation, we reported the average accuracy of classification results across all six CV cases. Furthermore, to avoid any possible bias in fold selection, the entire sixfold CV process was repeated 10 times, with a different random partitioning of samples each time. Finally, the average statistics of the 10 repetitions was reported. To carry out our proposed method and other competing algorithms, some parameters need to set, such as p-values in the two-sample t-test model, λ in the LASSO model (*Feature Selection Using a Two-Stage Approach*), and γ and α in the linear SVM model (*Classifier Learning and Fusing*). For fair comparison, we use nested CV to tune the parameters in each method. In particular, for each fold in the above sixfold CV, we perform another fivefold CV on the five subsets, which is used for training for the selection of parameters. The optimal values can be determined by this inner fivefold CV when the average classification accuracy reaches its optimum. Then, the selected parameters are used to learn a model based on the entire training dataset, which is further utilized for classification on the testing dataset. For our approach, we determine the optimal values for the parameters in the following range: p–values $\in [0.01 : 0.01 : 0.1]$,$\lambda \in [0.1 : 0.1 : 0.7]$, $\gamma \in \left[2^{-5}, 2^{-4}, \cdots, 2^{5}\right]$, and $\alpha \in [0.1 : 0.1 : 0.9]$.

As usual, we adopt six evaluation measures, i.e., classification accuracy (ACC), sensitivity or true positive rate (TPR), specificity or true negative rate (TNR), positive predictive value (PPV), negative predictive value (NPV), and F1 score, to comprehensively evaluate classification performance. Their definitions are given as follows:

$$\mathrm{ACC} = \frac{TP + TN}{TP + FP + TN + FN}, \tag{13}$$

$$\mathrm{TPR} = \frac{TP}{TP + FN}, \tag{14}$$

$$\mathrm{TNR} = \frac{TN}{FP + TN}, \tag{15}$$

$$\mathrm{PPV} = \frac{TP}{TP + FN}, \tag{16}$$

$$\mathrm{NPV} = \frac{TN}{FN + TN}, \tag{17}$$

$$\mathrm{F1} = \frac{2 \times TP}{2 \times TP + FN + FP}, \tag{18}$$

where TP, TN, FP, and FN indicate the true positive, true negative, false positive, and false negative, respectively. Note that we treat ASD patients as positive samples and NC as negative samples in this paper.

The Influence of Parameters on D-FCNs

In the construction of D-FCNs (including Lo-D-FCNs and Ho-D-FCNs) and feature extraction, there are three parameters to tune: (1) sliding window length T, (2) the step size between two successive windows S, and (3) the order of central moment d, which jointly affects the diagnosis accuracy of Lo-D-FCNs and Ho-D-FCNs. To evaluate the impact of these parameters on classification performance and select a suitable combination of parameters for the subsequent multiclassifier fusion, we vary the values of these parameters in specific range (i.e., $T = [40 : 10 : 90]$, $S = [2 : 2 : 12]$, $d = [1 : 1 : 7]$) and repeat the classification experiments based on different combinations of these parameters. It is worth noting that when $d = 1$, we use the mean value instead of the first-order moment so that the method can better reflect the sample characteristics.

Here, we use the average classification accuracy (ACC) to evaluate the applicability of parameter combination to ASD diagnosis. **Figure 4** displays the ACC achieved by Lo-D-FCNs and Ho-D-FCNs using different combinations of T, S, and d values. The higher the accuracy is, the longer the length and the warmer the color are.

As shown in **Figure 4A**, the optimal parameter combination for Lo-D-FCNs is $T = 60$, $S = 2$, and $d = 4$, its ACC is 79.4, while the minimum value of ACC is 54.0 when $T = 60$, $S = 10$, and $d = 3$. Likewise, from **Figure 4B**, we can see that the optimal parameter combination for Ho-D-FCNs is $T = 40$, $S = 12$, and $d = 2$, its ACC is 77.6, while the minimum is 56.1 when $T = 70$, $S = 8$, and $d =$ d. Therefore, based on **Figure 4**, we can observe that the classification preformation is rather sensitive to these parameters. For boosting the final classification accuracy, we set these optimal parameters (i.e., $T = 60$, $S = 2$, and $d = 4$ for Lo-D-FCNs and $T = 40$, $S = 12$, and $d = 2$ for Ho-D-FCNs) as the default parameter for the following experiments.

Fusion Results of the C-FCN, Lo-D-FCNs, and Ho-D-FCNs

We select the combination of parameters that can lead to the highest ACC from the SVMs of C-FCN, Lo-D-FCNs, and Ho-D-FCNs, respectively, and obtain the final classification result by linear fusion of the SVM ensemble decision scores. In addition to our model, we also added another recently developed high-order FC network approach (Zhou et al., 2018) for comparison. Similar to our approach, this method also used sliding window approach to capture the dynamic variation of FC, and a series of traditional FC networks are constructed. Then, both low-order (termed as LoM) and high-order FC (termed as HiO) networks are constructed by maximum likelihood estimation with the assumption that these D-FCNs follow the matrix variate normal distribution.

Table 2 shows the average classification performance of nine models. Among them, C_C denotes the feature derived

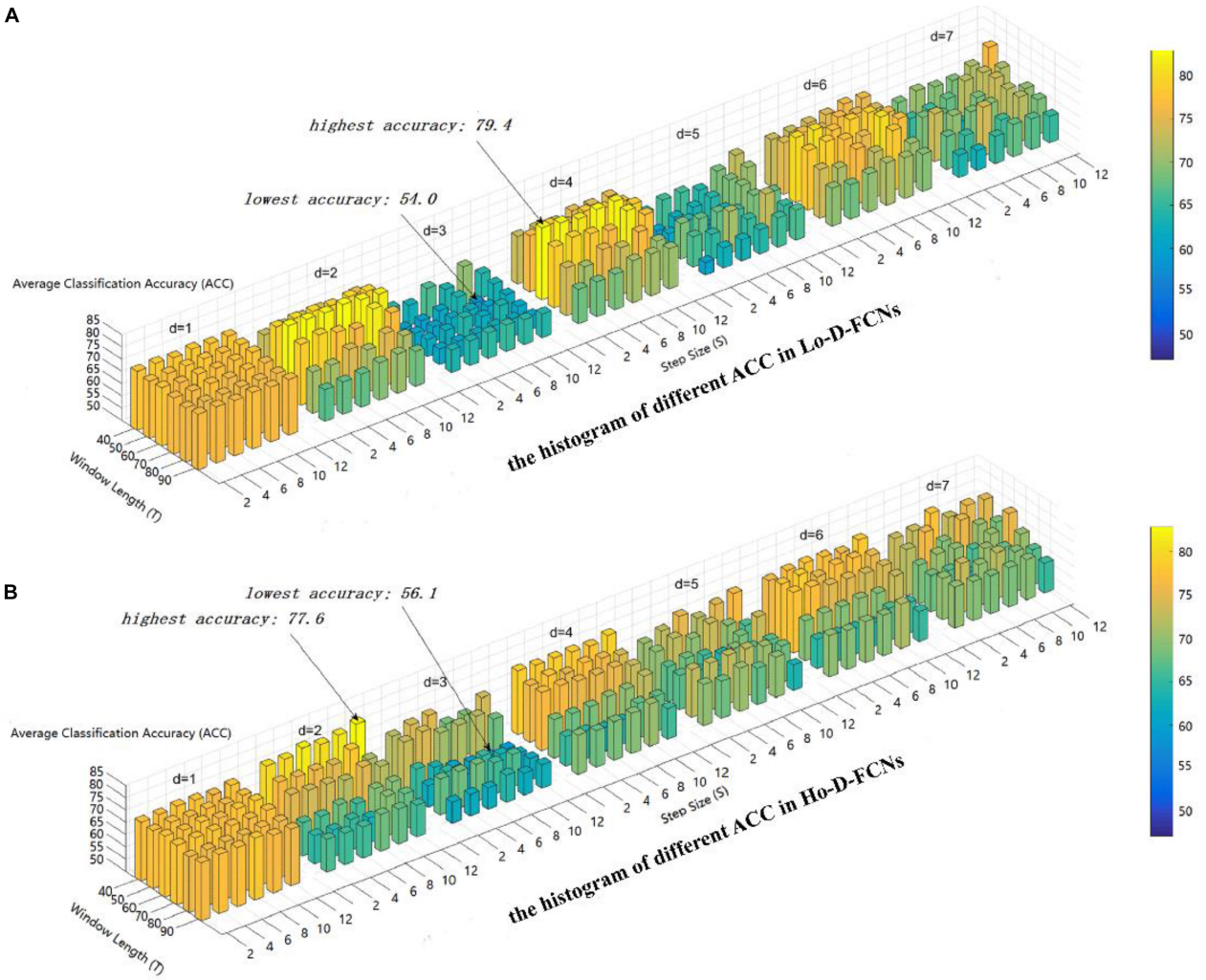

FIGURE 4 | The average classification (ACC) using different combinations of *T*, *S*, and *d* values. **(A)** The histogram of different ACC in Lo-D-FCNs. **(B)** The histogram of different ACC in Ho-D-FCNs.

TABLE 2 | Autism spectrum disorder (ASD) classification using different feature types and evaluation measures.

Model	ACC (%)	TPR (%)	TNR (%)	PPV (%)	NPV (%)	F1 (%)
C_C	74 ± 0.04	72 ± 0.23	76 ± 0.01	74 ± 0.05	74 ± 0.08	73 ± 0.07
$C_{Lo-D}(1)$	75 ± 0.12	73 ± 0.14	76 ± 0.29	74 ± 0.23	75 ± 0.08	74 ± 0.12
$C_{Lo-D}(4)$	79 ± 0.15	79 ± 0.10	79 ± 0.53	79 ± 0.38	79 ± 0.07	79 ± 0.12
$C_{Ho-D}(2)$	78 ± 0.06	79 ± 0.49	77 ± 0.24	76 ± 0.09	80 ± 0.25	77 ± 0.11
HiO	72 ± 0.16	71 ± 0.21	73 ± 0.32	72 ± 0.18	73 ± 0.28	72 ± 0.16
$C_C + C_{Lo-D}(4)$	80 ± 0.20	78 ± 0.25	82 ± 0.39	80 ± 0.38	79 ± 0.17	79 ± 0.20
$C_C + C_{Ho-D}(2)$	78 ± 0.11	79 ± 0.20	77 ± 0.26	77 ± 0.17	79 ± 0.12	77 ± 0.11
$C_{Lo-D}(4) + C_{Ho-D}(2)$	81 ± 0.06	82 ± 0.31	80 ± 0.11	80 ± 0.06	83 ± 0.17	81 ± 0.08
$C_C + C_{Lo-D}(4) + C_{Ho-D}(2)$	**83 ± 0.16**	**82 ± 0.10**	**84 ± 0.46**	**83 ± 0.34**	**83 ± 0.08**	**82 ± 0.13**

Values highlighted in bold show best results.

from the conventional correlation-based FC network (C-FCN), and $C_C + C_{Lo-D}$ denotes the fusion of C-FCN and Lo-D-FCNs. The number following C_{Lo-D} denotes the order of central moment used to extract features. For example, $C_{Lo-D}(1)$ means the low-order dynamic FC network with mean as central moment. Notice that the constructed LoM network in Zhou et al. (2018) is equivalent to our proposed Lo-D-FCNs when the order of central moment

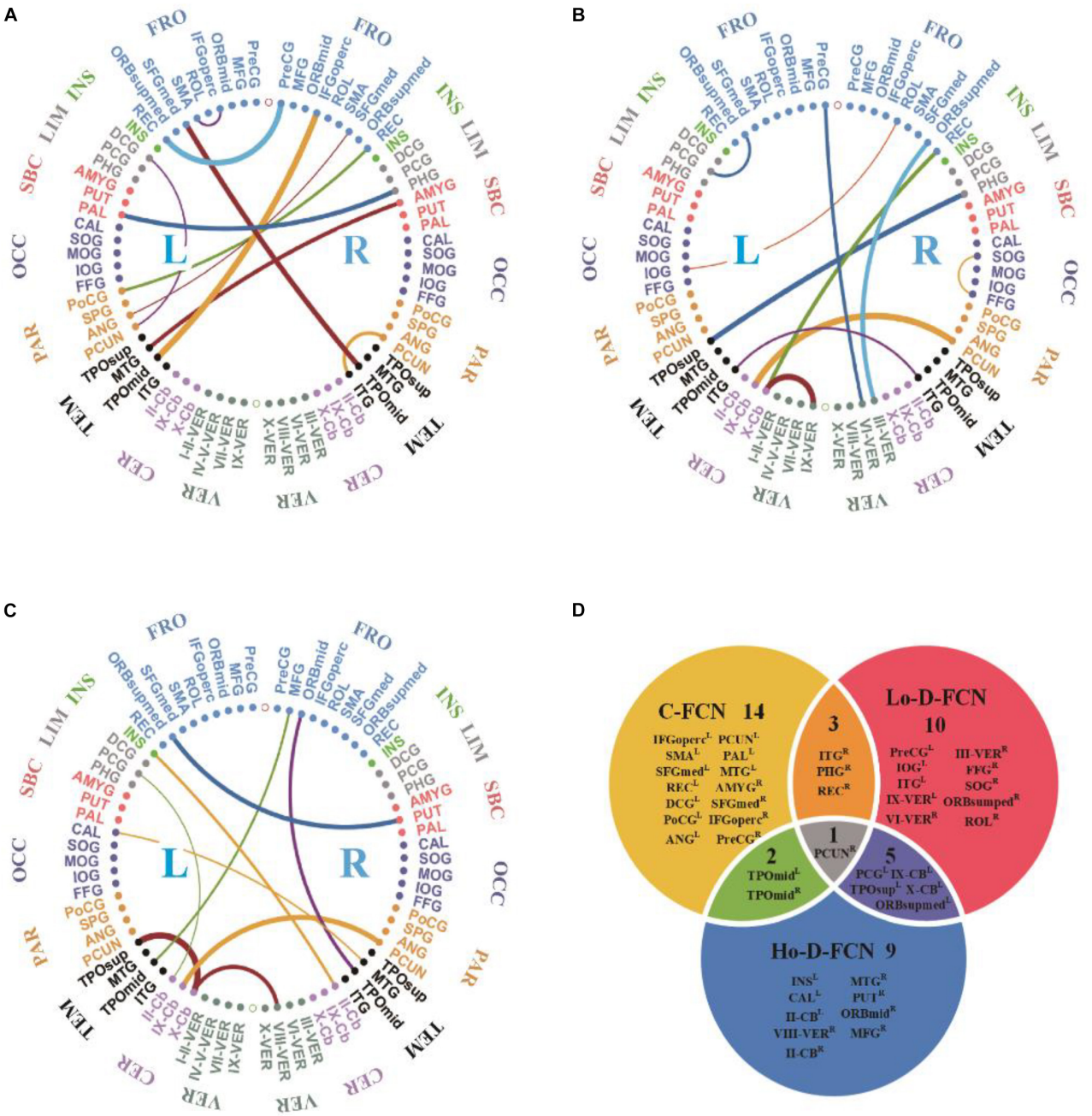

FIGURE 5 | The circular graphs and the involved brain regions of interest (ROIs) of the top 10 discriminative connections selected by our proposed method. **(A)** The correlation-based functional connectivity (FC) network (C-FCN), **(B)** the low-order dynamic FC network (Lo-D-FCNs), **(C)** the high-order dynamic FC network (Ho-D-FCNs), and **(D)** the mutual comparison among three sets of connections. The selection frequency is encoded by the thickness of each connecting curve, i.e., thicker curves indicate higher selection frequency. For brain region abbreviations, please refer to **Table 3**.

equals to 1, i.e., $C_{Lo-D}(1)$. We also report the standard deviation of the classification accuracy. The best results are highlighted in bold.

Based on **Table 2**, we can draw the conclusions below. (1) In terms of ACC and other evaluation measures, the performance of feature types derived from D-FCNs (i.e., Lo-D-FCNs and Ho-D-FCNs) are superior to that of C-FCN, in which ACC is increased by 4 and 5%, respectively, and other performance are also improved accordingly. This result indicates that the sliding-window-based D-FCNs can provide better

features for ASD classification. (2) The classification result of ensemble classifier consistently outperforms that of single feature type, which supports the assumption of integrating multiorder connectional features for boosting classification results. (3) The fusion of C-FCN, Lo-D-FCNs, and Ho-D-FCNs achieved the best classification performance, indicating that different-level FCNs can provide complementary relevant information for ASD diagnosis and classification, and the fusion of this information can further improve the classification performance. This result will also be reflected in the following experiments. (4) By comparing our model with the approach proposed in Zhou et al. (2018), we also find that our central-moment-based approach performs better in terms of accuracy. Actually, the performance of HiO is inferior to the corresponding low-order FC network [i.e.,$C_{Lo-D}(1)$], which is consistent with the results given in Zhou et al. (2018). This comparison also verifies the effectiveness of our central-moment features.

The Most Discriminative Features for ASD Diagnosis

We used *t*-test, followed by LASSO regression, to identify the most discriminative features in C-FCN, Lo-D-FCNs, and Ho-D-FCNs, respectively. In this study, we used the frequency, at which features are selected in all cross-validation cases, to quantify feature relevance to the target classification. The higher the feature frequency, the more reliable and discriminative it is regarded.

Figures 5A–C visualizes the top 10 most discriminative features of C-FCN, Lo-D-FCNs, and Ho-D-FCNs in the form of circular graphs, where each link corresponds to a connectional feature and represents the correlation between two brain regions (Krzywinski et al., 2009). **Figure 5D** also shows the mutual comparison among three sets of connections. We use link thickness to encode the degree of their correlation. The thicker the link is, the stronger the correlation is; also, the higher the frequency of the connection selected in cross-validation is, the greater the contribution to the target classification tasks is. For the abbreviations of brain regions in **Figure 5**, please refer to **Table 3**. In addition, we mark L (or R) following a brain region (or ROI) name to denote that it lies in the left hemisphere (or the right hemisphere), such as ANG^R means the right angular gyrus.

From **Figure 5** and **Table 3**, we can derive the following. (1) The discriminative connections is not limited to connect the same hemisphere or brain lobe but also includes transhemisphere and all brain lobe, which indicates that the brain function of ASD patients has an abnormal distribution pattern over the whole brain. (2) Most selected brain regions are associated with emotional expression, language understanding, and motion coordination, such as precentral gyrus, middle frontal gyrus, middle cingulate gyrus, posterior cingulate gyrus, amygdala, angular gyrus, and others. These observations are consistent with previous studies (Qiu et al., 2010; Ecker et al., 2015; Ha et al., 2015b; Huang et al., 2018). For example, we found that $SFGmed^L$ (Andrews-Hanna et al., 2014), ANG^R (Andrews-Hanna et al., 2014), $PCUN^L$ (Urbain et al., 2015), CAL^L (Perkins et al., 2015), FFG^R (Urbain et al., 2016), INS^L (Leung et al., 2015; Urbain et al., 2016) contributed more to ASD identification, which is in line with the recent finding reported in the existing literatures. (3) Features selected from C-FCN, Lo-D-FCNs, and Ho-D-FCNs have significant differences, which can be seen

TABLE 3 | Abbreviations of ROIs selected from conventional functional connectivity network (C-FCN), low-order dynamic FCNs (Lo-D-FCNs), and high-order D-FCNs (Ho-D-FCNs).

Abbreviation	ROI name	Abbreviation	ROI name
FRO: frontal lobe			
PreCG	Precentral gyrus	MFG	Middle frontal gyrus
ORBmid	Orbitofrontal cortex (middle)	IFGoperc	Inferior frontal gyrus (opercular)
ROL	Rolandic operculum	SMA	Supplementary motor area
SFGmed	Superior frontal gyrus (media)	ORBsupmed	Orbitofrontal cortex (medial)
REC	Rectus gyrus		
INS: insula			
INS	Insula		
LIM: limbic system			
DCG	Middle cingulate gyrus	PCG	Posterior cingulate gyrus
PHG	Parahippocampal gyrus		
SBC: subcortical structures			
AMYG	Amygdala	PUT	Putamen
PAL	Pallidum		
OCC: occipital lobe			
CAL	Calcarine cortex	SOG	Superior occipital gyrus
MOG	Middle occipital gyrus	IOG	Inferior occipital gyrus
FFG	Fusiform gyrus		
PAR: parietal lobe			
PoCG	Postcentral gyrus	SPG	Superior parietal gyrus
ANG	Angular gyrus	PCUN	Precuneus
TEM: temporal lobe			
TPOsup	Temporal pole (superior)	MTG	Middle temporal gyrus
TPOmid	Temporal pole (middle)	ITG	Inferior temporal
CER: cerebellum			
II-Cb	Crus II of cerebellar hemisphere	IX-Cb	Lobule IX of cerebellar hemisphere
X-Cb	Lobule X of cerebellar hemisphere		
VER: vermis			
I-II-VER	Lobule I, II of vermis	III-VER	Lobule III of vermis
IV-V-VER	Lobule IV, V of vermis	VI-VER	Lobule VI of vermis
VII-VER	Lobule VII of vermis	VIII-VER	Lobule VIII of vermis
IX-VER	Lobule IX of vermis	X-VER	Lobule X of vermis (nodulus)

from three aspects: first, the selected connected features by each FCN (i.e., the connectional lines in **Figures 5A–C** are almost entirely different from each other, except for the connected features (IX-Cb^L-$PCUN^R$) selected by both Lo-D-FCNs and Ho-D-FCNs although with different strength; second, according to the affiliation relation of the selected ROIs with respect to corresponding FCNs (**Figure 5D**), we find that most of the selected ROIs merely belong to one FCN, except one ROI ($PUCN^R$) that is jointly selected by all the three FCNs, four ROIs by C-FNC and Lo-D-FCNs (or Ho-D-FCNs), and five ROIs by Lo-D-FCNs and Ho-D-FCNs; and third, the regional distribution of the selected features has huge difference among the three FCNs. For example, the connectional features selected by C-FCN mainly distribute in TEM^L, PAR^L, OCC^L, SBC^{L-R}, LIM^{L-R}, INS^{L-R}, and FOR^{L-R} (**Figure 5A**). The features selected by Lo-D-FCNs mainly locate in INS^R, LIM^R, SBC^R, OCC^R, PAR^R, TEM^{R-L}, CRE^{L-R}, and VER^{L-R} (**Figure 5B**) and that of Ho-D-FCNs is in INS^L, LIM^L, SBC^L, TEM^{R-L}, and CER^{L-R} (**Figure 5C**). In summary, the above analysis of difference among three FCNs show that their network infrastructures exist significantly different, which indicate that FCNs of different level can provide complementary information for diagnosis. We think that the main reason causing the huge difference among the three FCNs is that each FCN actually reflects the correlation between brain regions from rather different viewpoints. C-FCN generally captures the static connectional feature since its FC is measured using the whole scanning time rs-fMRI series from any pair of ROIs, while Lo-D-FCNs reveals the dynamically connectional relationship between a pair of ROIs because its FC metric is similar to C-FCN, just using a short-time rs-fMRI series. Compared with C-FCN and Lo-D-FCNs, Ho-D-FCNs uses a vastly different metric to measure the connectional relationship between a pair of ROIs, i.e., using the synchronization of the short-time FC profile between two ROIs to represent their temporary correlation. Therefore, Ho-D-FCNs can reveal some new FC interaction among ROIs, thus providing supplementary information to C-FCN and Lo-D-FCNs.

CONCLUSION

In this paper, we proposed new Ho-D-FCNs and used the central-moment method to eliminate the phase mismatch problem of dynamic networks. Through the analysis of feature selection, we believed that the presented Ho-D-FCNs could provide complementary information to our previous research (C-FCN, Lo-D-FCNs). Therefore, we fused these three methods and got the optimal classification results. The experimental results have shown that: (1) Ho-D-FCNs was indeed helpful for mining the relevant information for ASD diagnosis; (2) different level FCNs could provide complementary information and improve the disease recognition rate through fusion; and (3) the central-moment method could help to solve the phase mismatch problem in dynamic networks, including Lo-D-FCNs and Ho-D-FCNs, which were covered in the paper. In addition, in the analysis of feature selection, we also found that most brain regions contributing to classification are related to emotional expression, language understanding, and motion coordination. These findings agree with the behavioral phenotype of ASD (Geschwind and Levitt, 2007; American Psychiatric Association, 2013).

Finally, it should be indicated that the fusion of the three methods based on the decision value of SVM might not adequately integrate the complementary information and thus have an impact on the classification accuracy. Therefore, feature fusion is a direction for future improvement, which will be our future work.

DATA AVAILABILITY STATEMENT

The datasets generated for this study can be found in the Autism Brain Imaging Data Exchange (ABIDE) database (http://fcon_1000.projects.nitrc.org/indi/abide/abide_I.html).

AUTHOR CONTRIBUTIONS

All authors listed have made a substantial, direct and intellectual contribution to the work, and approved it for publication.

FUNDING

FZ was supported in part by the National Natural Science Foundation of China (61773244, 61976125, 61272319, 61873117), Yantai Key Research and Development Program of China (2017ZH065, 2019XDHZ081), and Shandong Provincial Key Research and Development Program of China (2019GGX101069).

REFERENCES

Achard, S. (2006). A resilient, low-frequency, small-world human brain functional network with highly connected association cortical hubs. *J. Neurosci.* 26, 63–72.

Achard, S., Bassett, D. S., Meyer-Lindenberg, A., and Bullmore, E. (2008). Fractal connectivity of long-memory networks. *Phys. Rev.* 77(3 Pt 2):036104.

Admon, R., Bleich-Cohen, M., Weizmant, R., Poyurovsky, M., Faragian, S., and Hendler, T. (2012). Functional and structural neural indices of risk aversion in obsessive–compulsive disorder (OCD). *Psychiatry Res. Neuroimaging* 203, 207–213. doi: 10.1016/j.pscychresns.2012.02.002

American Psychiatric Association (2013). *Diagnostic, and Statistical Manual of Mental Disorders, 5th Edn. (DSM-5). Text Revision*. Washington, DC: American Psychiatric Association.

Anagnostou, E., and Taylor, M. J. (2011). Review of neuroimaging in autism spectrum disorders: what have we learned and where we go from here. *Mol. Autism* 2:4. doi: 10.1186/2040-2392-2-4

Andrews-Hanna, J. R., Smallwood, J., and Spreng, R. N. (2014). The default network and self-generated thought: component processes, dynamic control, and clinical relevance. *Ann. N. Y. Acad. Sci.* 1316, 29–52. doi: 10.1111/nyas.12360

Chen, X., Zhang, H., Gao, Y., Wee, C.-Y., Li, G., and Shen, D. (2016). High-order resting-state functional connectivity network for MCI classification. *Hum. Brain Mapp.* 37, 3282–3296. doi: 10.1002/hbm.23240

Cordes, D., Haughton, V. M., Arfanakis, K., Carew, J. D., Turski, P. A., Moritz, C. H., et al. (2001). Frequencies contributing to functional connectivity in the cerebral cortex in "resting-state" data. *Am. J. Neuroradiol.* 22, 1326–1333.

Cortes, C., and Vapnik, V. (1995). Support-vector networks. *Machine Learn.* 20, 273–297.

Damaraju, E., Allen, E. A., Belger, A., Ford, J. M., McEwen, S., Mathalon, D. H., et al. (2014). Dynamic functional connectivity analysis reveals transient states of dysconnectivity in schizophrenia. *NeuroImage Clin.* 5, 298–308. doi: 10.1016/j.nicl.2014.07.003

Deshpande, G., Libero, L. E., Sreenivasan, K. R., Deshpande, H. D., and Kana, R. K. (2013). Identification of neural connectivity signatures of autism using machine learning. *Front. Hum. Neurosci.* 7:670. doi: 10.3389/fnhum.2013.00670

Di Martino, A., Yan, C.-G., Li, Q., Denio, E., Castellanos, F. X., Alaerts, K., et al. (2013). The autism brain imaging data exchange: towards a large-scale evaluation of the intrinsic brain architecture in autism. *Mol. Psychiatry* 19, 659–667. doi: 10.1038/mp.2013.78

Ecker, C., Bookheimer, S. Y., and Murphy, D. G. M. (2015). Neuroimaging in autism spectrum disorder: brain structure and function across the lifespan. *Lancet Neurol.* 14, 1121–1134. doi: 10.1016/S1474-4422(15)00050-2

Fornito, A., Zalesky, A., and Breakspear, M. (2015). The connectomics of brain disorders. *Nat. Rev. Neurosci.* 16, 159–172. doi: 10.1038/nrn3901

Ganella, E. P., Bartholomeusz, C. F., Seguin, C., Whittle, S., Bousman, C., Phassouliotis, C., et al. (2017). Functional brain networks in treatment-resistant schizophrenia. *Schizophrenia Res.* 184, 73–81. doi: 10.1016/j.schres.2016.12.008

Geschwind, D. H., and Levitt, P. (2007). Autism spectrum disorders: developmental disconnection syndromes. *Curr. Opin. Neurobiol.* 17:103111.

Guo, H., Liu, L., Chen, J., Xu, Y., and Jie, X. (2017). Alzheimer classification using a minimum spanning tree of high-order functional network on fMRI dataset. *Front. Neurosci.* 11:639. doi: 10.3389/fnins.2017.00639

Ha, S., Sohn, I.-J., Kim, N., Sim, H. J., and Cheon, K.-A. (2015). Characteristics of brains in autism spectrum disorder: structure, function and connectivity across the lifespan. *Exp. Neurobiol.* 24:273. doi: 10.5607/en.2015.24.4.273

Hu, M. K. (1962). Visual pattern recognition by moment invariants. *IRE Trans. Inf. Theory* 8, 179–187.

Huang, H., Liu, X., Jin, Y., Lee, S.-W., Wee, C.-Y., and Shen, D. (2018). Enhancing the representation of functional connectivity networks by fusing multi-view information for autism spectrum disorder diagnosis. *Hum. Brain Mapp.* 40, 833–854. doi: 10.1002/hbm.24415

Hung, V. V., Lee, J., Masuda-Jindo, K., and Kim, L. (2006). First principles study of tantalum thermodynamics by the statistical moment method. *Comp. Mater. Sci.* 37, 565–571.

Hutchison, R. M., Womelsdorf, T., Allen, E. A., Bandettini, P. A., Calhoun, V. D., Corbetta, M., et al. (2013). Dynamic functional connectivity: promise, issues, and interpretations. *Neuroimage* 80, 360–378. doi: 10.1016/j.neuroimage.2013.05.079

Jie, B., Zhang, D., Gao, W., Wang, Q., Wee, C. Y., and Shen, D. (2014). Integration of network topological and connectivity properties for neuroimaging classification. *IEEE Trans. Biomed. Eng.* 61, 576–589.

Jin, Y., Wee, C.-Y., Shi, F., Thung, K.-H., Ni, D., Yap, P.-T., et al. (2015). Identification of infants at high-risk for autism spectrum disorder using multiparameter multiscale white matter connectivity networks. *Hum. Brain Mapp.* 36, 4880–4896. doi: 10.1002/hbm.22957

Krzywinski, M., Schein, J., Birol, I., Connors, J., Gascoyne, R., Horsman, D., et al. (2009). Circos: an information aesthetic for comparative genomics. *Genome Res.* 19, 1639–1645. doi: 10.1101/gr.092759.109

Kudela, M., Harezlak, J., and Lindquist, M. A. (2017). Assessing uncertainty in dynamic functional connectivity. *Neuroimage* 149, 165–177. doi: 10.1016/j.neuroimage.2017.01.056

Leung, R. C., Pang, E. W., Cassel, D., Brian, J. A., Smith, M. L., and Taylor, M. J. (2015). Early neural activation during facial affect processing in adolescents with autism spectrum disorder. *Neuroimage Clin.* 7, 203–212.

Li, W., Wang, Z., Zhang, L., Qiao, L., and Shen, D. (2017). Remodeling Pearson's correlation for functional brain network estimation and autism spectrum disorder identification. *Front. Neuroinform.* 11:55. doi: 10.3389/fninf.2017.00055

Lin, H. Y., Tseng, W. Y. I., Lai, M. C., Matsuo, K., and Gau, S. S. F. (2015). Altered resting-state frontoparietal control network in children with attention-deficit/hyperactivity disorder. *J. Int. Neuropsychol. Soc.* 21, 271–284. doi: 10.1017/S135561771500020X

Liu, F., Wang, Y., Li, M., Wang, W., Li, R., Zhang, Z., et al. (2016). Dynamic functional network connectivity in idiopathic generalized epilepsy with generalized tonic-clonic seizure. *Hum. Brain Mapp.* 38, 957–973. doi: 10.1002/hbm.23430

Morris, C., and Rekik, I. (2017). "Autism spectrum disorder diagnosis using sparse graph embedding of morphological brain networks," in *Proceedings of the Graphs in Biomedical Image Analysis, Computational Anatomy and Imaging Genetics: First International Workshop, GRAIL 2017, 6th International Workshop, MFCA 2017, and Third International Workshop, MICGen 2017, Held in Conjunction with MICCAI 2017*, eds M. J. Cardoso and T. Arbel (Québec City, QC: Springer).

Perkins, T. J., Bittar, R. G., McGillivray, J. A., Cox, I. I., and Stokes, M. A. (2015). Increased premotor cortex activation in high functioning autism during action observation. *J. Clin. Neurosci.* 22, 664–669. doi: 10.1016/j.jocn.2014.10.007

Plitt, M., Barnes, K. A., and Martin, A. (2015). Functional connectivity classification of autism identifies highly predictive brain features but falls short of biomarker standards. *Neuroimage Clin.* 7, 359–366. doi: 10.1016/j.nicl.2014.12.013

Qiao, L., Zhang, L., Chen, S., and Shen, D. (2018). Data-driven graph construction and graph learning: a review. *Neurocomputing* 312, 336–351.

Qiu, A., Adler, M., Crocetti, D., Miller, M. I, and Mostofsky, S. H. (2010). Basal ganglia shapes predict social, communication, and motor dysfunctions in boys with autism spectrum disorder. *J. Am. Acad. Child Adolesc. Psychiatry* 49, 539–551.e4. doi: 10.1016/j.jaac.2010.02.012

Ray, S., Gohel, S., and Biswal, B. B. (2015). Altered functional connectivity strength in abstinent chronic cocaine smokers compared to healthy controls. *Brain Connect.* 5, 476–486. doi: 10.1089/brain.2014.0240

Satterthwaite, T. D., Elliott, M. A., Gerraty, R. T., Ruparel, K., Loughead, J., Calkins, M. E., et al. (2013). An improved framework for confound regression and filtering for control of motion artifact in the preprocessing of resting-state functional connectivity data. *Neuroimage* 64, 240–256. doi: 10.1016/j.neuroimage.2012.08.052

Soussia, M., and Rekik, I. (2018). Unsupervised manifold learning using high-order morphological brain networks derived From T1-w MRI for autism diagnosis. *Front. Neuroinform.* 12:70. doi: 10.3389/fninf.2018.00070

Tibshirani, R. (1996). Regression shrinkage and selection via the lasso. *J. R. Stat. Soc. Series B (Methodological)* 58, 267–288.

Tomasi, D., and Volkow, N. D. (2010). Functional connectivity density mapping. *Proc. Natl. Acad. Sci. U.S.A.* 107, 9885–9890. doi: 10.1073/pnas.1001414107

Tzourio-Mazoyer, N., Landeau, B., Papathanassiou, D., Crivello, F., Etard, O., Delcroix, N., et al. (2002). Automated anatomical labeling of activations in SPM using a macroscopic anatomical parcellation of the MNI MRI single-subject brain. *Neuroimage* 15, 273–289.

Urbain, C., Vogan, V. M., Ye, A. X., Pang, E. W., Doesburg, S. M., and Taylor, M. J. (2016). Desynchronization of fronto-temporal networks during working memory processing in autism. *Hum. Brain Mapp.* 37, 153–164. doi: 10.1002/hbm.23021

Urbain, C. M., Pang, E. W., and Taylor, M. J. (2015). Atypical spatiotemporal signatures of working memory brain processes in autism. *Transl. Psychiatry* 5:e617. doi: 10.1038/tp.2015.107

Wang, J., Wang, Q., Zhang, H., Chen, J., Wang, S., and Shen, D. (2018). Sparse multiview task-centralized ensemble learning for ASD diagnosis based on age- and sex-related functional connectivity patterns. *IEEE Trans. Cybernetics* 49, 3141–3154. doi: 10.1109/TCYB.2018.2839693

Wee, C.-Y., Wang, L., Shi, F., Yap, P.-T., and Shen, D. (2013). Diagnosis of autism spectrum disorders using regional and interregional morphological features. *Hum. Brain Mapp.* 35, 3414–3430.

Wee, C.-Y., Yang, S., Yap, P.-T., and Shen, D. (2015). Sparse temporally dynamic resting-state functional connectivity networks for early MCI identification. *Brain Imaging Behav.* 10, 342–356. doi: 10.1007/s11682-015-9408-2

Yan, C.-G., Cheung, B., Kelly, C., Colcombe, S., Craddock, R. C., Di Martino, A., et al. (2013). A comprehensive assessment of regional variation in the impact of head micromovements on functional connectomics. *Neuroimage* 76, 183–201. doi: 10.1016/j.neuroimage.2013.03.004

Zhang, H., Chen, X., Shi, F., Li, G., Kim, M., Giannakopoulos, P., et al. (2016). Topographical information-based high-order functional connectivity and its application in abnormality detection for mild cognitive impairment. *J. Alzheimer's Dis.* 54, 1095–1112.

Zhang, H., Chen, X., Zhang, Y., and Shen, D. (2017c). Test-retest reliability of "High-Order" functional connectivity in young healthy adults. *Front. Neurosci.* 11:439. doi: 10.3389/fnins.2017.00439

Zhang, X., Hu, B., Ma, X., and Xu, L. (2015). Resting-state whole-brain functional connectivity networks for MCI classification using L2-regularized logistic regression. *IEEE Trans. NanoBiosci.* 14, 237–247. doi: 10.1109/TNB.2015.2403274

Zhang, Y., Zhang, H., Chen, X., Lee, S.-W., and Shen, D. (2017b). Hybrid high-order functional connectivity networks using resting-state functional MRI for mild cognitive impairment diagnosis. *Sci. Rep.* 7:6530. doi: 10.1038/s41598-017-06509-0

Zhang, Y., Zhang, H., Chen, X., and Shen, D. (2017a). Constructing multi-frequency high-order functional connectivity network for diagnosis of mild cognitive impairment. *Lecture Notes Comp. Sci.* 10511, 9–16. doi: 10.1007/978-3-319-67159-8_2

Zhao, F., Zhang, H., Rekik, I., An, Z., and Shen, D. (2018). Diagnosis of autism spectrum disorders using multi-level high-order functional networks derived from resting-state functional MRI. *Front. Hum. Neurosci.* 12:184. doi: 10.3389/fnhum.2018.00184

Zhou, Y., Qiao, L., Li, W., Zhang, L., and Shen, D. (2018). Simultaneous estimation of low-and high-order functional connectivity for identifying mild cognitive impairment. *Front. Neuroinform.* 12:3. doi: 10.3389/fninf.2018.00003

Zürcher, N. R., Bhanot, A., McDougle, C. J., and Hooker, J. M. (2015). A systematic review of molecular imaging (PET and SPECT) in autism spectrum disorder: current state and future research opportunities. *Neurosci. Biobehav. Rev.* 52, 56–73. doi: 10.1016/j.neubiorev.2015.02.002

Conflict of Interest: The authors declare that the research was conducted in the absence of any commercial or financial relationships that could be construed as a potential conflict of interest.

frontiers in Neuroscience

ORIGINAL RESEARCH
published: 11 June 2020
doi: 10.3389/fnins.2020.00493

The Profiles of Non-stationarity and Non-linearity in the Time Series of Resting-State Brain Networks

Sihai Guan[1], Runzhou Jiang[1], Haikuo Bian[1], Jiajin Yuan[2], Peng Xu[1], Chun Meng[1] and Bharat Biswal[1,3]**

[1] *MOE Key Laboratory for Neuroinformation, Center for Information in Medicine, School of Life Science and Technology, The Clinical Hospital of Chengdu Brain Science Institute, University of Electronic Science and Technology of China, Chengdu, China,* [2] *The Laboratory for Affect Cognition and Regulation (ACRLAB), Key Laboratory of Cognition and Personality of Ministry of Education, Faculty of Psychology, Southwest University, Chongqing, China,* [3] *Department of Biomedical Engineering, New Jersey Institute of Technology, Newark, NJ, United States*

The linearity and stationarity of fMRI time series need to be understood due to their important roles in the choice of approach for brain network analysis. In this paper, we investigated the stationarity and linearity of resting-state fMRI (rs-fMRI) time-series data from the Midnight Scan Club datasets. The degree of stationarity (DS) and the degree of non-linearity (DN) were, respectively, estimated for the time series of all gray matter voxels. The similarity and difference between the DS and DN were assessed in terms of voxels and intrinsic brain networks, including the visual network, somatomotor network, dorsal attention network, ventral attention network, limbic network, frontoparietal network, and default-mode network. The test-retest scans were utilized to quantify the reliability of DS and DN. We found that DS and DN maps had overlapping spatial distribution. Meanwhile, the probability density estimate function of DS had a long tail, and that of DN had a more normal distribution. Specifically, stronger DS was present in the somatomotor, limbic, and ventral attention networks compared to other networks, and stronger DN was found in the somatomotor, visual, limbic, ventral attention, and default-mode networks. The percentage of overlapping voxels between DS and DN in different networks demonstrated a decreasing trend in the order default mode, ventral attention, somatomotor, frontoparietal, dorsal attention, visual, and limbic. Furthermore, the ICC values of DS were higher than those of DN. Our results suggest that different functional networks have distinct properties of non-stationarity and non-linearity owing to the complexity of rs-fMRI time series. Thus, caution should be taken when analyzing fMRI data (both resting-state and task-activation) using simplified models.

Keywords: resting-state fMRI, degree of stationarity, degree of non-linearity, test-retest, overlapping spatial

OPEN ACCESS

Edited by:
Nanyin Zhang,
Pennsylvania State University (PSU), United States

Reviewed by:
Bing Zhang,
Nanjing Drum Tower Hospital, China
Jean Chen,
University of Toronto, Canada

****Correspondence:***
Chun Meng
chunmeng@uestc.edu.cn
Bharat Biswal
bbiswal@yahoo.com

Specialty section:
This article was submitted to Brain Imaging Methods, a section of the journal Frontiers in Neuroscience

Received: *10 December 2019*
Accepted: *20 April 2020*
Published: *11 June 2020*

Citation:
Guan S, Jiang R, Bian H, Yuan J, Xu P, Meng C and Biswal B (2020) The Profiles of Non-stationarity and Non-linearity in the Time Series of Resting-State Brain Networks. Front. Neurosci. 14:493. doi: 10.3389/fnins.2020.00493

INTRODUCTION

Functional magnetic resonance imaging (fMRI) has become an important method for investigating system-level brain activity (Biswal et al., 1995, 2010; He, 2013; Gordon et al., 2017; Gratton et al., 2018). The majority of fMRI research to date has used a simplified model based on the assumptions of stationarity and linearity (de Pasquale et al., 2010; Cabral et al., 2014; Panerai, 2014). Stationarity,

in general, implies that the statistic or model parameter of interest does not change over time (Smith et al., 2012, 2013; Liu and Duyn, 2013; Allen et al., 2014; Shine et al., 2016; Suk et al., 2016; Yaesoubi et al., 2018). The stationarity assumption is also important for the frequency analysis of fMRI time series, as the Fourier transform is suitable for stationarity (Beck et al., 2006). Since resting-state fMRI (rs-fMRI) is a powerful tool for studying human functional brain networks, it is necessary to understand stationarity in the rs-fMRI time series. However, only a few studies have used fMRI signals to characterize the non-stationarity of time series. For example, Ou et al., used a Bayesian connectivity change point model to statistically investigate rs-fMRI signals and found that it could differentiate the temporal dynamics of functional interactions between children with attention deficit hyperactivity disorder and matched controls (Ou et al., 2014). Results from the study suggested that functional connectivity or interactions had temporally non-stationary characteristics. Muhei-Aldin and colleagues used non-parametric testing, i.e., the reverse arrangement test, to examine the stationarity of the fMRI signal during a motor sequence learning task and showed that the time series were non-stationary (Muhei-aldin et al., 2014). Bullmore et al., provided a review of wavelet methods used for the analysis of potentially non-stationary fMRI time-series signals (Bullmore et al., 2004).

Recently, several studies have investigated the temporal fluctuations in functional connectivity, i.e., dynamic functional connectivity, in the human brain and have interpreted their findings as evidence of non-stationary switching of discrete brain states (Allen et al., 2014; Hansen et al., 2015). Hutchison and colleagues used the rs-fMRI and sliding-window approach to study stimulus-independent fluctuations of functional connectivity within resting-state networks (Hutchison et al., 2013). They found that resting-state functional connectivity is not static and that resting-state networks can exhibit non-stationary spontaneous relationships irrespective of conscious and cognitive processing. Theoretically, the activity of neuronal assemblies should be non-stationary since it reflects the different stages of a self-organized process (Schoner and Kelso, 1988; Jin et al., 2017). However, several papers have reported contradictory findings regarding the non-stationarity in fMRI time series (Gaschler-Markefski et al., 1997; Hindriks et al., 2016; Laumann et al., 2017). For example, Gaschler-Markefski and colleagues reported that auditory tasks increased the non-stationarity in the fMRI time series of the auditory cortex (Gaschler-Markefski et al., 1997). Laumann et al., reported that the resting state condition yielded mean kurtosis measures closer to the stationary null model than task conditions, which seemed to suggest stationarity in the rs-fMRI signal (Laumann et al., 2017). Hindriks et al., found that the variation leading to dynamic functional connectivity was related to the length of the sliding window (Hindriks et al., 2016). To better understand the fMRI signal profile underlying functional connectivity, it is necessary to clarify whether the underlying processes are actually stationary or non-stationary (Thompson, 2018). Previous studies inferred non-stationarity in time series using task-related fMRI or based on the evidence of dynamic functional connectivity (Muhei-aldin et al., 2014; Ou et al., 2014). The quantitative non-stationarity profiles of rs-fMRI signals and various brain regions remain unclear.

On the other hand, the linear time-invariant (LTI) system plays a crucial role in modeling the fMRI time series to generate a transfer function from the stimulus to the neural output. The hemodynamic response used in fMRI data analysis is assumed to be a linear model in which the neuronal activity is thought to be linearly convolved with the underlying blood flow/volume (hemodynamic) changes (Esposito et al., 2002). While the fMRI time series approximates an LTI system for medium-duration stimuli, the fMRI response has been found to be non-linear for short-duration stimuli. For example, Wager et al., reported that the non-linearity of fMRI data may substantially influence the detection of task-related activations, particularly in rapid event-related designs when considering the non-linear effects on the response magnitude, onset time, and time to peak (Wager et al., 2005). Therefore, the presence of non-linear or deterministic behavior has been postulated in various physiological and pathological states (Freeman, 2000). Non-linearity postulates that irregular and seemingly unpredictable behaviors are not necessarily attributed to random external inputs to the systems but, on the contrary, can be the result of deterministic dynamical systems (Stam, 2005). Therefore, the detection of non-linearity is important and should be the first step before any non-linear analysis. Previous studies have shown the non-linear dynamics of brain activities by using EEG (Stam, 2005) and rs-fMRI (LaConte et al., 2004; Deshpande et al., 2006; Xie et al., 2008). For example, Xie et al., studied the spatiotemporal non-linear dynamics property in rs-fMRI signals of the human brain by using the spatiotemporal Lyapunov exponent analysis (Xie et al., 2008). Furthermore, the Delay Vector Variance (DVV) method has been used to characterize the non-linearity in fMRI time series (Freeman, 2003). Gultepe et al. used the DVV method to identify whether resting-state fMRI signals are linear or non-linear and found that the default-mode network had more linear signals compared to the visual, motor, and auditory networks, while the visual network had more non-linear signals than the others (Gultepe and He, 2013). Taken together, it is important to comprehensively study the degree of non-linearity of rs-fMRI time series in various large-scale brain networks and across whole-brain gray matter.

To probe the complexity and stability of a system such as the human brain, it is necessary to investigate both the non-linearity and stationarity of underlying dynamic activities given the inherent association and distinction between non-linearity and stationarity. In this study, we aim to comprehensively assess the profiles of non-stationarity and non-linearity in rs-fMRI time series for whole-brain gray matter voxels and functional networks. We compute quantitative measures for the degree of stationarity (DS) and the degree of non-linearity (DN) in nine healthy subjects with 10 test-retest rs-fMRI scans. We then calculate the test-retest reliability of DS and DN measures. We hypothesize that voxels and networks with stronger degrees of non-stationarity and non-linearity partially overlap and have varied test-retest reliability.

MATERIALS AND METHODS

Data and Preprocessing

In total, 100 rs-fMRI scans were used in this study and were obtained from the Midnight Scan Club data (https://openneuro.org/datasets/ds000224/versions/1.0.0). Data were collected from 10 healthy, right-handed, young adult subjects (5 females and 5 males; age: 24–34 y) by using a Siemens Trio 3T MRI scanner over the course of 10 sessions conducted on separate days, each beginning at midnight. Within each session on 10 consecutive days, 30 min of rs-fMRI data were collected in which subjects visually fixated on a white crosshair presented against a black background. One subject (MSC08) was excluded due to the subject falling asleep during the scan, in line with the previous literature (Gordon et al., 2017). Therefore, the rs-fMRI data includes nine subjects, each with 10 sessions. The details about data acquisition and subject information have been reported previously (Gordon et al., 2017). Our data analysis included the following steps: (1) preprocess the rs-fMRI dataset; (2) calculate the DS of the preprocessed fMRI time series and create the network histogram map; (3) calculate the DN characterizations of the preprocessed fMRI time series and create the network histogram map; (4) determine the strength of DS and DN and identify their spatial overlap; (5) quantify the test-retest reliability of DS and DN.

The rs-fMRI preprocessing included the following: (1) discarding the first 10 volumes of each scan for signal equilibration, wherein subjects adapted to the environment; (2) slice time correction to account for temporal shifts in fMRI data acquisition; (3) correction for head motion; (4) use of the Friston-24 model to control head motion effects (Friston et al., 1996; Yan et al., 2013), followed by regressing out the signals from white matter and cerebrospinal fluid to reduce respiratory and cardiac effects (Fox and Raichle, 2007); (5) normalizing functional images into the standard MNI space by using the EPI template with the resampled voxel size of 4 mm; (6) spatially smoothing the result data using an 8-mm full width at half maximum (FWHM) Gaussian kernel; (7) band-pass filtering ($0.009\,\text{Hz} < f < 0.08\,\text{Hz}$); (8) extracting time series from whole-brain gray matter voxels and from functional networks based on Yeo's atlas (Yeo et al., 2011).

The DS Characterization of fMRI Time Series

The Hilbert-Huang transform (HHT) is an adaptive time-frequency analysis method (Huang et al., 1998) and has been used to analyze non-linear and non-stationary signals (Qian et al., 2015). Compared to the sliding window approach, HHT can directly and quantitatively characterize the degree of stationarity in the time series. In addition, the HHT method has high performance in terms of both time-space and frequency-space resolution, which facilitates precise expressions of instantaneous frequency and is conducive to feature extraction of biomedical signals (Huang and Shen, 2005). The HHT mainly consists of two parts, namely the empirical mode decomposition (EMD) and the Hilbert transformation (Huang and Shen, 2005). The EMD is an efficient and adaptive method for extracting a set of intrinsic mode functions (IMFs) from non-linear and non-stationary time series (Lin and Zhu, 2012).

Signal $x(n)$ of length N can be decomposed by EMD to obtain M basic mode components $c_1, c_2, \cdots, c_M$ and residual componentr_M.

$$x(n) = \sum_{j=1}^{M} c_j + r_M \tag{1}$$

For each of the IMFs, using Hilbert transform, we obtain

$$x(n) = \sum_{j=1}^{M} a_j(n)\, e^{iw_j(n)n} \tag{2}$$

The Hilbert spectrum of $x(n)$ can thus be expressed as:

$$H(w,n) = \sum b_j a_j(n)\, e^{iw_j(n)n} \tag{3}$$

where

$$b_j = \begin{cases} 1 & w_j = w \\ 0 & other \end{cases} \tag{4}$$

The boundary Hilbert spectrum of $x(n)$ is

$$h(w) = \sum_{n=0}^{N-1} H(w,n) \tag{5}$$

The average boundary spectrum is defined as

$$B(w) = \frac{1}{N} h(w) \tag{6}$$

Thus, the DS can be defined as

$$DS(w) = \frac{1}{N} \sum_{n=0}^{N-1} \left(1 - \frac{H(w,n)}{B(w)}\right)^2 \tag{7}$$

$DS(w)$ is capable of quantitatively detecting the stationarity of the data. For the stationarity process, the Hilbert spectrum does not change with time; it only contains the horizontal contour, that is $DS(w) = 0$. If the Hilbert spectrum is time-dependent, then $DS(w) > 0$, and as $DS(w)$ increases, the signal's non-stationarity is enhanced.

The DN Characterization of fMRI Time Series

The DVV method characterizes a time series based upon its predictability and compares the result to those obtained for linearized versions of the signal (surrogates) (Gautama et al., 2004). Based on a set of N delay vectors (DVs), denoted by $x(k) = [x_{k-m}, x_{k-m+1,\ldots}, x_{k-1}]$, a vector containing m consecutive time samples. Every DV $x(k)$ has a corresponding target, namely the following sample x_k. For a given embedding dimension m, the mean target variance, σ^{*2}, is computed over all sets Ω_k. A set Ω_k is generated by grouping those DVs that are within a certain distance from $x(k)$, which is varied in a manner standardized with respect to the distribution of pairwise distances between DVs. This way, the threshold automatically scales with

the embedding dimension m, as well as with the dynamical range of the time series at hand, and thus, the complete range of pairwise distances is examined. The proposed DVV method can be summarized as follows for a given embedding dimension m:

- The mean, μ_d, and standard deviation, σ_d, are computed over all pairwise distances between DVs, $\|x(i) - x(j)\| (i \neq j)$.
- The sets Ω_k are generated such that $\Omega n = \{x(i) \mid \|x(k) - x(i)\| \leq \tau_d\}$, i.e., sets that consist of all DVs that lie closer to $x(k)$ than a certain distance τ_d, taken from the interval $[min\{0, \mu_d - n_d\sigma_d\}]$, e.g., uniformly spaced, where n_d is a parameter controlling the span over which to perform the DVV analysis.
- For every set Ω_k, the variance of the corresponding targets, σ_k^2, is computed. The average over all sets Ω_k, normalized by the variance of the time series, σ_x^2, yields the measure of unpredictability, σ^*2:

$$\sigma^{*2} = \frac{1}{N}\sum_{k=1}^{N} c_j \sigma_k^2 \sigma_x^2 \tag{8}$$

The deviation from the bisector line is thus an indication of non-linearity and can be quantified by the root mean square error (RMSE) between the σ^{*2}'s of the original time series and the σ^{*2}'s averaged over the DVV plots of the surrogate time series (note that while computing this average, as well as with computing the RMSE, only the valid measurements are taken into account, and then the DN is obtained). In this way, a single test statistic is obtained, and traditional (right-tailed) surrogate testing can be performed (the deviation from the average is computed for the original and surrogate time series).

Threshold for Strong DS and DN

The quartile method (Hyndman and Fan, 1996), as shown in **Figure 1**, was used to determine the relative thresholds for strong DS and DN, which made use of the whole-brain DS and DN values. The quartile is a numerical value obtained when all values are arranged from small to large in statistics and are divided into four equal positions. The third quartile was arbitrarily selected as the threshold for strong DS and DN in this study.

Definition

$$\begin{cases} Q_{lower\ limit} < value\ DS \leq Q_1 & weak\ level\ non\text{-}stationary \\ Q_1 < value\ DS \leq Q_3 & medium\ level\ non\text{-}stationary \\ Q_3 < value\ DS \leq Q_{upper\ limit} & strong\ level\ non\text{-}stationary \end{cases} \tag{9}$$

$$\begin{cases} Q_{lower\ limit} < value\ DN \leq Q_1 & weak\ level\ non\text{-}linearity \\ Q_1 < value\ DN \leq Q_3 & medium\ level\ non\text{-}linearity \\ Q_3 < value\ DN \leq Q_{upper\ limit} & strong\ level\ non\text{-}linearity \end{cases} \tag{10}$$

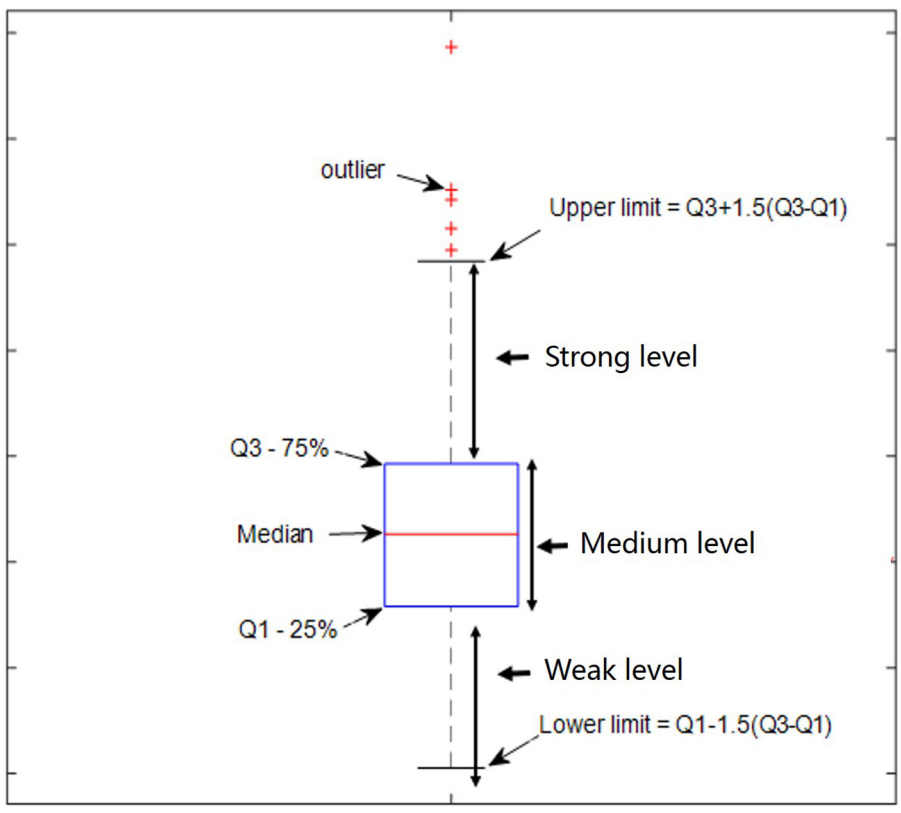

FIGURE 1 | Defined percentage ratio by using the quartile method.

Where

$$Q_{upper\ limit} = Q_3 + 1.5 \times (Q_3 - Q_1) \quad (11)$$

$$Q_{lower\ limit} = Q_1 - 1.5 \times (Q_3 - Q_1) \quad (12)$$

Histogram Map and Overlap Map

After calculating voxel-based values of DS and DN within the gray matter mask, 90 maps were obtained for nine subjects and their 10 test-retests. Resulting maps were combined to identify the histogram map of DS and DN and the distribution of strong DS and DN as well as the overlap and distinctions by using an *a priori* functional network atlas (Yeo et al., 2011) (including VN: visual network, SMN: somatomotor network, DAN: dorsal attention network, VAN: ventral attention network, LIMB: limbic network, FPN: frontoparietal network, and DMN: default-mode network). Finally, the percentage of overlapping voxels for each network was calculated.

Test-Retest Reliability

Test-retest studies are essential to determine the reliability of rs-fMRI measures (Noble et al., 2019). To evaluate the test-retest reliability as well as the within- and between-subjects variability of DS and DN, we computed the intraclass correlation (ICC) (Shrout and Fleiss, 1979) and obtained the test-retest reliability maps for DS and DN.

$$\mathrm{ICC} = \frac{\mathrm{BMS} - \mathrm{EMS}}{\mathrm{BMS} + (k-1)\mathrm{EMS}} \quad (13)$$

Equation (13) estimates the correlation of the subject signal intensities between sessions, modeled by a two-way analysis of variance, with random subject effects and fixed session effects. In this model, BMS is between-targets mean square, EMS is error sums of squares, and k is the number of repeated sessions. For statistical evaluations, a significance threshold of $p < 0.05$ was used.

Similarity Analysis

To explore the similarity of DS or DN between functional networks, Pearson's correlation was conducted across subjects and sessions by using average values within each network. Furthermore, we explored the similarity between DS and DN within 10 axial slices. Average values of DS and DN across subjects and sessions were correlated for each slice.

RESULTS

Distribution of DS and DN in Terms of Voxels and Networks

As displayed by three slice maps in terms of voxels across nine subjects and their 10 test-retest sessions, we found that the resting-state brain had varied DS and DN values in different regions (**Figures 2A–E**). Mean value maps were plotted by using the average values of DS and DN across subjects and sessions, respectively (**Figures 2A,D**). The variance value maps were plotted by using the variance values of DS and DN across subjects and sessions, respectively (**Figures 2B,E**). Although DS and DN largely shared the same regions, they still had their own unique distribution. For example, the peak intensity within seven networks differed between DS and DN (**Figures 2C,F**). For DS, the SMN (DS = 1.758 ± 0.00270) is composed of relatively higher non-stationary signals compared to the VN (DS = 1.752 ± 0.00240) and DAN (DS = 1.681 ± 0.00300) resting-state network time series, and the p-values from the two-sample t-tests are $p = 0.031$ and $p = 0$, respectively; LIMB (DS = 1.744 ± 0.00650) is composed of relatively higher non-stationary signals compared to the FPN (DS = 1.681 ± 0.00190) and DMN (DS = 1.685 ± 0.00170), and the p-values in the corresponding two-sample t-tests are both $p = 0$; VAN (DS = 1.735 ± 0.00280) has relatively higher non-stationarity signals than DAN (DS = 1.681 ± 0.00300), and the p-value in the two-sample t-test is $p = 0$. In addition, for DN, it was shown that the DAN (DN = 0.0955 ± 0.00026) has lower non-linearity relative to the SMN (DN = 0.1065 ± 0.00029), VN (DN = 0.1115 ± 0.00022), LIMB (DN = 0.1083 ± 0.00041), and VAN (DN = 0.103 ± 0.00024), and all the corresponding p-values from the two-sample t-tests are $p = 0$. The DMN (DN=0.1085 ± 0.00019) is composed of relatively higher non-linear signals compared to the FPN (DN=0.0966 ± 0.00022) resting-state network time series, and the p-value in the two-sample t-test is $p = 0$. Also, **Figures 2G,H** show a probability density estimate for voxel-wise DS and DN values for each subject and group average made by using ksdensity.m in MATLAB. In **Figures 2G,H**, 75% is the strong threshold level; we can use the quartile method (in **Figure 1**) to get it. As shown in **Figures 2G,H**, the statistical characteristics of DS were different from those of DN, in that DS has a long tail, while DN has tails more similar to a normal distribution (**Figures 2G,H**).

Distribution of Strong DS and DN in Terms of Voxels and Networks

Combining **Figure 1** and the distribution of DS and DN in terms of voxels (**Figure 2**) allows the distribution of strong DS and DN maps in the whole brain (shown in **Figures 3A,C**) to be obtained. The overlap maps between strong DS and strong DN are shown in **Figure 3E**. We found that the same regions exist in both DS and DN, but each has its own unique distribution. The histogram maps of percentage ratios of voxels of the DS and DN characterized networks are shown in **Figures 3B,D**, respectively, and we found that the percentage ratio of voxels for each network ranked from largest to smallest was: DMN, VN, SMN, FPN, DAN, VAN, and LIMB. Based on **Figure 3F**, the percentage ratio of overlap and non-overlap ranked from largest to smallest was overlapping DS and DN (25.72%), non-overlapping DN (24.72%), and non-overlapping DS (16.73%).

Test-Retest Reliability for DS and DN

Test-retest reliability for DS and DN was analyzed in terms of voxels and networks (**Figure 4**) by using all rs-fMRI data. First, the spatial distribution of test-retest reliability for DS and DN in terms of voxels as plotted, as shown in **Figure 4A**, and the ICC values of DS were found to be higher than those of DN. Then, test-retest reliability for DS and DN were analyzed in terms of networks, as presented in **Figure 4B**, which shows

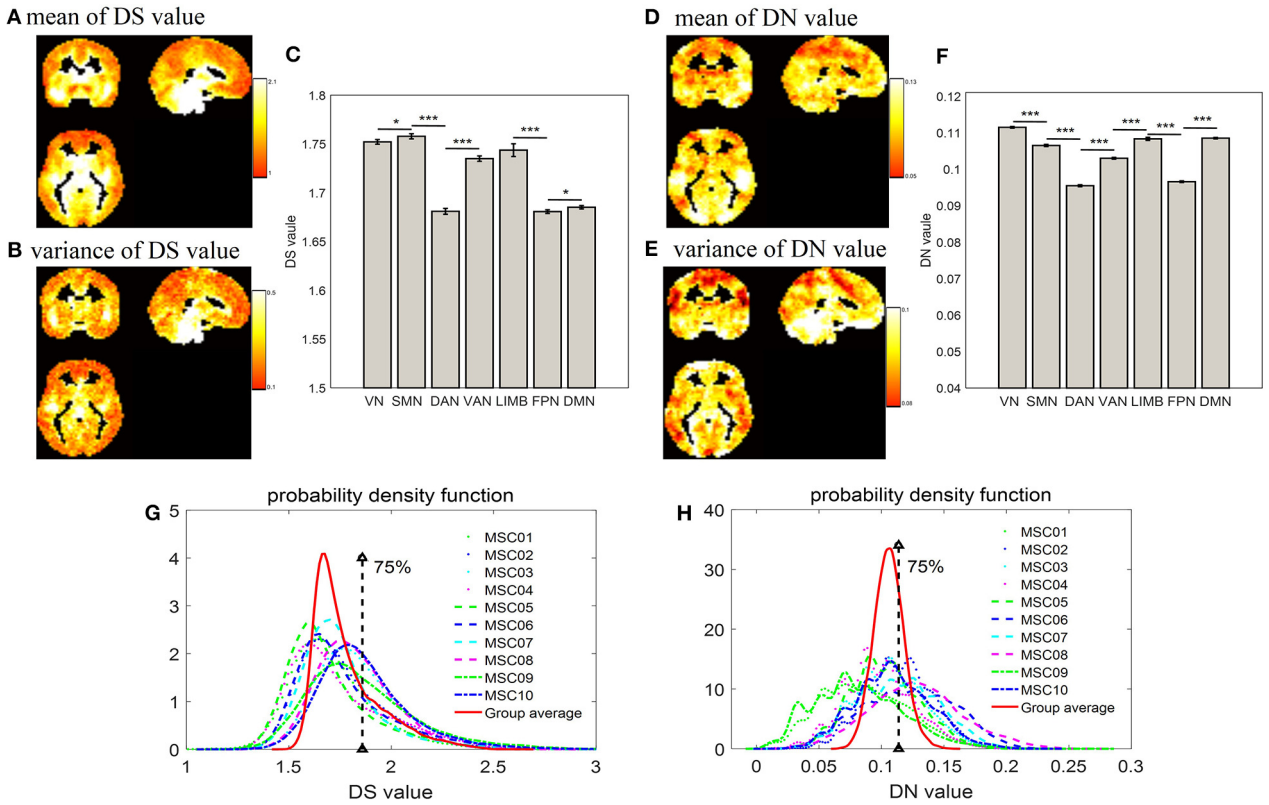

FIGURE 2 | Distribution of DS and DN in terms of voxels and networks. **(A)** and **(D)** show spatial distribution of group average DS and DN in terms of voxels across nine subjects and their 10 test-retest sessions; **(B,E)** show variance of spatial distribution of DS and DN in terms of voxels; **(C,F)** show bar plot of DS and DN, respectively, within intrinsic brain networks according to a priori functional network atlas (Yeo et al., 2011); **(G,H)** show probability density estimates of voxel-wise DS and DN values for each subject and group average, respectively; 75% is the strong threshold level, which is obtained by way of the quartile method (in **Figure 1**). The two-sample *t*-test showed the significant differences between each other (*$p < 0.05$, ***$p < 0.001$).

ICC maps from the DS and DN with networks: VN, SMN, DAN VAN, LIMB, FPN, and DMN. From **Figures 4A,B**, we found that the ICC values of DS and DN for each network were different and also found that the ICC values of DS were higher than those of DN in each network. Furthermore, upon inspecting **Figures 4A,B**, it was found that most of the voxels still have ICCs hovering around 0.2–0.3. Each network demonstrated lower ICC for DN and DS, while DS and DN displayed significant correlation (correlation coefficient $r = 0.3337$, $p < 0.001$) across voxels and networks as calculated by using the cftool.m in MATLAB. The spatial distribution of test-retest reliability for DS in terms of voxels when ICC $\geq$0.5 was plotted in **Figure 4C**. From **Figure 4C**, voxels reaching an ICC of at least 0.5 were mainly found on the DMN, FPN, LIMB, and VAN. More specific to the brain regions, there were also some voxels with ICC >0.5, such as Tempor_Pole_Sup_R (X = 34, Y = 6, Z = −24), Caudate_L (X = −18, Y = −6, Z = 24), Caudate_R (X = 18, Y = 6, Z = 20), Cingulum_Mid_R (X = 6, Y = −20, Z = 40), Rectus_R (X = −2, Y = 18, Z = −20), and Congulum_Ant_L (X = 2, Y = 30, Z = 0).

Similarity Analysis for DS and DN

For the similarity between networks (**Figure 5A**), we found that DAN and VAN were correlated for DS and DN ($r = 0.6559$, $p = 0$), whereas the association was not significant for the other five networks (**Figure 4A**). Furthermore, we used correlation matrices for the DS and DN associated with different spatial brain slices (**Figure 5B**). The slice-based similarity analysis showed a low correlation between DS and DN ($r = 0.3400$), which varied in different slices. High correlation corresponds to the similarity of the DS and DN in intra-slice variability and the correlation coefficients are different in different slices.

DISCUSSION

The human brain is a complex system, and there has been growing research interest in analyzing the complex brain networks by using rs-fMRI time series (Fox and Raichle, 2007; Biswal et al., 2010; de Pasquale et al., 2010; Liu and Duyn, 2013; Gao et al., 2018). In this work, the non-stationarity and non-linearity in rs-fMRI data of the human brain were detected by using the DS and DN measures. We quantified the degrees of non-stationarity and non-linearity in the time series of rs-fMRI by using the HHT and DVV methods. DS and DN were computed in terms of voxels across nine subjects and for their 10 test-retest sessions. We found that DS and DN had overlapped

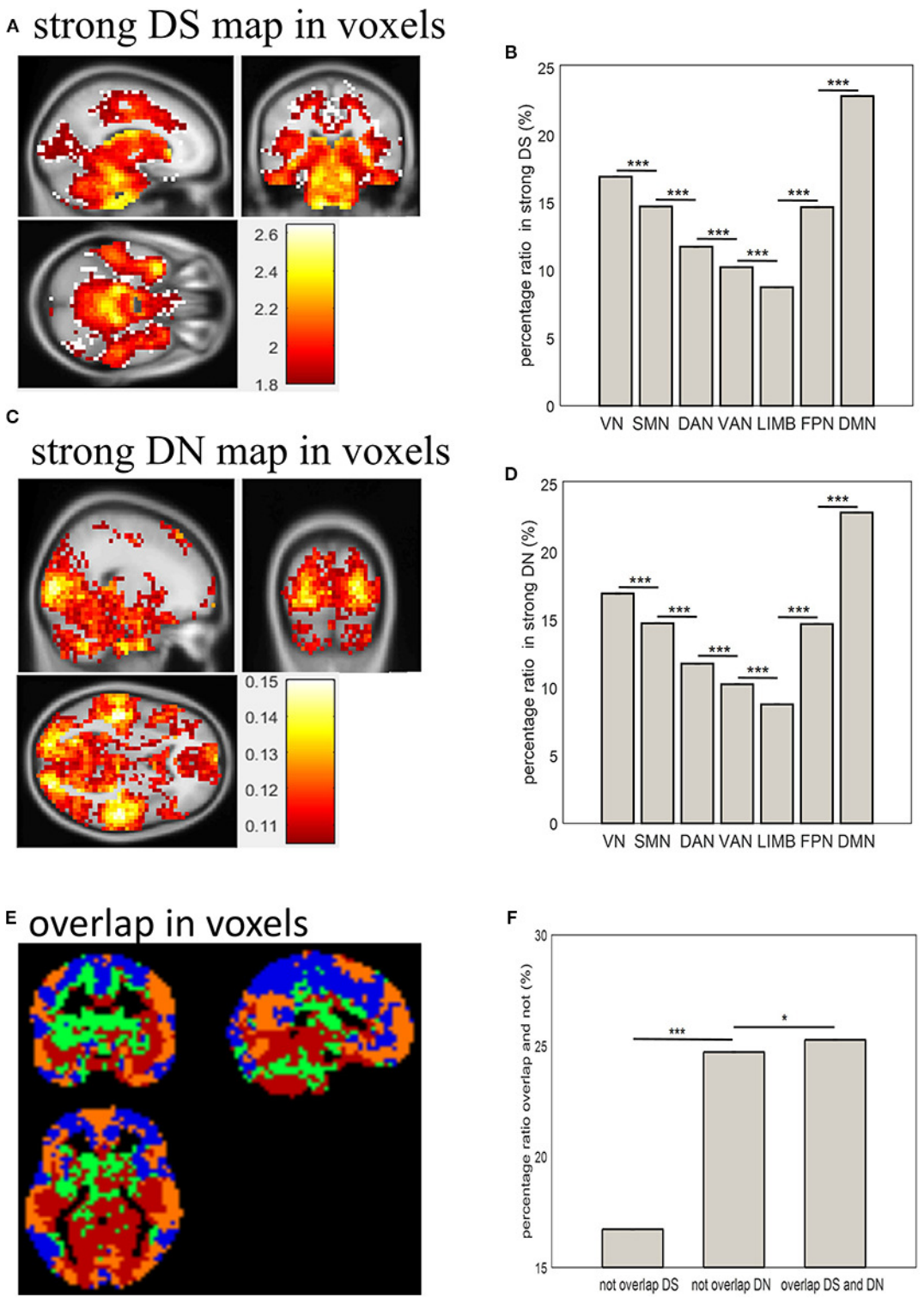

FIGURE 3 | Distribution of strong DS and DN in terms of voxels and networks. **(A,C)** show spatial distribution of strong DS and DN in terms of voxels; **(B,D)** show bar plots of percentage ratios of voxels of DS and DN, respectively, for seven networks; **(E)** shows spatial distribution of overlapping strong DS and DN in terms of voxels: blue indicates brain regions with weak DS and DN (below 75%); green and yellow indicated unique brain regions with strong DS and DN (above 75%) respectively; red indicates brain regions with strong overlapping DS and DN (above 75%); **(F)** shows a bar plot of the percentage ratios of voxels overlapping and not overlapping between strong DS and DN. Two-sample *t*-tests showed significant differences between them (*$p < 0.05$, ***$p < 0.001$).

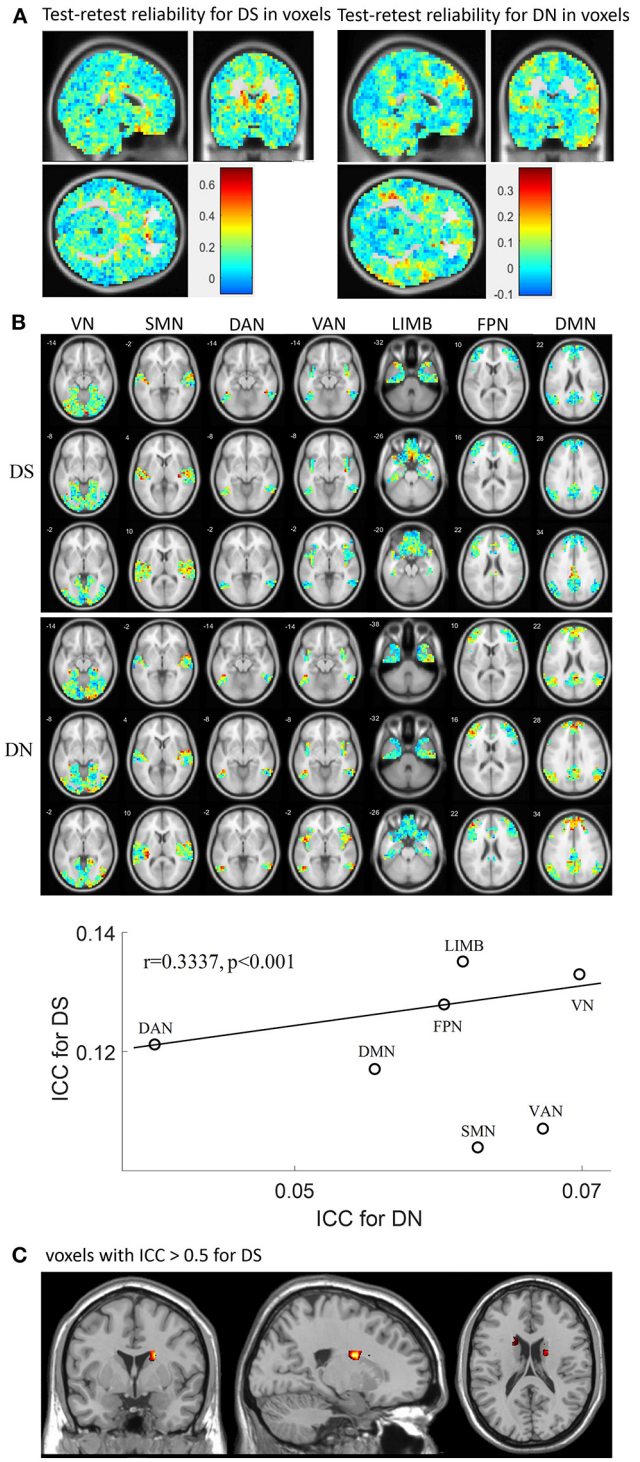

FIGURE 4 | Test-retest reliability for DS and DN. **(A)** shows spatial distribution of test-retest reliability for DS and DN, respectively, in terms of voxels calculated by using different session numbers; **(B)** ICC maps from the DS (first row) and DN (second row) with networks: VN SMN DAN VAN, LIMB, FPN, and DMN; in the third row, the correlation between ICC for DN and ICC for DS is displayed. **(C)** ICC maps from the DS when ICC $\geq$ 0.5.

spatial distributions together with varied characteristics across typical intrinsic brain networks, as well as different test-retest reliabilities. The DS and DN characterization of the rs-fMRI time series analysis has provided a new method of analyzing ongoing activities within the resting-state brain.

Distribution of DS

In this study, voxel-based and network-specific DS were examined. The mean DS value ranged from 0.1 to 2.1 over the whole brain, with the higher DS values in the brainstem, thalamus, striatum, temporal and occipital cortex, and cerebellum (**Figure 2A**), as well as in the networks SMN, VN, LIMB, and VAN (**Figure 2B**). From a theoretical point of view, the activity of neuronal assemblies should be non-stationary since it reflects the different stages of a self-organized process (Schoner and Kelso, 1988; Jin et al., 2017). A previous study revealed by analyzing EEG signals that brain activity is essentially non-stationary (Kaplan et al., 2005). An fMRI study also confirmed that there was non-stationary brain activity during an auditory task (Gaschler-Markefski et al., 1997). Using rs-fMRI, dynamic functional connectivity has been researched to delineate the non-stationary changes in brain activity synchronization (Xie et al., 2008; Ou et al., 2014). However, a recent study revealed that it is difficult to detect the non-stationarity in a typical rs-fMRI scan of 10 min using the sliding window approach because the effect of non-stationarity detection varies with the amount of data. Therefore, the authors pointed out that it is not optimal to use the sliding window approach for non-stationarity analysis (Hindriks et al., 2016). Using the HHT method, the current study demonstrated non-stationary signal fluctuation in widespread brain regions and functional networks, which confirmed the non-stationarity in the rs-fMRI signal and provides a quantitative DS map.

Distribution of DN

Using the DVV method, we found that voxels with strong DN are spatially distributed across different functional networks. From the DN value, the DAN showed a lower non-linear signal, and the VN, DMN, LIMB, and SMN showed higher non-linear signals (**Figure 2F**). The ranking of the DN value for each network from largest to smallest is as follows: VN, DMN, LIMB, SMN, VAN, FPN, and DAN. This suggests that despite the absence of external stimuli to VN, DMN, and LIMB, the baseline activity of those networks may be more complex than that of other systems. Both Gautama and Mandic have shown that the default-mode resting-state network time series is relatively more linear than time series in the auditory and motor networks (Gautama et al., 2003; Mandic et al., 2008). Gultepe and He previously reported that visual networks were more non-linear than the motor and auditory systems (Gultepe and He, 2013). Our finding supported the conclusion that without external stimulus, during resting state, the baseline activity of the visual cortex is more complex than the motor and auditory systems, which may be associated with complex functional organization for visual

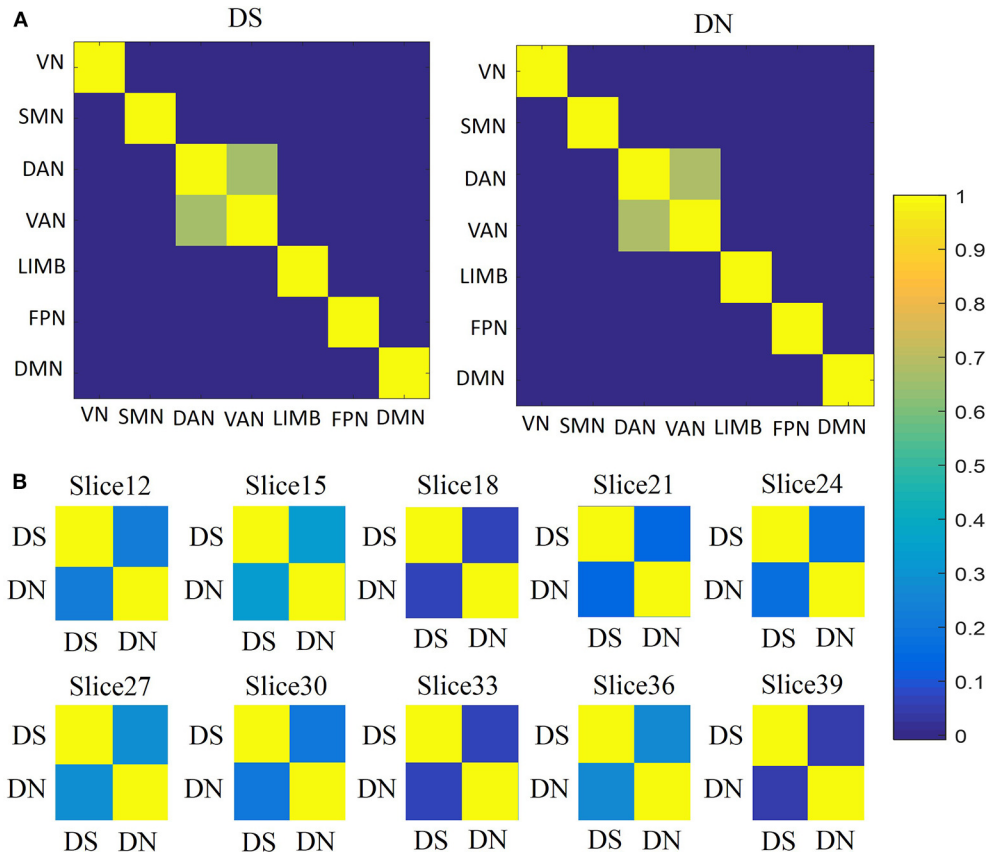

FIGURE 5 | Similarities analysis. **(A)** Between network similarities, using the average values of DS and DN within networks, across subjects and sessions by using Pearson's correlation. Correlation matrices for the DS (first column) and DN (second column) associated with networks: VN, SMN, DAN, VAN, LIMB, FPN, and DMN. **(B)** The similarities between DS and DN for each slice, across subjects and sessions, according to Pearson's correlation.

processing. Gultepe and He (2013) showed that in a task-based study using macaque BOLD and monocrystalline iron oxide particle (MION) signals the recruitment of physiological inputs such as cerebral blood volume, flow, and metabolic rate of oxygen into these two systems may be increased compared to in a resting state study where there is no task (Gautama et al., 2003). This may reflect their conclusion that the BOLD signal is more non-linear than the MION signal, which depends on fewer physiological parameters. The lower embedding dimension may be indicative of the lower complexity of resting-state systems within the brain; it is necessary to choose dimensions high enough to capture the phase space of the dynamical system (Gautama et al., 2004).

Overlap Between DS and DN

From the overlap of the spatial distributions of strong DS and DN in terms of voxels, the percentage ratio of voxels overlapping between strong DS and DN values was 25.72% and was relatively high compared to unique regions of strong DN (that is, those regions that have strong DN and weaker DS properties) (24.72%) and unique regions of strong DS (those regions that have strong DS and weaker DN properties) (16.73%). This suggests that regions that overlap between DS and DN exist but that each has its own unique distribution. Both stationarity and linearity can be determined by the complexity and stability of the activities of brain regions, making them inseparable. The two indicators reflect the profile of stationary time series and linear system, respectively, which have their own unique characteristics. For example, the larger the DS value in the fMRI signals, the more complex brain activities will be, while the larger the DN value, the more unstable brain activities will be. Thus, overlapping of strong DN and strong DS in certain regions demonstrated that those brain regions have simultaneous non-stationary and non-linear signals. The DMN showed the largest percentage ratio of voxels with strong DN and DS values. Thus, among the overlapping regions of strong DN and DS, DMN was the largest. This suggests that the DMN has both non-stationary and non-linear signals. It has been hypothesized that the activity of the DMN is related to spontaneous thoughts, i.e., intrinsic attention/information processing (Raichle et al., 2001). The DMN has been observed to be active at rest and deactivated during active task-states (Damoiseaux et al., 2008). In addition, the existence of unique regions of strong DN (24.72%) and unique regions of strong DS (16.73%) revealed that there are also some regions with their own unique characteristics, such as those with more complex and

more stable brain activities, contrasting with those with simpler and more unstable brain activities. This further demonstrates that the brain is a complex system.

Test-Retest Reliability and Similarity Analysis

We inferred that the ICC values of DS were larger than those of DN in terms of voxels and networks and that the ICC values of DS and DN for each network were different. DS and DN exhibited significant correlation across voxels and networks for each network. Moreover, the test-retest reliability values for DS and DN across 10 sessions were surprisingly low because most voxels had ICC values below 0.5. Most of the voxels had ICCs hovering around 0.2–0.3, while a few voxels reached 0.6, and voxels reaching an ICC of at least 0.5 were mainly found on certain brain regions, such as Tempor_Pole_Sup_R (X = 34, Y = 6, Z = −24), Caudate_L (X = −18, Y = −6, Z = 24), Caudate_R (X = 18, Y = 6, Z = 20), Cingulum_Mid_R (X = 6, Y = −20, Z = 40), Rectus_R (X = −2, Y = 18, Z = −20), and Congulum_Ant_L (X = 2, Y = 30, Z = 0); the ICC values in other brain regions were no larger than 0.5. These results provide a quantitative basis for the test-retest reliability of non-stationarity or non-linearity. In terms of similarity between networks, DAN and VAN were correlated for DS and DN, while the association was not significant for other networks. Thus, DS and DN can be recognized to have a good ability to predict network types. Moreover, the slice-based similarity analysis showed low correlation between DS and DN, which varied in different slices. High correlation corresponds to similarity of the DS and DN in intra-slice variability, and the correlation coefficients are different in different slices. The main reason for this is that the percentage ratio of overlapping voxels with strong DS and DN values was 25.72%. The overall reliability of topological measures was similar to that of other parameters derived from rs-fMRI, such as correlation significance, correlation valence (positive vs. negative correlations), and network membership (Shehzad et al., 2009). Resting-state data itself is a complex aggregation of different brain networks whose activity profiles overlap (Greicius et al., 2003), but this is also so in brain states that reflect cognitive and emotional processing (Damoiseaux et al., 2006).

Previous works have suggested that the fMRI signal consists of non-linear and non-stationary components (Xie et al., 2008; Ou et al., 2014), but these components have often been discarded in conventional generalized linear modeling and functional connectivity (analysis based on Pearson's correlation). In this study, we introduced a quantitative statistical method to identify the scale of non-linearity and non-stationarity in fMRI signals. The DS and DN measures enable the characterization of not only the brain's signal properties across specific regions but also the individual subject's brain dynamic features. Future fMRI research should compute DS and DN as part of the quality control step for preprocessing as indicators of data quality, particularly when dealing with cross-sectional comparisons. For example, individual DS and DN values should be identified for clinical populations and healthy controls, respectively, and then controlled as covariates in the group comparison of their functional connectivity. In the study of dynamic functional connectivity associated with non-stationary features, future research should investigate the potential relationship between dynamic measures and both DS and DN. It is also worth understanding the alterations of DS and DN linked with fMRI preprocessing, such as the complex influence of micromovement on fMRI signals. Taken together, the current study revealed that the quantitative map of the whole-brain DS/DN will provide a tool for future research to further explore the effect of DS/DN on fMRI measures such as functional connectivity.

LIMITATIONS

The present work has several potential limitations worth considering. In this paper, we estimated non-stationarity/non-linearity effects, respectively. Our major findings showed that these non-stationarity/non-linearity effects varied across different functional networks. One potential limitation was that this work focused on rs-fMRI signals and thus did not provide DS/DN measures based on task-fMRI data, although several previous studies have pointed out that non-stationarity/non-linear effects may differ among different tasks (Wager et al., 2005; Muhei-aldin et al., 2014; Ou et al., 2014). The second potential limitation of this study is that this work only focused on voxels and seven functional networks from Yeo's functional network atlas (Yeo et al., 2011). Depending on the parcellation number of functional networks (up to hundreds), the corresponding ICC may be different. The spatial extent of a region and how it may affect the ICC should be carefully investigated. The third limitation might be the imaging length of 30 min used in this study, which might affect the DS/DN. Previous studies have shown the ICC of functional connectivity is improved by long scan length (Braun et al., 2012; Birn et al., 2013). It is worth investigating the influence of scan length on the ICC of DS/DN. Lastly, there is the potential influence of scan sessions occurring at midnight, since we used the Midnight Scan Club dataset. Hill and Smith have examined the effect of time of day on the relationship between mood state, anaerobic power, and capacity, and they found that the relationship between mood state and subsequent performance is dynamic and is dependent upon the time of day (Hill et al., 1993). This study identified the whole-brain distribution of DS/DN in resting-state fMRI; however, it remains unclear whether DS/DN is more associated with neuronal activity or non-neuronal noises such as head motion. With the quantitative measures reported in the current study, more research is needed to further explore the mechanism underlying DS/DN in relation to fMRI preprocessing and the underlying functional connectivity.

CONCLUSION

In this paper, we investigated the degree of stationarity (DS) and the degree of non-linearity (DN) of rs-fMRI time series of

all gray matter voxels and intrinsic brain networks from the Midnight Scan Club datasets. Results from this study suggest that the baseline signals from the VN, LIMB, SMN, and DMN have relatively greater non-stationarity and non-linearity compared with those of the VAN, DAN, and FPN. This suggests that when we compute the "static" functional connectivity, it is necessary to take into account the relative contribution from the non-linearity and non-stationarity components from the respective brain regions. For example, when analyzing static functional connectivity, the VN needs to have more non-linear and non-stationary components eliminated than does the FPN. Moreover, the VN, LIMB, and DMN networks were more non-linear and non-stationary, so shorter-time data can be used, because the shorter the time, the closer the characteristics of the data are to being stationary and linear, so the optimal length of time is required. If the non-stationary and non-linear properties are not considered, then the results will be an approximate phenomenological description of the real characteristics. Our results suggest that different functional networks have distinct non-stationarity and non-linearity owing to the complexity and stability of rs-fMRI time series. Moreover, the DS and DN measures not only enable the characterization of the brain's regional signal properties but also of the individual subject's brain dynamic features. Therefore, this quantitative DS/DN method provides a tool for future research to further explore the effect of DS/DN on fMRI measures such as functional connectivity and to improve neural activity extraction or simulation by considering non-linear and non-stationary components.

DATA AVAILABILITY STATEMENT

Publicly available datasets were analyzed in this study. This data can be found here: the Midnight Scan Club data (https://openfmri.org).

AUTHOR CONTRIBUTIONS

SG made substantial contributions to the conception and design of the work, analysis, interpretation of data for the work, and the draft of the manuscript. RJ and HB made substantial contributions to the preprocessing analysis and interpretation of data for the work. JY and PX made a contribution to the revision of the manuscript. BB made a contribution to the conception and design of the work. As the corresponding author, BB and CM made great contributions to the interpretation of fMRI data and determined the final version to be published. All authors have read and approved the final manuscript.

FUNDING

This work was supported in part by the National Natural Science Foundation of China (NSFC) under Grant 61871420.

REFERENCES

Allen, E. A., Damaraju, E., Plis, S. M., Erhardt, E. B., Eichele, T., and Calhoun, V. D. (2014). Tracking whole-brain connectivity dynamics in the resting state. *Cereb. Cortex* 24, 663–676. doi: 10.1093/cercor/bhs352

Beck, T. W., Housh, T. J., Weir, J. P., Cramer, J. T., Vardaxis, V., Johnson, G. O., et al. (2006). An examination of the Runs Test, Reverse Arrangements Test, and modified Reverse Arrangements Test for assessing surface EMG signal stationarity. *J. Neurosci. Methods* 156, 242–248. doi: 10.1016/j.jneumeth.2006.03.011

Birn, R. M., Molloy, E. K., Patriat, R., Parker, T., Meier, T. B., Kirk, G. R., et al. (2013). The effect of scan length on the reliability of resting-state fMRI connectivity estimates. *Neuroimage* 83, 550–558. doi: 10.1016/j.neuroimage.2013.05.099

Biswal, B., Yetkin, F. Z., Haughton, V. M., and Hyde, J. S. (1995). Functional connectivity in the motor cortex of resting human brain using echo-planar MRI. *Magn. Reson. Med.* 34, 537–541. doi: 10.1002/mrm.1910340409

Biswal, B. B., Mennes, M., Zuo, X. N., Gohel, S., Kelly, C., Smith, S. M., et al. (2010). Toward discovery science of human brain function. *Proc. Natl. Acad. Sci. U.S.A.* 107, 4734–4739. doi: 10.1073/pnas.0911855107

Braun, U., Plichta, M. M., Esslinger, C., Sauer, C., Haddad, L., Grimm, O., et al. (2012). Test-retest reliability of resting-state connectivity network characteristics using fMRI and graph theoretical measures. *Neuroimage* 59, 1404–1412. doi: 10.1016/j.neuroimage.2011.08.044

Bullmore, E., Fadili, J., Maxim, V., Sendur, L., Whitcher, B., Suckling, J., et al. (2004). Wavelets and functional magnetic resonance imaging of the human brain. *Neuroimage* 23(Suppl. 1), S234–249. doi: 10.1016/j.neuroimage.2004.07.012

Cabral, J., Kringelbach, M. L., and Deco, G. (2014). Exploring the network dynamics underlying brain activity during rest. *Prog Neurobiol.* 114, 102–131. doi: 10.1016/j.pneurobio.2013.12.005

Damoiseaux, J. S., Beckmann, C. F., Arigita, E. J. S., Barkhof, F., Scheltens, P., Stam, C. J., et al. (2008). Reduced resting-state brain activity in the "default network" in normal aging. *Cerebral Cortex* 18, 1856–1864. doi: 10.1093/cercor/bhm207

Damoiseaux, J. S., Rombouts, S. A. R. B., Barkhof, F., Scheltens, P., Stam, C. J., Smith, S. M., et al. (2006). Consistent resting-state networks across healthy subjects. *Proc. Natl. Acad. Sci. U.S.A.* 103, 13848–13853. doi: 10.1073/pnas.0601417103

de Pasquale, F., Della Penna, S., Snyder, A. Z., Lewis, C., Mantini, D., Marzetti, L., et al. (2010). Temporal dynamics of spontaneous MEG activity in brain networks. *Proc. Natl. Acad. Sci. U.S.A.* 107, 6040–6045. doi: 10.1073/pnas.0913863107

Deshpande, G., Laconte, S., Peltier, S., and Hu, X. (2006). Tissue specificity of nonlinear dynamics in baseline fMRI. *Magn. Reson. Med.* 55, 626–632. doi: 10.1002/mrm.20817

Esposito, F., Formisano, E., Seifritz, E., Goebel, R., Morrone, R., Tedeschi, G., et al. (2002). Spatial independent component analysis of functional MRI time-series: to what extent do results depend on the algorithm used? *Hum. Brain Mapp.* 16, 146–157. doi: 10.1002/hbm.10034

Fox, M. D., and Raichle, M. E. (2007). Spontaneous fluctuations in brain activity observed with functional magnetic resonance imaging. *Nat. Rev. Neurosci.* 8, 700–711. doi: 10.1038/nrn2201

Freeman, W. J. (2000). Mesoscopic neurodynamics: from neuron to brain. *J. Physiol. Paris* 94, 303–322. doi: 10.1016/S0928-4257(00)01090-1

Freeman, W. J. (2003). Evidence from human scalp electroencephalograms of global chaotic itinerancy. *Chaos* 13, 1067–1077. doi: 10.1063/1.1596553

Friston, K. J., Holmes, A., Poline, J. B., Price, C. J., and Frith, C. D. (1996). Detecting activations in PET and fMRI: levels of inference and power. *Neuroimage* 4, 223–235. doi: 10.1006/nimg.1996.0074

Gao, W., Chen, S. D., Biswal, B., Lei, X., and Yuan, J. J. (2018). Temporal dynamics of spontaneous default-mode network activity mediate the association between

reappraisal and depression. *Soc. Cogn. Affect. Neurosci.* 13, 1235–1247. doi: 10.1093/scan/nsy092

Gaschler-Markefski, B., Baumgart, F., Tempelmann, C., Schindler, F., Stiller, D., Heinze, H.-J., et al. (1997). Statistical methods in functional magnetic resonance imaging with respect to nonstationary time-series: auditory cortex activity. *Mag. Reson. Med.* 38, 811–820. doi: 10.1002/mrm.1910380518

Gautama, T., Mandic, D. P., and Van Hulle, M. A. (2004). The delay vector variance method for detecting determinism and nonlinearity in time series. *Phys. D-Nonlinear Phenomena* 190, 167–176. doi: 10.1016/j.physd.2003.11.001

Gautama, T., Mandic, D. P., and Van Hulle, M. M. (2003). Signal nonlinearity in fMRI: A comparison between BOLD and MION. *IEEE Trans. Med. Imaging* 22, 636–644. doi: 10.1109/TMI.2003.812248

Gordon, E. M., Laumann, T. O., Gilmore, A. W., Newbold, D. J., Greene, D. J., Berg, J. J., et al. (2017). Precision functional mapping of individual human brains. *Neuron* 95, 791–807 e797. doi: 10.1016/j.neuron.2017.07.011

Gratton, C., Laumann, T. O., Nielsen, A. N., Greene, D. J., Gordon, E. M., Gilmore, A. W., et al. (2018). Functional brain networks are dominated by stable group and individual factors, not cognitive or daily variation. *Neuron* 98, 439–452 e435. doi: 10.1016/j.neuron.2018.03.035

Greicius, M. D., Krasnow, B., Reiss, A. L., and Menon, V. (2003). Functional connectivity in the resting brain: a network analysis of the default mode hypothesis. *Proc. Natl. Acad. Sci. U.S.A.* 100, 253–258. doi: 10.1073/pnas.0135058100

Gultepe, E., and He, B. (2013). A linear/nonlinear characterization of resting state brain networks in FMRI time series. *Brain Topogr.* 26, 39–49. doi: 10.1007/s10548-012-0249-7

Hansen, E. C., Battaglia, D., Spiegler, A., Deco, G., and Jirsa, V. K. (2015). Functional connectivity dynamics: modeling the switching behavior of the resting state. *Neuroimage* 105, 525–535. doi: 10.1016/j.neuroimage.2014.11.001

He, B. J. (2013). Spontaneous and task-evoked brain activity negatively interact. *J. Neurosci.* 33, 4672–4682. doi: 10.1523/JNEUROSCI.2922-12.2013

Hill, D. W., Hill, C. M., Fields, K. L., and Smith, J. C. (1993). Effects of jet-lag on factors related to sport performance. *Canad. J. Appl. Physiol.-Revue Canad. De Physiol. Appliquee* 18, 91–103. doi: 10.1139/h93-009

Hindriks, R., Adhikari, M. H., Murayama, Y., Ganzetti, M., Mantini, D., Logothetis, N. K., et al. (2016). Can sliding-window correlations reveal dynamic functional connectivity in resting-state fMRI? *Neuroimage* 127, 242–256. doi: 10.1016/j.neuroimage.2015.11.055

Huang, N. E., and Shen, S. S. (2005). *Hilbert-Huang Transform and its Applications*. London, Hackensack; NJ: World Scientific. doi: 10.1142/5862

Huang, N. E., Shen, Z., Long, S. R., Wu, M. L. C., Shih, H. H., Zheng, Q. N., et al. (1998). The empirical mode decomposition and the Hilbert spectrum for nonlinear and non-stationary time series analysis. *Proc. R. Soc. Mathemat. Phys. Eng. Sci.* 454, 903–995. doi: 10.1098/rspa.1998.0193

Hutchison, R. M., Womelsdorf, T., Gati, J. S., Everling, S., and Menon, R. S. (2013). Resting-state networks show dynamic functional connectivity in awake humans and anesthetized macaques. *Hum. Brain Mapp.* 34, 2154–2177. doi: 10.1002/hbm.22058

Hyndman, R. J., and Fan, Y. N. (1996). Sample quantiles in statistical packages. *Am. Statistic.* 50, 361–365. doi: 10.1080/00031305.1996.10473566

Jin, C. F., Jia, H., Lanka, P., Rangaprakash, D., Li, L. J., Liu, T. M., et al. (2017). Dynamic brain connectivity is a better predictor of PTSD than static connectivity. *Hum. Brain Mapp.* 38, 4479–4496. doi: 10.1002/hbm.23676

Kaplan, A. Y., Fingelkurts, A. A., Fingelkurts, A. A., Borisov, S. V., and Darkhovsky, B. S. (2005). Nonstationary nature of the brain activity as revealed by EEG/MEG: methodological, practical and conceptual challenges. *Signal Process.* 85, 2190–2212. doi: 10.1016/j.sigpro.2005.07.010

LaConte, S., Peltier, S., Kadah, Y., Ngan, S. C., Deshpande, G., and Hua, X. P. (2004). Detecting nonlinear dynamics of functional connectivity. *Med. Imaging* 5, 227–237. doi: 10.1117/12.535804

Laumann, T. O., Snyder, A. Z., Mitra, A., Gordon, E. M., Gratton, C., Adeyemo, B., et al. (2017). On the Stability of BOLD fMRI Correlations. *Cereb. Cortex* 27, 4719–4732.

Lin, C. F., and Zhu, J. D. (2012). Hilbert-Huang transformation-based time-frequency analysis methods in biomedical signal applications. *Proc. Inst. Mech. Eng. H* 226, 208–216. doi: 10.1177/0954411911434246

Liu, X., and Duyn, J. H. (2013). Time-varying functional network information extracted from brief instances of spontaneous brain activity. *Proc. Natl. Acad. Sci. U.S.A.* 110, 4392–4397. doi: 10.1073/pnas.1216856110

Mandic, D. P., Chen, M., Gautama, T., Van Hulle, M. M., and Constantinides, A. (2008). On the characterization of the deterministic/stochastic and linear/nonlinear nature of time series. *Proc. R. Soc.-Mathemat. Phy. Eng. Sci.* 464, 1141–1160. doi: 10.1098/rspa.2007.0154

Muhei-aldin, O., VanSwearingen, J., Karim, H., Huppert, T., Sparto, P. J., Erickson, K. I., et al. (2014). An investigation of fMRI time series stationarity during motor sequence learning foot tapping tasks. *J. Neurosci. Methods* 227, 75–82. doi: 10.1016/j.jneumeth.2014.02.003

Noble, S., Scheinost, D., and Constable, R. T. (2019). A decade of test-retest reliability of functional connectivity: a systematic review and meta-analysis. *Neuroimage* 203:116157. doi: 10.1016/j.neuroimage.2019.116157

Ou, J., Lian, Z., Xie, L., Li, X., Wang, P., Hao, Y., et al. (2014). Atomic dynamic functional interaction patterns for characterization of ADHD. *Hum. Brain Mapp.* 35, 5262–5278. doi: 10.1002/hbm.22548

Panerai, R. B. (2014). Nonstationarity of dynamic cerebral autoregulation. *Med. Eng. Phys.* 36, 576–584. doi: 10.1016/j.medengphy.2013.09.004

Qian, L., Zhang, Y., Zheng, L., Shang, Y. Q., Gao, J. H., and Liu, Y. J. (2015). Frequency dependent topological patterns of resting-state brain networks. *PLoS ONE* 10:e0124681. doi: 10.1371/journal.pone.0124681

Raichle, M. E., MacLeod, A. M., Snyder, A. Z., Powers, W. J., Gusnard, D. A., and Shulman, G. L. (2001). A default mode of brain function. *Proc. Natl Acad. Sci. U.S.A.* 98, 676–682. doi: 10.1073/pnas.98.2.676

Schoner, G., and Kelso, J. A. (1988). Dynamic pattern generation in behavioral and neural systems. *Science* 239, 1513–1520. doi: 10.1126/science.3281253

Shehzad, Z., Kelly, A. M. C., Reiss, P. T., Gee, D. G., Gotimer, K., Uddin, L. Q., et al. (2009). The resting brain: unconstrained yet reliable. *Cerebral Cortex* 19, 2209–2229. doi: 10.1093/cercor/bhn256

Shine, J. M., Bissett, P. G., Bell, P. T., Koyejo, O., Balsters, J. H., Gorgolewski, K. J., et al. (2016). The dynamics of functional brain networks: integrated network states during cognitive task performance. *Neuron* 92, 544–554. doi: 10.1016/j.neuron.2016.09.018

Shrout, P. E., and Fleiss, J. L. (1979). Intraclass correlations: uses in assessing rater reliability. *Psychol. Bull.* 86, 420–428. doi: 10.1037/0033-2909.86.2.420

Smith, S. M., Miller, K. L., Moeller, S., Xu, J., Auerbach, E. J., Woolrich, M. W., et al. (2012). Temporally-independent functional modes of spontaneous brain activity. *Proc. Natl. Acad. Sci. U.S.A.* 109, 3131–3136. doi: 10.1073/pnas.1121329109

Smith, S. M., Vidaurre, D., Beckmann, C. F., Glasser, M. F., Jenkinson, M., Miller, K. L., et al. (2013). Functional connectomics from resting-state fMRI. *Trends Cogn. Sci.* 17, 666–682. doi: 10.1016/j.tics.2013.09.016

Stam, C. J. (2005). Nonlinear dynamical analysis of EEG and MEG: review of an emerging field. *Clin. Neurophysiol.* 116, 2266–2301. doi: 10.1016/j.clinph.2005.06.011

Suk, H. I., Wee, C. Y., Lee, S. W., and Shen, D. (2016). State-space model with deep learning for functional dynamics estimation in resting-state fMRI. *Neuroimage* 129, 292–307. doi: 10.1016/j.neuroimage.2016.01.005

Thompson, G. J. (2018). Neural and metabolic basis of dynamic resting state fMRI. *Neuroimage* 180, 448–462. doi: 10.1016/j.neuroimage.2017.09.010

Wager, T. D., Vazquez, A., Hernandez, L., and Noll, D. C. (2005). Accounting for nonlinear BOLD effects in fMRI: parameter estimates and a model for prediction in rapid event-related studies. *Neuroimage* 25, 206–218. doi: 10.1016/j.neuroimage.2004.11.008

Xie, X., Cao, Z., and Weng, X. (2008). Spatiotemporal nonlinearity in resting-state fMRI of the human brain. *Neuroimage* 40, 1672–1685. doi: 10.1016/j.neuroimage.2008.01.007

Yaesoubi, M., Adali, T., and Calhoun, V. D. (2018). A window-less approach for capturing time-varying connectivity in fMRI data reveals the presence

of states with variable rates of change. *Hum. Brain Mapp.* 39, 1626–1636. doi: 10.1002/hbm.23939

Yan, C. G., Craddock, R. C., Zuo, X. N., Zang, Y. F., and Milham, M. P. (2013). Standardizing the intrinsic brain: towards robust measurement of inter-individual variation in 1000 functional connectomes. *Neuroimage* 80, 246–262. doi: 10.1016/j.neuroimage.2013.04.081

Yeo, B. T. T., Krienen, F. M., Sepulcre, J., Sabuncu, M. R., Lashkari, D., Hollinshead, M., et al. (2011). The organization of the human cerebral cortex estimated by intrinsic functional connectivity. *J. Neurophysiol.* 106, 1125–1165. doi: 10.1152/jn.00338.2011

Conflict of Interest: The authors declare that the research was conducted in the absence of any commercial or financial relationships that could be construed as a potential conflict of interest.

frontiers in Neuroscience

ORIGINAL RESEARCH
published: 02 July 2020
doi: 10.3389/fnins.2020.00700

Functional MRI Signal Complexity Analysis Using Sample Entropy

Maysam Nezafati[1], Hisham Temmar[1] and Shella D. Keilholz[1,2]**

[1] Department of Biomedical Engineering, Georgia Institute of Technology, Emory University, Atlanta, GA, United States, [2] Neuroscience Program, Graduate Division of Biological and Biomedical Sciences, Laney Graduate School, Emory University, Atlanta, GA, United States

Resting-state functional magnetic resonance imaging (rs-fMRI) is an immensely powerful method in neuroscience that uses the blood oxygenation level-dependent (BOLD) signal to record and analyze neural activity in the brain. We examined the complexity of brain activity acquired by rs-fMRI to determine whether it exhibits variation across brain regions. In this study the complexity of regional brain activity was analyzed by calculating the sample entropy of 200 whole-brain BOLD volumes as well as of distinct brain networks, cortical regions, and subcortical regions of these brain volumes. It can be seen that different brain regions and networks exhibit distinctly different levels of entropy/complexity, and that entropy in the brain significantly differs between brains at rest and during task performance.

Keywords: functional MRI, complexity, entropy, temporal analysis, resting state, computational neuroscience, neuro imaging

OPEN ACCESS

Edited by:
Nanyin Zhang, Pennsylvania State University (PSU), United States

Reviewed by:
Bharat B. Biswal, University of Electronic Science and Technology of China, China
Xi-Nian Zuo, Beijing Normal University, China

****Correspondence:***
Maysam Nezafati
maysam.nezafati@bme.gatech.edu
Shella D. Keilholz
shella.keilholz@bme.gatech.edu

Specialty section:
This article was submitted to Brain Imaging Methods, a section of the journal Frontiers in Neuroscience

Received: *16 December 2019*
Accepted: *09 June 2020*
Published: *02 July 2020*

Citation:
Nezafati M, Temmar H and Keilholz SD (2020) Functional MRI Signal Complexity Analysis Using Sample Entropy. Front. Neurosci. 14:700. doi: 10.3389/fnins.2020.00700

INTRODUCTION

Resting-state functional magnetic resonance imaging (rs-fMRI) uses the blood oxygenation level-dependent (BOLD) signal to characterize the spontaneous activity of the brain (Biswal et al., 2010). In functional connectivity analysis, correlation is calculated between the time series of different regions of interest (ROI). Analysis of regions with high correlation can aid in the identification of functional networks. However, both within and across networks, fMRI signals can exhibit dynamics that may reflect changes in brain state or mental activity (Chang and Glover, 2010; Hutchison et al., 2013; Keilholz et al., 2013, 2016; Keilholz, 2014). If the complexity or regularity of these fluctuations in the fMRI time-series could be evaluated and analyzed, it might provide insight into general brain activity, brain structures, and brain networks.

Entropy, in general, is defined as a lack of order or predictability in a system. In the context of physiologically time-based signals, entropy is a measure of disorderliness in the time dimension. This can also serve as a parallel for system complexity, as a more complex system will often produce more disorderly signals. The second law of thermodynamics indicates that the maximum entropy is reached when a closed system rests at an equilibrium state, so in order to preserve vital activities, living systems must constantly maintain low-levels of entropy, shying away from equilibrium (Schrödinger, 1945). The human brain is one such living system, and while it maintains a relatively low level of entropy when compared to a system at equilibrium, the complex nature of its various networks' spontaneous activities can cause a variation in local entropy that reflects differences in the function of those areas. By calculating the entropy of the signal acquired from the brain, these variations can be investigated, and the status of the resting brain can be compared across conditions to understand how the brain adapts during task performance (Bergström, 1969; Singer, 2009).

Establishment of a general algorithm for entropy requires a vast data set. The accurate estimation of the probability distribution function from the limited number of time points obtained in rs-fMRI studies is difficult. Sample entropy (Shalit, 1985), an extension of approximate entropy (Pincus, 1991), is an alternative technique that addresses these issues. The Kolmogorov (1998) complexity model is the basis for approximate and sample entropy (Wang et al., 2014), which can be evaluated even with relatively small data sets (Shalit, 1985; Pincus, 1991). This makes them well-suited for the analysis of rs-fMRI data, where the number of time points is typically relatively small (∼200–1000) compared to the number of voxels.

Previous analyses of the entropy of the BOLD signal have shown that brain signals exhibit various levels of disorder. Wang et al. (2014) performed a comprehensive study on the Sample entropy map of approximately 1000 healthy subjects. They observed a sharp low-high contrast between the neocortex and the rest of the brain, which may indicate the higher mental functions performed by cortex (Wang et al., 2014). Moreover, entropy differs in patients with attention deficient hyperactivity disorder (ADHD) (Sokunbi et al., 2013) and during the administration of different drugs (Ferenets et al., 2007).

Motivated by these findings, we performed a more extensive analysis of entropy to determine the amount of variability present across brain areas and networks. We compared findings from task-based and resting state data from the Human Connectome Project (Van Essen et al., 2012) to characterize how entropy changed across conditions. The results provide further evidence that the entropy of the BOLD signal reflects aspects of the brain's functional organization and may prove informative about neural processing.

MATERIALS AND METHODS

Data Acquisition

MRI Data was downloaded from the Human Connectome Project (Van Essen et al., 2012). This data came from 100 randomly selected, unrelated individuals, ranging from ages 22 to 36 (54 female – 46 male). One anatomical scan from each individual was used for preprocessing [T1-weighted three-dimensional magnetization-prepared rapid gradient echo (T1w 3D MPRAGE) sequence; TR = 2400 ms, TE = 2.14 ms, TI = 1000 ms, FA = 8°, FOV = 224 mm × 224 mm, voxel size 0.7 mm isotropic] (Milchenko and Marcus, 2013).

In addition, two resting-state functional scans per subject, each approximately 15 min long, were used, with the following parameters: TR = 720 ms, TE = 33.1 ms, FA = 52°, FOV = 208 mm × 180 mm (RO × PE), matrix = 104 × 90 (RO × PE), slice thickness = 2.0 mm; 72 slices; 2.0 mm isotropic voxels, multi-band factor = 8, echo spacing 0.58 ms, with right-to-left (RL) phase encode direction in one scan and left-to-right (LR) phase encode direction in the other (Feinberg et al., 2010; Chen et al., 2015). Two working memory task functional scans per subject, each approximately 5 min long, were used for comparison with the rest scans, also with RL phase encode direction in one scan and LR phase encode direction in the other. The working memory task, described in Barch et al. (2013), involves a version of the N-back task, assessing both working memory and cognitive control in a block format. Each task functional scan includes eight task blocks lasting 25 s as well as four fixation blocks lasting 15 s. Half the task blocks use a 0-back working memory task and the other half use a 2-back working memory task. These blocks are divided into four categories: tools, body parts, faces, and places. To adjust for the shorter length of the task scans, rest scans were truncated to the same length as the task scans.

Preprocessing Methods

Scans were preprocessed using both FSL 5.0 (Jenkinson et al., 2012) and MATLAB (Mathworks, Natick, MA, United States). First, FSL was used to register anatomical data to the 2 mm Montreal Neurological Institute (MNI) atlas using FMRIB's Linear Image Registration Tool (FLIRT) (Jenkinson and Smith, 2001; Jenkinson et al., 2002). Then the brain was extracted from the scan using BET, and segmented into gray matter, white matter, and CSF using FMRIB's Automated Segmentation Tool (FAST) (Zhang et al., 2001). Functional data was then motion correction using MCFLIRT (Jenkinson et al., 2002) and registered to MNI space using FLIRT.

The seven functional networks based on Yeo et al.'s (2011) parcellation method (were discriminated from each other. The mean and the standard deviation of sample entropy for each network were calculated and mapped to that network.

Entropy Calculation

A combination of home-designed MATLAB codes and the brain entropy mapping toolbox (BENtbx[1]) by Wang et al. (2014) from University of Pennsylvania were used to calculate the entropy for each voxel. The equation for sample entropy is described in BENtbx as follows:

$$B^m(r) = \frac{1}{(N-m)(N-m-1)} \sum_{i=1}^{N-m} B_i^m(r)$$

$$A^m(r) = \frac{1}{(N-m)(N-m-1)} \sum_{i=1}^{N-m} B_i^{m+1}(r)$$

$$SE(m, r, N, x) = -ln\left[\frac{A^m(r)}{B^m(r)}\right]$$

The fMRI data for one voxel is considered as $x = [x_1, x_2, \ldots, x_N]$, in this set "$N$" is the number of repetitions (N value is specified based on functional scan length and TR). In sample entropy a series of embedded vectors with m consecutive points are extracted from the data set x: $u_i = [x_i, x_{i+1}, \ldots x_{i+m-1}]$, ($i = 1$ to $N-m+1$, m: pre-defined dimension which specifies the pattern length). A distance threshold "r" is specified (tolerance value) and $B_m^r(r)$ counts the number of u_j ($j = 1$, to $N-m$, and $j \neq i$) whose distances to u_i are less than r, as does, $B_i^{m+1}(r)$ for the

[1]https://cfn.upenn.edu/~zewang/BENtbx.php

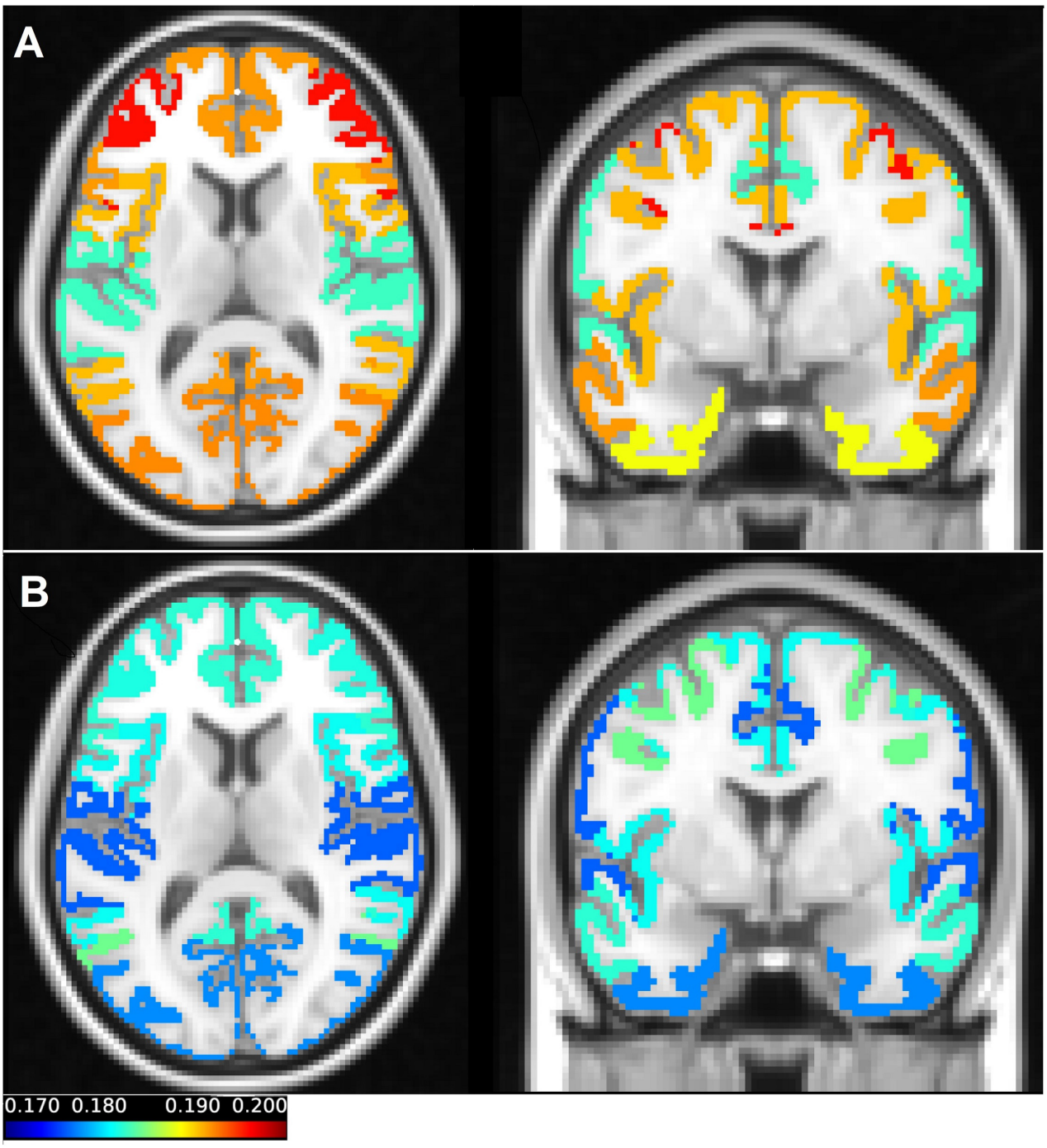

FIGURE 1 | The average entropy values across scans of each of the seven networks in resting state **(A)** and during a working memory task **(B)** were mapped on the T1-weighted image. The coronal and axial views were selected in a way that all parcellations can be presented in one figure. In **(A)** the axial view clearly demonstrates the frontoparietal network, which has the highest value of the entropy during resting state. The somatomotor and limbic networks have low values of the entropy in the resting state. In **(B)** the dorsal attention network which has the highest entropy during the working memory task can be seen both in the coronal and axial view. Also, in **(B)** the visual and limbic networks are presented, which have the lowest values of entropy in task.

dimension of $m+1$. Thus the sample entropy can be measured by averaging across all possible vectors (Wang et al., 2014). A small value for $\boldsymbol{m}$ results in improvement of sample entropy accuracy so in current study the value of $\boldsymbol{m}$ was equal to 3. Based on the previous studies the threshold of $r = 0.6$ SD would result in similar values of sample entropy even for different values of $\boldsymbol{m}$. Thus, in

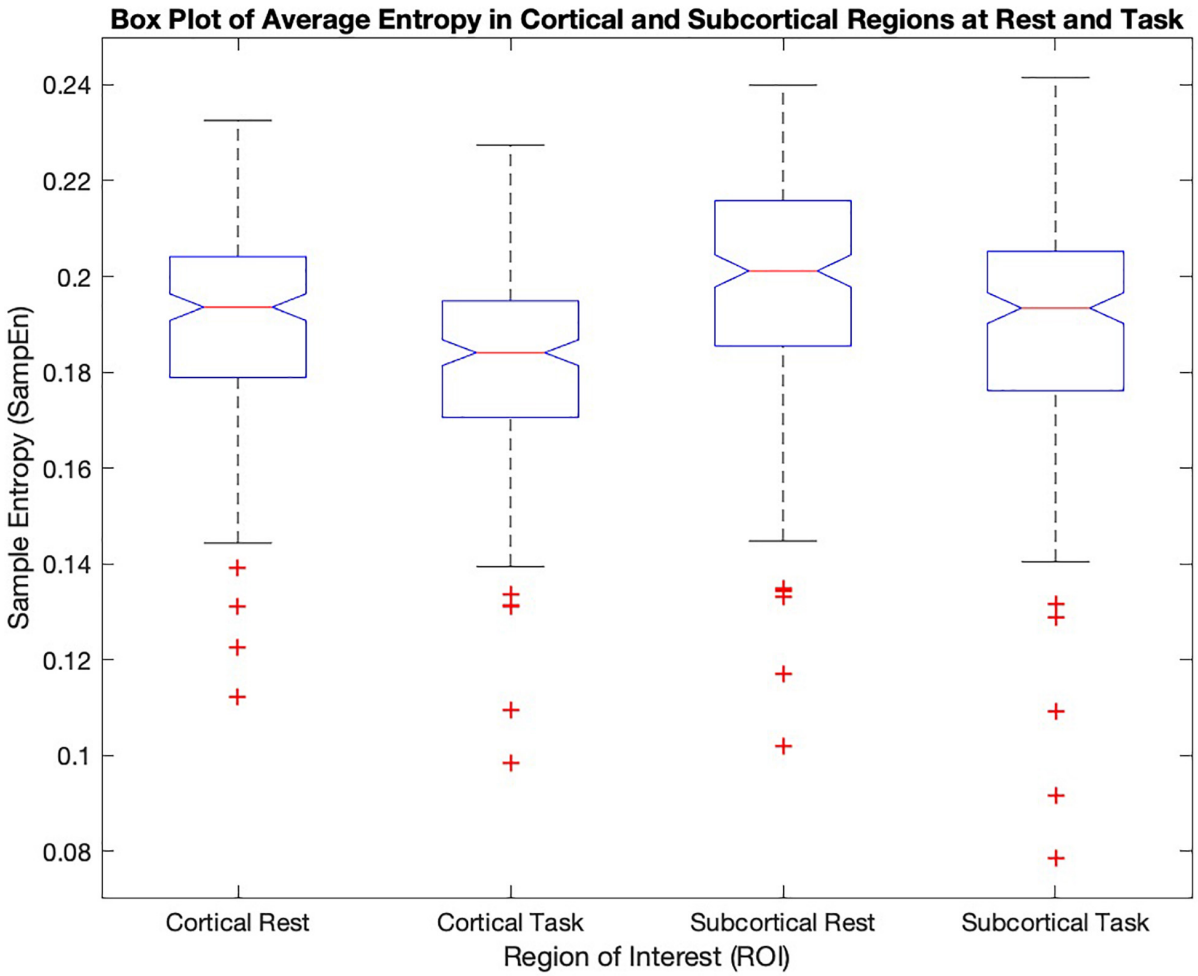

FIGURE 2 | The mean sample entropy of cortical regions and subcortical regions at rest and during the working memory task are shown. Subcortical regions have higher significantly higher entropy than cortical regions (p-value < 0.05) both in task and at rest. The cortical and subcortical regions in rest show significantly higher values compared to task (p-value < 0.05).

TABLE 1 | The mean and standard deviations of cortical and subcortical regions at rest and during the working memory task.

Region	Rest vs task	Mean	Standard deviation
Cortical	Rest	0.1912	0.0200
	Task	0.1815	0.0195
Subcortical	Rest	0.1981	0.0232
	Task	0.1897	0.0245

this study the value of $r = 0.6$ SD was used (Pincus, 1991; Richman and Moorman, 2000).

Correlation Matrices

Pearson correlation was calculated between 7 pre-identified brain networks (Yeo et al., 2011) and between cortical and subcortical regions (42 cortical regions and 21 subcortical regions) of the brain (Harvard-Oxford mask FSL) across scans. This was done in both rest and task entropy maps, to identify the dependence of networks and regions on each other in rest and task mode.

In the case of the seven functional networks, X and Y were length 200 vectors representing the mean sample entropy of a network in each scan. Correlation was then calculated for each pair of networks and placed into a 7×7 correlation matrix representing the correlation between each network and every other network. This was calculated for both for rest and task sample entropy maps.

The same process was repeated for the 63 cortical and subcortical regions, where X and Y represented length 200 vectors representing the mean sample entropy of a distinct subcortical or cortical ROI. This results in a 63×63 correlation matrix of both cortical and subcortical regions.

Paired *t*-Test and Reliability Evaluation

The paired t-test was used to compare brain entropy maps at rest and during the working memory task. This was performed

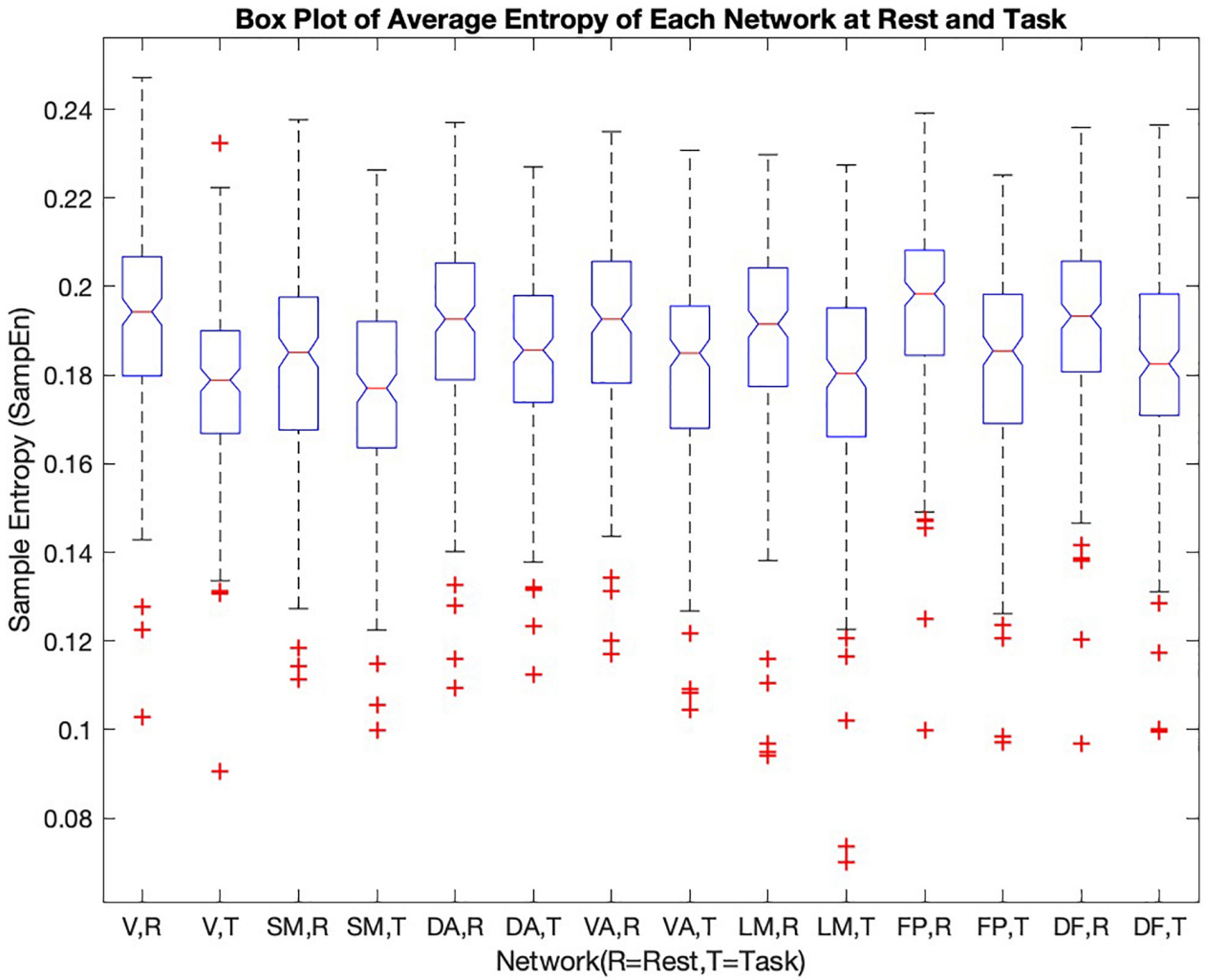

FIGURE 3 | He sample entropy value of each of the seven cortical networks [1-visual (V), 2-somatomotor (SM), 3-dorsal attention (DA), 4-ventral attention (VA), 5-limbic (LM), 6-frontoparietal (FP), 7-default (DF)] in rest and during the working memory task are shown in the box plot (R = rest, T = task). The mean sample entropy for each network in rest is significantly higher than during the working memory task (p-value < 0.05, see **Table 2**)

at voxel-level resolution to produce a whole brain volume t-test, as well as for the seven networks and the cortical/subcortical regions. In every case, the two paired samples are length 200 vectors representing entropy in each scan at rest and task. Due to multiple comparison, the Bonferroni correction was done to decrease the risk of a type I error. Box plots were produced for the seven networks as well as the subcortical and cortical regions to further highlight differences.

In order to examine the reproducibility of the entropy measurements, we calculated them separately for the first and second rsfMRI scans for each subject, and for the first and second fMRI scans for each subject. We then measured correlation between the values for the seven networks across individuals in the two scans. We also measured correlation between the final group level values for the seven networks across the two scans.

The intraclass correlation (ICC) was also used to evaluate the reliability of the entropy calculation of each functional network by comparing the variability of entropy of the two scans of the same subject to the total variation across all subjects (for resting state and for task performing) using a Microsoft Excel Add-in to calculate ICC (3,1) (Merisaari et al., 2019).

RESULTS

The sample entropy was calculated at each voxel in all fMRI task and rest scans (100 subjects, each of them scanned twice at rest and twice during task performance). **Figure 1** shows the sample entropy network-level maps of resting-state (**Figure 1A**) and task-performing (**Figure 1B**) groups, superimposed onto the T1-weighted image. As shown in the figure, the frontoparietal network has the highest entropy during rest, while the dorsal attention network has the highest entropy during task. The somatomotor network has the lowest entropy during rest, also the

limbic network and somatomotor have the lowest entropy during task. Entropy is generally higher during rest than during task.

Figure 2 shows quantitative values of Sample entropy for rest and task, divided into cortical and subcortical regions. The cortical regions in task have the average value of 0.1815 ± 0.0195. The average value of Sample entropy of cortical regions in rest is 0.1912 ± 0.0200, which is significantly higher than the same regions during the working memory task (p-value < 0.05). The subcortical regions in rest have the average value of 0.1981 ± 0.0232. The average value of Sample entropy for subcortical regions in task is 0.1897 ± 0.0245, which is significantly lower than the values of the same regions (subcortical) in rest. Interestingly, the subcortical regions during task show the widest spread of entropy values (standard deviation of 0.0245). **Table 1** shows the average value and standard deviation of cortical and subcortical regions in rest and during task performance.

To further examine the variability of entropy across brain networks, the values were separated by network (**Figure 3**).

The frontoparietal network has the highest entropy among all the cortical networks at rest. The somatomotor network with 0.1830 ± 0.0223 and limbic network with 0.1884 ± 0.0237 have the lowest entropy during rest. For each network, entropy during rest was significantly higher than during task (p-value is shown in the last column of **Table 2**).

During the working memory task, the dorsal attention network has the highest entropy. The limbic network, somatomotor network, and visual network have the low values of entropy during task performance.

Correlation between the entropy of the networks describes how entropy in different areas covaries across subjects (**Figure 4**). This correlation is generally high but decreases during the task in comparison to the resting state. The frontoparietal network and default mode network have the highest correlation in the resting state (0.95), followed by the frontoparietal network and ventral attention network (0.92). During the working memory task, entropy in the ventral attention network is strongly correlated with entropy in both the frontoparietal network and the somatomotor networks (0.89).The dorsal attention network and frontoparietal network are nearly as strongly correlated (0.88). The lowest correlation is between the limbic network and the visual network, both at rest and during the working memory task. In task, the correlation between the visual network and the somatomotor network is among the lowest correlations (0.55), which is different from the resting state.

We furthered examined the correlation of entropy values across the 42 cortical regions and 21 subcortical regions in rest and task (**Figure 5**). Correlation of entropy values is generally high within the cortical regions (average of 0.83) and within the subcortical regions (average of 0.89), but the correlation between cortical and subcortical regions is not as strong (average of 0.43). Also, by comparison of **Figures 5A,B** it can be observed that correlation between all ROIs is decreased during task, but this reduction in task mode is more severe in the cortical regions.

To determine the significance of the effects we observed, a two-factor ANOVA test was performed with the null hypotheses that

1- performing the memory task has no significant effect on the entropy of the brain (comparing ROI voxels)
2- brain regions (Cortical/subcortical) has no significant effect on the entropy of the brain.

As it is presented in **Table 3**, both the differences across rest and task and across cortex and subcortex were significant (p-value < 0.05), but there was no significant interaction effect. We performed a similar analysis on the data separated by network during rest and task.

The two null hypotheses were:

1- performing the working memory task has no significant effect on the entropy of the brain
2- brain cortical networks have no significant effect on the entropy of the brain.

As it is presented in **Table 4**, significant differences were observed between rest and task and across networks (p-value < 0.05). Moreover, the interaction term was significant, indicating that task performance affects entropy in a network-dependent manner.

Table 5 presents the consistency of entropy measurements across scans. Pearson correlation ranges from 0.46 to 0.59 for rest and from 0.36 to 0.47 for task. Interestingly, entropy values are more consistent across scans in rest than in task. The means of scan 1 and 2 within each network are not significantly different ($\alpha = 0.05$).

The ICC values are shown in **Table 5** as well. Zuo et al. (2019) and Xing and Zuo (2018) categorized the ICC values in to the following intervals $0 < ICC < 0.2$ (slight), $0.2 < ICC < 0.4$ (fair), $0.4 < ICC < 0.6$ (moderate), $0.6 < ICC < 0.8$ (substantial), $0.8 < ICC < 1.0$ (almost perfect) for reliability quantification. By considering those intervals, all seven networks can be categorized as having moderate reliability in resting state. In task, subjects' visual network, somatomotor network and ventral attention

TABLE 2 | Means and standard deviations of all seven cortical networks at rest and during working memory task.

	Network name	Rest vs task	Mean	Standard deviation	p-Value
1	Visual	Rest	0.1922	0.0212	1.01E-23
		Task	0.1779	0.0186	
2	Somatomotor	Rest	0.1830	0.0223	2.09E-33
		Task	0.1766	0.0239	
3	Dorsal attention	Rest	0.1908	0.0202	5.67E-29
		Task	0.1845	0.0203	
4	Ventral attention	Rest	0.1906	0.0212	7.86E-33
		Task	0.1816	0.0225	
5	Limbic	Rest	0.1884	0.0237	1.31E-24
		Task	0.1778	0.0241	
6	Frontoparietal	Rest	0.1958	0.0195	2.07E-29
		Task	0.1821	0.0221	
7	Default mode	Rest	0.1917	0.0200	3.28E-30
		Task	0.1825	0.0217	

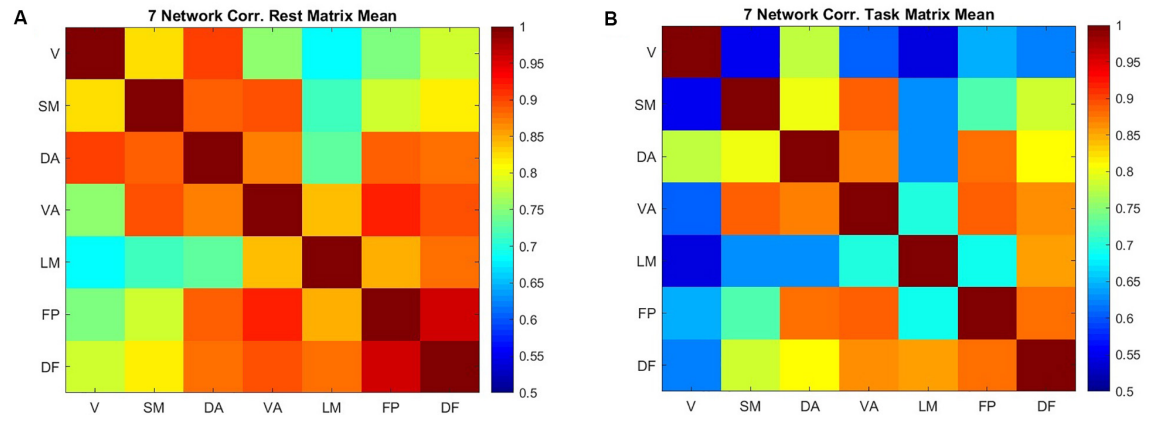

FIGURE 4 | The correlation between the mean value of sample entropy for seven cortical networks across 200 scans (100 subjects) in resting state **(A)** and performing a working memory task **(B)**.

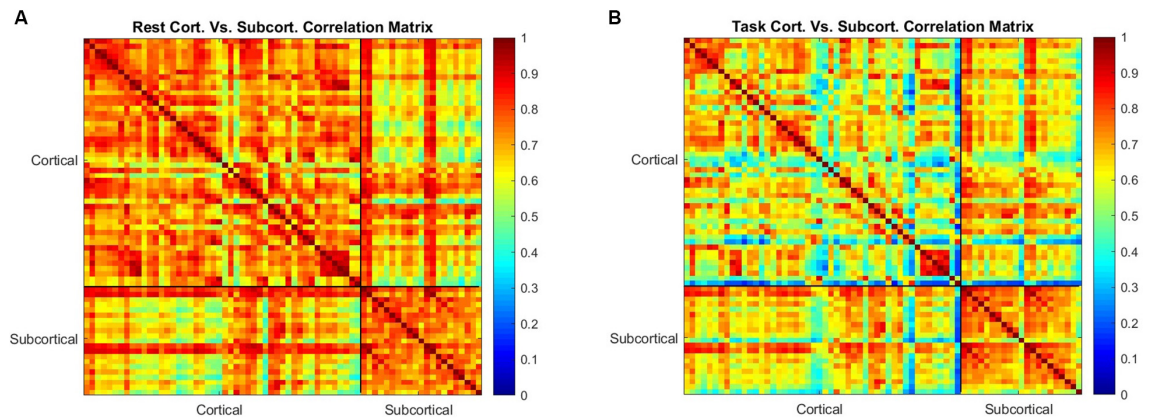

FIGURE 5 | The correlation between the mean value of sample entropy for 42 cortical and 21 subcortical regions of interest as a measure of similarity in rest is shown in **(A,B)** shows the correlation between the same regions during the working memory task. Correlation is generally reduced during task performance, but the subcortical regions are less affected than the cortical regions.

TABLE 3 | Two-factor ANOVA comparing mean cortical/subcortical entropies in 200 scans at task and rest.

Source	Sum of squares	d.f.	Mean square	F score	*p*-Value
Rest/task	0.0164	1	0.0164	34.2164	7.1983e-09
Cortical/ subcortical	0.0115	1	0.0115	23.9758	1.1815e-06
Interaction	8.7399e-05	1	8.7399e-05	0.1824	0.6695
Error	0.3815	796	4.7928e-04		
Total	0.4095	799			

TABLE 4 | Two-factor ANOVA comparing mean network entropies in 200 scans at task and rest.

Source	Sum of squares	d.f.	Mean square	F score	*p*-Value
Rest/task	0.0691	1	0.0691	148.3814	2.7085e-33
Networks	0.0231	6	0.0039	8.2657	6.8201e-09
Interaction	0.0062	6	0.0010	2.2006	0.0402
Error	1.2980	2786	4.6589e-04		
Total	1.394	2799			

network are categorized within moderate reliability and dorsal attention network, limbic network, frontoparietal network, and default mode network are categorized within fair reliability.

At the group level, the measurements are quite consistent. Values are given in **Table 6**. The correlation between average entropy values for the seven networks across the two scans is 0.96 during rest, and 0.87 during task. The lower group-level correlation during task is consistent with the reduced consistency during task observed at the individual level.

DISCUSSION

In this article sample entropy was used to quantify the temporal complexity of fMRI data. The complexity of time-series obtained from healthy subjects in resting state and during the performance

TABLE 5 | Consistency of entropy values in seven functional networks for scan 1 and scan 2.

	Rest			Task		
	ICC	***r***	***p* Two-tail**	**ICC**	***r***	***p* Two-tail**
Visual	0.454	0.456	0.883	0.429	0.432	0.845
Somatomotor	0.474	0.475	0.092	0.467	0.468	0.915
Dorsal attention	0.513	0.523	0.755	0.365	0.369	0.321
Ventral attention	0.586	0.587	0.834	0.454	0.466	0.177
Limbic	0.525	0.527	0.660	0.345	0.363	0.107
Frontoparietal	0.554	0.556	0.464	0.370	0.382	0.174
Default mode	0.535	0.539	0.700	0.381	0.400	0.377

TABLE 6 | The average entropy and standard deviation of each network for scan 1 and scan 2.

	Rest				Task			
	Scan 1 ($\bar{x}$)	**Scan 1 (σ)**	**Scan 2 ($\bar{x}$)**	**Scan 2 (σ)**	**Scan 1 ($\bar{x}$)**	**Scan 1 (σ)**	**Scan 2 ($\bar{x}$)**	**Scan 2 (σ)**
Visual	0.19235	0.02226	0.19202	0.02018	0.1781	0.0174	0.1777	0.0198
Somatomotor	0.18497	0.02280	0.18109	0.02171	0.1765	0.0231	0.1767	0.0247
Dorsal attention	0.19045	0.02187	0.19108	0.01849	0.1857	0.0189	0.1834	0.0217
Ventral attention	0.19084	0.02180	0.19043	0.02078	0.1832	0.0198	0.1800	0.0249
Limbic	0.18790	0.02287	0.18892	0.02466	0.1800	0.0199	0.1756	0.0276
Frontoparietal	0.19515	0.02043	0.19650	0.01854	0.1838	0.0192	0.1804	0.0247
Default mode	0.19129	0.02115	0.19204	0.01880	0.1836	0.0182	0.1814	0.0248

of a working memory task were calculated. Furthermore, Pearson correlation was calculated to examine the similarity between the complexities of different brain networks across individuals.

Our results add to existing studies of complexity in the BOLD signal to show that entropy varies across brain networks and during working memory as compared to rest. In general, entropy decreases during a task in a network-dependent manner. Moreover, when examined across subjects, entropy tends to change in the same way across many brain areas, giving rise to strong correlations within subcortical regions and within subcortical regions. Interestingly, the correlation is weaker between subcortical and cortical regions, suggesting that while entropy within each region tends to change in the same way across subjects, there is greater variability in the relation between the two regions at the individual level.

Entropy During Rest and Task Performance

Entropy across the brain has an average value of 0.1913 ± 0.023 (in rest) and 0.1815 ± 0.019 (in working memory task), indicating that it falls within a fairly narrow range. Within this range, however, there are distinct variations across networks and between cortical and subcortical structures. The cortical areas both in the task data and rest data demonstrate significantly lower entropy in comparison to the subcortical areas. These findings are consistent with previous work by Jia et al. (2017), who created a sample entropy map of the brain in healthy subjects and showed higher values in the caudate, the olfactory gyrus, the amygdala, and the hippocampus, and lower values in primary sensorimotor and visual areas. If entropy of the BOLD signal is taken as a surrogate for neural complexity, this indicates that the neural activity in the cortical areas is more organized than in subcortical areas, in line with the general view of the cortex as the primary site of most cognitive processes. The decrease in entropy in both cortical and subcortical areas during the working memory task might then reflect an increase in the coordination of activity needed to perform the task. Interestingly, the decrease in entropy was not limited to areas typically activated by the task. For example, the extensive activation during the task is observed in the frontoparietal network (Barch et al., 2013), but comparable changes in entropy are found in networks like the limbic network that are not typically activated. Moreover, the default mode network is deactivated during task performance, so that if entropy directly reflected activity, entropy there should increase during the task. In fact, we observe a decrease in entropy instead, evidence that entropy is sensitive to aspects of the BOLD signal that are not directly tied to activity levels. These findings are consistent with a previous study by Zhang et al. (2016), who observed differences in entropy across fMRI studies while subjects were listening passively to (i) emotionally neutral words alternating with no word as the control condition (neutral-blank), and (ii) threat-related words alternating with emotionally neutral word as the experimental condition (threat-neutral). The relative independence of entropy measures from changes in the BOLD signal associated with activation during a task suggests they may provide complementary insight into brain function.

Similarity Across Networks

In both rest and task, the entropy of both the visual network and the limbic network tends to be less coupled to other brain

networks across individuals. For the most part, the relationship between networks is similar across rest and task. However, during the working memory task, the entropy in the dorsal attention network becomes less coupled to entropy in the visual and somatomotor networks. When the brain is further divided into 69 parcels, the decoupling between areas is especially noticeable in the cortex, where there are clear differences in the amount of change in correlation between particular cortical areas during the task. This suggests that there may be an interesting amount of individual variability that relates to task performance, and future work should examine whether particular patterns of entropy changes during task predict performance on the task by the individual subject.

Limitations

As with all BOLD-based measurements, the entropy calculated here is based on the hemodynamic response to neural activity rather than the activity itself. The inherent lowpass filter of the vasculature limits the frequency content of the signal and reduces the amount of information it carries. However, the change in entropy observed during task performance is promising evidence that some of the information about the complexity of neural activity is preserved in the BOLD signal.

CONCLUSION

BOLD-based measurements of sample entropy vary across brain regions, with lower values in cortical than subcortical areas. During performance of a working memory task, entropy decreases across the whole brain but in a region-dependent manner. Both of these findings are consistent with the idea that entropy encodes information about the complexity of neural activity that is separate from simple measurements of activation. When examined across individuals, entropy changes are generally correlated, particularly within cortical and within subcortical areas. More variability in this correlation is observed during the working memory task, hinting at potentially important differences at the subject level that may be linked to performance.

DATA AVAILABILITY STATEMENT

The datasets generated for this study are available on request to the first author.

AUTHOR CONTRIBUTIONS

HT and MN performed the data preprocessing and analysis. SK and MN performed the results interpretation, comparison of obtained results with existing materials, preparation of document. All authors contributed to the article and approved the submitted version.

FUNDING

This work was supported by the National Science Foundation BCS INSPIRE 1533260, National Institutes of Health R01NS078095 and 1R01MH111416-01. Data were provided by the Human Connectome Project, WU-Minn Consortium (Principal Investigators: David Van Essen and Kamil Ugurbil; 1U54MH091657) funded by the 16 NIH Institutes and Centers that support the NIH Blueprint for Neuroscience Research; and by the McDonnell Center for Systems Neuroscience at Washington University.

ACKNOWLEDGMENTS

A sincere thanks to Behnaz Yousefi, Xiaodi Zhang, Anzar Abbas, Eric Maltbie and Wenju Pan for participating in lively discussions regarding this work.

REFERENCES

Barch, D. M., Burgess, G. C., Harms, M. P., Petersen, S. E., Schlaggar, B. L., Corbetta, M., et al. (2013). Function in the human connectome: task-fMRI and individual differences in behavior. *NeuroImage* 80, 169–189. doi: 10.1016/j.neuroimage.2013.05.033

Bergström, R. M. (1969). An entropy model of the developing brain. *Dev. Psychobiol.* 2, 139–152. doi: 10.1002/dev.420020304

Biswal, B. B., Mennes, M., Zuo, X. N., Gohel, S., Kelly, C., Smith, S. M., et al. (2010). Toward discovery science of human brain function. *Proc. Natl. Acad. Sci. U.S.A.* 107, 4734–4739. doi: 10.1073/pnas.0911855107

Chang, C., and Glover, G. H. (2010). Time-frequency dynamics of resting-state brain connectivity measured with fMRI. *NeuroImage* 50, 81–98. doi: 10.1016/j.neuroimage.2009.12.011

Chen, L., Vu, A. T., Xu, J., Moeller, S., Ugurbil, K., Yacoub, E., et al. (2015). Evaluation of highly accelerated simultaneous multi-slice EPI for fMRI. *NeuroImage* 104, 452–459. doi: 10.1016/j.neuroimage.2014.10.027

Feinberg, D. A., Moeller, S., Smith, S. M., Auerbach, E., Ramanna, S., Glasser, M. F., et al. (2010). Multiplexed echo planar imaging for sub-second whole brain fmri and fast diffusion imaging. *PLoS One* 5:e15710. doi: 10.1371/journal.pone.0015710

Ferenets, R., Vanluchene, A., Lipping, T., Heyse, B., and Struys, M. M. R. F. (2007). Behavior of entropy/complexity measures of the electroencephalogram during propofol-induced sedation: dose-dependent effects of remifentanil. *Anesthesiology* 106, 696–706. doi: 10.1097/01.anes.0000264790.07231.2d

Hutchison, R. M., Womelsdorf, T., Allen, E. A., Bandettini, P. A., Calhoun, V. D., Corbetta, M., et al. (2013). Dynamic functional connectivity: promise, issues, and interpretations. *NeuroImage* 80, 360–378. doi: 10.1016/j.neuroimage.2013.05.079

Jenkinson, M., Bannister, P., Brady, M., and Smith, S. (2002). Improved optimization for the robust and accurate linear registration and motion correction of brain images. *NeuroImage* 17, 825–841. doi: 10.1016/S1053-8119(02)91132-8

Jenkinson, M., Beckmann, C. F., Behrens, T. E. J., Woolrich, M. W., and Smith, S. M. (2012). Review FSL. *NeuroImage* 62, 782–790. doi: 10.1016/j.neuroimage.2011.09.015

Jenkinson, M., and Smith, S. (2001). A global optimisation method for robust affine registration of brain images. *Med. Image Anal.* 5, 143–156. doi: 10.1016/S1361-8415(01)00036-6

Jia, Y., Gu, H., and Luo, Q. (2017). Sample entropy reveals an age-related reduction in the complexity of dynamic brain. *Sci. Rep.* 7, 1–10. doi: 10.1038/s41598-017-08565-y

Keilholz, S. D. (2014). The neural basis of time-varying resting-state functional connectivity. *Brain Connect.* 4, 769–779. doi: 10.1089/brain.2014.0250

Keilholz, S. D., Billings, J. C. W., Wang, K., Abbas, A., Hafeneger, C., Pan, W. J., et al. (2016). "Multiscale network activity in resting state fMRI," in *Proceedings of the Annual International Conference of the IEEE Engineering in Medicine and Biology Society*, (Cuenca: EMBS), 61–64.

Keilholz, S. D., Magnuson, M. E., Pan, W. J., Willis, M., and Thompson, G. J. (2013). Dynamic properties of functional connectivity in the rodent. *Brain Connect.* 3, 31–40. doi: 10.1089/brain.2012.0115

Kolmogorov, A. N. (1998). On tables of random numbers. *Theor. Comput. Sci.* 207, 387–395. doi: 10.1016/S0304-3975(98)00075-9

Merisaari, H., Tuulari, J. J., Karlsson, L., Scheinin, N. M., Parkkola, R., Saunavaara, J., et al. (2019). Test-retest reliability of Diffusion Tensor Imaging metrics in neonates. *NeuroImage* 197, 598–607. doi: 10.1016/j.neuroimage.2019.04.067

Milchenko, M., and Marcus, D. (2013). Obscuring surface anatomy in volumetric imaging data. *Neuroinformatics* 11, 65–75. doi: 10.1007/s12021-012-9160-3

Pincus, S. M. (1991). Approximate entropy as a measure of system complexity. *Proc. Natl. Acad. Sci. U.S.A.* 88, 2297–2301. doi: 10.1073/pnas.88.6.2297

Richman, J. S., and Moorman, J. R. (2000). Physiological time-series analysis using approximate entropy and sample entropy. *Am. J. Physiol. Heart Circ. Physiol.* 278, H2039–H2049.

Schrödinger, E. (1945). *What is Life? The Physical Aspect of the Living Cell*. Cambridge: Cambridge University Press.

Shalit, H. (1985). PRACTITIONERS' CORNER calculating the gini index of inequality for individual data. *Oxf. Bull. Econ. Stat.* 47, 185–189. doi: 10.1111/j.1468-0084.1985.mp47002006.x

Singer, W. (2009). The brain, a complex self-organizing system. *Eur. Rev.* 17, 321–329. doi: 10.1017/S1062798709000751

Sokunbi, M. O., Fung, W., Sawlani, V., Choppin, S., Linden, D. E. J., and Thome, J. (2013). Resting state fMRI entropy probes complexity of brain activity in adults with ADHD. *Psychiatry Res. Neuroimaging* 214, 341–348. doi: 10.1016/j.pscychresns.2013.10.001

Van Essen, D. C., Ugurbil, K., Auerbach, E., Barch, D., Behrens, T. E. J., Bucholz, R., et al. (2012). The human connectome Project: a data acquisition perspective. *NeuroImage* 62, 2222–2231. doi: 10.1016/j.neuroimage.2012.02.018

Wang, Z., Li, Y., Childress, A. R., and Detre, J. A. (2014). Brain entropy mapping using fMRI. *PLoS One* 9:e89948. doi: 10.1371/journal.pone.0089948

Xing, X. X., and Zuo, X. N. (2018). The anatomy of reliability: a must read for future human brain mapping. *Sci. Bull.* 63, 1606–1607. doi: 10.1016/j.scib.2018.12.010

Yeo, B. T., Krienen, F. M., Sepulcre, J., Sabuncu, M. R., Lashkari, D., Hollinshead, M., et al. (2011). The organization of the human cerebral cortex estimated by intrinsic functional connectivity. *J. Neurophysiol.* 106, 1125–1165. doi: 10.1152/jn.00338.2011

Zhang, Y., Brady, M., and Smith, S. (2001). Segmentation of brain MR images through a hidden Markov random field model and the expectation-maximization algorithm. *IEEE Trans. Med. Imaging* 20, 45–57. doi: 10.1109/42.906424

Zhang, Y., Liang, J., Lin, Q., and Hu, Z. (2016). Exploiting complexity information for brain activation detection. *PLoS One* 11:e0152418. doi: 10.1371/journal.pone.0152418

Zuo, X. N., Xu, T., and Milham, M. P. (2019). Harnessing reliability for neuroscience research. *Nat. Hum. Behav.* 3, 768–771. doi: 10.1038/s41562-019-0655-x

Conflict of Interest: The authors declare that the research was conducted in the absence of any commercial or financial relationships that could be construed as a potential conflict of interest.

Advantages of publishing in Frontiers

OPEN ACCESS
Articles are free to read for greatest visibility and readership

FAST PUBLICATION
Around 90 days from submission to decision

HIGH QUALITY PEER-REVIEW
Rigorous, collaborative, and constructive peer-review

TRANSPARENT PEER-REVIEW
Editors and reviewers acknowledged by name on published articles

Frontiers
Avenue du Tribunal-Fédéral 34
1005 Lausanne | Switzerland

Visit us: www.frontiersin.org
Contact us: info@frontiersin.org | +41 21 510 17 00

REPRODUCIBILITY OF RESEARCH
Support open data and methods to enhance research reproducibility

DIGITAL PUBLISHING
Articles designed for optimal readership across devices

FOLLOW US
@frontiersin

IMPACT METRICS
Advanced article metrics track visibility across digital media

EXTENSIVE PROMOTION
Marketing and promotion of impactful research

LOOP RESEARCH NETWORK
Our network increases your article's readership